



## Water – A Microwave Material for Advanced Wave Control and Sensing

**Jacobsen, Rasmus Elkjær**

*Publication date:*  
2021

*Document Version*  
Publisher's PDF, also known as Version of record

[Link back to DTU Orbit](#)

*Citation (APA):*  
Jacobsen, R. E. (2021). Water – A Microwave Material for Advanced Wave Control and Sensing. Technical University of Denmark.

---

### General rights

Copyright and moral rights for the publications made accessible in the public portal are retained by the authors and/or other copyright owners and it is a condition of accessing publications that users recognise and abide by the legal requirements associated with these rights.

- Users may download and print one copy of any publication from the public portal for the purpose of private study or research.
- You may not further distribute the material or use it for any profit-making activity or commercial gain
- You may freely distribute the URL identifying the publication in the public portal

If you believe that this document breaches copyright please contact us providing details, and we will remove access to the work immediately and investigate your claim.



Technical University of Denmark

**DTU Fotonik**  
Department of Photonics Engineering

**DTU Electrical Engineering**  
Department of Electrical Engineering

# Water – A Microwave Material for Advanced Wave Control and Sensing

Rasmus Elkjær Jacobsen<sup>1</sup>

PhD Thesis  
2018 – 2021

**Supervisors:** Andrei V. Lavrinenko<sup>1</sup> & Samel Arslanagić<sup>2</sup>,

<sup>1</sup>Department of Photonics Engineering

<sup>2</sup>Department of Electrical Engineering

**Department of Photonics Engineering**

**Technical University of Denmark**

Ørstedes Plads

Bygning 345A

2800 Kongens Lyngby, Denmark

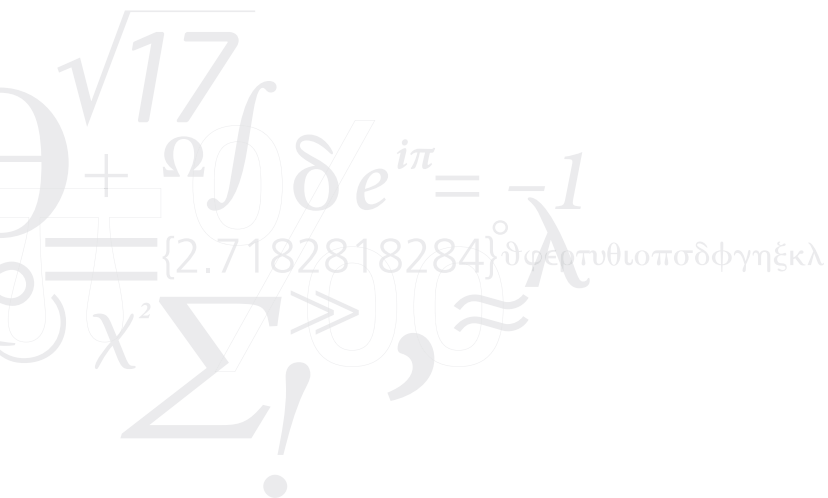
**Department of Electrical Engineering**

**Technical University of Denmark**

Ørstedes Plads

Bygning 348

2800 Kongens Lyngby, Denmark



# Abstract

---

Tunable microwave devices are of great interest as they offer adjustability to their operation, although many of them use rare and expensive materials. In a world with increasing focus on ecological compatibility and recyclability, immense efforts are being made to find bio-friendly alternatives. However, in some cases, one does not have to look far. At microwave frequencies, a high-permittivity dielectric, namely water, is readily available in every household. Recent studies have shown that compact Mie resonators, which are the fundamental blocks in all-dielectric metamaterials and dielectric resonator antennas (DRAs), can be realized with small water inclusions. The temperature-dependent permittivity and liquidity of water enable several ways to reconfigure and tune water-based devices. Moreover, being a polar solvent, water easily dissolves various physiologically important electrolytes, which potentially can be exploited in a sensor design.

In this thesis, we review and demonstrate different water-based devices for microwave control and sensing. First, we review the electromagnetic properties of water and its interaction with microwaves. Subsequently, we study the scattering and absorption of microwaves in single inclusions, and examine how these can be used in various microwave devices including DRAs, metasurfaces, absorbers, radio-frequency components and a structure with a so-called bound state in the continuum (BIC). In our work, we demonstrate a metasurface reflectarray, an electrically small DRA, a Huygens DRA, a microwave heating design and a novel BIC structure. The work comprises both numerical and experimental investigations of their dynamic properties and tunabilities. In particular, we present for the first time a practical BIC localized in a single metal-water resonator exhibiting exciting opportunities for sensing applications.

Our results showcase the potential of water-based devices to be simple, cheap, bio-friendly and tunable alternatives for many microwave applications.



# Resumé

---

Justerbare mikrobølgeenheder har stor interesse, da de tilbyder konfigurerbarhed i deres drift, selvom mange af dem bruger sjældne og dyre materialer. I en verden med stigende fokus på økologisk kompatibilitet og genanvendelighed udøves en enorm indsats for at finde miljøvenlige alternativer. Men i nogle tilfælde behøver man ikke lede længe. Ved mikrobølgefrekvenser er et højt-permittivitet-dielektrikum, nemlig vand, let tilgængeligt i enhver husstand. Nylige undersøgelser har vist, at kompakte Mie-resonatorer, som er de grundlæggende blokke i fuld-dielektriske metamaterialer og dielektriske resonator-antenner (DRA), kan realiseres med små vandindeslutninger. Vands temperaturafhængige permittivitet og væskeform muliggør flere måder at omkonfigurere og justere vandbaserede enheder på. Desuden er vand en polær solvent, og kan dermed let opløse forskellige fysiologisk vigtige elektrolytter, hvilket potentielt kan udnyttes i et sensordesign.

I denne afhandling, demonstrerer og gennemgår vi forskellige vandbaserede enheder til kontrol af og føling med mikrobølger. Først gennemgår vi vands elektromagnetiske egenskaber og dets interaktion med mikrobølger. Derefter studerer vi spredningen og absorptionen af mikrobølger i enkelte indeslutninger, samt undersøger, hvordan disse kan anvendes i forskellige mikrobølgeenheder, såsom DRA'er, meta-flade, radiofrekvenskomponenter og en struktur med en såkaldt bunden tilstand i kontinuemet (BIC). I vores arbejde demonstrerer vi en meta-flade reflektionsarray, en elektrisk lille DRA, en Huygens DRA, et mikrobølgeopvarmningsdesign og en innovativ BIC-struktur. Arbejdet omfatter både numeriske og eksperimentelle undersøgelser af deres dynamiske egenskaber og justerbarheder. Navnlig præsenterer vi for første gang en praktisk BIC lokaliseret i en enkelt metal-vand resonator, som udviser spændende muligheder for sensing-anvendelser.

Vores resultater viser potentialet i vandbaserede enheder som enkle, billige, miljøvenlige og justerbare alternativer til mange mikrobølgeanvendelser.



# Acknowledgements

---

To begin, I would like to express my deepest gratitude to my supervisors Andrei V. Lavrinenko and Samel Arslanagic. Your dedication and complimentary contributions to the project have been invaluable. I believe that this project showcase the example of excellent collaboration between two departments, and what that can transpire into. Your trust and faith in me as a student, but also as a teacher, have helped me mature as a professional academician. I am also very thankful for your understanding of my commitment to my family. Without that, I would not have been able to complete this thesis.

I am grateful to the Plasmonic and Metamaterials group for acknowledging me and my research despite the differences in our work. The group meetings have widen my knowledge and experience within electromagnetics, and helped me grow as a professional.

I am sincerely grateful to the Electromagnetic Systems group for letting me be part of the group, and inviting me to both group meetings and social activities. In particular, I would like to thank all persons involved in my experiments. Without your assistance, I would not have accomplished these result. Furthermore, I want to thank Anne Kok for all our casual conversations giving me sometimes much needed breaks from the studies.

I want to thank Andrea Alú and Alex Krasnok for hosting and helping me during my external stay in the New York. You helped me leverage my research and academic knowledge.

I would also like to thank Polina Kapitanova and the people from ITMO University for hosting me and making my stay in St. Petersburg a pleasant experience.

I am very grateful for all the travel grants from Otto Mønsteds Fond, Augustinus Fonden, Thomas B. Thriges Fond, Marie & M. B. Richters Fond, Reinholdt W. Jorck og Hustrus Fond, Knud Højgaards Fond and William Demant Fonden, which I received during my time as a PhD student. Without them, I would not have been able to go on my external stays as well as participate in conferences.



At last, I would like to thank my family for their invaluable support and reminding me that life is more than work. A special thanks goes to my wife Anna Guldamner, who has always been there for me and our children.

# Publication list

---

Journal papers and conference contributions produced in the project.

## Journal papers

1. **R. E. Jacobsen**, S. Arslanagić and A. V. Lavrinenko, "Review: water-based devices for advanced control of electromagnetic waves," *submitted*, Apr. 2021.
2. **R. E. Jacobsen**, S. Arslanagić and A. V. Lavrinenko, "Mie resonances in water spheres for microwave metamaterials and antennas," *URSI Radio Science Letters*, vol. 1, Dec. 2019. doi:10.46620/19-0011
3. **R. E. Jacobsen**, J. Ø. Nielsen, A. V. Lavrinenko and S. Arslanagić, "Tunable water-based metasurface for anomalous wave reflection," *Journal of Physics D: Applied Physics*, vol. 53, 505104, Oct. 2020. doi:10.1088/1361-6463/abb2bb
4. **R. E. Jacobsen**, A. V. Lavrinenko and S. Arslanagić, "Electrically small water-based hemispherical dielectric resonator antenna," *Applied Sciences*, vol. 9, 4848, Nov. 2019. doi:10.3390/app9224848
5. **R. E. Jacobsen**, A. V. Lavrinenko and S. Arslanagić, "A water-based Huygens dielectric resonator antenna," *IEEE Open Journal of Antennas and Propagation*, vol. 1, pp. 493-499, Sept. 2020. doi:10.1109/OJAP.2020.3021802
6. **R. E. Jacobsen**, A. Krasnok, S. Arslanagić, A. V. Lavrinenko and A. Alú, "Boundary-induced embedded eigenstate in a single resonator for advanced sensing," *submitted*, Dec. 2020. <https://arxiv.org/abs/2103.03685>

## Conference contributions

1. **R. E. Jacobsen**, A. Krasnok, S. Arslanagić, A. V. Lavrinenko and A. Alú, "Embedded eigenstate in a single resonator," accepted in *the Conference on Lasers and Electro-Optics 2021 (CLEO)*, San Jose (CA), US, May 9-14, 2021.

2. **R. E. Jacobsen**, M. H. Vandborg, A. V. Lavrinenko and S. Arslanagić, "Water-based microwave antennas," in the proceedings of *the 14th European Conference on Antennas and Propagation (EuCAP)*, Online, Copenhagen, Denmark, Mar. 15-20, 2020.
3. J. Ø. Nielsen, **R. E. Jacobsen**, A. V. Lavrinenko and S. Arslanagić, "Water-based microwave reflectarrays," in the proceedings of *the 14th European Conference on Antennas and Propagation (EuCAP)*, Online, Copenhagen, Denmark, Mar. 15-20, 2020.
4. S. Arslanagić, **R. E. Jacobsen**, A. V. Lavrinenko and J. Ø. Nielsen, "Water-based microwave metasurfaces and electrically small antennas," in the proceedings of *the 13th International Congress on Artificial Materials for Novel Wave Phenomena and Metamaterials*, Rome, Italy, Sep. 16-21, 2019.
5. **R. E. Jacobsen**, S. Arslanagić and A. V. Lavrinenko, "Mie resonance-based continuous heating microwave systems," in the proceedings of *the 17th International Conference on Microwave and High Frequency Heating (AMPERE) 2019*, Valencia, Spain, Sep. 9-12, 2019.
6. **R. E. Jacobsen**, S. Arslanagić and A. V. Lavrinenko, "Continuous heating microwave system based on Mie resonances," in the proceedings of *the 4th International Conference on Metamaterials and Nanophotonics (METANANO) 2019*, St. Petersburg, Russia, Jul. 15-19, 2019. doi:10.1088/1742-6596/1461/1/012035
7. **R. E. Jacobsen**, S. Arslanagić and A. V. Lavrinenko, "Fundamental properties of Mie resonances in water cylinders – TM and TE case studies," in the proceedings of *the 2019 International Symposium on Electromagnetic Theory (EMTS)*, San Diego, US, May 27-31, 2019. doi:10.23919/ursi-emts.2019.8931486
8. **R. E. Jacobsen**, S. Arslanagić and A. V. Lavrinenko, "Fundamental properties of Mie resonances in water spheres," in the proceedings of *the 2019 International Symposium on Electromagnetic Theory (EMTS)*, San Diego, US, May 27-31, 2019. doi:10.23919/ursi-emts.2019.8931459
9. **R. E. Jacobsen**, S. Arslanagić and A. V. Lavrinenko, "Low-loss water-based metasurface in waveguide environment," in the proceedings of *the 48th European Microwave Conference (EuMW)*, Madrid, Spain, Sept. 25-27, 2018, pp. 819-822. doi:10.23919/EuMC.2018.8541501

10. **R. E. Jacobsen**, S. Arslanagić and A. V. Lavrinenko, "Thermal tuning of a microwave water-based metasurface," in the proceedings of *the Swedish Microwave Days 2018*, Lund, Sweden, May 24-25, 2018.

## **Additional contributions**

S. Arslanagić, **R. E. Jacobsen** and A. V. Lavrinenko, "Vand som alternativt elektromagnetisk materiale i mikrobølge- og antennteknik," *KVANT*, vol. 31, no. 2, Jun. 2019.



# Contents

---

<b>Abstract</b>	<b>i</b>
<b>Resumé</b>	<b>iii</b>
<b>Acknowledgements</b>	<b>v</b>
<b>Publication list</b>	<b>vii</b>
<b>Contents</b>	<b>xi</b>
<b>1 Introduction</b>	<b>1</b>
<b>2 Wave-water interactions – fundamentals</b>	<b>5</b>
2.1 Electromagnetic properties of water . . . . .	5
2.1.1 Polarization of water . . . . .	7
2.2 Scattering and absorption of electromagnetic waves in water . . . . .	15
2.2.1 Scattering and absorption from passive water volumes . . . . .	16
2.2.2 Radiation from water volumes with integrated radiators . . . . .	17
2.3 Summary . . . . .	18
<b>3 Applications of water in microwave devices</b>	<b>21</b>
3.1 Overview . . . . .	21
3.2 Mie resonances in single water inclusions . . . . .	22
3.3 Metamaterials and metasurfaces . . . . .	27
3.3.1 Simple and tunable metasurfaces . . . . .	27
3.3.2 Metasurface absorbers . . . . .	30
3.3.3 Metasurface reflectarrays . . . . .	33
3.4 Antennas . . . . .	36
3.4.1 Dielectric resonator antennas . . . . .	37
3.4.2 Directive antennas . . . . .	39
3.4.3 Saltwater antennas . . . . .	42

---

3.5	RF circuit components . . . . .	43
3.6	Intriguing modes . . . . .	44
3.6.1	Toroidal modes . . . . .	44
3.6.2	Bound states in the continuum . . . . .	46
3.7	Heating systems . . . . .	51
3.8	Summary . . . . .	55
<b>4</b>	<b>Summary and outlook</b>	<b>57</b>
<b>A</b>	<b>Paper 1: "Review: water-based devices for advanced control of electromagnetic waves"</b>	<b>61</b>
<b>B</b>	<b>Paper 2: "Mie resonances in water spheres for microwave metamaterials and antennas"</b>	<b>85</b>
<b>C</b>	<b>Paper 3: "Tunable water-based metasurface for anomalous wave reflection"</b>	<b>91</b>
<b>D</b>	<b>Paper 4: "Electrically small water-based hemispherical dielectric resonator antenna"</b>	<b>99</b>
<b>E</b>	<b>Paper 5: "A water-based Huygens dielectric resonator antenna"</b>	<b>111</b>
<b>F</b>	<b>Paper 6: "Boundary-induced embedded eigenstate in a single resonator for advanced sensing"</b>	<b>119</b>
<b>G</b>	<b>Equations and values for the extended water permittivity model</b>	<b>141</b>
	<b>References</b>	<b>143</b>

“

*Water is the driving force of all nature.*

”

– Leonardo Da Vinci (1452–1519)

Water covers more than two third of Earth’s surface and is essential to all known life forms [1–3]. The ubiquity of water in the history and religions of mankind segments its status as perhaps the most crucial substance of our World. Therefore, the importance of freshwater is advocated annually on the 22nd of March by the UN observance day named ‘World Water Day’ [4]. The unique properties of water have been studied intensively for centuries [5–16], and yet some still remain mysteries [17]. Its simple and highly compact molecular structure is an asymmetric arrangement of one oxygen and two hydrogen atoms providing it with a strong polarity and the ability to establish up to four hydrogen bonds. Moreover, it attains extraordinary high heat capacity and enthalpy of vaporization, and it is an excellent solvent and has both cohesive and adhesive abilities. In the presence of an electric field, the water molecules respond through their alignment making bulk water polarized. The polarization of water is usually described by the complex permittivity, and depends on dynamic parameters such as frequency of the electric field and the temperature of water [8]. Compared to other polar substances, water sustains its relatively high permittivity even at higher microwave frequencies. This has been exploited in various microwave devices, primarily demonstrated over the last two decades, including antennas [18–66], metamaterials (MMs) [67–71], metasurfaces (MSs) [72–124], passive single resonators [125–131], MRI systems [132, 133], radio frequency (RF) circuit components [134, 135], sensors [136–141] and heating systems [142–147]. The first water-based antenna originates from the work by Kingsley and O’Keefe published in 1999 [39], and was a simple dielectric resonator antenna (DRA) with multiple



probes. In 2015, inspired by Rybin et al. [70, 71] as well as Popa and Cummer [148], Andryieuski et al. [123] demonstrated the potential of using the dynamic properties of water in microwave all-dielectric MSs. Same year, Yoo et al. [82] demonstrated a MS, consisting of periodic droplets on a flame retardant 4 (FR4) substrate, with wideband absorption. These launched a series of publications on water-based devices as illustrated in Figure 1.1. In general, water-based devices utilize the high permittivity of water to tailor the phase and amplitude of microwaves by invoking strong fields in water inclusions situated in a low-permittivity host. Such high-permittivity inclusions are known to exhibit resonant modes widely referred to as Mie resonances (see e.g. [149, 150]). These modes are the principal mechanisms behind dielectric resonators used in all-dielectric MMs and MSs [151] as well as dielectric resonator antennas [152]. Besides its abundance and natural ecological compatibility, water holds a major advantage over conventional microwave high-permittivity dielectrics: it simply takes up the shape of the container it is put in. The recent progress of 3-D printers enables complex and flexible host structures for water (see e.g. [83, 97]), in which it would be impossible to integrate solid dielectrics such as high-permittivity ceramics. Moreover, water brings several means to reconfigure and tune the devices through modification of the water volume such as redistribution/re-shaping, tempera-

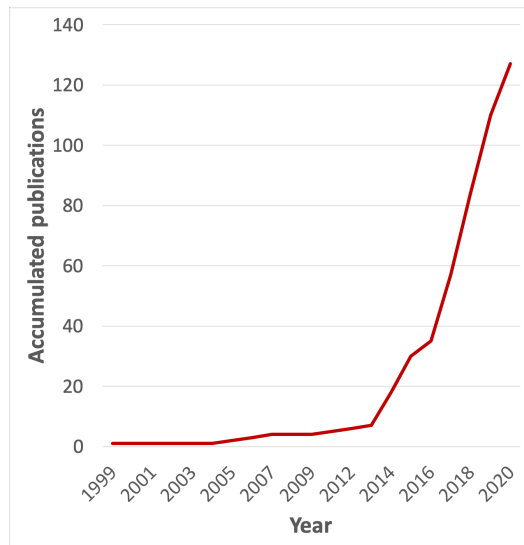


**Figure 1.1:** Accumulated publications on water-based devices from 1999 to 2020.

ture shifts and dissolution of salts, see e.g. [115,123]. This makes water an intriguing alternative material for extremely cheap, simple, ecological compatible and versatile microwave systems, albeit the losses at higher frequencies reduce the overall efficiency.

The purpose of the present work is to investigate water as a material platform for advanced control of microwaves including potential applications within microwave sensing. As a first step, we study the fundamental resonances in single canonical structures [125,128,131], which we later utilize in our work on MSs and antennas. We demonstrate water-based DRAs of various shapes [38,40,51] including a highly subwavelength hemispherical antenna, which can be reconfigured for excitation of either magnetic or electric dipole modes. A Huygens antenna is also investigated with the purpose of increasing the maximum antenna directivity, which is achieved with a simultaneous excitation of both magnetic and electric dipole modes. The measurements of the fabricated prototype antennas are in excellent agreement with the numerical results. Moreover, the tunabilities and reconfigurabilities of our antenna designs are examined through temperature shifts and volume changes of the water as well as repositioning of the embedded feed. In our work on MSs, we first study the frequency-tuning capabilities through temperature-shifts of the water resonators in a MS design from a previous work [116,117]. Secondly, we present a MS based on water cylinders with great on/off switching capabilities of the reflection [109]. Moreover, we examine a MS for anomalous reflection of plane waves enabled and controlled by water resonator disks [110,119]. A prototype is built able to reflect a normally incident plane wave at an angle of  $51.3^\circ$ . The potential of heating water using small water resonators placed inside a simple rectangular waveguide is also investigated [146,147]. Our heating system is self-matched, thus avoiding the need of tuning stubs for matching, and is designed to heat a continuous stream of water. In our latest work [140,141], we demonstrate a novel bound state in the continuum (BIC) structure showcasing for the first time the realization of a simple and compact BIC structure with great sensing potential. Our approach shows that high-Q BICs are possible in single resonator structures in the absence of exotic materials, which otherwise have been necessary thus far.

The thesis is a collection of the manuscripts produced in this project, and is divided into four chapters: The present Chapter 1 is the introduction. In Chapter 2, the general electromagnetic properties of water and its interaction with electromag-

netic waves are summarized. The single relaxation Debye model for the permittivity of water is derived and extended models are presented. We discuss the validity of the water models and examine the dynamic water permittivity. Concluding the chapter, we present and discuss the basic concepts of scattering and absorption by lossy dielectric volumes. Water-based microwave devices are reviewed and summarized in Chapter 3. We present the early development as well as the state of the art in water-based devices and their applications including our own contributions. Finally, in Chapter 4, we summarise and conclude the thesis as well as discuss the outlook of water-based devices. The journal manuscripts are enclosed in Appendices A to F, and are referred to as Paper 1–6, respectively. In addition, the equations for the water permittivity model are provided in Appendix G.

Throughout the thesis, the time factor  $\exp(j\omega t)$ , with  $\omega$  being the angular frequency and  $t$  being the time, is assumed and suppressed.

## CHAPTER 2

# Wave-water interactions – fundamentals

---

In this chapter, we briefly review the electromagnetic properties of water and its interaction with electromagnetic waves. We take outset in its molecular structure and describe how its dipole moment provides a remarkable strong interaction with electric fields. We derive the single relaxation Debye model normally used for the dispersion of water, though recent studies have shown that the underlying reorientation of the water molecules are not Brownian motions (diffusive), but in fact discontinuous 'jumps' instead. Subsequently, we provide the permittivity model by Ellison [8] used for all calculations in this project, and briefly discuss its validity. In Section 2.2 we present and discuss the basic concepts and key parameters of scattering and absorption of electromagnetic waves by water volumes. At last, we summarize the chapter in Section 2.3.

### 2.1 Electromagnetic properties of water

Water is the name of the inorganic molecule dihydrogen monoxide ( $\text{H}_2\text{O}$ ) in its liquid state. In its two other states, it is called ice (solid state) and steam (gaseous state). Uniquely, all three states exist naturally on Earth. However, water is perhaps the most fascinating. It has several uncontested properties with one of them being its very large reaction to electric fields even at high frequencies as well as small and compact spaces such as protein pockets [7]. Water's unique properties stem from its simple molecular structure [6], see a sketch of a single water molecule in Figure 2.1. The molecule consists of two positively charged hydrogen atoms covalently bonded to one negatively charged oxygen atom. The electrons are attracted to the oxygen atom, coming from its higher electronegativity of 3.4 (Pauling scale) over the hydrogen atoms, each holding an electronegativity of 2.2. Thus, the hydrogen atoms are shifted towards one side of the molecule with an angle of  $104.5^\circ$  between the covalent bonds. Coming from the asymmetric arrangement of the atoms, a total positive charge ( $+q_w$

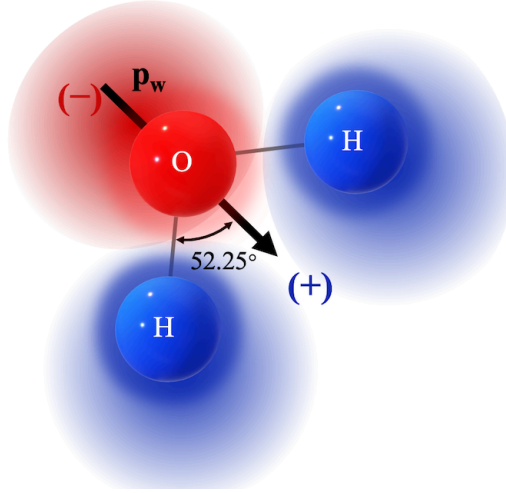


**Figure 2.1:** Sketch of a single water molecule.

[C]) is formed on the side of the hydrogen atoms, whereas on the other side of the molecule, it is negatively charged ( $-q_w$ ), see Figure 2.1. According to Coulomb's law, the two effective charges will exert an electrostatic force on each other. The electrostatic force (i.e. the charges are at rest) acting on the negative charge due to the positive charge is [153]

$$\mathbf{F}_{+-} = -(\hat{\mathbf{r}}_{+-}) \frac{q_w^2}{4\pi\epsilon_0 d_w^2} \quad [\text{N}], \quad (2.1)$$

where  $\epsilon_0$  [F/m] is the free-space permittivity and  $\hat{\mathbf{r}}_{+-}$  is the unit vector pointing from the positive charge to the negative charge. The sign in Eq. (2.1) denotes that the electrostatic force is attractive, and the charges will therefore stay together. Such a formation of two opposite charges is called an electrostatic dipole with the electrostatic dipole moment  $\mathbf{p}_w = \hat{\mathbf{p}}_w q_w d_w$  [C·m], where  $\hat{\mathbf{p}}_w = -\hat{\mathbf{r}}_{+-}$  is the direction of the dipole and  $d_w$  [m] is the distance between the charges. The electrostatic force acting on the negative charge is due to an electrostatic field coming from the positive charge, which is [153]

$$\mathbf{E}_+ = -\frac{\mathbf{F}_{+-}}{q_w} \quad [\text{V/m}], \quad (2.2)$$

Similarly, we can find the electrostatic force acting on the positive charge due to the electric field coming from the negative charge.

The diameter of the water molecule is around 3 Å and the average distance between the molecules is slightly more than 3 Å [6]. This makes water highly compact

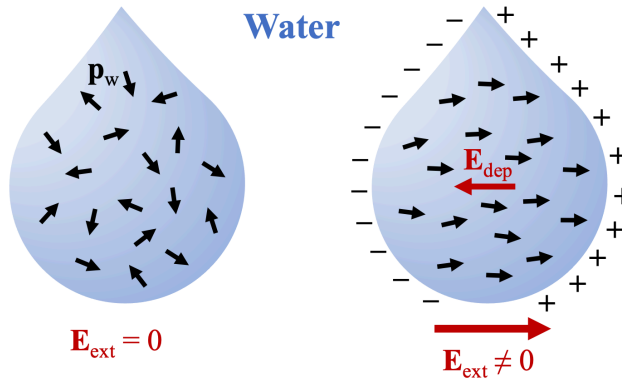


**Figure 2.2:** Sketch of molecular electrostatic dipoles (black arrows) in water with and without an external electric field.

and a water volume of 1 nL has on the order of  $10^{16}$  molecules. In such a bulk water volume, each molecule will form hydrogen bonds to neighbouring molecules, and thus, there will be intermolecular forces as well. At rest, and in the absence of an external electric field  $\mathbf{E}_{ext}$ , the electrostatic dipole moment of each molecule will have different orientations across a small portion of the water volume, see Figure 2.2. This means that the sum of the electrostatic forces coming from all electrostatic dipoles are balanced and thus nets to zero effectively making the material neutral (uncharged). Said in another way, the microscopic electrostatic forces are not translated to the macroscopic level due to the irregular orientations of the electrostatic dipoles. If the electrostatic net force was non-zero, the water would exert an electrostatic force on uncharged bodies, which would contradict observations made in nature.

### 2.1.1 Polarization of water

If we apply an external electric field,  $\mathbf{E}_{ext}$ , in a bulk water volume, Eq. (2.2) shows that a force will be exerted on the electrostatic dipoles. The electrostatic dipoles will try to work against the external field and thus, they will align as shown in Figure 2.2. The induced alignment of the electrostatic dipoles will produce a macroscopic electric field opposite to that of the external field, sometimes called the depolarization field  $\mathbf{E}_{dep}$ . Therefore, the total macroscopic electric field inside the water ( $\mathbf{E}_{dep} + \mathbf{E}_{ext}$ ) is lower than the external electric field, and thus we say that the material is polarized. In water, it is the induced alignment of the electrostatic dipoles that provides the

strong polarization, which we will study in this section.

In Eq. (2.1), we considered the charges to be stationary, however, the water molecules will constantly be in motion as well as break and form new bonds continuously taking place within 1 ps [6]. Furthermore, the water is dispersive and thus will response differently to time-varying fields. In this project, the smallest water volume considered is 10  $\mu\text{L}$ , and the operating wavelengths of the electromagnetic waves are much longer than the distance between the molecules. Therefore, we can safely consider the macroscopic electromagnetic properties of water only. The macroscopic Maxwell equations in the time-harmonic form are [153]

$$\begin{aligned}\nabla \times \mathbf{E} &= -j\omega\mathbf{B}, & \nabla \times \mathbf{H} &= j\omega\mathbf{D} + \mathbf{J}, \\ \nabla \cdot \mathbf{D} &= \rho, & \nabla \cdot \mathbf{B} &= 0.\end{aligned}\quad (2.3)$$

$\mathbf{E}$  [V/m] and  $\mathbf{H}$  [A/m] are the time-harmonic electric and magnetic fields, respectively, and  $\mathbf{D}$  [C/m<sup>2</sup>] and  $\mathbf{B}$  [Wb/m<sup>2</sup>] are the electric and magnetic flux densities, respectively.  $\omega = 2\pi f$  [rad/s] is the angular frequency, where the frequency  $f$  [Hz] denotes the time-harmonic cycle of the fields. The electric source terms are  $\rho$  [C/m<sup>3</sup>] and  $\mathbf{J}$  [A/m<sup>2</sup>] being the free volume charge density and the electric volume current density, respectively.  $j$  denotes the imaginary unit. Please note that fields and quantities in Eq. (2.3) are macroscopic, whereas in Eq. (2.2), they are microscopic.

The polarization of water, as well as any other dielectric, can be described by the polarization vector [153]

$$\mathbf{P} = \lim_{V \rightarrow 0} \frac{\sum_{i=1}^N \mathbf{p}_i}{V} \quad [\text{C/m}^2], \quad (2.4)$$

which is simply implying that we sum  $N$  induced electric dipole moments,  $\mathbf{p}_i$ , in an infinitesimal volume  $V$  [m<sup>3</sup>] of the dielectric. The polarization vector is included in the electric flux density, defined as [153]

$$\mathbf{D} = \varepsilon_0\mathbf{E} + \mathbf{P}, \quad (2.5)$$

In general,  $\mathbf{P}$  can change with position inside the dielectric (in-homogeneity) and the magnitude of the external electric field (nonlinearity) as well as have different direction (an-isotropicity). Furthermore,  $\mathbf{P}$  can depend on other parameters such as the frequency of the external electric field as well as temperature and density of the dielectric. Presently, we consider the water to be homogeneous, linear and isotropic.

Thus,  $\mathbf{P} = \varepsilon_0 \chi_e \mathbf{E}$  with  $\chi_e$  being the electric susceptibility of the dielectric. Eq. (2.5) can then be simplified to

$$\mathbf{D} = \varepsilon \mathbf{E} , \quad (2.6)$$

where  $\varepsilon = \varepsilon_0 \varepsilon_r = \varepsilon_0(1 + \chi_e)$  [F/m] is the permittivity of the dielectric with  $\varepsilon_r$  being the relative permittivity. When a material is polarized, not all the electromagnetic energy is stored in the dielectric. During the polarization process, some of the electromagnetic energy is absorbed by the dielectric. This is due to a momentary delay in the material polarization known as dielectric relaxation. Furthermore, the dielectric can contain ions causing conduction losses. The absorption mechanisms can be included in the imaginary part of the complex permittivity  $\varepsilon = \varepsilon' - j\varepsilon''$ . If the dielectric is lossless,  $\varepsilon'' = 0$ , which can be assumed in some cases for some dielectrics, but generally all dielectrics have losses. Furthermore, all dielectrics are also dispersive (frequency-dependent permittivity). Very often a band of frequencies is investigated, and therefore it is important to have a well-described dispersion model for the materials that are used. Sometimes the dispersion is negligible in the working frequency band, so that the value of  $\varepsilon$  can be considered to be constant. As we will illustrate in the next section, water is certainly dispersive and lossy at microwave frequencies. Moreover, water's permittivity also depends on temperature. Variations of other physical parameters, as e.g. pressure, result in very small changes in water's permittivity, and therefore, we neglect those [8].

### The single relaxation Debye model

The dielectric relaxation of water can be modelled by the Debye relaxation model, which we will derive in this section. To do this, we use the mechanical harmonic oscillator model [153]. Often, the linear displacement of two opposite charges are considered, however, in the case with water, it is perhaps more appropriate to consider a pendulum type setup. Evidently, the two approaches lead to similar result. We consider two charges,  $Q_+$  and  $Q_-$ , with the dipole moment  $\mathbf{p} = \mathbf{r}Q_+$ , see Figure 2.3. We then assume that the negative charge (i.e. the oxygen atom in the water molecule) has a larger mass, and thus the positive charge (the hydrogen atoms) will rotate around the negative charge. The positive charge is then moved by  $\boldsymbol{\theta}$  [m] such that it has a constant motion, i.e. the acceleration is zero, and such that the distance between the charges remains the same. The movement can be done by e.g. applying



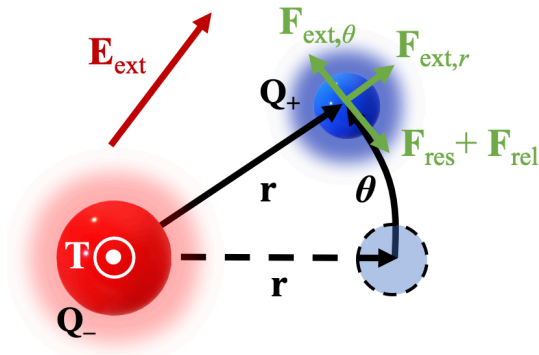


**Figure 2.3:** Sketch of the reorientation of a permanent dipole.

an external electric field. The forces acting on the positive charge will each induce a torque  $\mathbf{T} = \mathbf{r} \times \mathbf{F}$  [N·m] (or  $\mathbf{T} = \mathbf{p} \times \mathbf{E}$ ) on the dipole. The forces are a restoring force  $\mathbf{F}_{\text{res}} = -s\boldsymbol{\theta}$ , a relaxation force  $\mathbf{F}_{\text{rel}} = -Gd\boldsymbol{\theta}/dt$  and a driving force  $\mathbf{F}_{\text{ext}} = \mathbf{E}_{\text{ext}}Q_+ = (\mathbf{E}_{\text{ext},r} + \mathbf{E}_{\text{ext},\theta})Q_+$ . The restoring force works to move the positive charge back to its initial position, and is modelled by a spring, with the tension coefficient  $s$  [kg/s<sup>2</sup>], between the charge and the initial position. The relaxation is due to intrinsic resistance with the damping coefficient  $G$  [kg/s]. Using Newton's first law of motion, we have that

$$\mathbf{F}_{\text{res}} + \mathbf{F}_{\text{rel}} + \mathbf{F}_{\text{ext}} = 0 \iff \gamma \frac{d\boldsymbol{\theta}}{dt} + \omega_0^2 \boldsymbol{\theta} = \frac{Q_+}{m_{Q_+}} \mathbf{E}_{\text{ext},\theta} , \quad (2.7)$$

where  $\gamma = G/m_{Q_+}$  [Hz] and  $\omega_0^2 = s/m_{Q_+}$  are the angular relaxation and resonance frequencies, respectively, with  $m_{Q_+}$  [kg] being the mass of the positive charge. Assuming time harmonic motion,  $\exp(j\omega t)$ , with the angular frequency  $\omega$ , we obtain

$$(j\gamma\omega + \omega_0^2)\boldsymbol{\theta} = \frac{Q_+}{m_{Q_+}} \mathbf{E}_{\text{ext},\theta} . \quad (2.8)$$

We see that it is only the  $\theta$ -component of the driving electric field that contributes to the rotation in Eq. (2.8). As we want to investigate the macroscopic effect, we express Eq. (2.8) in terms of the polarization vector. With direct translation, we assume that the dipole-dipole interaction is zero. This is actually not correct, however, in the case with water, it turns out we still obtain results that fit the permittivity of water [14,16]. Also, we are interested in how the dipoles align with  $\mathbf{E}_{\text{ext}}$ , and not the rotations of dipoles. Therefore, we define the average dipole moment in a volume  $V$  with  $N$

dipole moments as  $\mathbf{p}_{\text{av}} \approx \mathbf{P}V/N \approx \mathbf{r}Q_+$ . Assuming that the macroscopic process takes similar form as Eq. (2.8), we obtain

$$(j\gamma\omega + \omega_0^2)\mathbf{P} = \varepsilon_0\omega_p^2\mathbf{E}_{\text{ext}} , \quad (2.9)$$

where  $\omega_p^2 = NQ_+^2/\varepsilon_0VmQ_+$ . Here we have assumed that the driving electric field is now in parallel with the polarization vector. We then isolate  $\mathbf{P}$  in Eq. (2.9)

$$\mathbf{P} = \varepsilon_0 \frac{\omega_p^2}{\omega_0^2 + j\gamma\omega} \mathbf{E}_{\text{ext}} = \varepsilon_0\chi_e\mathbf{E}_{\text{ext}} , \quad (2.10)$$

and recall that

$$\varepsilon_r(\omega) = 1 + \chi_e = 1 + \frac{\omega_p^2}{\omega_0^2 + j\gamma\omega} . \quad (2.11)$$

We see  $\varepsilon_r(\omega \rightarrow \infty) \rightarrow 1$ , which is not true. Many dielectrics have a finite relative permittivity larger than one at very high frequencies. Therefore, we say that  $\varepsilon_r(\omega \rightarrow \infty) \rightarrow \varepsilon_\infty$ , which is called the optical relative permittivity. Furthermore,  $\varepsilon_r(\omega = 0) = \varepsilon_s = \varepsilon_\infty + \omega_p^2/\omega_0^2$ , which is the static relative permittivity. Substituting these findings into Eq. (2.11), we obtain the general single relaxation Debye model

$$\varepsilon_r(\omega) = \varepsilon_\infty + \frac{\varepsilon_s - \varepsilon_\infty}{1 + j\omega\tau} , \quad (2.12)$$

where  $\tau = \gamma/\omega_0^2 = G/s$  [s] is the relaxation time. The Debye-Stokes model for  $\tau$  describes the relaxation as a sphere of radius  $R$  [m] rotating in a medium with shear viscosity  $\eta(T_{w,K})$  [kg/(m·s)] such that [16]

$$\tau = \frac{4\pi\eta(T_{w,K})R^3}{k_B T_{w,K}} , \quad (2.13)$$

where  $k_B$  [m<sup>2</sup>·kg/(s<sup>2</sup>·K)] is the Boltzmann constant and  $T_{w,K}$  [K] is the temperature of water. For a water molecule,  $R \approx 1.5 \text{ \AA}$ .

In Figure 2.4, we show the relative permittivity spectrum of the single relaxation Debye model for water at the temperature 20 °C. The parameter values are provided in the figure caption and are taken from [8]. The  $\varepsilon_r''$  is maximum at the frequency  $(2\pi\tau)^{-1} \approx 16.5 \text{ GHz}$ , where the slope of  $\varepsilon_r'$  is largest. At higher frequencies,  $\varepsilon_r'$  becomes constant with a value of around  $\varepsilon_\infty = 6.32$ . This would be a very high permittivity at optical frequencies, unfortunately, it is not correct. In fact, the relative permittivity is only around 1.77 in the visible frequencies. Thus, the single relaxation Debye model is not sufficient to cover the full spectral range, and Ellison states that

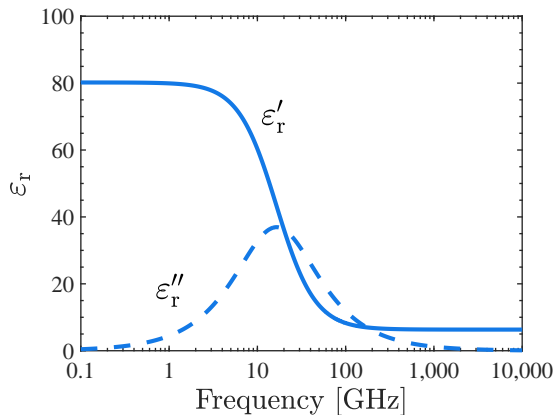


**Figure 2.4:** The single relaxation Debye model for water permittivity at temperature 20 °C. The parameter values used for the calculation are  $\varepsilon_s = 80.2$ ,  $\varepsilon_\infty = 6.32$  and  $\tau = 9.65$  ps, and are taken from [8]. Moreover,  $\varepsilon_r = \varepsilon_r' - j\varepsilon_r''$ .

it holds from DC to around 50 GHz [8]. To increase the frequency range, the permittivity model must be extended, which we will show later, after we have discussed the validity of the Debye model.

Theoretically, it should be possible to use the Debye model for other polar substances besides water. However, it turns out that the fits are poor, and therefore other models, such as e.g. the Cole-Cole relaxation model, should be used instead [154]. Despite of these alternatives, the validity of the Debye model has been questioned and it is now generally accepted that its standard form, which assumes Brownian motions and ignores dipole-dipole interactions, is wrong. These assumptions are not valid for any polar substances, even in the simple case of water [13, 14, 16]. Several explanations to the underlying physics behind water's dispersion have been presented over the last decades. Recent experiments have shown that the reorientation of the water molecules is not diffusive, but occurs as discontinuous 'jumps' due to breaking of the hydrogen bonds. According to [13], the reorientation occurs as the water molecules encounters an appropriate 'defect' of the hydrogen bond network. Otherwise, the water molecules remains in a holding position. This also explains the longer relaxation time in the liquid state (10 ps at 20 °C) compared to the gaseous state (1 ps), where the water molecules move 'freely' around.

### The extended permittivity model for water

The model presented in the previous section only holds up to 50 GHz, and we have not included the temperature-dependence in the model. Several other permittivity models for water have been proposed, see e.g. [16] for a table overview. A very useful model for distilled water (sometimes called 'pure water') was proposed by Ellison in [8]. We must emphasize that the underlying physics of the dispersion models, used by Ellison, is wrong since it is (partially) based on the Debye model. However, the permittivity model fits well with the experimental data for an extremely large frequency band (0-25 THz) and all temperatures (0-100 °C). The model contains three Debye relaxations (first sum) and two molecular resonance terms (second sum), and takes the form

$$\begin{aligned} \varepsilon_{r,w}(\omega, T_w) = \varepsilon_s(T_w) - j\omega \sum_{n=1}^3 \frac{\varepsilon_{\infty,n}(T_w)\tau_n(T_w)}{1 + j\omega\tau_n(T_w)} \\ - j\frac{\omega}{2} \sum_{n=4}^5 \left[ \frac{\varepsilon_{\infty,n}(T_w)\tau_n(T_w)}{1 + j\tau_n(T_w)(\omega + \omega_n)} + \frac{\varepsilon_{\infty,n}(T_w)\tau_n(T_w)}{1 + j\tau_n(T_w)(\omega - \omega_n)} \right], \end{aligned} \quad (2.14)$$

where  $\varepsilon_s(T_w)$  and  $\varepsilon_{\infty,n}(T_w)$  are the static and optical relative permittivities, respectively, and  $\tau_n(T_w)$  are the relaxation times.  $T_w$  [°C] is the temperature of water. The equations and values for the parameter in Eq. (2.14) are provided in Appendix G.

In many cases the full permittivity model provided in Eq. (2.14) is not needed. Depending on the frequencies of interests, the model can be adjusted as displayed in Table G.2. However, one should note that the values of the parameters in Table G.1 changes slightly, due to the extrapolated parameter values varying for different frequency bands. Therefore, one should generally take out the relevant values in Ellison's article [8]. Again, the differences are small (around 1 %), and are smaller than the experimental errors reported by Ellison: Around 85 % of the experimental permittivity values differ by less than 5 % of the estimated permittivity values.

In Figure 2.5, the relative permittivity of water is shown as a function of frequency from 0.1 GHz to 25 THz and for different temperatures from 0 °C to 100 °C. Some permittivity values are also included in Table 2.1. At low frequencies. the permittivity gets smaller as the temperature rises. However, at higher frequencies (see e.g. Table 2.1,  $f = 10$  GHz), it is only the imaginary part that decreases with increasing temperature, whereas the real part increases. In this work, we have primarily considered frequencies below 3 GHz, where, generally, it is the dynamics of the real

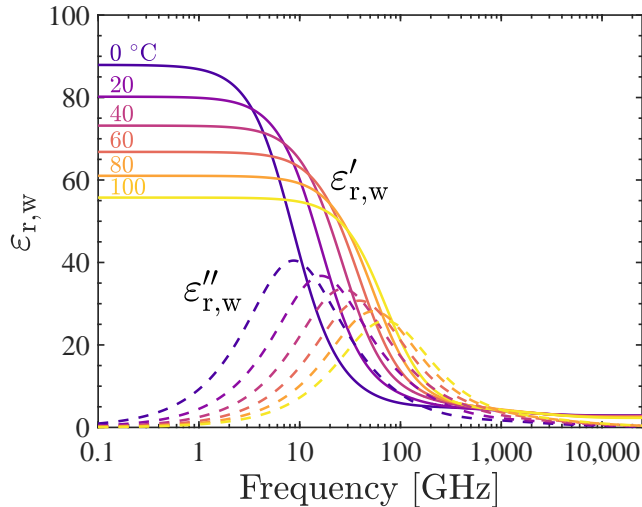


**Figure 2.5:** Relative complex permittivity spectrum of water for different water temperatures. The calculations was done with a simple Matlab script, made by the present author, and is based on the model in Eq. (2.14) with  $\varepsilon_{r,w} = \varepsilon'_{r,w} - j\varepsilon''_{r,w}$ .

**Table 2.1:** Relative permittivity values of water.

$T_w$ [°C]	$f = 0.3$ GHz	$f = 1$ GHz	$f = 2$ GHz	$f = 10$ GHz
15	$82.1 - j1.60$	$81.7 - j5.30$	$80.6 - j10.4$	$57.0 - j35.4$
20	$80.2 - j1.35$	$79.9 - j4.49$	$79.1 - j8.88$	$60.2 - j32.7$
25	$78.4 - j1.16$	$78.2 - j3.84$	$77.6 - j7.62$	$62.4 - j29.9$
30	$76.6 - j0.996$	$76.5 - j3.31$	$76.0 - j6.58$	$63.8 - j27.1$

part that receive the most attention, since the imaginary part is just associated with losses. Interestingly, it is not the real part that experiences the largest change with temperature adjustments at these frequencies. For example, the imaginary part is nearly halved at 2 GHz when the temperature is raised from 15 °C to 30 °C, whereas the real part is only reduced by around 6 %. Still, a temperature change from 0 °C to 100 °C reduces the real part of approximately 34 % at 2 GHz. Later, we will see that such a change corresponds to a spectral blue-shift of water-based devices.

## 2.2 Scattering and absorption of electromagnetic waves in water

Our present investigations involve the scattering and absorption characteristics of water-based devices. Therefore, we want to define some key parameters to describe their properties. In general, we can divide the water-based devices into passive and active configurations. For the passive configurations, no active components are integrated into them, and they are illuminated by waves from the outside. The active configurations have integrated active components such as radiators (antennas).

When a water volume (or in general any dielectric volume) is illuminated by an electromagnetic wave with the fields  $(\mathbf{E}_{\text{inc}}, \mathbf{H}_{\text{inc}})$ , there will be scattered fields outside  $(\mathbf{E}_{\text{sca}}, \mathbf{H}_{\text{sca}})$ , as well as inside  $(\mathbf{E}_{\text{ins}}, \mathbf{H}_{\text{ins}})$ , the water volume. The configuration is sketched in Figure 2.6 for a water volume placed in free-space. At the interface of the water volume and free-space, the tangential fields must be continuous according to the boundary conditions

$$\hat{\mathbf{n}} \times (\mathbf{E}_{\text{ins}} - \mathbf{E}_{\text{inc}} - \mathbf{E}_{\text{sca}}) = 0 , \quad (2.15a)$$

$$\hat{\mathbf{n}} \times (\mathbf{H}_{\text{ins}} - \mathbf{H}_{\text{inc}} - \mathbf{H}_{\text{sca}}) = 0 , \quad (2.15b)$$

where  $\hat{\mathbf{n}}$  is the outward normal vector to the interface. Here, we have assumed that no free surface currents exists at the interface. Furthermore, the normal fields are discontinuous at the interface

$$\hat{\mathbf{n}} \cdot (\varepsilon_{\text{r,w}} \mathbf{E}_{\text{ins}} - \mathbf{E}_{\text{inc}} - \mathbf{E}_{\text{sca}}) = \rho_{\text{free}} / \varepsilon_0 , \quad (2.15c)$$

$$\hat{\mathbf{n}} \cdot (\mathbf{H}_{\text{ins}} - \mathbf{H}_{\text{inc}} - \mathbf{H}_{\text{sca}}) = 0 , \quad (2.15d)$$

where  $\rho_{\text{free}}$  [C/m<sup>2</sup>] is the free charge surface density, which can exist on lossy dielectrics. Eq. (2.15) are the key to determine the scattered and induced fields created by known sources in all electromagnetic studies. For example, in our studies of scattering and absorption of canonical water volumes, in particular the plane wave incidence on single spheres and cylinders, we used Eqs. (2.15a) and (2.15b) to determine the field amplitude coefficients. In Section 3.2, we will present a case study of a single water sphere illuminated by a linearly polarized plane wave.

### 2.2.1 Scattering and absorption from passive water volumes

To characterize the plane wave scattering from passive objects, the total scattering cross section is normally used, which is defined as [149]

$$C_{\text{sca}} = \frac{W_{\text{sca}}}{S_{\text{inc}}} [\text{m}^2], \quad (2.16)$$

where  $S_{\text{inc}} [\text{W}/\text{m}^2]$  is the power density of the incident plane wave and  $W_{\text{sca}} = \int_{\Omega} \mathbf{S}_{\text{sca}} \cdot \hat{\mathbf{n}}_{\Omega} d\Omega [\text{W}]$  is the scattered power that crosses the surface  $\Omega [\text{m}^2]$  of an imaginary sphere of radius  $r_{\Omega} [\text{m}]$  enclosing the scattering object.  $\hat{\mathbf{n}}_{\Omega}$  is the outward normal vector to the imaginary sphere and  $\mathbf{S}_{\text{sca}} = \text{Re}\{\mathbf{E}_{\text{sca}} \times \mathbf{H}_{\text{sca}}^*\}/2$  is the scattered time-averaged Poynting vector, which is usually calculated or measured sufficiently far away from the scattering object such that we are in the far-field region, i.e.  $r_{\Omega} \rightarrow \infty$ . Sometimes, scattering in a specific direction is investigated. In this case, the differential scattering cross section  $dC_{\text{sca}}/d\Omega = r_{\Omega}^2 \hat{\mathbf{n}}_{\Omega} \cdot \mathbf{S}_{\text{sca}}/S_{\text{inc}} [\text{m}^2]$  is used instead.

As the scattering object not only scatters, but also absorbs power, the total power extinct ( $W_{\text{ext}}$ ) from the incident plane wave is the sum of the scattered and absorbed power ( $W_{\text{abs}}$ ). Thus, we define an total extinction cross section, which is

$$C_{\text{ext}} = C_{\text{abs}} + C_{\text{sca}} = \frac{W_{\text{ext}}}{S_{\text{inc}}}, \quad (2.17)$$

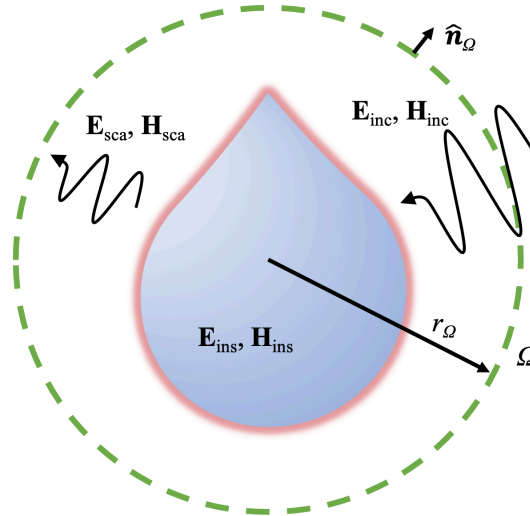


**Figure 2.6:** Passive configuration: sketch of the scattering from a purely dielectric and passive object.

where  $C_{\text{abs}}$  is the total absorption cross section and  $W_{\text{ext}} = -\int_{\Omega} \mathbf{S}_{\text{ext}} \cdot \hat{\mathbf{n}}_{\Omega} d\Omega$  is the total extinct power with  $\mathbf{S}_{\text{ext}}$  being the extinction Poynting vector.

The power absorption in the lossy dielectric happens during the polarization process, where the absorbed electromagnetic energy is converted into heat. For frequencies below the molecular resonances, this loss occurs due to resistance of charges and dipoles being forced away from their equilibrium. The absorbed power in a lossy dielectric can be found via Poynting's theorem on conservation of electromagnetic energy, and is [153]

$$P_{\text{abs}} = \frac{\omega \varepsilon_0}{2} \int_V \varepsilon_r'' |\mathbf{E}_{\text{ins}}|^2 dV, \quad (2.18)$$

where  $V$  is the volume of the lossy dielectric and  $dV$  is the infinitesimal volume element. If the dielectric is water, then  $\varepsilon_r''$  will change with the temperature of water. As the electric field intensity can vary across the water volume, local hot spots can occur. This can result in uneven heating of the water, where  $\varepsilon_r''$  (as well as  $\varepsilon_r'$ ) will vary inside the water volume. If salts (ions) are added to the water,  $\varepsilon_r''$  increases. From Eq. (2.18), we would think that this leads to an increase in  $P_{\text{abs}}$ . However, this can also lead to a reduction in  $\mathbf{E}_{\text{ins}}$  as well, and since  $P_{\text{abs}}$  is proportional to  $|\mathbf{E}_{\text{ins}}|^2$ ,  $P_{\text{abs}}$  is often reduced when  $\varepsilon_r''$  increases. This is especially the case for resonant water-based system, where the field intensities are high, as we will see in Chapter 3. We must note that in the case with low-loss dielectrics, small increases of  $\varepsilon_r''$  will cause a growth in  $P_{\text{abs}}$ .

## 2.2.2 Radiation from water volumes with integrated radiators

In the situation of an active configuration, such as antennas, the source is placed inside or near the dielectric object. That could be a radiator as sketched in Figure 2.7. The radiator induces the internal fields in the dielectric object, which give rise to fields radiated into the surrounding medium. Similarly to Eq. (2.16), we can define the total radiated power,  $P_{\text{rad}} = \int_{\Omega} \mathbf{S}_{\text{rad}} \cdot \hat{\mathbf{n}}_{\Omega} d\Omega$  [W]. If we know the power accepted by the radiator,  $P_{\text{acc}}$  [W], we can define a radiation efficiency as

$$\eta_{\text{rad}} = P_{\text{rad}}/P_{\text{acc}}. \quad (2.19)$$

In antenna setups, the impedance matching of the radiator to an attached feed line is crucial. In this case,  $P_{\text{acc}} = (1 - |S_{11}|^2)P_{\text{in}}$ , where  $P_{\text{in}}$  is the input power to the



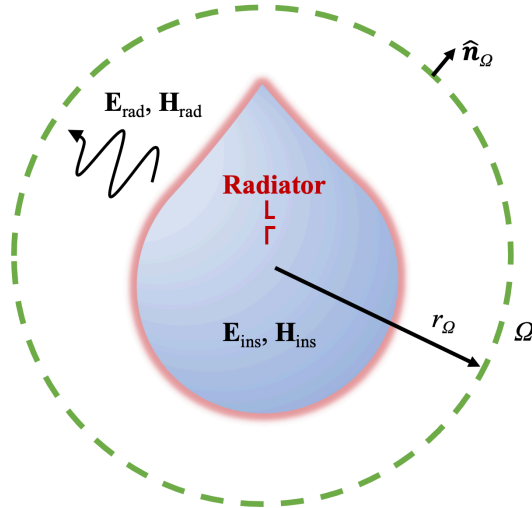


**Figure 2.7:** Active configuration: sketch of the radiation from a dielectric object with a radiator inside.

feed line and  $S_{11}$  is the reflection coefficient given by

$$S_{11} = \frac{Z_{\text{in}} - Z_0}{Z_{\text{in}} + Z_0}. \quad (2.20)$$

$Z_{\text{in}} [\Omega]$  is the input impedance of the antenna and  $Z_0$  is the characteristic impedance of the feed line. A total efficiency can then be defined as

$$\eta_{\text{eff}} = P_{\text{rad}}/P_{\text{in}} = \eta_{\text{rad}}(1 - |S_{11}|^2). \quad (2.21)$$

In Eq. (2.21), the reductions to the radiated power due to both impedance mismatch and absorption are included. In many antenna studies, a lot of effort is devoted to minimize  $S_{11}$ . However, for water-based antennas, the absorption (i.e. radiation losses  $\eta_{\text{rad}}$ ) is just as important as we will show in the next chapter.

## 2.3 Summary

In this chapter, we summarized and reviewed the electromagnetic properties of water. The polarization mechanism of water was discussed and described. We derived the single relaxation Debye model used for the water permittivity for frequencies from DC to 50 GHz. A permittivity model with extended frequency bandwidth was also presented, and we discussed the validity of the permittivity models as recent studies

---

show that the models are based on incorrect assumptions of the motions of water molecules. We found that strong polarization provides water with a relatively high permittivity, but also losses, at microwave frequencies. Moreover, we examined both the frequency- and temperature-dependency of the water permittivity.

In Section 2.2, we presented some key parameters used to describe the scattering and absorption of electromagnetic fields waves in water. We considered both passive and active structures, and discussed the convolution of power absorption in lossy dielectrics.

In the next chapter, we show how water's permittivity can be exploited to realize small Mie resonators, which are the foundations of the water-based devices.



## CHAPTER 3

# Applications of water in microwave devices

---

In this chapter, we review and demonstrate different applications of water in microwave devices. First, we give a table overview of water-based devices. Then we examine the underlying mechanisms of most water-based devices, namely, Mie resonances excited in small water inclusions. Subsequently, various water-based devices are shown including MSs, MMs, antennas, RF circuit components and structures with intriguing modes. Additionally, we show the potential of microwave heating of water. The main results of the project, primarily from Paper 1–6 included in Appendices A to F, are presented along with the work by others. At last, we summarize the chapter in Section 3.8.

### 3.1 Overview

The high permittivity of water at microwave frequencies is utilized in various systems and devices. The most widespread one is perhaps the microwave oven, where the heating of foods is generally connected with the water content. In fact, microwave systems for heating of solids and liquids are an established industry [142–145]. Also rain-radars make use of water drops' ability to scatter microwaves [137–139]. These microwave systems exploit water's high permittivity, but they are not based on water. The microwave oven consists of a metallic cavity with a microwave radiator installed, whereas the rain-radar is composed of an antenna system. These systems function without water and therefore, they are not water-based. Contrary, a water-based device has water integrated as one of its key functional components. It must be said, that some of the devices, particularly antennas, apply water with ions like e.g. NaCl, to increase the conductivity. Normally, the term 'water' is used when distilled or deionized water is used, whereas the term 'liquid' is used for the rest (e.g. saltwater, liquid metal, etc.). However, liquid is the general term for one of the fundamental states of matter, and thus all materials can be liquids. Furthermore, saltwater is

**Table 3.1:** Overview of water-based devices.

Device	Type	References
Single resonator	General study	[125–131]
	MRI	[132, 133]
	BIC sensor	[140, 141]
Metamaterial	Non-resonant	[67]
	Negative index	[68]
	Topological transition	[69]
	Fano resonance	[70]
	Phys. demonstration	[71]
Metasurface	Absorber	[72–107]
	Reflector	[108–120]
	Toroidal mode	[121]
	Sensor	[122]
Antenna	General study	[123, 124]
	Monopole	[18–32]
	DRA	[33–51]
	Helical	[52, 53]
	Patch	[54–57]
	Microstrip loading	[58–63]
	Hybrid	[64]
	Array	[65]
	Yagi-Uda	[66]
RF component	RF tuner	[134]
	RF switches	[135]
Heating system	Continuous heating	[146, 147]

primarily water and is the most widespread liquid on Earth. Therefore, we will also term the devices that utilize saltwater as being water-based. Thus far, these water-based microwave devices have primarily been single resonators [125–133], MMs [67–71], MSs [72–124] and antennas [18–66]. However, recently, water has also found its way into RF circuit tuners [134], RF circuit switches [135], and structures with BICs [140, 141], also known as embedded eigenstates. An overview of some of the microwave devices exploiting the high permittivity of water is provided in Table 3.1. In the following sections, we will discuss the important mechanisms, functionalities and aspects of these devices.

### 3.2 Mie resonances in single water inclusions

The underlying mechanisms behind all-dielectric MMs and MSs are Mie resonances excited in high-permittivity dielectric inclusions situated in low-permittivity dielectric

hosts [151]. As in many other cases, the general theory was developed many years ago and is referred to in many ways such as 'Mie theory', 'Lorenz-Mie theory' or 'Mie scattering' [149, 150, 153]. As the wavelength of electromagnetic waves ( $\lambda_0$ ) scales with  $1/\sqrt{\epsilon_r}$ , the electromagnetic waves in high permittivity dielectrics are severely compressed compared to those in air. This allows the formation of subwavelength resonators composed of high permittivity inclusions. These inclusions take many forms providing different mode(s) excitations and thus allowing engineering of the response of meta-structures. Their forms can be simple spheres or disks, but also more sophisticated shapes, see e.g. [151]. The fundamental modes of the resonators are the magnetic and electric dipoles, but also dark modes such as quadrupoles or even toroidal modes can be excited.

In optics, all-dielectric MSs provide a route to optical magnetism as well as around the problem of intrinsic losses in metallic MSs. At microwave frequencies, the losses in metals are not as pronounced, however, the microwave MSs often consist of both metals and dielectrics, and therefore suffer from both metallic and dielectric losses [155, 156]. Furthermore, metallic MSs often lag tuning parameters limiting their usability. To realize all-dielectric MSs, we need high permittivity dielectrics. Here, water is an obvious candidate at microwave frequencies providing an extraordinary high real part of the relative permittivity of around 80 at room temperature, see Figure 2.5. Furthermore, water brings several tuning parameters coming from its temperature-dependent permittivity and liquid state. In contrast, the widely applied material silicon has a real relative permittivity of 12.

As an example, we investigate the scattering of a linearly polarized plane wave incidence on a water sphere of radius  $r_w$  positioned in free-space, see a sketch of the configuration in Figure 3.1. The incident wave will induce fields inside and around the sphere and give rise to scattered waves. Furthermore, some of the electromagnetic energy extinct from the incident wave is absorbed effectively heating the water. Such a configuration was investigated in Paper 2 and was treated analytically. The expansion coefficients of the scattered fields outside the sphere are given by (see e.g. [149])

$$a_n = \frac{\epsilon_{r,w} j_n(k_w r_w) j_n'(k_0 r_w) - j_n'(k_w r_w) j_n(k_0 r_w)}{\epsilon_{r,w} j_n(k_w r_w) h_n^{(2)'}(k_0 r_w) - j_n'(k_w r_w) h_n^{(2)}(k_0 r_w)} \quad (3.1a)$$

$$b_n = \frac{j_n(k_w r_w) j_n'(k_0 r_w) - j_n'(k_w r_w) j_n(k_0 r_w)}{j_n(k_w r_w) h_n^{(2)'}(k_0 r_w) - j_n'(k_w r_w) h_n^{(2)}(k_0 r_w)}, \quad (3.1b)$$

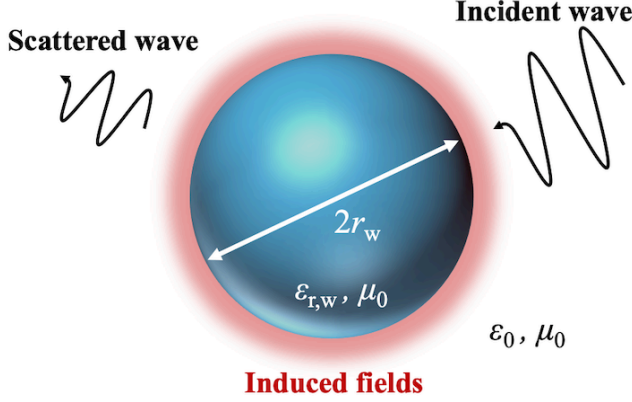


**Figure 3.1:** Sketch of a water sphere in free space illuminated by a plane wave.

where  $k_0 = \omega\sqrt{\varepsilon_0\mu_0}$  is the free-space wavenumber and  $k_w = k_0\sqrt{\varepsilon_{r,w}}$  is the wavenumber in water.  $j_n$  and  $h_n^{(2)}$  are the  $n$ th order spherical Bessel function of the first kind and spherical Hankel function of the second kind, respectively. The prime ' denotes the operation  $g'_n(x) = d[xg_n(x)]/dx$ . To evaluate the response of the sphere, we use the absorption ( $Q_{\text{abs}}$ ), extinction ( $Q_{\text{ext}}$ ) and scattering ( $Q_{\text{sca}}$ ) efficiencies, which are related by

$$Q_{\text{abs}} = Q_{\text{ext}} - Q_{\text{sca}} \quad (3.2a)$$

where

$$Q_{\text{ext}} = \frac{C_{\text{ext}}}{\pi r_w^2} = \frac{2}{(k_0 r_w)^2} \sum_{n=1}^{\infty} (2n+1) \text{Re}\{a_n + b_n\}, \quad (3.2b)$$

$$Q_{\text{sca}} = \frac{C_{\text{sca}}}{\pi r_w^2} = \frac{2}{(k_0 r_w)^2} \sum_{n=1}^{\infty} (2n+1) (|a_n|^2 + |b_n|^2). \quad (3.2c)$$

$C_{\text{ext}}$  and  $C_{\text{sca}}$  are the total extinction and scattering cross sections defined in Eqs. (2.16) and (2.17), respectively.

As an example, we consider a sphere radius of 21.6 mm and set the water temperature to 20 °C. The spectra of the scattering and absorption efficiencies are shown in Figure 3.2. We can divide the response into three parts. Part I: Resonance-free region. The electric dipole is only weakly excited and the incident wave passes almost unperturbedly. Part II: Resonance region. Significant variation of scattering and absorption properties caused by the excitations of dipoles. Part III: Resonance-free

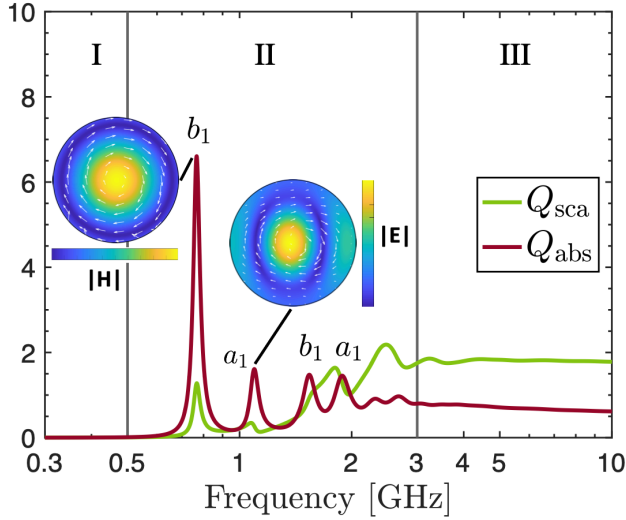


**Figure 3.2:** Scattering and absorption efficiencies spectra from a plane wave incidence on a water sphere with radius 21.6 mm, see the sketch of the configuration in Figure 3.1. The insets show the cross sections of the fields inside the water sphere. The magnetic field (colors) and electric field (arrows) are shown at the magnetic dipole resonance frequency (767 MHz). The electric field (colors) and magnetic field (arrows) are shown at the electric dipole resonance frequency (1092 MHz). The Roman numerals denote the different scattering/absorption regions.

region. As opposed to the region in part I, the response is notable and similar to that of a metallic sphere on the account of its electrically large sizes.

Investigating Part II further, we find two types of modes causing the absorption and scattering peaks. The first mode (the one with the lowest resonance frequency at 767 MHz) corresponds to a magnetic dipole resonance coming from the denominator of  $b_1$  in Eq. (3.1b) going towards the minimum. The second mode (at 1092 MHz) is an electric dipole resonance and is due to the denominator of  $a_1$  in Eq. (3.1a) going towards its minimum value. The fields inside the sphere at the two resonance frequencies are shown in Figure 3.2 as insets. A strong magnetic (electric) field is induced in the center of the sphere with circulating electric (magnetic) fields at 767 MHz (1092 MHz). All higher order modes ( $n > 1$ ) are greatly suppressed by the losses in water with minimal, if any at all, contribution to the scattering and absorption. If the losses were smaller, a narrow-banded magnetic quadrupole would appear as the third resonance, see e.g. [150]. The other absorption peaks in Part II of Figure 3.2 are higher order dipole modes. In general, the absorption is higher than the scattering,



and later we find out that this property gets inherited by a MS arrangement of such spherical particles. A very important aspect of MSs is that their inclusions must be subwavelength in sizes i.e. much smaller than  $\lambda_0$ . In our example, the electrical sizes of the sphere at the fundamental dipole resonances are  $2r_s \approx \lambda_0(767 \text{ MHz})/9$  and  $2r_s \approx \lambda_0(1095 \text{ MHz})/6$ . Compared to many other dielectric resonators, these are indeed very small. For example a silicon sphere ( $\epsilon_r \approx 12$ ) is electrically 2.5 times larger. However, the fundamental problem of these water-based resonators is their blatant absorption. There are different ways to minimize the absorption, and thus increase the scattering, which we list here

- 1. Increase the water temperature:** The permittivity is decreased (both real and imaginary part) resulting in lower absorption as the losses are smaller and the electrical size is larger. The latter makes the maximum electric field intensity lower, and thus reduces the absorbed power, Eq. (2.18). *Complications:* Complex and energy-consuming heating system required.
- 2. Go to lower frequencies:** The losses are smaller at lower frequencies effectively reducing the absorption. *Complications:* Physically larger systems and limited applications operating at these low frequencies ( $< 300 \text{ MHz}$ ).
- 3. Utilize the higher order dipoles:** The larger electrical size reduces the absorption effectively making higher frequency operation available. *Complications:* Physically larger systems are required and resonances are less pronounced.
- 4. Hybrid designs:** Combining water with low-loss dielectric and/or metals. *Complications:* More complicated and expensive designs.

Items 1 and 2 were investigated theoretically in Paper 2 and [125, 128]. Items 3 and 4 are exercised in some antenna and MS designs, and we will present some examples in the following sections.

In [128], we also studied the response of an infinitely long water cylinder. We considered plane wave incidences of different linear polarizations, namely TM and TE polarizations. For the TM polarization, the response was saturated by a very broadband electric dipole mode as the lowest frequency mode (sometimes referred to as a monopole mode). The response for the TE polarization was very similar to that of the sphere. It must be mentioned that realizing a cylinder of infinite length is not feasible. However, adding absorbers around the ends of a truncated cylinder or

inserting it in metallic microwave waveguides are good ways to minimize the proximity effects, see e.g. [109, 121].

### 3.3 Metamaterials and metasurfaces

A few water-based MMs and several MSs have been realized, see Table 3.1. The losses in water limit the usability of MMs as the microwaves propagate inside the structures. This is also why a MM of non-resonant inclusions was investigated in [67]. However, MMs are generally not needed as full wavefront control can be achieved with their 2-D counterparts, MSs [151, 155, 156]. For this reason, we will concentrate on MSs in this section and refer to Paper 1 for more information on water-based MMs. Thus far, most of the water-based MSs have been absorbers, see Table 3.1. The reason is simple: the high permittivity (both real and imaginary part) of water offers an easy and inexpensive route to realize subwavelength resonant inclusions with high absorption and large bandwidth. However, other types of MSs are also achievable, as for example advanced reflectors and switches, which we will show in this section as well.

#### 3.3.1 Simple and tunable metasurfaces

The opportunities with water-based MSs were demonstrated in [82, 123, 124]. For example a MS with a square lattice of identical water spheres was numerically investigated in [123]. The sphere radius is the same as in our example in Figure 3.2 ( $r_w = 21.6$  mm) and the lattice constant is  $a = 75$  mm. A sketch of the configuration is shown in Figure 3.3(a), and its reproduced response for a normally incident plane wave is shown in Figure 3.3(b). The results were obtained in COMSOL Multiphysics. We find that the spectrum is shaped by the Mie resonances in the single sphere: around 770 MHz, the transmission is reduced to approximately 20 % due to the magnetic dipole excited in the spheres. Similarly, the electric dipole excited at 1100 MHz reduces the transmission to around 60 %. In correspondence with the results for a single sphere in Figure 3.2, we see that the absorption is larger than the reflection.

As the resonant water spheres drive the response of the MS, any perturbations to the shape of the water volume or its permittivity will cause a change in the re-

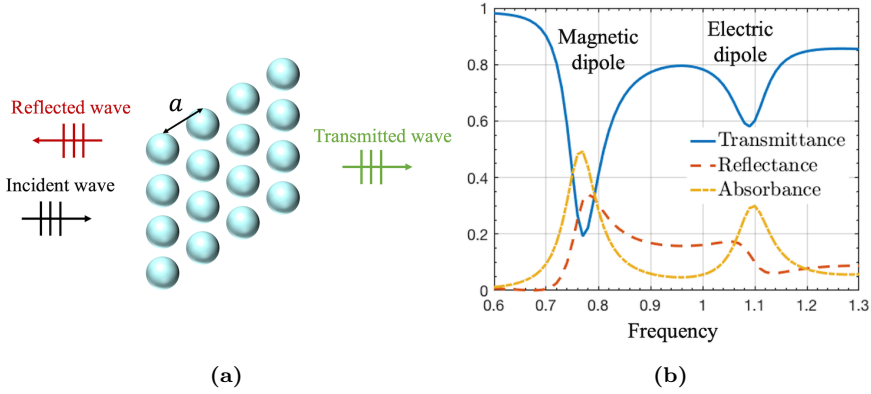


**Figure 3.3:** (a) Sketch of a normal plane wave incidence on a MS consisting of a square lattice of water spheres. (b) Transmittance, reflectance and absorbance spectra of the MS with the sphere radius  $r_s = 21.6$  mm (corresponding to a volume of  $a^3/10$ ) and lattice constant  $a = 75$  mm.

sponse of the MS, see Figure 3.4 [123]. The perturbations can be induced chemically and thermally as well as mechanically with the use of e.g. stretching and pushing plates and acoustic vibrations. The temperature-tuning of the MS is shown with the transmittance spectra for different temperatures in Figure 3.4(a). Increasing the temperature blue-shifts the spectrum and intensifies the resonances (narrowing of the line widths of the minima), and thus follow the tendencies of the single sphere in Section 3.2. This is caused by the lower water permittivity, when the temperature is increased. The change in the transmittance spectrum, due to reshaping of the water inclusions, is shown in Figure 3.4(b). We see that the resonance frequencies can be adjusted almost individually by changing the shape of the water inclusions. For example, the MS of inclusions with horizontal diagonal of  $h = 1.1$  cm has a wider stop band (wider bandwidth with low transmittance) coming from the spectrally close resonances. The adjustable parameters allow tuning of the MS response or utilization as a sensor. However, the general problem with the latter is the low quality factor (Q-factor) of the resonances, which is perhaps why only a few suggest sensing as an application of the water-based MSs, see e.g. [55, 112, 122].

The control of the transmission and reflection can also be achieved by utilizing gravity, see Figure 3.5(a) [124]. By partially filling cavities in a MS, the MS can be rotated, and thus the transmission is changed. The measurements were performed in anechoic conditions and the MS response to both linear and circular polarizations

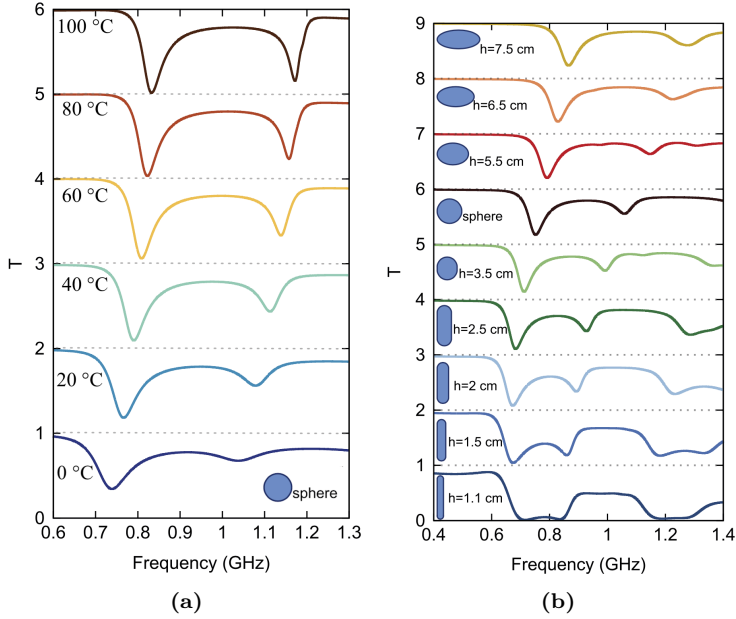


**Figure 3.4:** Perturbations of the MS in Figure 3.3: The transmittance (T) spectra of the MS with water inclusions of different **(a)** temperatures and **(b)** shapes. The lattice constant  $a = 75$  mm and the volume of each water inclusions is  $a^3/10$ . The water temperature is 20 °C and  $h$  designates the horizontal diagonal of the water inclusions in **(b)**. The offset for each spectrum is shown as a dotted grey line. The figures are taken from [123].

was investigated. The measured transmission for different rotation angles of the MS, shown in Figure 3.5(a), is done at a frequency of 1.25 GHz.

In a previous work, we demonstrated a MS with rod-like water inclusions in a Rohacell 51 HF host having switching capabilities, see Figure 3.5(b) [116]. A prototype was fabricated for measurement in a rectangular waveguide. Magnetic dipole resonances were excited in the water inclusions for the original position of the MS ( $0^\circ$  rotation angle) resulting in high reflection of the incident wave. Through  $90^\circ$  rotation of the inclusions, the transmission was greatly enhanced as no resonances were excited. In addition, stacking multiple MSs further decreased the transmission for  $0^\circ$  rotation and increased the transmission for  $90^\circ$  rotation. The tuning potential through temperature control of the MS was presented in [117]. We have also demonstrated a MS consisting of water cylinders having wider switching bandwidth [109]. This was provided by broadband electric dipoles excited in the water cylinders.

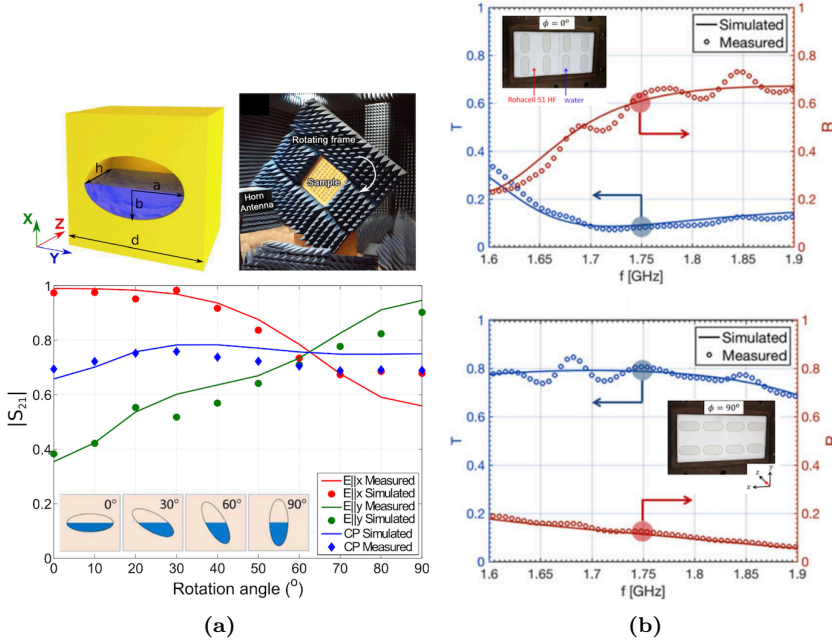


**Figure 3.5:** Control of transmission and reflection by rotation of the MS. **(a)** Measured transmittance spectra of a MS with partially filled cavities for different rotations of a the MS. **(b)** Measured transmittance and reflectance spectra for a MS of rod-like water inclusions with different orientations. The figures in **(a)** and **(b)** are taken from [124] and [116], respectively.

### 3.3.2 Metasurface absorbers

Water-based MS absorbers also make use of resonant water inclusions. They utilize the high permittivity of water to induce spectral series of both magnetic and electric modes as well as other resonance types such as Fabry-Perót resonances. These resonances, together with the losses in water, provide the high absorption. The first water-based MS absorber was presented by Yoo et al. in [82]. The MS consisted of patterned water droplets on a FR4 substrate with hydrophobic/hydrophilic surface patterning on the frontside and a ground conducting plane on the backside, see Figure 3.6(a) for photographs of the MS. The absorption spectra for different volumes of the water droplets are shown in Figure 3.6(b). The MS had an absorption bandwidth (absorptivity higher than 90 %) that covered 43 % of the central frequency, which was achieved with three resonances excited in the MS distributed across its spectrum.

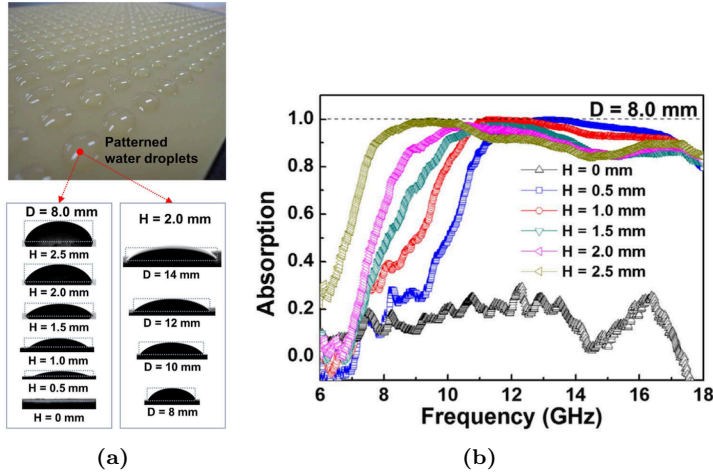


**Figure 3.6:** MS absorber of periodic water droplets. (a) Photograph of MS and contact angle images of a water droplet. (b) Measured absorption spectra for different water droplet heights. Figures are taken from [82].

Since [82], many other MS absorbers have been demonstrated each with improved performance, such as wider bandwidth or less sensitivity to temperature or angle of incidence variations. In Figure 3.7(a), the relative absorption bandwidth is shown as a function of the center frequency for different MS absorbers (see Paper 1 for references). The trend shows that the relative bandwidth increases with the increasing center frequency. We believe that this stems from the dispersion of water's permittivity: the quality factor of the resonances simply decreases as the loss tangent of the water increases, effectively permitting larger relative bandwidths at higher frequencies. It must be emphasized that the tendency will stop as the water permittivity decreases dramatically at even higher frequencies. Many different inclusion shapes have been presented with some being more complex than others. A MS with 3-D printed Swastika-shaped inclusions were investigated in [96], see Figure 3.7(b). The MS is made of polylactic acid host structure with water inclusions connected by fluidic channels. The thickness of the MS is between  $1/10$  and  $6/10$  of the free-space wavelength in the frequency operation band. Here, we emphasize that, besides Mie resonances in the water inclusions, other mechanisms like e.g. Fabry-P rot resonances contribute to the absorption. The MS had wide absorption bandwidth (136 %) and low sensitivity to changes in angle of incidence, wave polarization and temperature.

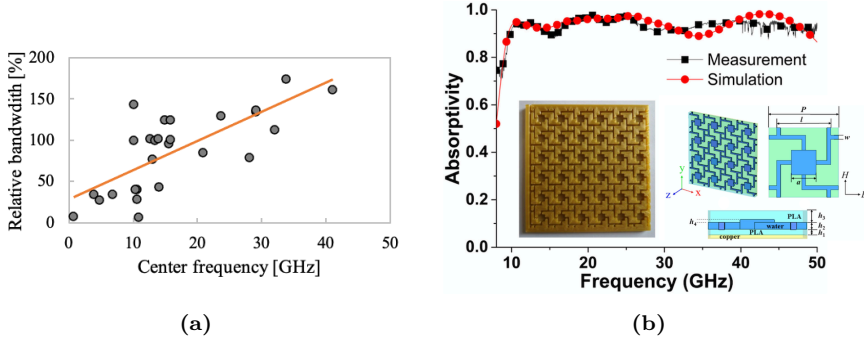


**Figure 3.7:** (a) Relative bandwidth vs. the center frequency for different water-based MS absorbers. (b) Measured and simulated absorptivity spectra of a 3-D printed Swastika-shaped MS absorber. The insets show a photograph and sketch of the MS. The figures in (a) and (b) are taken from Paper 1 and [96], respectively.

Thus, the MS can be employed under various conditions as long as the water does not freeze or boils.

Many of the MS absorbers are backed by a conducting ground plane (normally assumed to be a perfect electric conductor, PEC) effectively reducing the thickness, but also boosting the absorption. The directions of the induced dipoles are tangential to the ground plane and thus the images of the magnetic (electric) dipoles will be in (out of) phase according to the image theorem. In addition, satisfying Kerker's condition in the resonators minimizes the reflection as long as the lattice constant is subwavelength ( $< \lambda_0$ ). Since no transmission is allowed by the ground plane, the incident power is fully absorbed by the MS, when the reflection is zero. Kerker's condition is satisfied with the relationship between the induced magnetic ( $m$ ) and electric ( $p$ ) dipole moments being  $p = cm$ , where  $c$  the speed of light, see e.g. [100,157]. Sometimes, it is stated that the high absorption is achieved with the condition of matching the surface impedance of the MS ( $Z_S$ ) to the characteristic impedance of the surroundings, often assumed to be that of free space,  $Z_0$ . This entails  $Z_S = Z_0$ , and thus the reflection will be zero, since

$$r = \frac{Z_S - Z_0}{Z_S + Z_0}, \quad (3.3)$$

where  $r$  is the reflection coefficient. This is correct, however, often it is then stated, that this is achieved, when  $Z_S = \sqrt{\mu_{\text{eff}}/\epsilon_{\text{eff}}} = \sqrt{\mu_0/\epsilon_0}$ , where  $\mu_{\text{eff}}$  and  $\epsilon_{\text{eff}}$  are the effective permeability and permittivity of the MS. Unfortunately, these parameters

can only be defined for MMs and not MSs, and thus it is not possible to calculate these bulk material parameters, see for example [74].

### 3.3.3 Metasurface reflectarrays

Changing the water volume, or even water temperature, can also be applied in a periodic fashion across the MS to tailor the reflection of the MS [110–114]. Such a MS is called a MS reflectarray [156]. The foundation of these types of MSs lies in the generalized Snell’s law of reflection

$$\sin \theta_r - \sin \theta_i = \frac{\Delta\phi}{k_0 a}, \quad (3.4)$$

where  $\theta_i$  and  $\theta_r$  are the incidence and reflection angles, respectively, and  $\Delta\phi$  is the linear phase change of the reflected field between each inclusion of the MS. In Paper 3, we demonstrated a normally incident plane wave being reflected anomalously, see Figure 3.8. First, a cylindrical water inclusion with a magnetic dipole resonance was identified. Then through variation of the height of the water inclusions, a linear phase shift of  $2\pi$  was induced across a periodic supercell comprising  $N$  inclusions in one direction of the MS. To enhance the reflection, we supported the MS with a conducting ground plane behind it. The fabricated MS consisted of a Rohacell 51 HF host, with permittivity close to that of air, in which holes were drilled, see Figure 3.8(c). Through different distributions of distilled water in the inclusions, the MS can reflect a normally incident wave at various angles. For example, a MS with supercells of  $N = 8$  inclusions provides a reflection at around  $51^\circ$  at 1 GHz for both  $x$ - and  $y$ -polarizations according to Eq. (3.5). Around 90 % of the reflected power is channelled into the targeted angle with the remaining reflected power being reflected normally and at  $-51^\circ$ , see Figure 3.8(b). Due to the water losses, simulations show that around 63 % of the incident power is absorbed. A sketch of the experimental setup is shown in Figure 3.8(c), and consisted of two horn antennas mounted on a metal beam hoisted 2.64 meter above the floor with two tripods. The antennas constituted a two-port system with one antenna (P1) pointing directly at the ground, where the MS was positioned. The position and angle of the other antenna (P2) were adjusted for various angular receptions. The fabricated MS consisted of only four supercells, however, we were still able to observe an enhancement to the reflection at the expected reflection angle, see Figure 3.8(d). The reduced efficiency of the



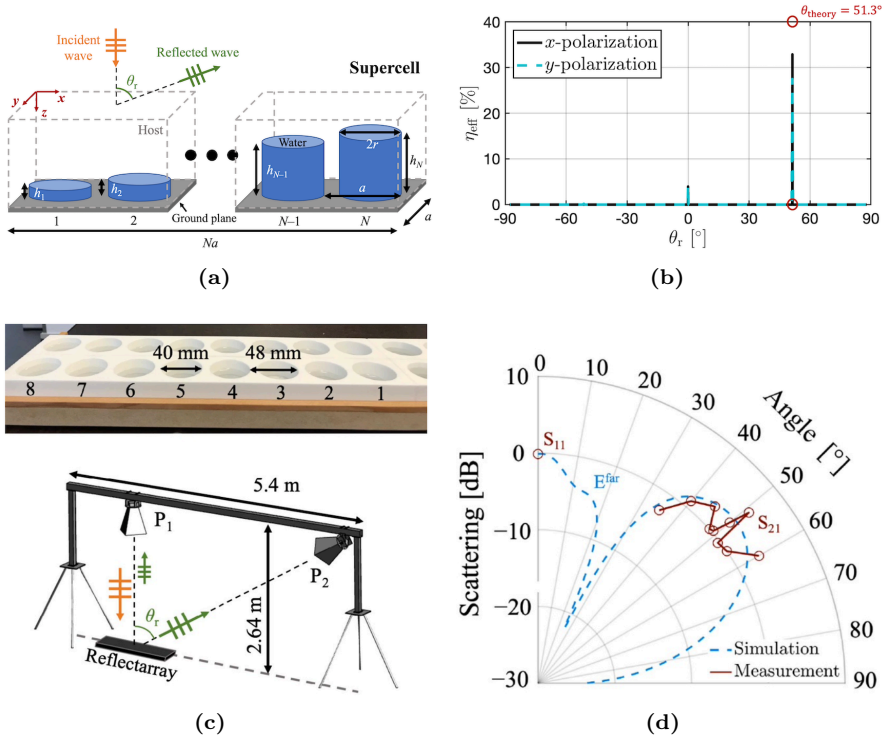


**Figure 3.8:** MS reflectarray. (a) Sketch of the supercell of the reflectarray MS based on cylindrical water-filled inclusions. (b) Simulated reflection efficiency,  $\eta_{\text{eff}} = P_r(\theta_r)/P_{\text{in}}$ , as a function of the reflection angle for both  $x$ - and  $y$ -polarized normal plane wave incidences. (c) Photograph of fabricated MS and sketch of the experimental setup. (d) Simulated and measured scattering as a function of the reflection angle. Figures are taken from Paper 3.

MS is due to the strong resonance and losses in water. A simple way to improve the efficiency is to go to lower frequencies where the losses in water are significantly reduced. Similarly, increasing the water temperature will also reduce the losses in water, however, this would require the addition of a heating system. Alternatively, some of the water can be substituted with a different material like e.g. metal or low-loss dielectric. The Rohacell material used for the prototype is not essential for the functionality and can be replaced with a cheaper and more bio-friendly alternative. This mindset can be expanded to the complete design, such that all materials are ecological compatible that can be recycled or directly decomposed in nature. More details and results can be found in Paper 3.

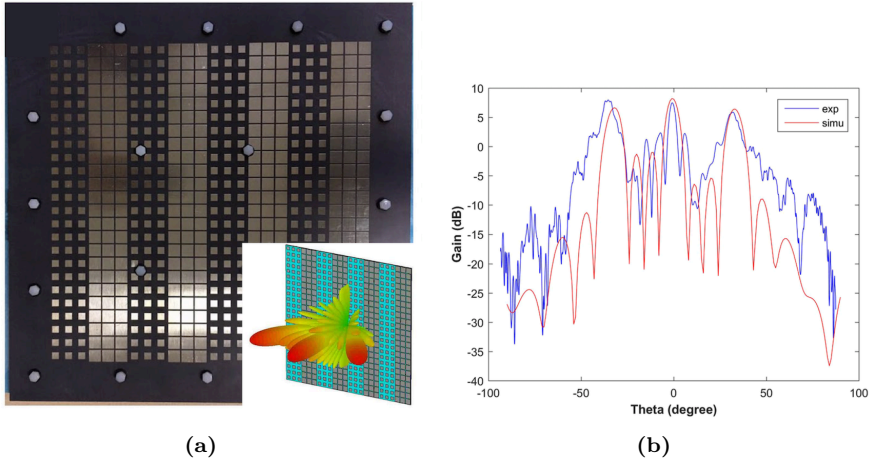


**Figure 3.9:** MS reflectarray with metal-water inclusions. (a) Photograph of the fabricated MS with the coding sequence '01010101'. Inset shows the scattering pattern of the MS with water (b) The measured and simulated scattering pattern (gain in dB). Figures are taken from [112].

A MS consisting of metallic and water inclusions was investigated in [112], see Figure 3.9. Through different 'coding' sequences of the inclusions, the reflection of the MS could be engineered. The MS consisted of a sheet of Teflon woven glass (F4B) with metallic patches of different sizes backed with a saline water substrate and metallic ground conducting plane. The reflection was controlled by varying the water salinity. Additionally, the scattering pattern could be altered by reconfiguration of the metal coding pattern. In Figure 3.9(a), the MS with the metallic patch coding sequence '01010101' is shown. The simulated and measured scattering pattern is shown in Figure 3.9(b). This coding pattern generates three main lobes, whereas another coding pattern is shown to produce five main lobes. In another work [114], diodes were incorporated into the MS providing another mean of tuning by switching the bias voltage of the diodes between on/off.

Besides the reflectarray, we have also investigated the potential of a water-based transmitarray [158]. Such a configuration, would require the removal of the ground plane in Figure 3.8 to allow transmission. As the ground plane mirrors the resonator, and thus contributes to the induced phase shift, we cannot achieve a full  $2\pi$  phase shift with the excitation of a single mode in the water. Hence, we need to excite multiple modes. From our study of Mie resonances in single water inclusions, Figure 3.2,

we know that only magnetic and electric dipole modes can be excited in the water inclusions. In a previous project [159], we demonstrated a water inclusion exhibiting balanced magnetic and electric dipoles. The inclusions provided the desired phase shift, albeit with increased absorption. The anomalous transmission of our best design based on water was only 18 % at 800 MHz operation [158]. We believe that better transmission can be achieved with a hybrid design of water and metal.

### 3.4 Antennas

Many different types of water-based antennas have been demonstrated, see Table 3.1, with most of them being dielectric resonator antennas (DRAs). In this section, we show a few different antenna designs including our own, and discuss their advantages and disadvantages over conventional antennas. Several other antennas have been investigated, which are not shown here. Instead, we refer to Table 3.1 or a detailed review on liquid antennas [33] for more information.

The basic idea of water-based DRAs is to take a single water inclusion and excite it with a small metallic radiator such as a short monopole antenna fed against a large conducting ground plane as sketched in Figure 3.10. The input power  $P_{in}$  is inserted into the feed line, in this case a coaxial transmission line. Without water,

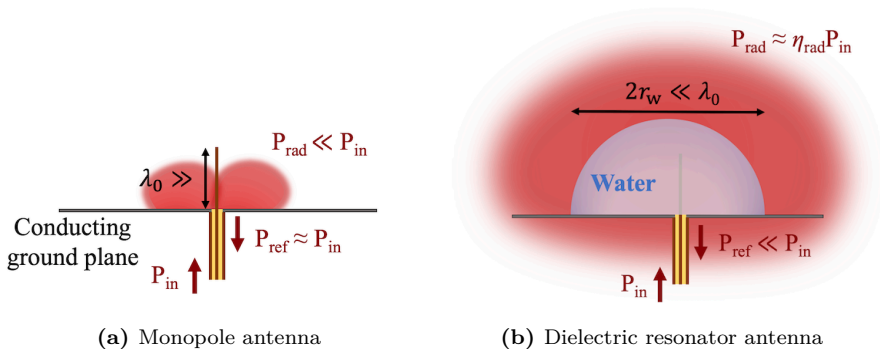


**Figure 3.10:** Sketch of (a) a short monopole antenna and (b) dielectric resonator antenna (DRA). The short monopole antenna is poorly matched to the feed line and free-space, and therefore the radiated power is low. We match the system by encapsulating the short monopole antenna with a hemispherical water volume as well as making minor adjustments to the length and position of the monopole, dramatically increasing the radiated power.

the short monopole antenna brings a very large input impedance nearly impossible to match to a standard feed line of e.g.  $50 \Omega$ , see Figure 3.10(a). Thus, the input power is reflected ( $P_{\text{ref}} \approx P_{\text{in}}$ ) and nearly no power is accepted by the monopole and subsequently radiated to the surroundings. In this section, we will present different types of DRAs as well as a MS antenna and a saltwater antenna.

### 3.4.1 Dielectric resonator antennas

To maximize the radiated power of the monopole antenna in Figure 3.10(a), its length must be increased to  $\lambda_0/4$ , however, this is not very attractive in some situations where space is limited. Alternatively, the monopole antenna is encapsulated by a water element, in this case a hemispherical water volume, as sketched in Figure 3.10(b). By suitable excitation of the natural mode(s) of the water volume (also called eigenmodes), the input impedance of the antenna can be matched to the feed line and efficiently release the power into the surroundings even though the antenna is highly subwavelength. This exact configuration was investigated in Paper 4, see Figure 3.11, representing the smallest water-based antenna to date with  $r_w \approx \lambda_0/18$ . Interestingly, it is possible to excite both magnetic and electric modes in the water volume, albeit at different frequencies, thus enabling control of the radiation pattern. The fabricated antenna was realized by milling a hemispherical cavity in a Rohacell 51

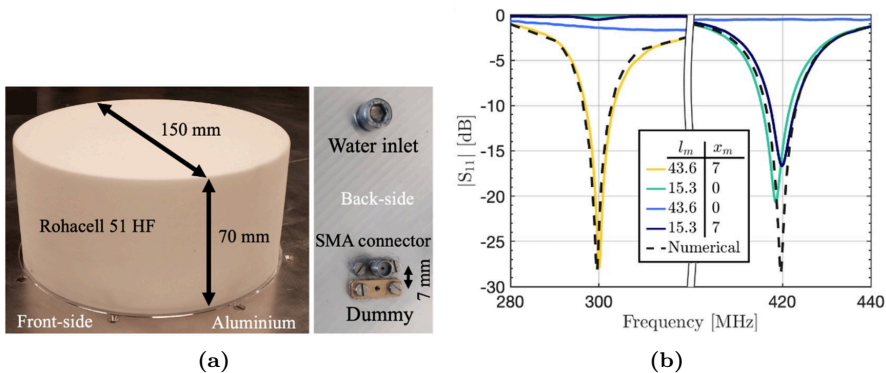


**Figure 3.11:** Hemispherical DRA. (a) Photographs of fabricated antenna. (b) Measured and simulated reflection coefficient spectra for two different configurations of the antenna.  $x_m$  and  $l_m$  are the position and length of the embedded monopole antenna. Figures are taken from Paper 4 [38].

HF block and gluing the block onto an aluminum plate. Water was inserted into the cavity from sealable holes in the aluminum plate, see Figure 3.11(a). The simulated and measured reflection coefficient spectra are shown in Figure 3.11(b). For one placement and size of the embedded monopole antenna, the magnetic dipole resonance is excited around 300 MHz, whereas the electric dipole resonance is excited around 420 MHz with another configuration of the monopole antenna. The small size and losses in water reduced the total efficiency of around  $\eta_{\text{eff}} = P_{\text{rad}}/P_{\text{in}} \approx 30\%$  with the excitation of the magnetic dipole mode. For the excitation of the electric dipole mode,  $\eta_{\text{eff}} \approx 16\%$ . The maximum directivity of the antenna (see Eq. (3.5) for definition) is limited to 3 due to the small size and the excited single dipole mode.

We also investigated various ways of tuning the antenna by e.g. changing the position of the monopole antenna inside the cavity, water temperature shifts and extraction of water. The results can be found in Paper 4. Instead we would like to show another antenna with great tunability and reconfigurability. In [36], a high-efficiency DRA was demonstrated. The DRA is composed of acrylic plastic reservoir boxes on a ground conducting plane. From beneath the ground plane, see Figure 3.12(a), the reservoirs were filled with water, and the water volumes were controlled with an electrical pump system. The measured reflection coefficient spectra for different water fillings are shown in Figure 3.12(b). Through careful control of the water volumes, it is possible to frequency-reconfigure the DRA from 168 MHz to 474 MHz with only a small reduction in the total efficiency from around 95% to 80%. The size of the

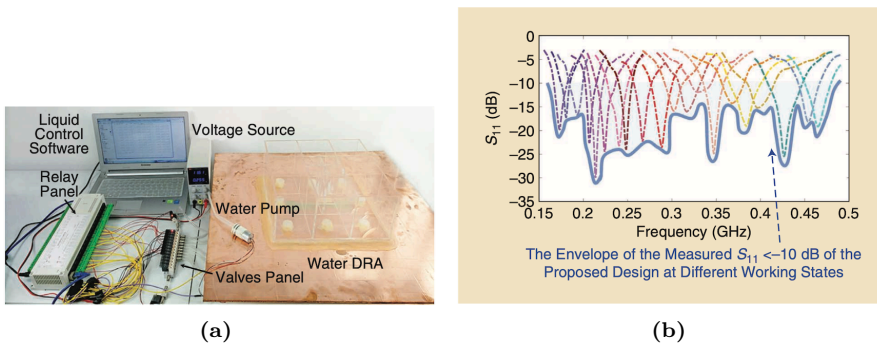


**Figure 3.12:** High-efficiency DRA. (a) Photograph of prototype antenna with the water control system. (b) Measured reflection coefficient spectra for different 'states' (water fillings) of the DRA. Figures are taken from [36].

antenna is approximately  $\lambda_0/8$ , which is more than double the size of our DRA in Figure 3.11. The excited modes are magnetic dipoles, therefore the maximum directivity of the antenna is around 3, same as our DRA. In the next section, we will present different configurations with increased maximum directivities.

### 3.4.2 Directive antennas

The ability of an antenna to channel its radiated power into one direction is described by the maximum directivity defined as

$$D_{\max} = \frac{4\pi U_{\max}}{P_{\text{rad}}}, \quad (3.5)$$

where  $U_{\max}$  is the maximum radiation intensity defined as the maximum power radiated from an antenna per unit solid angle [162]. The maximum directivity of an electrically small dipole is 1.5 (3 with a ground plane). It means that the maximum radiated power is 1.5 times the average radiated power ( $P_{\text{rad}}/4\pi$ ). More widespread is the half-wavelength dipole, which has a slightly higher directivity of 1.67. For higher directivity, usually, larger antennas are needed such as horn antenna, array antenna and parabolic antenna, see Figures 3.13(a) and 3.13(b) for photographs of some of these antennas. The directivity of such antennas span from 5 to  $10^6$ . In the following section, we will present our antenna, which uses a different method to enhance the directivity.

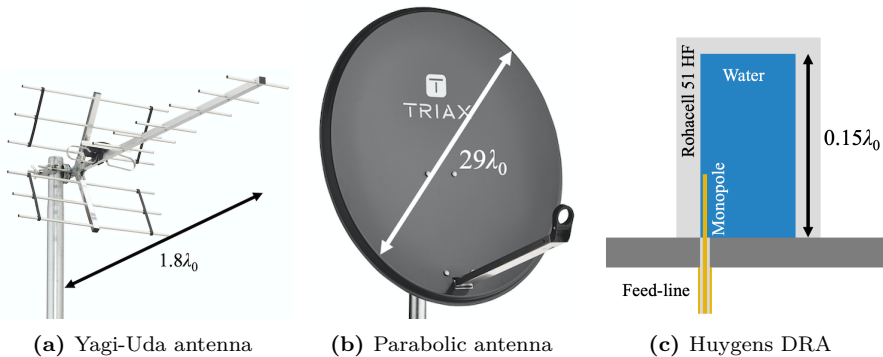


**Figure 3.13:** Photograph of (a) a Yagi-Uda antenna (500 MHz operation,  $D_{\max} \approx 10$ ) taken from [160] and (b) a parabolic antenna (12 GHz operation,  $D_{\max} \approx 10,000$ ) taken from [161]. (c) shows a sketch of our water-based Huygens antenna for 350 MHz operation with  $D_{\max} \approx 6$ . Figure is taken from Paper 5.

## Huygens antenna

It has been shown that the simultaneous excitation of electric and magnetic modes in a subwavelength structure, such that the modes are balanced in a specific way, enhances the radiated power into one direction and reduce it in the other direction(s) [163]. These structures satisfy the so-called (generalized) Kerker's conditions [157], which were discussed in Section 3.3.2. In antenna configurations, they are usually called Huygens sources or Huygens antennas [164]. In Paper 5, we demonstrate a Huygens DRA with balanced magnetic and electric dipoles. The antenna is composed of a cuboid-shaped water-filled cavity on a ground plane, see Figure 3.13(c). The simulated and measured reflection coefficient, as well as radiation pattern, are shown in Figure 3.14. The maximum directivity is 6, which is expected with the two dipoles and the ground plane ( $2 \cdot 1.5 \cdot 2 = 6$ ). The cost of the enhanced directivity is a slightly larger antenna structure ( $\lambda_0/6$ ), however, it is still smaller than e.g. the water-based Yagi-Uda antenna presented in [66] and the antennas shown in Figure 3.13. The total efficiency of the antenna is also larger (60 %), compared the hemispherical antenna in Figure 3.11, which is due to the larger size. Similar to Paper 4, we demonstrated various means of tuning the Huygens antenna, see Paper 5 for more details and results.

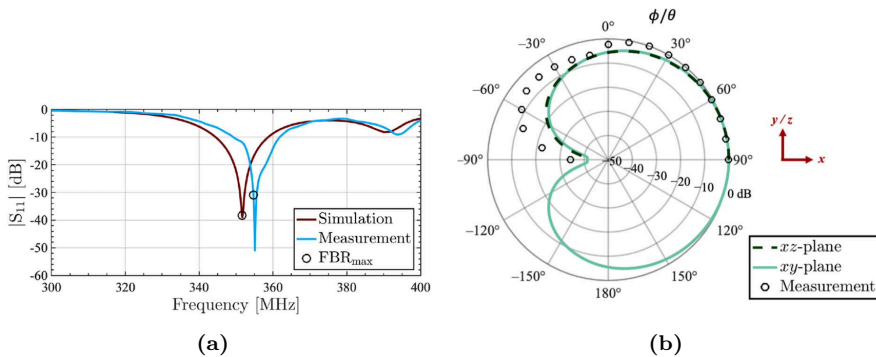


**Figure 3.14:** Results for the Huygens antenna shown in Figure 3.13(c). Simulated and measured (a) reflection coefficient and (b) radiation pattern (normalized directivity). Figures are taken from Paper 5.

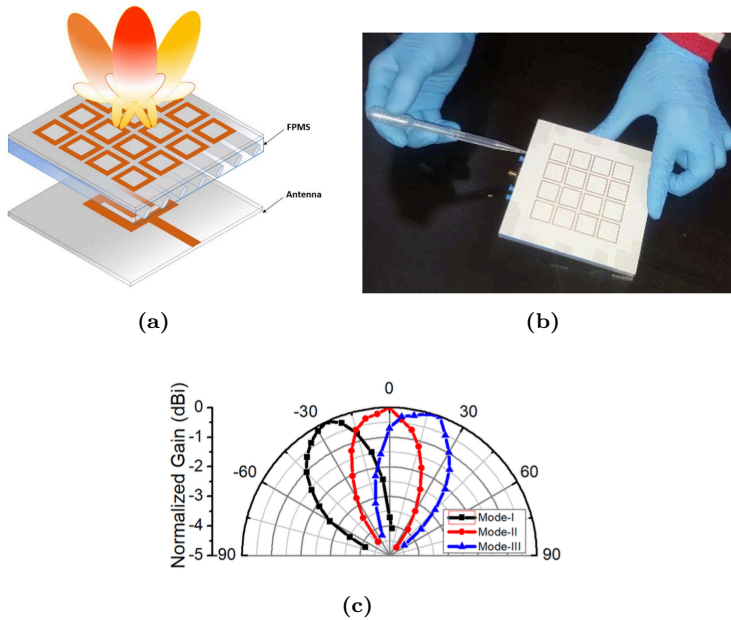


**Figure 3.15:** Array antenna with fluidic channels. (a) Sketch of the antenna and (b) photograph of the fabricated antenna. (c) Measured radiation pattern (normalized gain). Figures are taken from [65].

### Metasurface antennas

MS antennas are great alternatives to the complex, bulky and costly phase array antennas with beam-steering capabilities [156]. Different kinds of tuning of the radiation pattern have been demonstrated including electronic (using e.g. varactor-diodes or electromechanical system) and mechanical. Recently, a MS antenna with embedded fluidic channels for beam-steering control was investigated [65], see Figure 3.15. Through different filling combinations of the fluidic channels, the beam of the antenna could be scanned between  $-20^\circ$  and  $+20^\circ$ . The antenna operates at 2.6 GHz and its thickness is only  $0.06\lambda_0$ . The antenna is matched to its feed line (low reflection coefficient), and the total efficiency of the antenna is mostly affected by the radiation losses. With water (no water), the radiation efficiency is around 45 % (70 %). The area of the antenna is  $(1.04\lambda_0)^2$  and the maximum directivity is approximately 9.2 dB. Thus, the MS antenna has a larger directivity than our Huygens antenna, however, it also has a much larger size. Sometimes, the maximum realized



gain,  $G_{\text{real,max}} = \eta_{\text{tot}} D_{\text{max}}$ , is more appropriate to use when comparing antennas. The MS antenna has  $G_{\text{real,max}} \approx 5.7$  dBi (dBi stands for decibels with respect to an isotropically radiating antenna), whereas the Huygens antenna has  $G_{\text{real,max}} \approx 5.4$  dBi. Thus, their radiation power levels are nearly identical, even though the MS antenna is around six times larger.

### 3.4.3 Saltwater antennas

Some water-based antennas use water with salts to increase their conductivity corresponding to increasing the imaginary part of the permittivity. The higher conductivity pushes the fields towards the surface of the saltwater, and thus the water volume of the antenna behaves as a metallic radiator. In most cases, saltwater antennas comprise a monopole-like structure, see Figure 3.16(a). The theoretical, simulated and measured reflection coefficient and radiation efficiency spectra are shown in Figures 3.16(b) and 3.16(c). The height is approximately 1 m, and a metallic monopole of same height would have a minimum in reflection coefficient at the frequency 75 MHz. which is very close to that of the saltwater antenna. The radiation efficiency is around 75 %, which is lower than a metallic monopole antenna of similar height. The real advantages of the saltwater antenna are its reconfigurability and larger bandwidth. The height of the water can be adjusted, thus frequency-reconfiguration of the

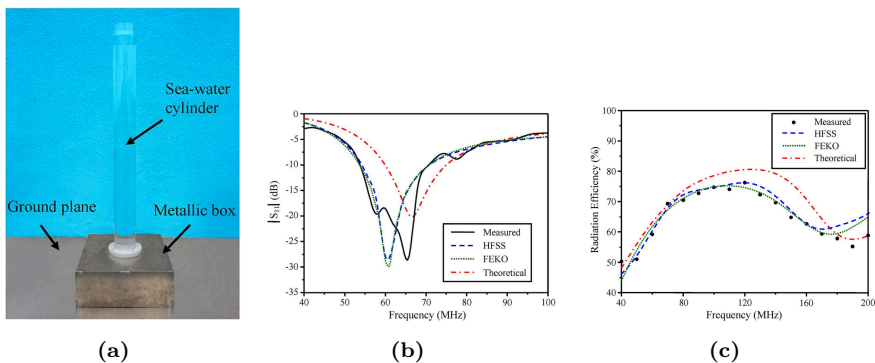


**Figure 3.16:** A monopole saltwater antenna with teflon base. (a) Photograph of the antenna. The height is 1050 mm and the diameter is 100 mm. The relative real part of the saltwater permittivity is 78.7 and the effective conductivity  $\sigma = 4.5$  S/m ( $\epsilon'' = \sigma/\omega$ ). Theoretical, simulated and measured (b) reflection coefficient and (c) radiation efficiency spectra. Figures are taken from [24].

antenna. In general, saltwater antennas are larger than water-based DRAs. However, their bandwidth and efficiency are higher (when comparing all antennas), which come from the fields being concentrated at the surface of the saltwater, whereas the fields go deep into the water volume of the DRAs.

All saltwater antennas – as well as most of those based on distilled water – are not electrically small i.e.  $k_0 r_A < 1$  (0.5 when supported with ground plane), where  $r_A$  is the radius of the sphere enclosing the antenna. The simple explanation is that the smaller the antenna is, the higher the field intensities are, thus resulting in higher absorption. However, the water-based antennas hold some advantages over conventional metallic ones: water brings multiple tuning parameters and transparency and, compared to other high-permittivity dielectrics, it is both cheap and ecologically compatible. On the other side, their losses decrease the overall efficiency and they are not weather-stable. However, some have shown efficiencies above 90 %, and there are different ways to reduce water's melting point, which can be done by e.g. adding an antifreeze additive or salts [64].

### 3.5 RF circuit components

Until recently, the inclusion of liquids in RF circuit components was nearly an unexplored territory. Fluidic microwave components display a way towards tunable passive microwave components. So far, mostly liquid-metal has been employed in a wide variety of component types [165]. Some water-based components have been demonstrated, see Figure 3.17. In [135], a coplanar waveguide (CPW) with a water drop placed on top was examined. The response could be switched between transmission and absorption states by simply changing the position of the water drop. In addition, the CPW line can be suspended in bulk water for maximum absorption of waves.

An RF circuit tuner with distilled water inclusions has also been demonstrated [134]. A photograph is included in Figure 3.17(b). Through water filling of cascaded water containers, the operational frequency could be tuned between 0.9 GHz and 2.4 GHz. As a proof of concept, it was successfully incorporated with an RF amplifier.

Additionally, we want to mention a field-effect transformer (FET) with a water drop atop presented in [166]. The electrostatic characteristics of the FET was exam-

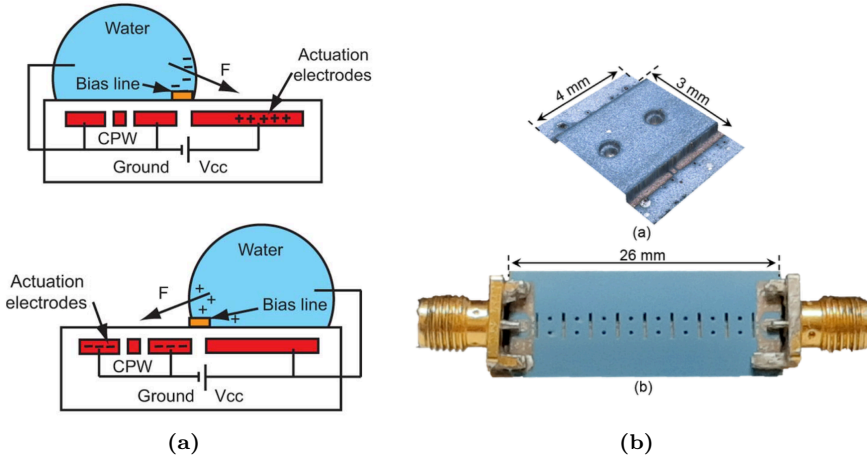


**Figure 3.17:** Water in RF circuit components. **(a)** Sketch of a coplanar waveguide (CPW) loaded with a drop of water. Figure is taken from [135]. **(b)** Photograph of the RF tuner. The figure is taken from [134].

ined. With the water drop, the FET could support rapid bias changes, high on/off current ratios, near-ideal sub-threshold swing and enhanced short-channel behavior. We think that its characteristics for microwave frequencies operation would be interesting to investigate.

### 3.6 Intriguing modes

Although dipole modes are versatile and relatively easy to excite, they also possess limited Q-factor and scatter in many directions. Therefore, extensive effort is expended in the research of other modes. In this section, we show different structures with complex mode excitations including toroidal modes and BICs. In the latter, we present our recent ground-breaking results demonstrating a BIC in a single resonator, which is utilized for advanced sensing analyses in a drop of water.

#### 3.6.1 Toroidal modes

Toroidal dipoles are the terms in multipole expansion of moments, which can be excited in structures of toroidal topology. They are of great interest in MMs and MSs due to their low scattering. In particular, when they are co-excited with an electric

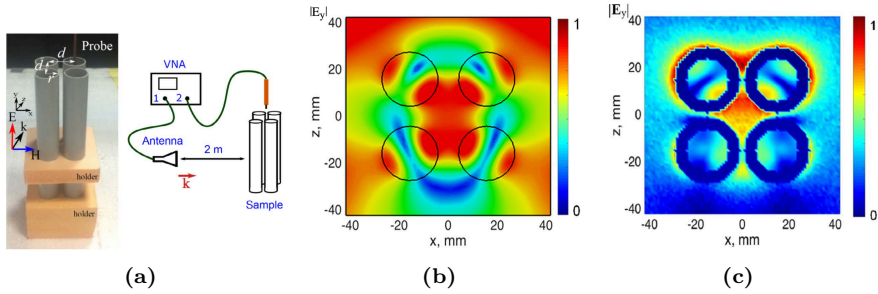


**Figure 3.18:** Toroidal mode in a structure of four water cylinders. (a) Sketch and photograph of the experimental setup. (b) Simulated (1.1 GHz) and measured (0.98 GHz)  $y$ -component of the electric field. Figures are taken from [130].

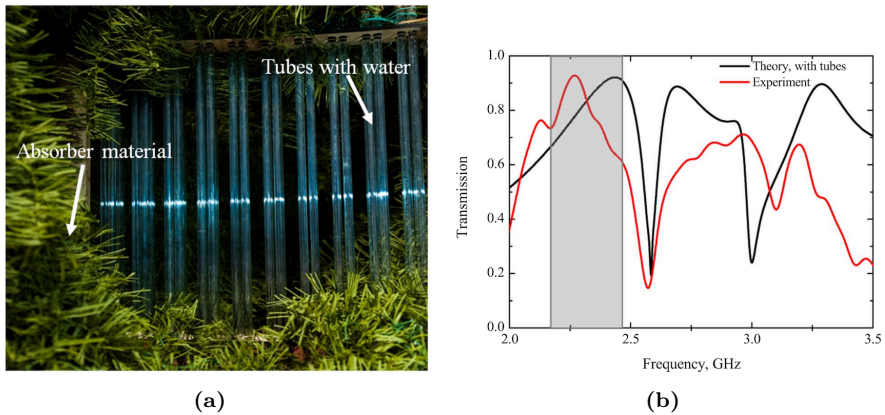


**Figure 3.19:** Water-based MS with toroidal mode. (a) Photograph of the MS in the experimental setup. (b) Simulated and measured transmission spectra. The grey area highlights the frequencies of the toroidal mode. Figures are taken from [121].

dipole mode such that an anapole mode is achieved. Several metastructures have utilized toroidal modes. However, until very recently, the experimental demonstration of these modes had been missing because of their far-field scattering being identical to that of the electric dipole. It is only in the near-field that the toroidal modes can be distinguished from other modes. The local field was measured in [130] with a cluster of four water cylinders, see Figure 3.18(a). As water is a liquid, it was possible to insert a probe into the cylinders, as well as around them, to map the local field, see Figures 3.18(b) and 3.18(c). The experiment shows how water can be utilized for

advanced physics demonstrations, otherwise impossible with solids.

Sufficient excitation of toroidal modes requires complex and low-loss structures. The losses limit the potential of water-based MS with toroidal moments. Still, a MS composed of clusters of four cylindrical water inclusions, similar to those in Figure 3.18, was investigated [121], see Figure 3.19. Excitation of the toroidal mode was observed through an enhancement in the transmission, Figure 3.19(b). The grey area displays a broad region of which the toroidal mode should be excited. As toroidal dipoles are dark modes (i.e. non-scattering), the applications of this MS are limited to absorption and sensing, albeit the potential of the later is low due to the limited Q-factor.

### 3.6.2 Bound states in the continuum

In the past few years, BICs, also known as embedded eigenstates, have been showcasing several exciting advances for the physics, engineering and optics communities at large [167–169]. However, all the experimental realizations of BICs to date have inherently relied on very large arrays, requiring large footprints and failing to enhance the local density of states (LDOSs) or serve as sensors [170]. More compact implementations have traded footprint with available Q-factors, yielding more localized modes, but inherently limited in terms of field enhancements and line widths, known as quasi-BICs. The smaller the structures, the more radiation loss and limited performance. Quasi-BICs in subwavelength structures have shown Q-factors limited to a few tens. Such Q-factors can arguably be achieved with several other techniques, e.g. structures based on Mie resonances.

In general, BICs can be classified according to the number of eigenmodes involved in the scattering process (single or multiple) and to the nature of their underlying interference mechanisms (symmetry-enabled or accidental BICs). For example, Liu et al. demonstrated a symmetry-protected BIC in a MS made of Silicon Mie resonators operating at 189 THz, and is shown in Figure 3.20 [171]. Due to the symmetry of the MS, a BIC emerges at the  $\Gamma$ -point of the first Brillouin zone, which cannot be excited with a normal plane wave incidence even though the resonance frequency is above the light line. By breaking the symmetry of the resonators, the BIC is no longer protected, and now a quasi-BIC appears in the radiation spectrum as a sharp Fano line shape with a Q-factor of around 20,000 for a MS with  $27^2$  elements. The problem with this

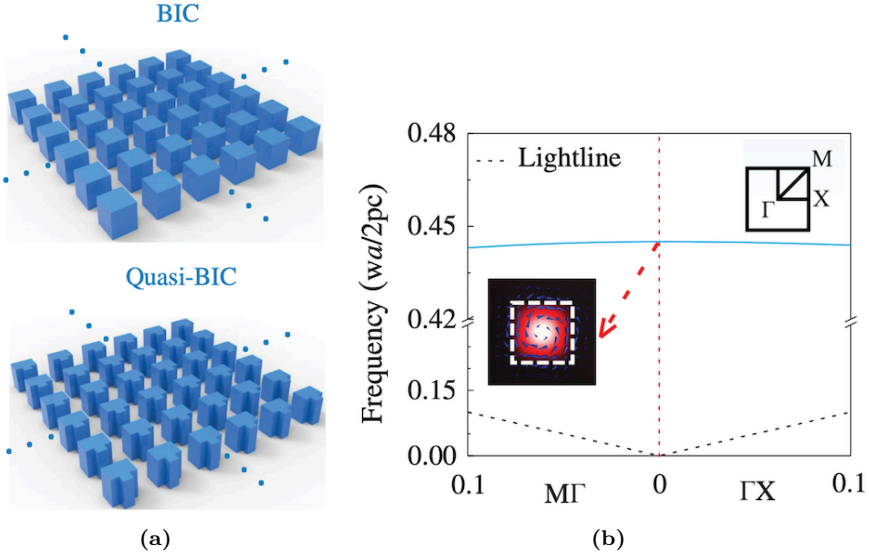


**Figure 3.20:** Symmetry-protected BIC MS. (a) Sketch of the MS without and with breaking of its symmetry. (b) Dispersion diagram of the symmetry-protected MS. Figures are taken from [171].

technique is that the symmetry-breaking is permanent and has to be extended to all resonators for a sufficient excitation of the quasi-BIC. A single resonator BIC have been proposed [172], however, exotic materials, such as epsilon-near-zero (ENZ), are required, which are generally subjected to losses in practical realizations.

In Paper 6, we show for the first time that this trade-off between BIC localization and achievable quality factor is actually not necessary at all. By controlling the boundary conditions around a single resonator, we show that it is possible to implement a new form of BIC, highly localized and with large Q-factors. Because of the localization of this non-radiating mode, the LDOS can diverge, yielding extreme sensitivity, which we exploit in our work to demonstrate advanced sensing functionalities and to trace chemical reactions. Based on a simple tabletop experiment, we are able to trace the dissolution of NaCl in water, determining evaporation rates of distilled and salted water with a resolution of less than 1  $\mu\text{L}$  on a standard laboratory equipment.

The single resonator constitutes a vertical electric dipole in the form of a metallic cylindrical disk backed by a conducting ground plane. The scattering pattern of

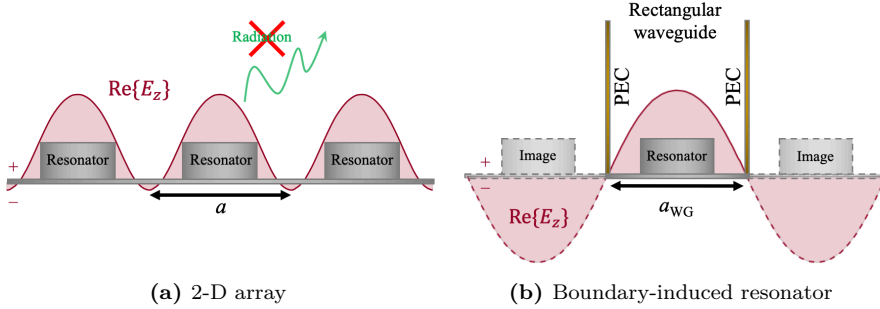


**Figure 3.21:** Boundary-induced BIC. **(a)** Formation of a symmetry-protected BIC in a 2-D array of vertical dipole resonators. **(b)** Symmetry-protected BIC induced by the images of the resonator placed between two lateral perfect electric conductor (PEC) walls. Figures are taken from Paper 6.

such a resonator will have a null along the cylinder axis. In a 2-D periodic array under a normal incidence plane wave illumination, these resonators will have identical induced dipoles as sketched in Figure 3.21(a). If the distance between the resonators is subwavelength, the incident wave will be fully reflected by the structure. In this way, a non-radiating mode above the light line emerges at the  $\Gamma$ -point of the first Brillouin zone, just as in Figure 3.20. The mode is bound to the array as long as the symmetry is preserved, and thus it is a symmetry-protected BIC. By breaking the symmetry of the configuration, a quasi-BIC emerges in the reflection spectrum. However, as in Figure 3.20, the symmetry breaking has to be extended to the whole array, which is impractical and often impossible after fabrication.

At microwave frequencies, rectangular metallic waveguide can be used to mimic periodic structures such as MSs [116]. The conducting walls of the waveguide function as mirrors. Assuming the walls are perfect electric conductors (PEC), the neighbor images of the vertical electric dipole resonator inserted in the waveguide will be out of phase according to the image theorem and as illustrated in Figure 3.21(b). Still, a symmetry-protected BIC emerges at the  $\Gamma$ -point of the fundamental propagating mode ( $\text{TE}_{10}$ ) of the waveguide. We experimentally demonstrated that an asymmetric placement of a water drop atop of the resonator breaks the symmetry, and thus introduces a dip in the reflection spectrum. Photographs of the resonator placed in the waveguide section are shown in Figures 3.22(a) and 3.22(b), and a sketch of the experimental setup is shown in Figure 3.22(c). The experiment was a simple setup

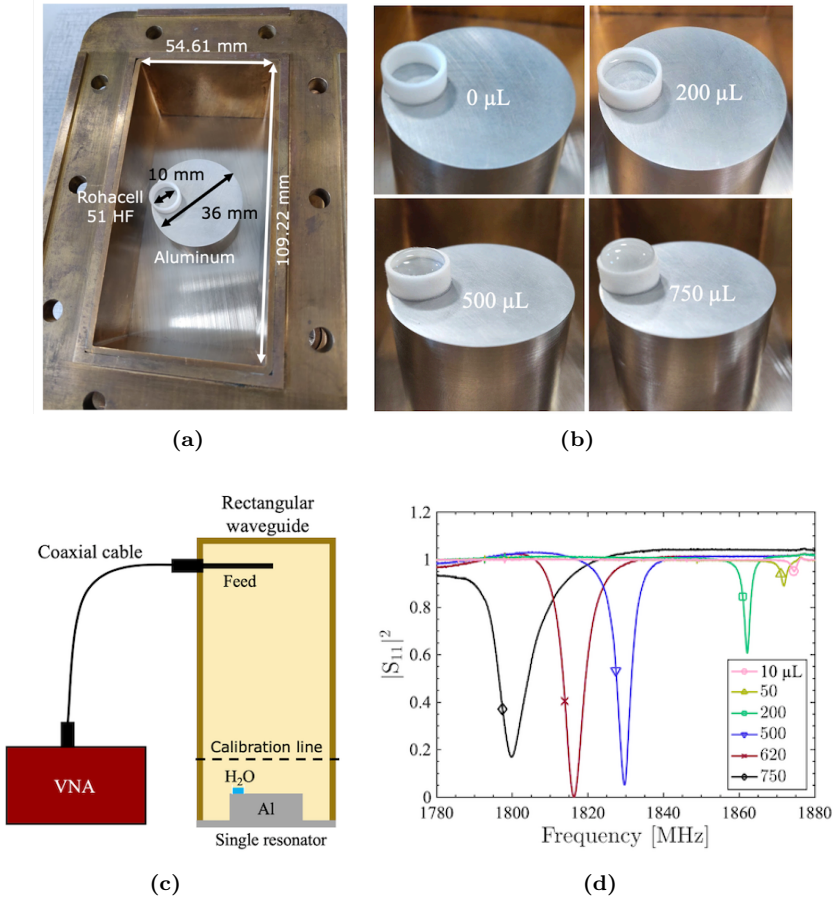


**Figure 3.22:** Boundary-induced BIC experiment. Photographs of (a) the fabricated resonator inserted into a rectangular waveguide section and (b) the resonator with different water volumes in the Rohacell container. (c) Sketch of the experimental setup and (d) normalized measured reflectance spectra for different water volumes in the Rohacell container. VNA stands for vector network analyzer. Figures are taken from Paper 6.

of a vector network analyzer (VNA) connected, with a coaxial cable, to a WR-430 rectangular waveguide in which the resonator was inserted.

The resonance frequency, as well as the Q-factor, is controlled by the amount of water and its permittivity. Figure 3.22(d) shows the normalized measured reflectance spectra for different water volumes inserted in the Rohacell container. Without water, the system has a Q-factor of around 1,000, whereas with full coupling to the mode (zero reflection) by inserting a water volume of 620  $\mu\text{L}$ , the Q-factor is reduced to



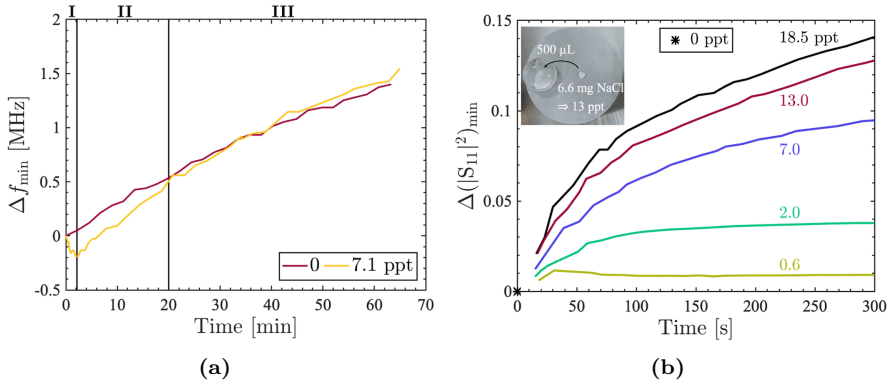


**Figure 3.23:** Sensing analyses with BIC structure. **(a)** Chemical reaction and evaporation of water. Shows measured change in resonance frequency as a function of time from first measurement. 0 parts per thousand (ppt) is distilled water and 7.1 ppt is distilled water with 0.71 % NaCl. Initial water volume is 500  $\mu$ L. **(b)** Tracing of chemical reaction of NaCl crystals added to 500  $\mu$ L of distilled water. Shows measured change in reflection coefficient at the resonance frequency as a function of time from the crystal was added. The experiment is conducted for different concentrations of NaCl in distilled water. Inset shows a photograph of the resonator and a NaCl crystal before adding the crystal to the water. Figures are taken from Paper 6.

250. We exploit the quasi-BIC for various advanced sensing analyses of small perturbations in the water volume. For example, we successfully sense deeply subwavelength variations to the water volume, as well as small changes in its refractive index. In particular, we can determine the evaporation rates of distilled and salted water with sub- $\mu$ L precision. This we do by tracking the change in the reflection response, see Figure 3.23(a), which shows the measured change in the resonance frequency as a function of time from first measurement. For distilled water, the resonance frequency experiences a linear increase with time due to evaporation of the water volume from the open Rohacell container. From the slope of the curve, and comparing it with our initial volume measurements (see Figure S5D in the appendix of Paper 6), we can estimate the evaporation rate of the water volume to be 213 nL/min.

We then reset the experiment, and added water and a small NaCl-crystal. In this way, we could trace the dissolving of the crystal in the water, see Figure 3.23(a). The addition of a NaCl crystal triggers a rapid change in the response (see Figure 3.23(a), period I). The NaCl density is lower when dissolved in water, thus the volume expands and we observe a red-shift in the resonance frequency. Hereafter (period II),

the resonance frequency is blue-shifted as  $\text{Na}^+$  and  $\text{Cl}^-$  ions are dispersed in water (hydration), effectively increasing the solution density. Furthermore, the conductivity increases, thus increasing the reflection. After 20 minutes, the NaCl is fully dissolved (period III), and the slope is stabilized, such that we can estimate the evaporation rate to be 201 nL/min. The concentration of the solution was 7.1 parts per thousand (ppt) after the NaCl being fully dissolved. The salted water evaporates slower than the distilled water, since water molecules are attracted to the dissolved salt ions, and more energy is thus required to break them apart.

We also experimented with different sizes of NaCl crystals, see Figure 3.23(b). Larger NaCl crystals change the response faster due to their size, but it also takes longer time to dissolve them, as seen by the slope changes. Even a small NaCl crystal of 0.3 mg ( $\approx 0.6$  ppt in 500  $\mu\text{L}$  water) can be clearly measured. Such a small change in salinity corresponds to an increase in the loss tangent of approximately 0.0066 [7.7 %, [173]].

We believe that these findings are truly important in the context of BICs, both from the fundamental scientific as well as applied point of view, and in line of the several implications for enhanced light-matter interactions, not limited to sensing, but also extended to enhanced nonlinearities and a plethora of photonics applications. For more details and results, see the full manuscript in Appendix F, Paper 6.

### 3.7 Heating systems

Heating and cooling of water is essential for our daily lives both in households and industry. Conventional methods are based on electrical heating or heating by combustion. For example, a regular household boiler uses electrical energy to heat up a resistor, and is working on the principle of Joule heating, see Figure 3.24(a). Instead of wires directly connected to the resistor, a coil can be placed below the resistor, and works on the principle of induction (the resistor must contain ferrous metal for efficient heating). In both cases, the power, dissipated as heat in the resistor with resistance  $R$  [ $\Omega$ ], is proportional to  $RI^2$ , where  $I$  [A] is the current induced in the resistor. Heating by combustion uses fuels (e.g. gas) to create flames for heating a container with the water, see Figure 3.24(b). Both methods heat the volume water locally at the interface between the water and, usually, metal. Through (mostly) con-

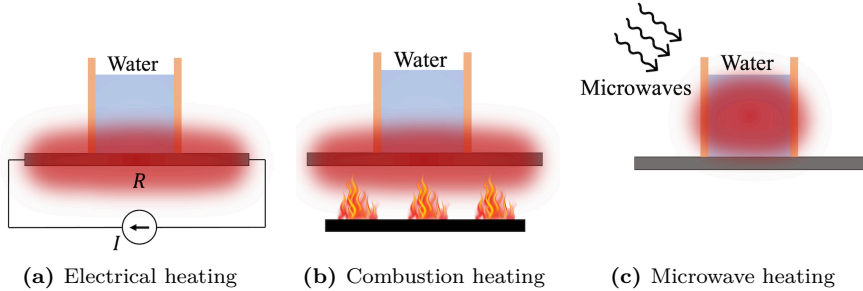


**Figure 3.24:** Sketches of three different heating methods of water. (a) Electric heating, (b) combustion heating and (c) microwave heating. The red color show the area of heating. The wires in (a) can be replaced by a coil placed under the resistor for inductive heating.

vection, the water volume is heated entirely, however, if the water volume is heated rapidly, the bottom part near the heating plate will be much warmer than the top part.

An alternative heating method is by microwaves, see Figure 3.24(c). As they penetrate the water volume, microwaves get absorbed by it, thereby effectively heating the water. Thus, the water volume is heated from the inside and does not need to be in contact with a heating plate as it can be heated externally. Furthermore, it can be turned on/off immediately, whereas the heated plate in Figures 3.24(a) and 3.24(b) will continue to be warm (except for heating by induction). The main disadvantage with microwave heating is that high power microwaves are needed for sufficient heating, and thus a closed system is required (e.g. a metallic cavity). Also the radiation and absorption of microwaves must be highly efficient in order to compete with the conventional methods in Figures 3.24(a) and 3.24(b).

In general, heating water requires a lot of energy due to water's very large heat capacity of  $c_p \approx 4.2 \text{ J}/(\text{g}\cdot\text{K})$ . In many cases, the user is more concerned about the time it takes to heat some water, e.g. a cup of water. The time  $\Delta t$  it takes to heat a volume of water  $V_w$  by a temperature increase of  $\Delta T_w$  is [6]

$$\Delta t = c_w \rho_w V_w \Delta T_w / P_{\text{abs}} \text{ [s]}, \quad (3.6)$$

where  $\rho_w$  ( $\approx 1 \text{ g}/\text{mL}$  at  $20 \text{ }^\circ\text{C}$ ) is the density of water. The only parameter we can control is the power absorption  $P_{\text{abs}} = \eta_{\text{eff}} P_{\text{in}}$ , where  $P_{\text{in}}$  and  $\eta_{\text{eff}}$  are the input power and efficiency of the heating process, respectively. No systems are perfect

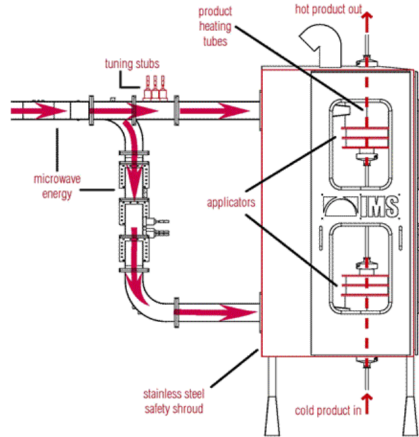


**Figure 3.25:** Microwave system for heating water. Sketch of the IMS cylindrical heating system taken from [143].

( $\eta_{\text{eff}} < 1$ ) as some of the input power will be lost during the heating process. This can be unwanted heating of the surrounding air, particularly for combustion heating, or power lost during the generation of electric current or microwaves. In the case of microwave heating, the most substantial loss is the scattering/reflection by the water volume, which can vary significantly with different water temperature and the frequency of the microwaves. Therefore, the microwave heating device must be designed carefully.

In Figures 3.25 and 3.26, we have shown two different systems for heating water. Industrial Microwave Systems (IMS) sell the device shown in Figure 3.25. Using rectangular waveguides, the microwaves are guided into two cylindrical metallic cavities (called applicators) inside a metallic shroud. A tube with water goes through the applicators. Tuning stubs are to be used for efficient power insertion into the applicators, and has to be adjusted depending on the permittivity of the water to be heated.

We proposed a simpler setup in [146, 147], see Figure 3.26(a). It consists of water-filled tubes going through a rectangular waveguide (such as WR-430). The waveguide is 'shorted', and thus is a single port system, and we operate it at its fundamental  $\text{TE}_{10}$  mode. The objective is to minimize the reflected power by adjusting e.g. the sizes and positions of the tubes. Here, we design the tubes with water to support the excitation of the magnetic dipole resonance. Due to the characteristics of the

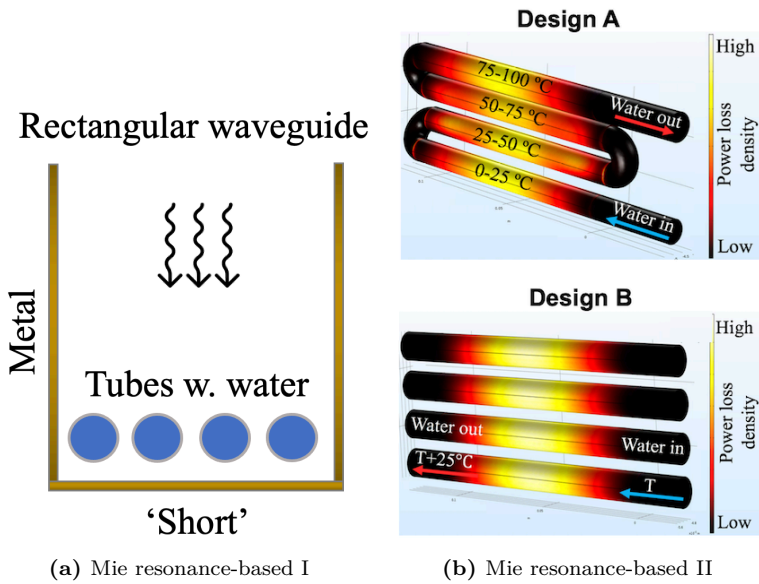


**Figure 3.26:** Microwave system for heating water. (a) Cross-sectional sketch of the system based on Mie resonances proposed by us in [146,147]. (b) The power loss density in the two designs we considered.

waveguide, as discussed in Section 3.6.2, the tubes are effectively imaged and thus the configuration behaves as a MS backed with a reflecting surface. Since the water permittivity is temperature-dependent, different tube sizes are needed for different water temperatures. We came up with the two designs shown in Figure 3.26(b). Design A is a compact single waveguide system with four different tube sizes optimized for different water temperatures. Design B consists of four identical tubes going through four parallel waveguides, where the tube size in each waveguide is optimized for different water temperatures. Figure 3.26(b) shows the power loss density at the surface of the tubes filled with water at the magnetic dipole resonance. The total efficiencies are estimated numerically to be 86 % (design A) and 93 % (design B) for heating of distilled water. As the reflected power low for all water temperatures, tuning stubs are not needed in this setup.

### 3.8 Summary

In this chapter, we reviewed and demonstrated water-based microwave devices. We showed how water's high permittivity could be exploited to realize small Mie resonators, which constitute the foundation of the water-based devices. We used the example of a single water sphere to study these resonances, and showed that they drive the response of water-based MSs and antennas. Several types of MSs were presented including absorbers, reflectarrays and switches. Also different types of antennas were shown including DRAs, a Huygens DRA, monopole saltwater antenna and a MS antenna.

In Section 3.6, we examined structures with more advanced modes. First, we investigated the excitation of toroidal modes in metastructures composed of clusters of water cylinders. Next, we presented work ground-breaking results concerning the utilization of a BIC in a single resonator situated in a rectangular waveguide. We investigated how the BIC structure can be used for advanced sensing analyses in a small drop of water.

At last, we studied various microwave systems for heating water. We presented our proposal on a continuous heating system, where we utilize cylindrical Mie resonators in a MS configuration in a rectangular waveguide. Through adjustment of the resonators, we minimize (maximize) the reflected (absorbed) power, and thus exclude the need for tuning stubs.



## CHAPTER 4

# Summary and outlook

---

In this thesis, the uprising of water-based devices for microwave control and sensing was demonstrated. With its abundance, ecological compatibility, liquid state and relatively high and temperature-dependent permittivity, water offers many advantages over conventional microwave dielectrics such as expensive ceramics. These properties have been exploited in our work to achieve a wide range of different tunable water-based devices including antennas, MSs, passive single resonators, BIC structures and heating systems.

The electromagnetic properties of water were reviewed in Chapter 2. The general Debye model used for the permittivity of water was derived, and we discussed its validity. A more advanced model by Ellison [8] was included, providing the complex permittivity of distilled water for frequencies from DC to 25 THz as well as water temperatures from 0 °C to 100 °C. Subsequently, we discussed the interaction of microwaves with water, and presented the key parameters to describe the scattering and absorption from water structures.

In Chapter 3, the main mechanisms behind water-based devices were examined, specifically the excitation of Mie resonances in small water inclusions. We studied the scattering and absorption from single canonical configurations, and showed that primarily magnetic and electric dipole modes can be excited, whereas the higher order modes were suppressed by the absorption in water. For most resonator sizes and water temperatures, the absorption was higher than the scattering. We examined different water-based MSs including absorbers, reflectarrays and tunable MSs. In particular, we presented our work on a water-based MS reflectarray with reconfigurable reflection angle by a simple redistribution of the water volume in an array of basic water inclusions. The tunable reflection properties of the MS were achieved with a magnetic dipole mode induced in the water inclusions. A prototype was fabricated, and the experimental results were in good agreement with the numerical predictions.

We also showed various water-based antennas such as DRAs and MS antennas. In our work, we presented the smallest water-based DRA to date and a water-based Huy-



gens DRA. The first shows that we can excite the natural Mie resonances of a sphere in a hemispherical water-filled cavity supported by a ground plane. Both magnetic and electric dipole modes could be excited, however, for different feed configurations and operational frequencies. With sufficient excitation of the dipole modes, the antenna was matched to the feedline, albeit the total efficiency was limited due to the compact antenna size and losses in water. Moreover, the dipole mode excitation carried limited maximum antenna directivity. With a rectangular cavity instead, namely the Huygens DRA, we could excite both magnetic and electric dipole modes in a similar antenna setup and frequency, providing enhanced maximum antenna directivity. We demonstrated several means of tuning and reconfiguring the antennas by extraction of water, changing the water temperature as well as moving the feed position. Both antennas were fabricated and characterized experimentally with excellent agreement achieved between the numerical and experimental results.

Toroidal modes were recently confirmed in clusters of water cylinders [121, 130]. These intriguing high-Q modes are non-scattering and highly sensitive, and are of great interests for MSs and MMs. BICs are another type of high-Q modes, which have seen increasing attention. We demonstrated a novel symmetry-protected BIC structure based on a single resonator in a rectangular waveguide. By introducing a small drop of water asymmetrically on the resonator, the symmetry was broken and a high-Q resonance (quasi-BIC) was excited appearing as a narrow reduction in the reflection spectrum. As opposed to photonic arrays, where asymmetry must be tailored across the entire array, the asymmetry introduced to a single resonator in a waveguide gets perfectly replicated periodically on the account of the image theorem. This considerably simplifies the overall design procedure and displays the main advantage of boundary-induced microwave BICs. The liquid state and high permittivity of water enables many ways to tailor the reflection spectrum, which we demonstrated experimentally, including addition/removal of water, temperature shifts and dissolution of salts in the water. In addition, we conducted highly advanced sensing analyses such as tracing the processes of the dissolution of salt crystals in water as well as detecting evaporation of water volumes less than 1  $\mu\text{L}$ . The overall and very sensitive BIC response brings unique opportunities for simple and powerful microwave sensors.

At last, we discussed the concept of heating water using microwaves. When

electromagnetic energy is absorbed in water, the water is effectively heated. The advantages of microwave heating are fast on/off switching and that the heating also takes place inside the bulk water. We proposed systems for heating water built on Mie resonances. The designs consist of water cylinders passing through a shunt rectangular waveguide. In this way, a continuous stream of water can be heated. The absorption is maximized with the resonant water cylinders, and therefore also reducing the reflected power. In this way, tuning stubs for reducing the reflection are not needed.

In a nutshell, water is an intriguing alternative material for extremely cheap, simple and versatile microwave systems, albeit the losses at higher frequencies limit the total efficiency. The latter constitutes the primary problem of using water in many microwave systems, especially for frequencies above 2 GHz. This is why MS absorbers have been the most promising application of water thus far. In addition, many different tunable water-based antennas have been demonstrated, where perhaps saltwater antennas have most potential. Both areas have matured and the latest progresses present only minor improvements. Saltwater antennas have already been piloted as sea antennas for military usage [20]. In the same way, the future water-based MS absorbers should be designed for actual applications. That could be as microwave absorbing windows or as absorbers in anechoic chambers. The later could be as a flat absorber floor or even mid-room walls, which can emptied, and thus the room size can be adjusted on the demand. Typically, the absorbers in anechoic chambers are pyramidal polyurethane foam blocks loaded with carbon particles, which potentially pose a health risk to direct contact personnel. Furthermore, they are very expensive and bulky. Here, water-based MS absorbers can serve as bio-friendly, recyclable and flexible alternatives. As for the other types of water-based MSs, the low efficiency and weather-instability constitute major challenges which have to be resolved before they can compete with existing technology.

Recent work have shown new exciting applications of water in RF circuit tuner, CPW switch and semiconductor. Also, our work on a BIC structure with greatly enhanced sensing capacities opens up for new unexplored areas with profound potential for not only microwave systems, but photonics as well. For instance, the demonstrated enhanced sensitivity can be directly translated into enhanced light-matter interactions, offering a unique platform for drastically enhanced nonlinearities. In

the context of qubits, these localized resonances may enable much enhanced quantum coherence times [174, 175]. Our BIC structure is designed for a rectangular waveguide, however, we believe that it is also possible to realize BICs with a single resonator in other platforms such as resonant cavities, striplines, microstrip lines and dielectric waveguides. Also, the investigation of BICs with a single magnetic dipole would be interesting as the mirror images would be in-phase in the rectangular waveguide. These investigations are of great importance, and particularly, the theoretical formulation (e.g. equivalent circuit diagrams) of the existence of BIC modes in these configurations are of immense importance. Such results would simplify and accelerate the design process of the BIC structures, and can potentially expand the microwave and optical technology fields.

## APPENDIX A

# Paper 1: "Review: water-based devices for advanced control of electromagnetic waves"

---

This manuscript reviews water-based devices. The manuscript has been submitted. The citations in the manuscript refer to reference list included at the end of the manuscript.

Work contributions by the present author: Numerical calculations and manuscript drafting.

Reference information:

**R. E. Jacobsen**, S. Arslanagić and A. V. Lavrinenko, "Review: water-based devices for advanced control of electromagnetic waves," *submitted*, Apr. 2021.

# Review: Water-Based Devices for Advanced Control of Electromagnetic Waves

**AUTHORS:** Rasmus E. Jacobsen<sup>1</sup>, Samel Arslanagic<sup>2</sup>, Andrei V. Lavrinenko<sup>1\*</sup>

## **AFFILIATIONS:**

<sup>1</sup>Department of Photonics Engineering, Technical University of Denmark, Bld. 345A, Ørstedes Plads, 2800 Kgs. Lyngby, Denmark (e-mail: [rajac@fotonik.dtu.dk](mailto:rajac@fotonik.dtu.dk), [alav@fotonik.dtu.dk](mailto:alav@fotonik.dtu.dk)).

<sup>2</sup>Department of Electrical Engineering, Technical University of Denmark, Bld. 348, Ørstedes Plads, 2800 Kgs. Lyngby, Denmark (e-mail: [sar@elektro.dtu.dk](mailto:sar@elektro.dtu.dk)).

\*Corresponding author. Email: [alav@fotonik.dtu.dk](mailto:alav@fotonik.dtu.dk)

## **ABSTRACT**

Tunable devices are of great interest as they offer reconfigurability to their operation, although many of them employ rare and expensive materials. In a world with increasing focus on ecological compatibility and recyclability, immense efforts are being made to find bio-friendly alternatives. However, in some cases, one does not have to look far, because water, a high-permittivity dielectric at microwave frequencies, is readily available. Recent studies have shown that compact Mie resonators, which are the fundamental blocks in all-dielectric metamaterials and dielectric resonator antennas, can be realized with small water elements. In a variety of applied physics areas, encompassing frequencies from the radio to the optical parts of the spectrum, all-dielectric implementations have received immense attention. When it comes to water, its temperature-dependent permittivity and liquidity enable a multitude of unprecedentedly simple means to reconfigure and tune the resulting devices. Moreover, being a polar solvent, water easily dissolves various physiologically important electrolytes, which potentially can be exploited in a sensor design. Presently, we review water-based devices for advanced microwave control and sensing. We show and discuss the dynamic properties of water, and examine the microwave scattering and absorption characteristics of single water elements. We investigate how such water elements can be employed in various microwave designs including single resonators, metamaterials, metasurfaces, antennas, absorbers and radio-frequency components. The main complications of water are its losses, especially at higher microwave frequencies, and its stability. We discuss how to overcome these, and show that even highly loss-sensitive modes, namely toroidal modes and bound states in the continuum, can be realized with water-based devices. We believe that water-based devices usher the route to meet the UN proclaimed goals on global sustainability and human-friendly environment.

## **1. Introduction**

Water – covering more than two thirds of Earth’s surface, vital for all life, known as ‘the universal solvent’, etc. – is perhaps the most important and unique substance in our World [1–3]. Although the most studied inorganic compound, scientists continue to dwell upon the remarkable properties of water [4–15], and yet some remain mysteries [16]. Water’s unique properties stem from the arrangement of its polar molecules. The water molecule constitute an asymmetric alignment of one

negatively charged oxygen atom ( $O^-$ ) and two positively charged hydrogen atoms ( $H^+$ ). A sketch of the water molecule is shown in Fig. 1(a). The atomic positioning form two even, but oppositely charged poles i.e. a permanent dipole. In the liquid state, the water molecules (or dipoles) react to an applied electric field through their alignment with the field, thereby polarizing the bulk water. As the water molecules are very densely spaced, the polarization mechanism provides water an exceptionally high polarization vector even in small and compact volumes such as protein pockets [8]. With no applied electric field, the orientations of the permanent molecular dipoles are random, resulting in zero net polarization. The polarization properties of water are typically described by its complex relative permittivity (dielectric function)  $\epsilon_r = \epsilon_r' + i\epsilon_r''$ , which is shown in Fig. 1(b), and depends on dynamic parameters such as frequency of the electric field and water temperature [9]. Unlike that of many other polar substances, the permittivity of water is notable even at GHz frequencies. In 2015, inspired by Rybin et al. [17] as well as Popa and Cummer [18], Andryieuski et al. demonstrated for the first time the possibilities with exploiting water's dynamic properties in microwave all-dielectric metasurfaces (MSs) [19]. This launched a series of publications on water-based (WB) microwave devices such as tunable metamaterials (MMs) [20–23] and MSs [24–33], as well as MS reflectors [34–38], MS absorbers [39–71] and many more [72–79], see Table 1 for a thorough overview. While the recent efforts on WB MSs have certainly given new life to water as an interesting microwave material, it must be mentioned that its use within the area of microwave antennas has been around for many years and still constitutes an active research field [80–126]; see Table 1 for more details on particular antenna types. A very detailed review on water- and other liquid-based antennas is given in [127]. In addition, switching of guided waves on a coplanar waveguide with a water drop was demonstrated in 2007 [128]. Recently, new applications of water have been presented including a radio frequency (RF) tuner [129] and a bound state in the continuum (BIC) structure [130,131]. The latter concerns an important concept, known from quantum physics and extended to acoustics and photonics, which has recently been realized in a simple microwave single-resonator structure well-suited for advanced microwave sensing of water. In general, WB devices exploit the high permittivity of water to tailor the phase and amplitude of microwave fields by invoking strong field intensities in the bulk water volumes. In fact, such high-permittivity bodies are known to exhibit Mie resonances (see e.g. [132,133]), which are the driving mechanisms behind dielectric resonators used in dielectric resonator antennas [134] as well as all-dielectric MMs and MSs [135].

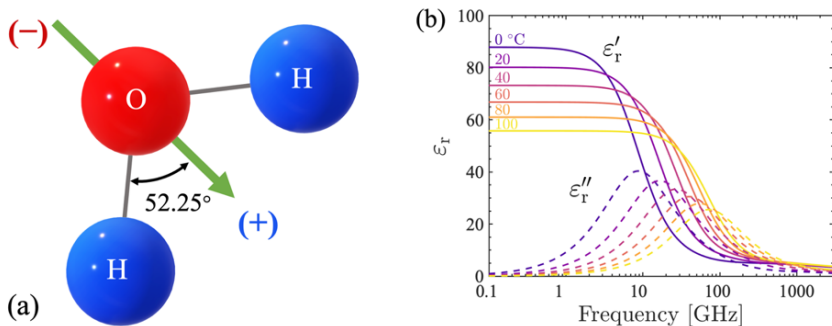


**Figure 1.** (a) Sketch of a water molecule with the poles and dipole moment (green arrow). (b) Relative permittivity of water as a function of frequency for temperatures from 0 °C to 100 °C. The permittivity model includes three relaxation processes and is taken from [9].

A major difference between water and conventional microwave dielectrics is its liquid state at room temperature, which in general holds a major advantage: water simply takes up the shape of the container it is put in. With the recent progresses of 3-D printers, it is possible to produce routinely complex and flexible structures with cavities (see e.g. [40,52]) otherwise extremely challenging with e.g. high-permittivity ceramics. A simple redistribution, reshaping and/or temperature shift of water alters the system response in the form of a perturbation of the local fields, frequency shift and/or transmission/reflection change. It is also possible to alter the permittivity of water by dissolution of e.g. electrolytes and salts in it, which offers another route of tuning (see e.g. [25,34,81]). Furthermore, as water is transparent at optical frequencies, it is possible to make the WB MS visually transparent, while blocking or absorbing microwaves (see e.g. [44,60,70]). The abundance, low cost, bio-friendly nature and dynamic properties of water make it a very interesting alternative component for extremely cheap, simple, bio-friendly and versatile microwave systems, albeit the losses at higher frequencies limit the total efficiency in non-absorbing devices. WB microwave devices cover a wide range of applications such as electromagnetic waves absorption, beam-steering, radar cross section (RCS) reduction, antennas, radomes, circuit components, heating and sensing.

The purpose of the present work is to provide an overview of the properties of WB microwave devices, and pros and cons of their applications. The manuscript is organized as follows. Section 2 introduces and discusses the permittivity model of water as well as the power absorption in lossy dielectrics as this plays a major role in the performance of the WB devices. In Section 3, we investigate the resonant properties of a single spherical water element and an array of such elements to shed light on the fundamental characteristics of simple WB MSs. Subsequently, we present and discuss a variety of WB MMs and MSs with a range of functionalities such as wideband absorption as well as tunable reflection and transmission control. In Section 4, various WB antennas are discussed including a transparent patch antenna and a Huygens antenna for increased focusing of the radiated power. WB RF components including a coplanar waveguide switch and an RF tuner are presented in Section 5. In Section 6, we show WB structures utilizing peculiar modes such as toroidal modes and BICs. The later represents our very recent work showcasing how water can be exploited for symmetry-breaking of a BIC. At last, we discuss the applications and outlook of WB devices in Section 7.

**Table 1.** Overview of water-based devices.

Device	Types	References
Single resonators	General study	[72–76,78,79]
	MRI	[77,136]
	BIC sensor	[130,131]
Metamaterial	Non-resonant	[23]
	Negative index	[21]
	Topological transition	[22]
	Fano resonance	[17]
	Material phase study	[20]
Metasurface	Absorber	[39–71]
	Reflector	[34–38]
	Toroidal mode	[32]
	Sensor	[137]
	All-dielectric	[24–31]
	Water/metal	[33]
Antenna	Monopole	[80–85,92,103,122–126]
	DRA	[86–91,93–101,119,120]
	Helical	[102,104]
	Patch	[105–108]
	Microstrip loading	[109–113,115]
	Hybrid	[116]
	Array	[114,117]
	Yagi-Uda	[118,121]
RF components	Switch	[128]
	Tuner	[129]

## 2. Permittivity of water

The permittivity of water fits the single relaxation Debye model with a good approximation from static to 50 GHz at room temperature (see e.g. [15] for an overview of permittivity models). However, recent studies show that the underlying reorientation of the water molecules are not Brownian motions, but discontinuous ‘jumps’, when an appropriate defect occurs in the hydrogen network [6,7,15]. Furthermore, the Debye model ignores the dipole-dipole interaction, which is also considered to be incorrect. Still, the experimental data can be fitted very well with the Debye model. Ellison [9] presented a very useful analytical model of the permittivity based on the fitting of experimental data for frequencies from static to 25 THz and temperatures 0 – 100 °C. Presently, we provide Ellison’s simplified permittivity model based on three relaxation processes fitted for frequencies from DC to 3 THz for temperatures 0 – 100 °C,

$$\varepsilon_r(\omega, T_w) = \varepsilon_s(T_w) + i\omega \sum_{n=1}^3 \frac{\varepsilon_{\infty,n}(T_w)\tau_n(T_w)}{1 - i\omega\tau_n(T_w)}, \quad (1)$$

assuming the time factor  $\exp(i\omega t)$  with  $t$  being the time,  $\omega$  - the angular frequency and  $T_w$  - the temperature given in °C. The static permittivity  $\varepsilon_s(T_w) = 87.9 - 0.404T_w + 9.59 \times 10^{-4}T_w^2 - 1.33 \times 10^{-6}T_w^3$ , the optical permittivity  $\varepsilon_{\infty,n}(T_w) = a_n \exp(-b_n T_w)$  and the relaxation time



$\tau_n(T_w) = d_n \exp\left(-\frac{T_n}{T_w+T_c}\right)$  with the critical temperature  $T_c = 132$  °C. Other constants are provided in Table 2.

**Table 2.** Values for the constants in Eq. (1).

$n$	$a_n$	$b_n \times 10^{-3}$ [°C <sup>-1</sup> ]	$d_n$ [fs]	$T_n$ [°C]
1	79.3	4.33	135	653
2	3.61	10.7	0.365	1220
3	1.97	2.52	5.10	396

In Fig. 1(b), we show the frequency and temperature dependence of the relative permittivity of water from 0.1 to 3,000 GHz. At low frequencies (< 1 GHz),  $\epsilon_r'$  is high, while  $\epsilon_r''$  (responsible for material losses) is low. At room temperature (20 °C), the real part is approximately 80 from low frequencies up to 3 GHz. It decreases dramatically at higher frequencies, while the absorption increases and peaks around 20 GHz. The two other relaxation processes start at frequencies above 100 GHz and decreases the permittivity even further.

We see that increasing the temperature of water blue shifts the permittivity spectrum, and at low frequencies, the permittivity decreases. Bringing the water temperature from 0 °C to 100 °C, decreases the permittivity from  $86.8 + i9.2$  to  $55.8 + i0.71$  at 1 GHz. Interestingly, it is often the change in  $\epsilon_r'$  that is highlighted, whereas in fact, it is the imaginary part  $\epsilon_r''$ , which is more affected by the temperature shift. Despite of this, we must emphasize, that it is the high  $\epsilon_r'$ , which allows for the strongly induced fields in the WB devices, and thus providing their particular properties.

Next, we present an important aspect of the power absorption in resonant water structures. From Poynting's theorem, one finds that the absorbed electromagnetic power in lossy dielectrics can be determined as [138]

$$P_{\text{abs}} = \frac{\omega \epsilon_0}{2} \int_{V_w} \epsilon_r''(T_w) |\mathbf{E}|^2 dV, \quad (2)$$

where  $\epsilon_0$  is the free-space permittivity,  $\mathbf{E}$  is the electric field,  $dV$  is the infinitesimal volume element and  $V_w$  is the volume of water. Since water can attain different temperatures in its volume,  $\epsilon_r''(T_w)$  is placed inside the integral. We emphasize that  $P_{\text{abs}}$  is not only proportional to  $\epsilon_r''(T_w)$ , but also to  $|\mathbf{E}|^2$ . At resonance,  $|\mathbf{E}|$  is maximum, however, if  $\epsilon_r''(T_w)$  increases, the intensity of the resonance, and therefore,  $|\mathbf{E}|$  decreases. For low-loss dielectrics, increasing  $\epsilon_r''(T_w)$  causes a growth in  $P_{\text{abs}}$  as the intensity is only slightly decreased. For lossy dielectrics, e.g. water, the opposite can happen because the intensity of the electric field is greatly reduced by the losses.

### 3. Metasurfaces and metamaterials

In this section we present several water-based MSs and MMs, which pave the route towards cheap, tunable and bio-friendly alternatives for many microwave applications. In general, they are based on dielectric resonators, also known as Mie resonators, and take the form of small water inclusions in low-dielectric hosts. Therefore, we will start by presenting the case of a single water inclusion, namely a sphere, and investigate its scattering and absorption characteristics.

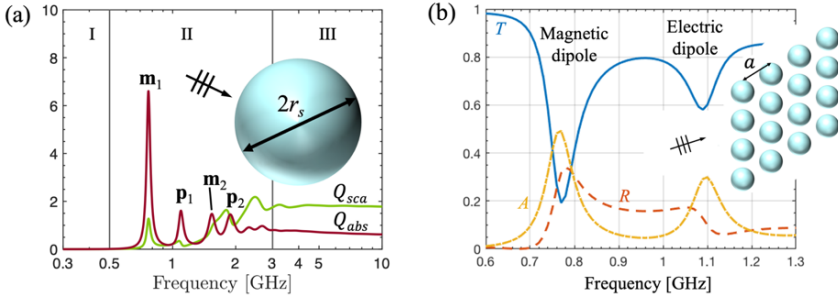


**Figure 2.** (a) Scattering and absorption efficiency spectra when a plane wave is incident on a single water sphere (the configuration is shown in the inset). (b) Transmittance ( $T$ ), reflectance ( $R$ ) and absorption ( $A$ ) spectra of a MS consisting of a square lattice of water spheres under normal plane wave incidence. The sphere radius is  $r_s = 21.6$  mm and the lattice constant  $a = 75$  mm.

### 3.1 Mie resonances in single water inclusions

High relative permittivity of water enables realization of compact Mie resonators with high energy extinction. In fact, this is the mechanism behind the Internet parlor trick pertaining the sparking of two cut grape hemispheres inserted into a microwave oven [78]. As an example, let us take the classical case study of a plane wave incidence on a dielectric sphere, which was also investigated in [74]. The water sphere has radius  $r_s = 21.6$  mm and temperature  $T_w = 20$  °C and is placed in free space. Of course, the water cannot sustain the spherical shape without being placed in a container, however, there are many solid dielectrics available to this end with permittivities close to that of air in the microwave frequencies, see e.g. [139]. The spectrum of the scattering and absorption efficiencies are shown in Fig. 2(b). We can divide the spectrum into three parts: I. Below 0.5 GHz, the incident wave passes the sphere nearly unperturbed; II. From 0.5 to 3 GHz, resonances drive the response; III. Above 3 GHz, the water sphere scatters as a metallic object of similar size. We are, of course, interested in the part where the resonances govern. There are several resonances, and their frequencies are controlled by judiciously changing the water amount, shape and permittivity of the water volume. E.g., by increasing the temperature, we effectively reduce the permittivity, and thus blue shift the spectrum (see e.g. [17,19,89]).

According to the Mie theory, different types of multipole modes can be excited in the dielectric sphere. However, due to the losses in water, only dipole modes are excited efficiently, namely magnetic ( $\mathbf{m}$ ) and electric dipoles ( $\mathbf{p}$ ) with the first being the most pronounced. All other modes like quadrupoles or even octupoles are suppressed by the losses. Furthermore, the losses cause the high absorption and broadening of the resonances. Two ways to reduce losses (i.e. making  $\epsilon_r''$  smaller) are by either increasing the size of the sphere, corresponding to red shifting the spectrum or increasing the temperature (see e.g. [74]). Other types of water-based inclusions have been investigated including cylinders [73], a water-metal hybrid structure [79] and even more complex shapes [47,59]. Their fundamental electromagnetic properties display various performance characteristics providing a variety of options for the designing of WB devices composed of resonators.

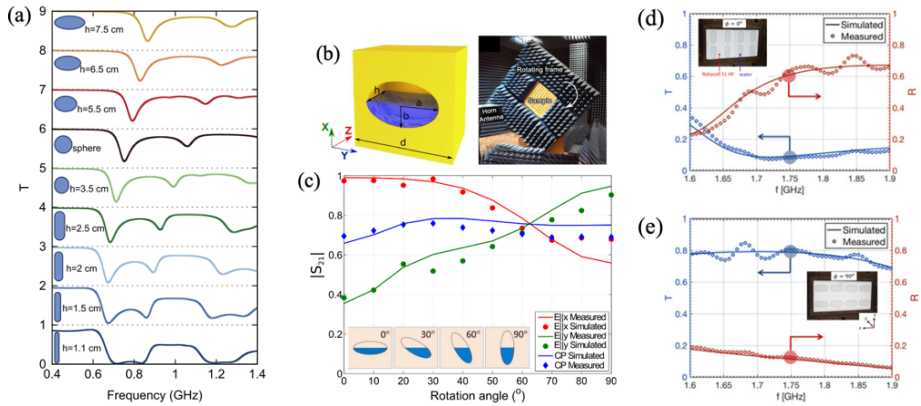


**Figure 3.** Control of transmission and reflection with simple WB MSs. (a) Simulated transmittance spectra for a WB MS with different stretching/compressing of its water spheres. The excitation is a linearly polarized plane wave at normal incidence. (b) and (c) MS with partially water-filled inclusions in foam host. (b) Sketch of one MS element (left) and photograph of the MS putted in the experimental setup (right). (c) The measured and simulated transmission of waves with different polarizations is changed through simple mechanical rotations. (d) and (e) Measured and simulated reflection and transmission spectra of a MS with rod-like water elements in a Rohacell 51 HF host material. The measurements are performed in a rectangular waveguide, which emulates an infinite periodic extension of the MS. (d) shows the  $0^\circ$  rotation of the MS and (e) the  $90^\circ$  rotation. Insets show the MS placed in a waveguide section. Figures are reproduced with permission from: (a), [19]; (b)–(c), [24]; (d)–(e), [28].

### 3.2 Resonances in simple metasurfaces for wave control

All-dielectric MSs are composed of a matrix of high permittivity inclusions in a low permittivity host. First, we show results for a simple all-dielectric WB MS of identical water spheres in Fig. 2(c), similar to a MS proposed in [19]. The lattice constant is  $a = 75$  mm and the radius and temperature are the same as in our example in Section 3.1 with the single sphere. We find that the dipole resonances drive the response of the MS and cause a significant change in transmission, reflection and absorption. Most of the extinct energy is absorbed, but it is not as pronounced as in the case of a single sphere. This is due to the coupling of the spheres, which provides yet another tuning parameter.

By changing the shape of the water, it is possible to control the spectrum as demonstrated in Fig. 3(a), where the sphere is stretched/compressed in different ways [19]. Depending on stretching/compression of the water volume, the dipole resonances can be moved spectrally closer to or away from each other. Gravity can also be utilized to control the water shape. By mechanical rotation of the structure with partially filled containers, it is possible to alter the transmission and reflection as shown in Fig. 3(b) [24]. The measurements were performed in anechoic conditions and the MS response to both linear and circular polarizations was investigated. In Fig. 3(c), a MS consisting of rod-like water inclusions in a Rohacell 51 HF host was demonstrated to have switching capabilities through  $90^\circ$  mechanical rotation of the MS [28]. Magnetic dipole resonances were excited in the water inclusions for the original position of the MS ( $0^\circ$  rotation angle) resulting in high reflection of the incident wave – the non-transmissive state. Rotating the MS by  $90^\circ$  greatly increased the transmission as no resonances were excited. The experiment was conducted using a rectangular waveguide, which emulated a periodic extension of the MS consisting of only 6 elements. Furthermore, stacking multiple MSs further decreased the transmission for  $0^\circ$  rotation and increased the transmission for  $90^\circ$  rotation. The latter was provided by the balancing of electric and magnetic

dipoles satisfying Kerker's condition, see e.g. [133,140,141] for more information about Kerker's condition and small directive scatterers.

The temperature tuning capability of the MSs in Fig 3(a) and (c) was investigated numerically, both depicting a linear frequency blue-shift of around 0.14 %/°C and 0.25 %/°C, respectively, when increasing from 0 °C to 100 °C [19,29]. Heating of the MS can be done by various stimuli, for example, by light, microwaves, chemical reactions, mechanical friction and electrical current. All methods make the system more complex, and due to water's exceptional heat capacity, significant energy is required for heating. This is perhaps why experimental studies of temperature tuning of WB MSs are scarce [17,20,51,65].

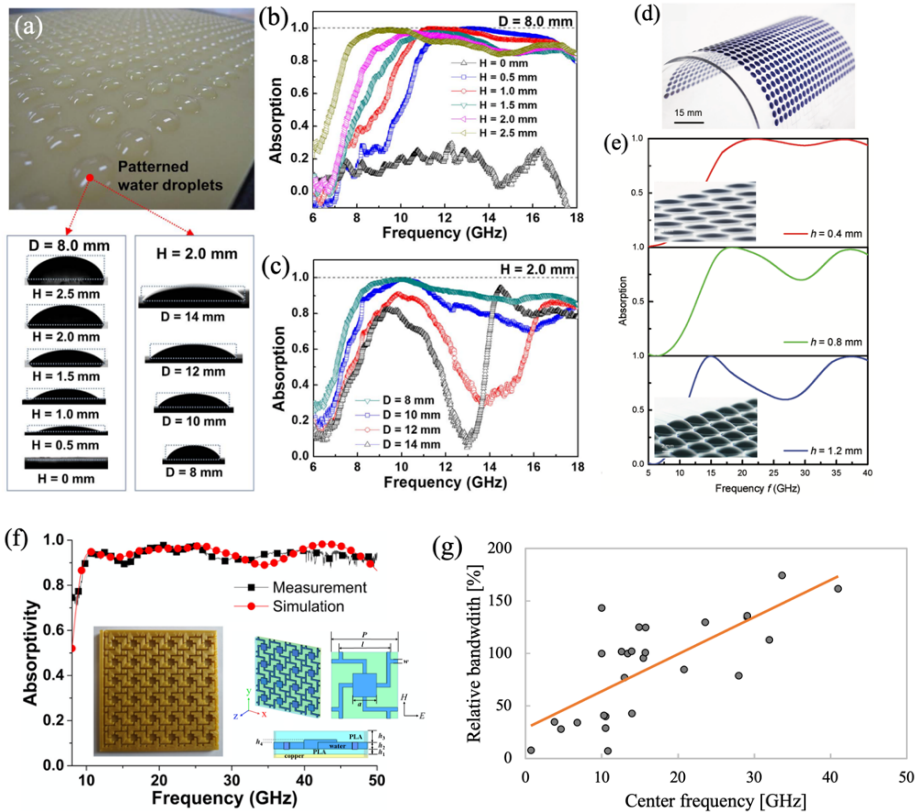


**Figure 4.** WB MS absorbers. (a) Photograph of a MS absorber of periodic water droplets. (b) and (c) show the measured absorption spectra for different droplet sizes. (d) Photograph and (e) measured absorption spectra of a flexible MS absorber for various water fillings. (f) Measured and simulated absorption spectra of a 3-D printed Swastika-shaped MS absorber. The insets show a photograph and sketch of the MS. (g) Relative bandwidth vs. the center frequency for different WB MS absorbers [39–60,62,63,66–71]. Figures are reproduced with permission from: (a)–(c) [39]; (d)–(e), [40]; (f), [59].

### 3.3 Metasurface absorbers

Perhaps the most successful application of WB MSs is with absorption of microwaves [39–71]. The high permittivity and losses of water makes it an excellent material for both narrow and broadband absorbers, see Fig 4. The first WB MS absorber was proposed by Yoo et al. in 2015 [39], Fig. 4(a)-(c). It consisted of distilled water droplets on a FR4 substrate with hydrophobic/hydrophilic surface patterning on the frontside and a ground conducting plane on the backside. The height of the droplets was controlled with simple addition/removal of water effectively changing the absorption bandwidth. Additionally, the diameter was also adjusted with different hydrophobic/hydrophilic surface patterning. The MS had an absorption bandwidth (absorptivity higher than 90 %) that covered 43 % of the central frequency, which was achieved with three resonances excited in the MS distributed across its spectrum.

Beside the large absorption bandwidth, WB MS absorbers can function for both TE and TM polarizations as well as for a wide range of incidence angles. Furthermore, they are also less sensitive to temperature-changes compared to other WB devices. As noted previously, water also introduces additional advantages besides those provided by its high permittivity. Some of the WB MS absorbers feature visual transparency [43,44,60,70], which opens for the possibility of windows for stealth vehicles, vessels and aircrafts as well as anechoic chambers. WB MSs can also be made flexible as is the case for the MS proposed in [40], see Fig. 4(d). The flexibility was provided by a dielectric substrate of methyl methacrylate (PMMA) host making it possible to cover objects of different shapes with the MS. Similar to [39], the height of the water drops could be adjusted, albeit here microfluidic channels were used instead, see Fig. 4(e).

More complicated designs have been proposed for further performance enhancement. Recently, a MS composed of 3-D printed Swastika-shaped water inclusions have been investigated in [59] showing ultrabroadband absorption bandwidth of 136 % (9.3–49 GHz), see Fig. 4(f). The MS is made of polylactic acid host structure with water inclusions connected by fluidic channels. The thickness of the MS is between 1/10 and 6/10 of the free-space wavelength in the frequency operation band. Here, we emphasize that, besides Mie resonances in the water inclusions, other mechanisms like e.g. Fabry-Pérot resonances contribute to the absorption. Simulation results show minimal dependence on changes in water permittivity due to temperature shifts, and thus, the MS can be employed under various conditions as long as the water does not freeze or boils. Furthermore, the absorption efficiency is above 80 % for TE (TM) waves with incidence angles below 45° (60°).

A map of the center frequencies and relative bandwidths of all WB MS absorbers operating in the frequency band 0.7-74 GHz is shown in Fig. 4(g). The trend shows that the relative bandwidth increases with the increasing center frequency. We believe that this stems from the dispersion of water's permittivity: the quality factor of the resonances simply decreases as the loss tangent of the water increases, effectively permitting larger relative bandwidths at higher frequencies.

A WB MS absorber operating in the THz-regime was recently proposed [61]. The band of potential 90 % absorption extended with 66.5 % bandwidth is centered around the center frequency of 6.77 THz. The MS consists of water inclusions in a polytetrafluoroethylene (PTFE) layer sandwiched by a biased graphene layer on the top and a gold layer on the bottom. The MS can potentially be tuned dynamically by changing the bias of the graphene layer.

Implementations of WB MS absorbers in microwave systems have been few so far. One has been absorbers in radomes, which are designed to reflect/absorb the frequencies outside the pass band [64,65]. Frequency tuning of the WB absorber for radomes by mechanical perturbation and temperature shift of the water volume was demonstrated in [65].

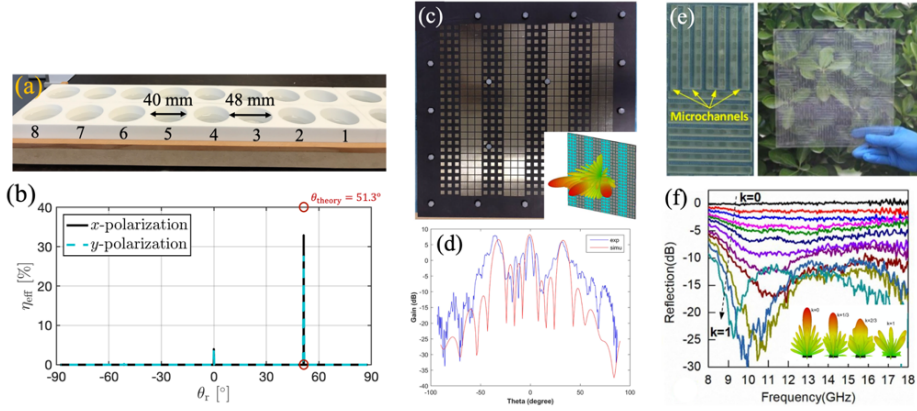


**Figure 5.** Reflection control with WB MS reflectarrays. (a) and (b) MS reflectarray in the form of cylindrical water inclusions in a Rohacell 51 HF host backed with ground conducting plane. (a) Photograph of the fabricated MS. (b) The reflection efficiency as a function of the reflection angle for  $x$ - and  $y$ -polarized plane waves at normal incidence. (c) and (d) MS with tunable reflection properties through different water-filling coding sequences. Both distilled water and NaCl solutions are used for the filling. (e) Photograph of the fabricated MS with the coding sequence “01010101” and (d) the measured and simulated radiation pattern (gain in dB). The inset in (c) shows a sketch of the MS and the radiation pattern. (e) and (f) Reflection tuning of transparent MS with microfluidic channels. (e) Photograph of the fabricated MS and (f) measured reflection spectra for different water-fillings. Inset in (d) shows the simulated far-field scattering. Figures are reproduced with permission from: (a)–(b) [36]; (c)–(d), [34]; (e)–(f), [37].

### 3.4 Reflection control with metasurfaces – towards WB reflectarrays

MSs exhibiting anomalous reflection are called MS reflectarrays. They carefully manipulate the amplitudes and phases of the local scattered fields across the MS to tailor the reflected waves at will. This is governed by the generalized Snell’s law for a structure with the spatial phase variation  $\Phi(x,y)$  across its surface

$$\sin \theta_r - \sin \theta_i = \frac{\lambda_0}{2\pi} \frac{\partial^2 \Phi(x,y)}{\partial x \partial y} \quad (3)$$

with  $\theta_i$  and  $\theta_r$  being the incidence and reflection angles, respectively, and  $\lambda_0$  being the free-space wavelength. In MS reflectarrays, subwavelength scatterers, placed across the MS, are used to provide discontinuous phase shifts, effectively changing the reflection angle of the reflected wave. The main task is to find these scatterers providing the required phase shift, while maintaining a high reflection. For example, if an anomalous plane wave reflection is desired, then a periodic linear phase shift of  $2\pi$  each  $x$  and/or  $y = \lambda_0$  is required. Many metallic and a few dielectric microwave MS reflectarrays have been demonstrated with very high efficiencies, however, they lag tuning capabilities [142]. Introducing tuning parameters to the systems has shown inevitable efficiency reductions.

Different configurations of WB MS reflectarrays have been used [34–37], as shown in Fig. 5. The simplest one perhaps is composed of cylindrical water inclusions in a Rohacell 51 HF host backed with a metallic ground conducting plane [36], see Fig. 5(a) and (b). Almost a full  $2\pi$  phase control was obtained with a magnetic dipole resonance induced in the water cylinders (water temperature of 20 °C) through variation of the cylinder height. A supercell of eight elements anomalously reflected a normally incident plane wave at a reflection angle of 51.3°. Nearly all reflected power was

channeled into the desired direction, albeit the water losses limited the total reflected power to around 37 % of the incident power. Potentially, the MS can be reconfigured for different reflection angles or frequency operation by simply changing the height of water in the cylindrical inclusion or by changing its permittivity (with temperature and/or salinity changes). Since the containers for the water are identical, the number of inclusions in the supercells can be adjusted as well.

Another type of WB MS reflectarray was investigated in [34], see Fig. 5(c) and (d). The MS consisted of a sheet of Teflon woven glass (F4B) with metal coding pattern backed with a saline water substrate and metallic ground conducting plane. Reflection was controlled by varying the water salinity. Furthermore, the radiation pattern could be tailored by reconfiguration of the metal coding pattern. In [35], diodes were incorporated into the MS to introduce another means for tuning. The radiation pattern was altered by switching the bias voltage of the diodes between on and off.

A similar MS design was reported in [37], Fig. 5(e) and (f). The MS consisted of a periodic element with films of Indium Tin Oxide (ITO) spaced with a PMMA substrate. Water inclusions were embedded into the substrate and were connected with microfluidic channels. Through rotation of the element, a checkered subarray pattern was constructed. The water inclusion volumes were varied illustrating dynamic tuning of the reflection, see Fig. 5(f). Interestingly, the MS is very transparent at visible frequencies making it possible to employ it in situations, where visual transparency is desired, while impeding microwaves.

WB MS reflectarrays show promising tunability and/or reconfigurability. However, many of them are slow, and the water losses cause modest efficiencies. Still, the purpose of using water is to make simple, cheap and bio-friendly alternatives to conventional devices.

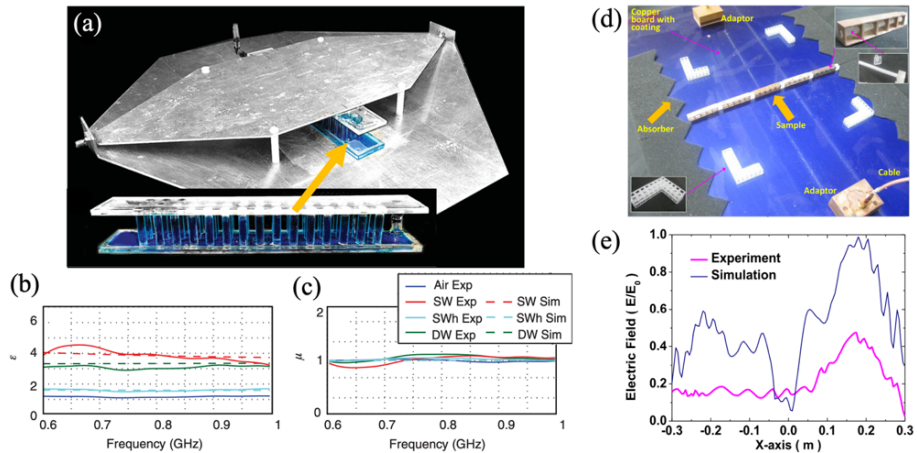


**Figure 6.** (a)–(b) Demonstration of WB MM consisting of non-resonant water-filled cylindrical containers. Tuning of the MM is demonstrated by changing of water content as well the salinity level of water. (a) shows photographs of the MM and the experimental setup consisting of an open TEM waveguide. (b) and (c) show the effective permittivity and permeability spectra, respectively, for air and different fillings of saltwater (SW) and distilled water (DW). (d)–(e) Metamaterial structure with equivalent negative refractive index. (d) Photograph of the experiment composed the metamaterial placed in a TEM waveguide. (e) Simulated and measured normalized electric field as along the axis parallel to the metamaterial. Figures are reproduced with permission from: (a)–(c), [23]; (d)–(e), [33].

### 3.5 Metamaterials

The high permittivity of water enables realization of MMs with very low filling ratios [20,23]. A WB MM consisting of water-filled cylindrical containers with tunable properties was proposed in [23], see Fig. 6(a) and (b). By changing the permittivity of water and/or filling of the cylindrical containers, the effective material parameters can be tuned. Refractive indices between 1 and 2 over a broad frequency band and with filling ratios less than 0.07 were achieved. The MM is simple and cheap and can be applied for transformation optics, lenses or demonstration of wave physics.

A simple MM composed of metallic frames and water cylinders exhibit effective properties of a negative refractive index material [33]. Such materials, not naturally existing in nature, have attracted much attention in recent years with the potential of realizing devices such as lenses and waveguides that can go beyond the diffraction limit [143]. A magnetic dipole is excited in the water cylinders, which provides the negative magnetic response. The metallic frame brings the equivalent negative permittivity, and the effective refractive index is calculated to be  $-1.0$  at 3.4 GHz. The experimental setup as shown in Fig. 6(d) is composed of a TEM rectangular waveguide with the MM placed in between the transmitter and the receiver of the waveguide. The MM has a flat surface towards the transmitter, whereas the surface towards the receiver is inclined by 11 degrees. The simulated and measured normalized electric field along a line parallel to the MM is shown in Fig. 6(e). The incidence wave is mostly refracted in the opposite direction than normally happens with natural materials. This is the consequence of the negative effective refractive index.

WB MMs have been few in numbers thus far, which is not surprising due the losses in water. To minimize the losses, non-resonant inclusions were applied in [23], whereas in [33], the MM was not a full 3-D periodic material. A WB MM capable of topological transitions was proposed in [22], and consists of water-coated copper wires embedded in a ceramic host medium. By exploiting water permittivity's temperature dependence, potential of tuning the dispersion of the MM from being elliptic to flat and further to hyperbolic was demonstrated. However, we must emphasize that the water losses were neglected in the study, and thus the real response of the MM remains missing.

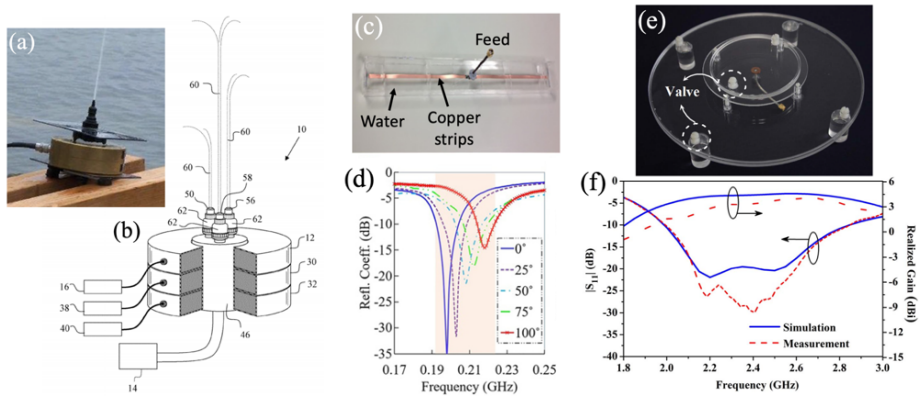


**Figure 7.** WB microwave antennas. (a) Photograph and (d) schematic of a seawater antenna. (c) Photograph of a water-loaded dipole antenna with the temperature-tuning capabilities shown in (d). (e) Photograph of a transparent WB patch antenna with (f) the measured and simulated reflection coefficient and realized gain spectra. Figures are reproduced with permission from: (a)–(b), [92,103]; (c)–(d), [94]; (e)–(f), [105].



#### 4. Antennas

The first water-based antenna was proposed and demonstrated by Kingsley and O’Keefe in 1999 [91]. It is a dielectric resonator antenna (DRA) composed of a water-filled (distilled) cylindrical polyvinyl chloride (PVC) container with an aluminum plate on the outer side. The container was placed on a conducting ground plane with five switchable coaxial monopole antenna feeds enabling beam-steering capabilities. Afterwards, several water-based antenna designs have been proposed, see Table 1. Some exploit the high permittivity of distilled water [84–91,93–96,98,102,105–107,110–113,116,118,119], while other utilize the conductivity of saltwater [80–83,97,99,100,104,108,109,117,121–125]. An example of the latter is shown in Fig. 7(a) and (b) [92,103]. It is a monopole antenna composed of a continuous stream of seawater pumped out via a nozzle. In transmission state, an electric current is induced in the seawater stream with a magnetic feed consisting of circular ferrite magnets. Through control of the height of the seawater stream, the operational frequency is tuned between 2 MHz and 400 MHz.

Another type of a WB antenna is shown in Fig. 7(c) and (d) [94]. It is a water-loaded dipole antenna consisting of copper strips embedded into a water-filled box. The water allows for shrinking of the dipole antenna, which normal size is half of the free-space wavelength ( $\lambda_0$ ), however, on the cost of reduced total efficiency. The prototype shown in Fig. 7(c) is approximately  $\lambda_0/4$  in dimension and operates at around 0.2 GHz. By changing the temperature of the water, the antenna can be frequency-tuned as shown by the reflection coefficient spectrum in Fig. 7(d). As the temperature increases, the total efficiency increases slightly stemming from the lower water absorption losses. The efficiency reduction due to the increased water volume was also investigated showing significant reduction for box thicknesses greater than  $0.04\lambda_0$ . For higher frequencies, this bound is even lower. A transparent WB antenna is shown in Fig. 7(e) and (f). It consists of a small metallic feed surrounded by circular patches of water, see the image in Fig. 7(e) [105]. The antenna operates around 2.4 GHz with excellent matching (reflection coefficient below  $-20$  dB) and modest realized gain (above  $-5$  dB), see Fig. 7(f).

Many WB antennas are designed with a large metallic ground conducting plane, which limits their applications, see e.g. Fig. 8(a)–(c). Instead, a patch of water can be employed as demonstrated with the WB patch antenna in Fig. 7(c).

In many antenna applications, a signal is desired to be transmitted/received in/from a specific direction. Therefore, antennas with more directive radiation, and thus higher gain, must be used. Such Yagi-Uda WB antennas [118,121] and array WB antennas [114,117] have been reported. A microstrip patch antenna loaded with a MS embedded with fluidic channels and operating at 2.62 GHz is shown in Fig. 8(a)–(c). The beam of the antenna can be steered through reconfiguration of the water-fillings in the fluidic channels, see Fig. 8(c). Not surprisingly, the gain is the highest, when the channels are without water (Mode II). Adding water to the fluidic channels allows for steering of the beam, albeit halving the maximum gain. Nonetheless, the antenna constitutes a simple and compact alternative for beam-steering without the need of active electronic components.

A different approach towards increased gain can be achieved in compact DRAs with simultaneous excitation of multiple modes [141]. A subwavelength WB Huygens DRA was demonstrated in [93] where balanced magnetic and electric modes were excited in the DRA at 350 MHz. As the result, Kerker’s condition is satisfied, see Fig. 8(d)–(f). The DRA comprises a short monopole antenna fed against a large ground conducting plane and encapsulated by a rectangular cuboid-shaped distilled water volume. The two excited dipole modes provided the DRA with twice the directivity as compared to a single dipole mode. The radiated power is diverted in one direction, providing an

excellent front-to-back radiation ratio of around 40 dB. Furthermore, the DRA was self-matched to a 50 Ohm load with a very low reflection coefficient of approximately  $-40$  dB.

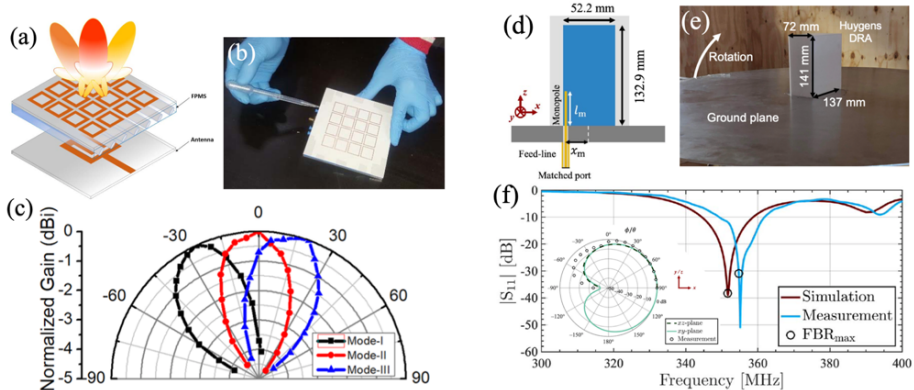


**Figure 8.** Directive WB microwave antennas. (a) Sketch and (b) photograph of a beam-steering antenna with a WB MS. (c) Measured radiation pattern (normalized gain) for different water-fillings of the fluidic channels in the MS. (d) Sketch and (e) photograph of a WB Huygens DRA. (f) The simulated and measured reflection coefficient spectra with the inset showing the simulated and measured radiation pattern. Figures are reproduced with permission from: (a)–(c), [117]; (d)–(f), [93].

The general issue with WB antennas is their reduced efficiencies due to the absorption losses in water. As the absorbed power is proportional to the square of the electric field magnitude, c.f. Eq. (2), the small DRAs with high intensity fields suffer most from these losses. This was investigated for an electrically small WB hemispherical DRA in [89] with a size 18 times smaller than the free-space wavelength. Designed for 300 MHz operation, the efficiency was only 30 %, whereas, when designed for 1 GHz operation, the efficiency is reduced three-fold due to the increased water losses at higher frequencies.

## 5. RF components and waveguides

Fluidic microwave components display a way towards tunable passive microwave components. Mostly liquid-metal has been employed in a wide variety of component types, see review [144]. A few WB components have been demonstrated and some of them are shown in Fig. 9 [128,129,145]. A coplanar waveguide (CPW) with a water drop placed on top was examined in [128], see Fig. 9(a) and (b). By moving the drop, the wave response could be switched between the transmission and reflection states. Instead of a drop atop of the CPW, the CPW line can be suspended in water for absorption of waves.

A WB RF tuner was demonstrated in [129]. Through different fillings of the small cavities in a CPW, the impedance of the line was tuned, see Fig. 9(c). As a proof of concept, the RF tuner was connected to an RF amplifier, which could be frequency-tuned with different cavity fillings combinations, Fig 9(d).

Additionally, we want to mention a field-effect transformer (FET) with a water drop atop presented in [145]. The electrostatic characteristics of the FET were investigated. With the water drop, the FET could support rapid bias changes, high on/off current ratios, near-ideal sub-threshold swing and

enhanced short-channel behavior. Such FET would be interesting to characterize on microwave frequencies.

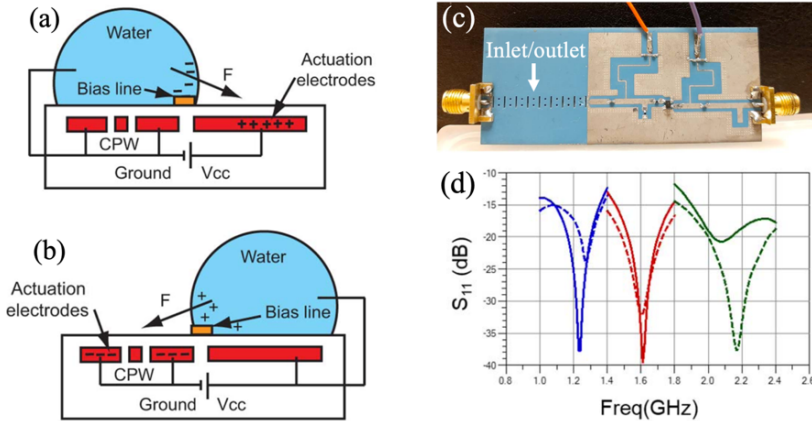


**Figure 9.** RF components utilizing water. a) and b) Sketches of a water drop placed on a coplanar waveguide with different biases for on/off switching of guided waves [128]. (c) Photograph of a RF tuner integrated with a RF amplifier and (d) reflection coefficient spectra [129]. The solid (dashed) lines show the simulation (measurement) results for different fillings of the cavities. Figures are reproduced with permission from: (a)–(b) [128]; (c)–(d) [129].

## 6. Structures with intriguing modes

Dynamic toroidal moments with high Q-factor attracted a lot of attention since their first demonstration [146]. For efficient excitation such resonant modes require complex structures. A MS composed of clusters of four cylindrical water inclusions was demonstrated to exhibit a toroidal dipole around 1 and 2.5 GHz [32,76], see Fig. 10(a)–(d). At first, enhancement in the transmission was used to point on the excitation of the toroidal moment, Fig. 10(d). Later, the final proof of the existence of the toroidal dipole was done by the near field characterization [76]. Toroidal dipoles are dark modes (i.e. non-scattering) and thus their applications are limited, for example to absorbers and sensing.

In recent years, BICs have become a very hot topic within photonics and acoustics [147,148], whereas only few have been realized at microwave frequencies [149–151]. A BIC is a perfectly confined resonant mode of a system open for radiation. Theoretically, it possesses an infinite Q-factor, and is, therefore, of great interest for many applications including sensing, energy harvesting, lasing etc. BICs can be classified according to the number of eigenmodes involved in the scattering process (single or multiple) as well as to the nature of their underlying interference mechanisms (symmetry-enabled or accidental BICs). When losses are present and/or symmetry is broken, the BIC is turned into a quasi-BIC, resulting in a sharp Fano line-shape in the radiation spectrum. A general problem of BIC structures is that all of their experimental realizations to date have inherently relied on very large arrays requiring large footprints. Thus, it certainly limits their applications when enhanced local density of states is on demand, for example in sensing. If only a few elements are included in a BIC array, the Q-factor is limited to a few dozens, which can be easily achieved with several more conventional modes.

Very recently, a novel symmetry-protected BIC structure has been demonstrated. It is composed of a single metallic resonator placed in a rectangular waveguide, see Fig 10(e)–(g). Due to the

symmetry of the resonator, the natural modes of the waveguide could not couple to a mode existing in the configuration, and thus a BIC emerged. To break the symmetry, a water drop was added asymmetrically atop of the resonator. Thus, the BIC was turned into a quasi-BIC, revealed by the measured reflection coefficient in a simple tabletop experiment, Fig 10(f) and (g). The response depends on the shape, volume, position, temperature and salinity of the water drop. These dependencies were utilized to make highly advanced sensing analyses including the dissolution of salt crystals in water and the evaporation of tiny water volumes from the drop. Such simple, well-controlled and cost-effective approach being quite universal can be transferred to the lower (RF) and higher (photonics) frequency ranges with a row of promising applications.

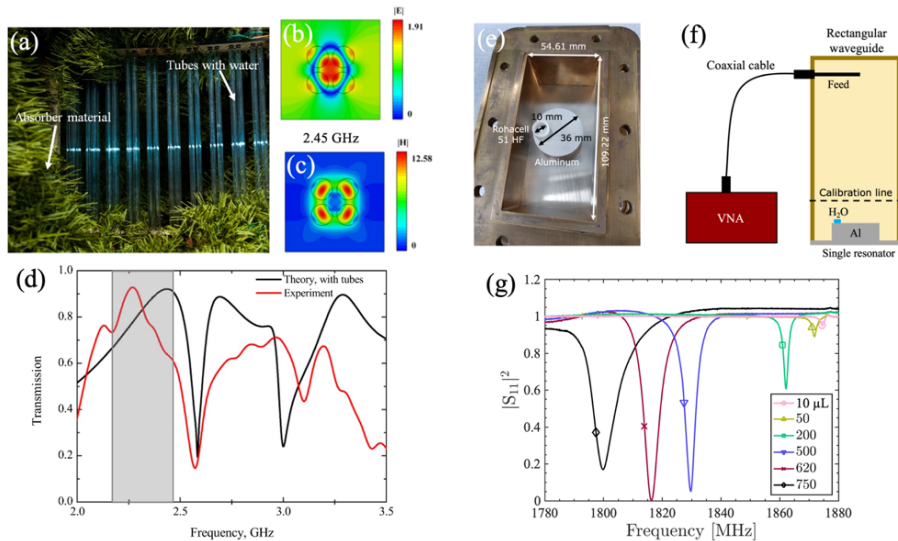


**Figure 10.** (a)–(d) Demonstration of toroidal modes in an array composed of clusters of four cylindrical containers filled with water. (a) shows a photograph of the fabricated array with absorbing materials around it. (b) and (c) show the electric (top) and magnetic (bottom) field magnitudes in one cluster of cylinders. (d) shows the transmission spectra with the gray area indicating the frequency band of the toroidal mode. (e)–(g) A boundary-induced BIC for advanced sensing. (e) photograph of the fabricated resonator placed in a rectangular waveguide section. (f) Sketch of the experimental setup and (g) normalized measured reflection coefficient for different water volume insertions. Figures are reproduced with permission from: (a)–(d), [32]; (e)–(g), [130].

## 7. Applications and outlook

WB devices have the potential to be simple, cheap, bio-friendly and tunable alternatives for many microwave applications. They find relevance in today’s increasing focus on recyclability and low environmental footprint of products. So far, numerous WB devices of different functionalities have been demonstrated showcasing advanced and diverse electromagnetic wave control with simple materials. Some WB devices contain rare and/or expensive materials. In these cases, the benefits of using water vanish, and thus it can be exchanged with low-loss dielectrics instead.

The advantages of using water include a broad potential of dynamical reconfigurability of devices basing on shape flexibility, provided by water’s liquid state, easiness of volume tuning, temperature-dependent complex permittivity and strongly nonlinear interplay of self-heating of water volumes

due to absorption and changes in permittivity caused by this. The progresses within 3D-printing technology enable easy and efficient fabrication of advanced host containers for water of peculiar shapes on demand. In particular, WB MSs that are configured with arrays of water inclusions are well-suited for 3D-printing, see e.g. Fig. 4(f).

Thus far, the most elaborated application of WB MS has been microwave absorbers. The area of WB MS absorbers has already matured offering various thin and flat alternatives to conventional absorbers. Therefore, as the forthcoming natural step we anticipate their implementations in real systems, such as in the case of absorbers [64,65], combination of radomes with absorbers. Besides, flexible and highly absorptive surfaces of anechoic chambers, camouflaging of big reflecting surfaces and transparent windows terminating all microwave radiation are likely to be the first among potential applications. Typically, the absorbers in anechoic chambers are pyramidal polyurethane foam blocks loaded with carbon particles, which pose a potential health risk to direct contact personnel. Furthermore, such foam blocks are very expensive and bulky. Here, WB MS absorbers can serve as bio-friendly, recyclable and flexible alternatives. As for the other types of WB MSs, the low efficiency and weather-instability constitute major challenges which have to be resolved before they can compete with existing technology.

WB antennas are still viewed as impracticable in real-life implementations by microwave engineers due to their low stability and/or reduced efficiency. Several ways to overcome these limitations have been presented, and hopefully challengers of WB antennas applications will be lifted off in the nearest years. Other liquids, including salted water, both with dielectric and conducting properties are becoming the point of attention [127]. As a matter of fact, a sea antenna has already been piloted for military usage [92].

Recent research efforts have demonstrated new possibilities of water as a new element in conventional systems [129,130]. In particular, the single resonator structure with a localized BIC, in which water was used to break the symmetry of the system, enables the possibility of practical microwave BICs. Besides the obvious advantages of simple and low-cost microwave setups, such localized BICs can overcome many intrinsic limitations of the more traditional microwave modes. They may thus open the possibility of truly novel and highly tunable microwave devices including MSs for advanced microwave control and sensing. We believe that the WB circuitry and just single water elements adding functionalities to the systems are in the beginning of the research boom, which will be driven in a long term by the UN proclaimed goals on global sustainability and human-friendly environment.

## REFERENCES AND NOTES

1. M. Sargen, "Biological Roles of Water: Why is water necessary for life?," Harvard University (September 26, 2019).
2. Howard Perlman, "Water, the Universal Solvent," USGS Water Science School (2016).
3. P. Ball, *Life's Matrix: A Biography of Water*, 1st ed. (Farrar, Straus & Giroux, 1999).
4. J. D. Smith, C. D. Cappa, K. R. Wilson, B. M. Messer, R. C. Cohen, and R. J. Saykally, "Energetics of hydrogen bond network rearrangements in liquid water," *Science* **306**, 851–853 (2004).
5. F. Franks, *Water: A Comprehensive Treatise, Vol. 1-5*, 1st ed. (Plenum Press, 1975).
6. I. Popov, P. Ben Ishai, A. Khamzin, and Y. Feldman, "The mechanism of the dielectric relaxation in water," *Phys. Chem. Chem. Phys.* **18**, 13941–13953 (2016).
7. D. Laage and J. T. Hynes, "A molecular jump mechanism of water reorientation," *Science* **311**, 832–835 (2006).
8. M. Sharma, R. Resta, and R. Car, "Dipolar correlations and the dielectric permittivity of water," *Phys. Rev. Lett.* **98**, 247401 (2007).
9. W. J. Ellison, "Permittivity of pure water, at standard atmospheric pressure, over the frequency range 0-25 THz and the temperature range 0-100 oC," *J. Phys. Chem. Ref. Data* **36**, 1–18 (2007).
10. R. L. Fulton, "The nonlinear dielectric behavior of water: Comparisons of various approaches to the nonlinear dielectric increment," *J. Chem. Phys.* **130**, 204503 (2009).

11. H. J. Bakker and J. L. Skinner, "Vibrational spectroscopy as a probe of structure and dynamics in liquid water," *Chem. Rev.* **110**, 1498–1517 (2010).
12. N. C. Burch, H. Jusuja, and K. S. Walton, "Water stability and adsorption in metal-organic frameworks," *Chem. Rev.* **114**, 10575–10612 (2014).
13. J. O. Richardson, C. Pérez, S. Lobsiger, A. A. Reid, B. Temelso, G. C. Shields, Z. Kisiel, D. J. Wales, B. H. Pate, and S. C. Althorpe, "Concerted hydrogen-bond breaking by quantum tunneling in the water hexamer prism," *Science* **351**, 1310–1313 (2016).
14. D. C. Elton and M. Fernandez-Serra, "The hydrogen-bond network of water supports propagating optical phonon-like modes," *Nat. Commun.* **7**, 10193 (2016).
15. D. C. Elton, "The origin of the Debye relaxation in liquid water and fitting the high frequency excess response," *Phys. Chem. Chem. Phys.* **19**, 18739–18749 (2017).
16. P. Ball, "Water: Water - an enduring mystery," *Nature* **452**, 291–292 (2008).
17. M. V. Rybin, D. S. Filonov, P. A. Belov, Y. S. Kivshar, and M. F. Limonov, "Switching from visibility to invisibility via fano resonances: Theory and experiment," *Sci. Rep.* **5**, 8774 (2015).
18. B. I. Popa and S. A. Cummer, "Water-based metamaterials: Negative refraction of sound," *Nat. Mater.* **14**, 363–364 (2015).
19. A. Andryieuski, S. M. Kuznetsova, S. V. Zhukovsky, Y. S. Kivshar, and A. V. Lavrinenko, "Water: Promising Opportunities For Tunable All-dielectric Electromagnetic Metamaterials," *Sci. Rep.* **5**, 13535 (2015).
20. M. V. Rybin, D. S. Filonov, K. B. Samusev, P. A. Belov, Y. S. Kivshar, and M. F. Limonov, "Phase diagram for the transition from photonic crystals to dielectric metamaterials," *Nat. Commun.* **6**, 10102 (2015).
21. Z. Shen, H. Yang, X. Huang, and Z. Yu, "Design of negative refractive index metamaterial with water droplets using 3D-printing," *J. Opt.* **19**, 115101 (2017).
22. M. A. Gorchak, M. Song, A. P. Slobozhanyuk, A. A. Bogdanov, and P. A. Belov, "Topological transition in coated wire medium," *Phys. Status Solidi - Rapid Reson. Lett.* **10**, 900–904 (2016).
23. L. Liu, A. R. Katko, D. Li, and S. A. Cummer, "Broadband electromagnetic metamaterials with reconfigurable fluid channels," *Phys. Rev. B* **89**, 245132 (2014).
24. M. Odit, P. Kapitanova, A. Andryieuski, P. Belov, and A. V. Lavrinenko, "Experimental demonstration of water based tunable metasurface," *Appl. Phys. Lett.* **109**, 11901 (2016).
25. X. Yang, D. Zhang, S. Wu, Y. Yin, L. Li, K. Cao, and K. Huang, "Reconfigurable all-dielectric metasurface based on tunable chemical systems in aqueous solution," *Sci. Rep.* **7**, 3190 (2017).
26. A. V. Lavrinenko, R. E. Jacobsen, S. Arslanagic, S. Kuznetsova, A. Andryieuski, M. Odit, and P. Kapitanova, "Tunable microwave metamaterials based on ordinary water," in *Proceedings of the 2017 47th European Microwave Conference (IEEE, 2017)*, pp. 492–495.
27. A. V. Lavrinenko, R. E. Jacobsen, and S. Arslanagic, "Low-loss Water-based Metasurface in Waveguide Environment," in *Proceedings of the 2018 48th European Microwave Conference (IEEE, 2018)*, pp. 819–822.
28. R. E. Jacobsen, A. V. Lavrinenko, and S. Arslanagic, "Water-Based Metasurfaces for Effective Switching of Microwaves," *IEEE Antennas Wirel. Propag. Lett.* **17**, 571–574 (2018).
29. R. E. Jacobsen, S. Arslanagic, and A. V. Lavrinenko, "Thermal tuning of a microwave water-based metasurface," in *Swedish Microwave Days* (2018).
30. M. Odit, A. Sayanskiy, I. Munina, and P. Belov, "Functional metasurfaces based on water," in *Journal of Physics: Conference Series* (IOP Publishing, 2018), Vol. 1092, p. 12103.
31. P. Kapitanova, A. Sayanskiy, M. Odit, A. Miroshnichenko, A. Lavrinenko, and P. Belov, "All-dielectric Metasurfaces as an Efficient Tool for Electromagnetic Waves Manipulation," in *2018 20th Anniversary International Conference on Transparent Optical Networks (ICTON)* (IEEE, 2018), Vol. 2018-July.
32. I. V. Stenishchev and A. A. Basharin, "Toroidal response in all-dielectric metamaterials based on water," *Sci. Rep.* **7**, 9468 (2017).
33. X. Cai, S. Zhao, M. Hu, J. Xiao, N. Zhang, and J. Yang, "Water based fluidic radio frequency metamaterials," *J. Appl. Phys.* **122**, 184101 (2017).
34. L. Chen, H. L. Ma, X. J. Song, Y. Ruan, and H. Y. Cui, "Dual-functional tunable coding metasurface based on saline water substrate," *Sci. Rep.* **8**, 2070 (2018).
35. L. Chen, H. L. Ma, Y. Ruan, and H. Y. Cui, "Dual-manipulation on wave-front based on reconfigurable water-based metasurface integrated with PIN diodes," *J. Appl. Phys.* **125**, 23107 (2019).
36. R. E. Jacobsen, J. Ø. Nielsen, A. V. Lavrinenko, and S. Arslanagic, "Tunable water-based metasurface for anomalous wave reflection," *J. Phys. D: Appl. Phys.* **53**, 505104 (2020).
37. Y. Pang, M. Mo, Y. Li, B. Qu, S. Xia, S. Qu, and Z. Xu, "Dynamically controlling electromagnetic reflection using reconfigurable water-based metasurfaces," *Smart Mater. Struct.* **29**, 115018 (2020).
38. M. Odit, A. Sayanskiy, V. Asadchy, and P. Belov, "Microwave reflecting focusing metasurface based on water," in *2018 IEEE Antennas and Propagation Society International Symposium and USNC/URSI National*

*Radio Science Meeting, Apsursi 2018 - Proceedings* (IEEE, 2018), pp. 773–774.

39. Y. J. Yoo, S. Ju, S. Y. Park, Y. Ju Kim, J. Bong, T. Lim, K. W. Kim, J. Y. Rhee, and Y. Lee, "Metamaterial Absorber for Electromagnetic Waves in Periodic Water Droplets," *Sci. Rep.* **5**, 14018 (2015).
40. Q. Song, W. Zhang, P. C. Wu, W. Zhu, Z. X. Shen, P. H. J. Chong, Q. X. Liang, Z. C. Yang, Y. L. Hao, H. Cai, H. F. Zhou, Y. Gu, G. Q. Lo, D. P. Tsai, T. Bourouina, Y. Leprince-Wang, and A. Q. Liu, "Water-Resonator-Based Metasurface: An Ultrabroadband and Near-Unity Absorption," *Adv. Opt. Mater.* **5**, 1601103 (2017).
41. J. Zhao, S. Wei, C. Wang, K. Chen, B. Zhu, T. Jiang, and Y. Feng, "Broadband microwave absorption utilizing water-based metamaterial structures," *Opt. Express* **26**, 8522–8531 (2018).
42. J. Xie, W. Zhu, I. D. Rukhlenko, F. Xiao, C. He, J. Geng, X. Liang, R. Jin, and M. Premaratne, "Water metamaterial for ultra-broadband and wide-angle absorption," *Opt. Express* **26**, 5052–5059 (2018).
43. Y. Shen, J. Zhang, Y. Pang, J. Wang, H. Ma, and S. Qu, "Transparent broadband metamaterial absorber enhanced by water-substrate incorporation," *Opt. Express* **26**, 15665–15674 (2018).
44. Y. Pang, Y. Shen, Y. Li, J. Wang, Z. Xu, and S. Qu, "Water-based metamaterial absorbers for optical transparency and broadband microwave absorption," *J. Appl. Phys.* **123**, 155106 (2018).
45. Z. Shen, X. Huang, H. Yang, T. Xiang, C. Wang, Z. Yu, and J. Wu, "An ultra-wideband, polarization insensitive, and wide incident angle absorber based on an irregular metamaterial structure with layers of water," *J. Appl. Phys.* **123**, 225106 (2018).
46. D. J. Gogoi and N. S. Bhattacharyya, "Metasurface absorber based on water meta molecule for X-band microwave absorption," *J. Appl. Phys.* **124**, 75106 (2018).
47. P. J. Bradley, M. O. M. Torricco, C. Brennan, and Y. Hao, "Printable all-dielectric water-based absorber," *Sci. Rep.* **8**, 14490 (2018).
48. D. J. Gogoi and N. S. Bhattacharyya, "Microwave metamaterial absorber based on aqueous electrolyte solution for X-band application," *J. Appl. Phys.* **125**, 125107 (2019).
49. H. F. Zhang, X. L. Tian, G. B. Liu, and X. R. Kong, "A Gravity Tailored Broadband Metamaterial Absorber Containing Liquid Dielectrics," *IEEE Access* **7**, 25827–25832, 8643996 (2019).
50. E. Yang, F. Yang, J. Pei, X. Zhang, S. Liu, and Y. Deng, "All-dielectric ultra-broadband metamaterial absorber based on imidazole ionic liquids," *J. Phys. D: Appl. Phys.* **52**, 395501 (2019).
51. Y. Pang, J. Wang, Q. Cheng, S. Xia, X. Y. Zhou, Z. Xu, T. J. Cui, and S. Qu, "Thermally tunable water-substrate broadband metamaterial absorbers," *Appl. Phys. Lett.* **110**, 104103 (2017).
52. Z. Wu, X. Chen, Z. Zhang, L. Heng, S. Wang, and Y. Zou, "Design and optimization of a flexible water-based microwave absorbing metamaterial," *Appl. Phys. Express* **12**, 57003 (2019).
53. F. Yang, J. Gong, E. Yang, Y. Guan, X. He, S. Liu, X. Zhang, and Y. Deng, "Ultrabroadband metamaterial absorbers based on ionic liquids," *Appl. Phys. A Mater. Sci. Process.* **125**, 149 (2019).
54. J. Xie, S. Quader, F. Xiao, C. He, X. Liang, J. Geng, R. Jin, W. Zhu, and I. D. Rukhlenko, "Truly all-dielectric ultrabroadband metamaterial absorber: Water-based and ground-free," *IEEE Antennas Wirel. Propag. Lett.* **18**, 536–540 (2019).
55. H. Xiong and F. Yang, "Ultra-broadband and tunable saline water-based absorber in microwave regime," *Opt. Express* **28**, 5306–5316 (2020).
56. Q. Liang, Z. Yang, J. Guo, Z. Li, T. Chen, and D. Li, "A high-efficient tunable liquid metal-based electromagnetic absorbing metamaterial," *J. Mater. Sci. Mater. Electron.* 1–6. (2020).
57. X. Zhang, F. Yan, X. Du, W. Wang, and M. Zhang, "Broadband water-based metamaterial absorber with wide angle and thermal stability," *AIP Adv.* **10**, 55211 (2020).
58. B. X. Khuyen, V. T. H. Hanh, B. S. Tung, V. D. Lam, Y. J. Kim, Y. Lee, H. T. Tu, and L. Y. Chen, "Narrow/broad-band absorption based on water-hybrid metamaterial," *Crystals* **10**, 415 (2020).
59. X. Zhang, D. Zhang, Y. Fu, S. Li, Y. Wei, K. Chen, X. Wang, and S. Zhuang, "3-D Printed Swastika-Shaped Ultrabroadband Water-Based Microwave Absorber," *IEEE Antennas Wirel. Propag. Lett.* **19**, 821–825 (2020).
60. Q. Wang, K. Bi, and S. Lim, "All-Dielectric Transparent Metamaterial Absorber With Encapsulated Water," *IEEE Access* **8**, 175998–176004 (2020).
61. H. Zhang, F. Ling, H. Wang, Y. Zhang, and B. Zhang, "A water hybrid graphene metamaterial absorber with broadband absorption," *Opt. Commun.* **463**, 125394 (2020).
62. W. Zhu, I. D. Rukhlenko, F. Xiao, C. He, J. Geng, X. Liang, M. Premaratne, and R. Jin, "Multiband coherent perfect absorption in a water-based metasurface," *Opt. Express* **25**, 15737–15745 (2017).
63. K.-L. Zhang, X.-D. Cheng, Y.-J. Zhang, M. Chen, H. Chen, Y. Yang, W.-L. Song, and D. Fang, "Weather-Manipulated Smart Broadband Electromagnetic Metamaterials," *ACS Appl. Mater. Interfaces* **10**, 40815–40823 (2018).
64. S. K. Patel, K. H. Shah, and J. S. Sonagara, "Broadband liquid metamaterial radome design," *Waves Random Complex Media* **30**, 328–339 (2018).
65. X. Yan, X. Kong, Q. Wang, L. Xing, F. Xue, Y. Xu, S. Jiang, and X. Liu, "Water-based reconfigurable

- frequency selective rasorber with thermally tunable absorption band," *IEEE Trans. Antennas Propag.* **68**, 6162–6171 (2020).
66. D. J. Gogoi and N. S. Bhattacharyya, "Embedded dielectric water "atom" array for broadband microwave absorber based on Mie resonance," *J. Appl. Phys.* **122**, 175106 (2017).
  67. X. Huang, H. Yang, Z. Shen, J. Chen, H. Lin, and Z. Yu, "Water-injected all-dielectric ultra-wideband and prominent oblique incidence metamaterial absorber in microwave regime," *J. Phys. D: Appl. Phys.* **50**, 385304 (2017).
  68. Z. Han, J. Zhao, and Y. Feng, "A tunable water-based metamaterial microwa absorber," in *2017 IEEE 6th Asia-Pacific Conference on Antennas and Propagation, Apcap 2017 - Proceeding* (IEEE, 2017), p. 8420663.
  69. Y. Shen, J. Zhang, Y. Pang, L. Zheng, J. Wang, H. Ma, and S. Qu, "Thermally Tunable Ultra-wideband Metamaterial Absorbers based on Three-dimensional Water-substrate construction," *Sci. Rep.* **8**, 4423 (2018).
  70. Y. Shen, J. Zhang, S. Sui, Y. Jia, Y. Pang, J. Wang, H. Ma, and S. Qu, "Transparent absorption-diffusion-integrated water-based all-dielectric metasurface for broadband backward scattering reduction," *J. Phys. D: Appl. Phys.* **51**, 485301 (2018).
  71. J. Ren and J. Y. Yin, "Cylindrical-water-resonator-based ultrabroadband microwave absorber," *Opt. Mater. Express* **8**, 2060–2071 (2018).
  72. R. E. Jacobsen, S. Arslanagic, and A. V Lavrinenko, "Fundamental Properties of Mie Resonances in Water Spheres," in *Proceedings of 2019 International Symposium on Electromagnetic Theory* (IEEE, 2019).
  73. R. E. Jacobsen, S. Arslanagic, and A. V Lavrinenko, "Fundamental Properties of Mie Resonances in Water Cylinders - TM and TE Case Studies," in *Proceedings of 2019 International Symposium on Electromagnetic Theory* (IEEE, 2019), p. 8931486.
  74. R. E. Jacobsen, S. Arslanagic, and A. V Lavrinenko, "Mie Resonances in Water Spheres for Microwave Metamaterials and Antennas," *URSI Radio Sci. Lett.* **1**, (2020).
  75. P. Kapitanova, V. Ternovski, A. Miroschnichenko, N. Pavlov, P. Belov, Y. Kivshar, and M. Tribelsky, "Giant field enhancement in high-index dielectric subwavelength particles," *Sci. Rep.* **7**, 731 (2017).
  76. N. Pavlov, I. Stenishchev, A. Ospanova, P. Belov, P. Kapitanova, and A. Basharin, "Toroidal Dipole Mode Observation In Situ," *Phys. Status Solidi B Basic Reson.* **257**, 1900406 (2020).
  77. E. Motovilova, S. Sandeep, M. Hashimoto, and S. Y. Huang, "Water-Tunable Highly Sub-Wavelength Spiral Resonator for Magnetic Field Enhancement of MRI Coils at 1.5 T," *IEEE Access* **7**, 90304-90315,8756238 (2019).
  78. H. K. Khattak, P. Bianucci, and A. D. Slepko, "Linking plasma formation in grapes to microwave resonances of aqueous dimers," in *Proceedings of the National Academy of Sciences of the United States of America* (National Academy of Sciences, 2019), Vol. 116, pp. 4000–4005.
  79. H. W. Wu, H. J. Chen, H. F. Xu, R. H. Fan, and Y. Li, "Tunable multiband directional electromagnetic scattering from spoof Mie resonant structure," *Sci. Rep.* **8**, 8817 (2018).
  80. M. Wang and Q. X. Chu, "High-efficiency and wideband coaxial dual-tube hybrid monopole water antenna," *IEEE Antennas Wirel. Propag. Lett.* **17**, 799–802 (2018).
  81. H. Fayad and P. Record, "Broadband liquid antenna," *Electron. Lett.* **42**, 133–134 (2006).
  82. Y.-H. Qian and Q.-X. Chu, "A Broadband Hybrid Monopole-Dielectric Resonator Water Antenna," *IEEE Antennas Wirel. Propag. Lett.* **16**, 1360–1363 (2017).
  83. L. Xing, J. Zhu, Q. Xu, D. Yan, and Y. Zhao, "A circular beam-steering antenna with parasitic water reflectors," *IEEE Antennas Wirel. Propag. Lett.* **18**, 2140–2144 (2019).
  84. A. Singh, I. Goode, and C. E. Saavedra, "A Multistate Frequency Reconfigurable Monopole Antenna Using Fluidic Channels," *IEEE Antennas Wirel. Propag. Lett.* **18**, 856–860 (2019).
  85. J. J. Liang, G. L. Huang, K. W. Qian, S. L. Zhang, and T. Yuan, "An azimuth-pattern reconfigurable antenna based on water grating reflector," *IEEE Access* **6**, 34804–34811 (2018).
  86. M. Wang and Q. X. Chu, "A Wideband Polarization-Reconfigurable Water Dielectric Resonator Antenna," *IEEE Antennas Wirel. Propag. Lett.* **18**, 402–406 (2019).
  87. L. Xing, Q. Xu, J. Zhu, Y. Zhao, S. Aljaafreh, C. Song, and Y. Huang, "A High-Efficiency Wideband Frequency-Reconfigurable Water Antenna With a Liquid Control System: Usage for VHF and UHF Applications," *IEEE Antennas Propag. Mag.* **63**, (2021).
  88. Y. Chen and C. F. Wang, "Dual-band directional/omni-directional liquid dielectric resonator antenna designs using characteristic modes," in *IEEE Antennas and Propagation Society, AP-S International Symposium (Digest)* (Institute of Electrical and Electronics Engineers Inc., 2014), pp. 848–849.
  89. R. E. Jacobsen, A. V Lavrinenko, and S. Arslanagic, "Electrically small water-based hemispherical dielectric resonator antenna," *Appl. Sci.* **9**, 4848 (2019).
  90. S. G. O'Keefe and S. P. Kingsley, "Tunability of liquid dielectric resonator antennas," *IEEE Antennas Wirel. Propag. Lett.* **6**, 533-536,907916 (2007).



91. S. P. Kingsley and S. G. O'Keefe, "Beam steering and monopulse processing of probe-fed dielectric resonator antennas," in *IEE Proceedings: Radar, Sonar and Navigation* (IEE-INST ELEC ENG, 1999), Vol. 146, pp. 121–125.
92. John Pavlus, "Navy Antenna Using Seawater instead of Metal," <https://www.technologyreview.com/2010/11/18/198879/navy-antenna-using-seawater-instead-of-metal/>.
93. R. E. Jacobsen, A. V. Lavrinenko, and S. Arslanagic, "A Water-Based Huygens Dielectric Resonator Antenna," *IEEE Open J. Antennas Propag.* **1**, 493–499 (2020).
94. A. T. Mobashsher and A. Abbosh, "Reconfigurable water-substrate based antennas with temperature control," *Appl. Phys. Lett.* **110**, 253503 (2017).
95. M. Lapiere, Y. M. M. Antar, A. Ittipiboon, and A. Petosa, "Ultra wideband monopole/dielectric resonator antenna," *IEEE Microw. Wirel. Components Lett.* **15**, 7–9 (2005).
96. M. Zou, Z. Shen, and J. Pan, "Frequency-reconfigurable water antenna of circular polarization," *Appl. Phys. Lett.* **108**, 14102 (2016).
97. G. H. Huff, D. L. Rolando, P. Walters, and J. McDonald, "A frequency reconfigurable dielectric resonator antenna using colloidal dispersions," *IEEE Antennas Wirel. Propag. Lett.* **9**, 288–290 (2010).
98. Z. Gong, C. Bartone, F. Yang, and J. Yao, "High-efficiency water-loaded microwave antenna in ultra-high-frequency band," *Appl. Phys. Lett.* **112**, (2018).
99. Z. Chen and H. Wong, "Liquid Dielectric Resonator Antenna with Circular Polarization Reconfigurability," *IEEE Trans. Antennas Propag.* **66**, 444–449 (2018).
100. L. Xing, Y. Huang, Q. Xu, and S. Alja' Afreh, "Wideband, hybrid rectangular water antenna for DVB-H applications," *Microw. Opt. Technol. Lett.* **57**, 2160–2164 (2015).
101. R. E. Jacobsen, M. H. Vandborg, A. V. Lavrinenko, and S. Arslanagic, "Water-Based Microwave Antennas," in *14th European Conference on Antennas and Propagation (EuCAP)* (2020).
102. Z. Ren, S. S. Qi, Z. Hu, Z. Shen, and W. Wu, "Wideband Water Helical Antenna of Circular Polarization," *IEEE Trans. Antennas Propag.* **67**, 6770–6777 (2019).
103. D. W. S. Tam, "Patent: Electrolytic Fluid Antenna with Signal Enhancer," U.S. patent US8368605 (2013).
104. G. Li, Y. Huang, G. Gao, C. Yang, Z. Lu, and W. Liu, "A broadband helical saline water liquid antenna for wearable systems," *Int. J. Electron.* **105**, 645–658 (2018).
105. J. Sun and K. M. Luk, "A Wideband Low Cost and Optically Transparent Water Patch Antenna with Omnidirectional Conical Beam Radiation Patterns," *IEEE Trans. Antennas Propag.* **65**, 4478–4485, 7987716 (2017).
106. J. Sun and K. M. Luk, "A compact-size wideband optically-transparent water patch antenna incorporating an annular water ring," *IEEE Access* **7**, 122964–122971 (2019).
107. Y. Li and K. M. Luk, "A Water Dense Dielectric Patch Antenna," *IEEE Access* **3**, 274–280, 7080869 (2015).
108. Z. Chen and H. Wong, "Wideband Glass and Liquid Cylindrical Dielectric Resonator Antenna for Pattern Reconfigurable Design," *IEEE Trans. Antennas Propag.* **65**, 2157–2164 (2017).
109. M. Koneca and P. A. Warr, "A Frequency-Reconfigurable Antenna Architecture Using Dielectric Fluids," *IEEE Trans. Antennas Propag.* **63**, 5280–5286 (2015).
110. J. D. Barrera and G. H. Huff, "A fluidic loading mechanism in a polarization reconfigurable antenna with a comparison to solid state approaches," *IEEE Trans. Antennas Propag.* **62**, 4008–4014 (2014).
111. C. Murray and R. R. Franklin, "Independently Tunable Annular Slot Antenna Resonant Frequencies Using Fluids," *IEEE Antennas Wirel. Propag. Lett.* **13**, 1449–1452 (2014).
112. Y. H. Qian and Q. X. Chu, "A polarization-reconfigurable water-loaded microstrip antenna," *IEEE Antennas Wirel. Propag. Lett.* **16**, 2179–2182 (2017).
113. H. Tang and J. X. Chen, "Microfluidically Frequency-Reconfigurable Microstrip Patch Antenna and Array," *IEEE Access* **5**, 20470–20476 (2017).
114. R.-G. Fan, Y.-H. Qian, and Q.-X. Chu, "Frequency and pattern reconfigurable saline-water antenna array," *Microw. Opt. Technol. Lett.* **59**, 2284–2289 (2017).
115. S. K. Patel and Y. Kosta, "Liquid metamaterial based microstrip antenna," *Microw. Opt. Technol. Lett.* **60**, 318–322 (2018).
116. L. Xing, Y. Huang, Q. Xu, S. Alja' Afreh, and T. Liu, "A Broadband Hybrid Water Antenna for Hand-Portable Applications," *IEEE Antennas Wirel. Propag. Lett.* **15**, 174–177 (2016).
117. A. H. Naqvi and S. Lim, "A Beam-Steering Antenna with a Fluidically Programmable Metasurface," *IEEE Trans. Antennas Propag.* **67**, 3704–3711 (2019).
118. Y.-H. Qian and Q.-X. Chu, "A pattern-reconfigurable water-loaded MIMO antenna," *Microw. Opt. Technol. Lett.* **59**, 1608–1613 (2017).
119. R. Zhou, H. Zhang, and H. Xin, "Liquid-based dielectric resonator antenna and its application for measuring liquid real permittivities," *IET Microwave, Antennas Propag.* **8**, 255–262 (2014).

120. C. Song, E. L. Bennett, J. Xiao, A. Alieidin, K. M. Luk, and Y. Huang, "Metasurfaced, broadband, and circularly polarized liquid antennas using a simple structure," *IEEE Trans. Antennas Propag.* **67**, 4907–4913 (2019).
121. S. Wang, Z. Hu, W. Wang, S. Qi, and W. Wu, "Analysis and design of sea-water monopole Yagi-Uda antenna with pattern reconfigurability," *Int. J. RF Microw. Comput. Eng.* **28**, e21399 (2018).
122. C. Borda-Fortuny, L. Cai, K. F. Tong, and K. K. Wong, "Low-Cost 3D-Printed Coupling-Fed Frequency Agile Fluidic Monopole Antenna System," *IEEE Access* **7**, 95058–95064 (2019).
123. C. Hua, Z. Shen, and J. Lu, "High-efficiency sea-water monopole antenna for maritime wireless communications," *IEEE Trans. Antennas Propag.* **62**, 5968–5973 (2014).
124. C. Hua and Z. Shen, "Shunt-Excited Sea-Water Monopole Antenna of High Efficiency," *IEEE Trans. Antennas Propag.* **63**, 5185–5190 (2015).
125. L. Xing, Y. Huang, Y. Shen, S. Al Ja'afreh, Q. Xu, and R. Alrawashdeh, "Further investigation on water antennas," *IET Microwave, Antennas Propag.* **9**, 735–741 (2015).
126. L. Xing, X. Meng, L. Yang, B. Xu, and Y. Pan, "A wideband water antenna for WiFi applications," in *2018 IEEE International Workshop on Antenna Technology, IWAT2018 - Proceedings* (IEEE, 2018), pp. 1–3.
127. E. Motovilova and S. Y. Huang, "A review on reconfigurable liquid dielectric antennas," *Materials* (Basel). **13**, 1863 (2020).
128. C. H. Chen and D. Peroulis, "Liquid RF MEMS wideband reflective and absorptive switches," *IEEE Trans. Microw. Theory Tech.* **55**, 2919–2929 (2007).
129. D. Bahloul and A. B. Kouki, "LTCC-Based fluidic tuners for low microwave frequency reconfigurable circuits," *IEEE Trans. Microw. Theory Technol.* **68**, 3308–3317 (2020).
130. R. E. Jacobsen, A. Krasnok, S. Arslanagic, A. V. Lavrinenko, and A. Alú, "Boundary-Induced Embedded Eigenstates in a Single Resonator for Advanced Sensing," Submitted (2021).
131. R. E. Jacobsen, A. Krasnok, S. Arslanagic, A. V. Lavrinenko, and A. Alú, "Embedded eigenstate in a single resonator for sensing," in *Conference on Lasers and Electro-Optics 2021 (CLEO)* (2021), pp. 1–2.
132. C. F. Bohren and D. R. Huffman, *Absorption and Scattering of Light by Small Particles*, 1st ed. (John Wiley & Sons: Hoboken, 1983).
133. D. Tzarouchis and A. Sihvola, "Light Scattering by a Dielectric Sphere: Perspectives on the Mie Resonances," *Appl. Sci.* **8**, 184 (2018).
134. A. Petosa and A. Ittipiboon, "Dielectric resonator antennas: A historical review and the current state of the art," *IEEE Antennas Propag. Mag.* **52**, 91–116 (2010).
135. S. Jahani and Z. Jacob, "All-dielectric metamaterials," *Nat. Nanotechnol.* **11**, 23–36 (2016).
136. A. G. Webb, "Visualization and characterization of pure and coupled modes in water-based dielectric resonators on a human 7T scanner," *J. Magn. Reson.* **216**, 107–113 (2012).
137. A. Keshavarz and Z. Vafapour, "Water-Based Terahertz Metamaterial for Skin Cancer Detection Application," *IEEE Sens. J.* **19**, 1519–1524 (2019).
138. J. D. Jackson, *Classical Electrodynamics*, 3rd ed. (John Wiley & Sons, 1999).
139. "ROHACELL HF - High-performance structural foam cores," <https://www.rohacell.com/product/rohacell/en/products-services/rohacell-hf/>.
140. R. Alaee, R. Filter, D. Lehr, F. Lederer, and C. Rockstuhl, "A generalized Kerker condition for highly directive nanoantennas," *Opt. Lett.* **40**, 2645 (2015).
141. R. W. Ziolkowski, "Using Huygens multipole arrays to realize unidirectional needle-like radiation," *Phys. Rev. X* **7**, 031017 (2017).
142. S. B. Glybovski, S. A. Tretyakov, P. A. Belov, Y. S. Kivshar, and C. R. Simovski, "Metasurfaces: From microwaves to visible," *Phys. Rep.* **634**, 1–72 (2016).
143. M. Kadic, G. W. Milton, M. van Hecke, and M. Wegener, "3D metamaterials," *Nat. Rev. Phys.* **1**, 198–210 (2019).
144. K. Entesari and A. P. Saghati, "Fluidics in microwave components," *IEEE Microw. Mag.* **17**, 50–75 (2016).
145. Y. Huang, E. Sutter, L. M. Wu, H. Xu, L. Bao, H. J. Gao, X. J. Zhou, and P. Sutter, "Thick Layered Semiconductor Devices with Water Top-Gates: High On-Off Ratio Field-Effect Transistors and Aqueous Sensors," *ACS Appl. Mater. Interfaces* **10**, 23198–23207 (2018).
146. T. Kaelberer, V. A. Fedotov, N. Papasimakis, D. P. Tsai, and N. I. Zheludev, "Toroidal dipolar response in a metamaterial," *Science* **330**, 1510–1512 (2010).
147. C. W. Hsu, B. Zhen, A. D. Stone, J. D. Joannopoulos, and M. Soljacic, "Bound states in the continuum," *Nat. Rev. Mater.* **1**, 16048 (2016).
148. A. Krasnok, D. Baranov, H. Li, M.-A. Miri, F. Monticone, and A. Alú, "Anomalies in light scattering," *Adv. Opt. Photonics* **11**, 892 (2019).
149. T. Lepetit, E. Akmansoy, J. P. Ganne, and J. M. Lourtioz, "Resonance continuum coupling in high-permittivity

- dielectric metamaterials," *Phys. Rev. B - Condens. Matter Mater. Phys.* **82**, 195307 (2010).
150. T. Lepetit and B. Kanté, "Controlling multipolar radiation with symmetries for electromagnetic bound states in the continuum," *Phys. Rev. B - Condens. Matter Mater. Phys.* **90**, 241103 (2014).
151. Z. F. Sadrieva, M. A. Belyakov, M. A. Balezin, P. V. Kapitanova, E. A. Nenasheva, A. F. Sadreev, and A. A. Bogdanov, "Experimental observation of a symmetry-protected bound state in the continuum in a chain of dielectric disks," *Phys. Rev. A* **99**, 053804 (2019).

## APPENDIX B

# Paper 2: "Mie resonances in water spheres for microwave metamaterials and antennas"

---

In this manuscripts, Mie resonances in single water spheres are investigated. The manuscript is published.

The citations in the manuscript refer to reference list included at the end of the manuscript.

Work contributions by the present author: Numerical calculations and manuscript drafting.

Reference information:

**R. E. Jacobsen**, S. Arslanagić and A. V. Lavrinenko, "Mie resonances in water spheres for microwave metamaterials and antennas," *URSI Radio Science Letters*, vol. 1, Dec. 2019. doi:10.46620/19-0011

# Mie Resonances in Water Spheres for Microwave Metamaterials and Antennas

Rasmus E. Jacobsen, Samel Arslanagić, and Andrei V. Lavrinenko

**Abstract** – All-dielectric metamaterials rely on high-permittivity inclusions, which support Mie resonances. At microwave frequencies, distilled water exhibits a relatively high permittivity with tunable dynamic properties that are interesting for microwave devices, although absorption in water reduces their efficiency. In this paper, we investigate the scattering and absorption of single water spheres of various sizes and temperatures. The study is based on analytical calculations of Mie resonances. We also investigate the balanced electric/magnetic dipole excitation for more directive scattering in the forward direction. Finally, we discuss the major differences and similarities between water spheres and water cylinders. The results can be used as guidelines for metamaterial-based components as well as for dielectric resonator antenna designs.

## 1. Introduction

All-dielectric metamaterials (MMs) and metasurfaces (MSs) are preferred over the metallic versions because they possess lower intrinsic losses and potentially higher efficiency [1]. They are typically composed of high-index inclusions in a low-index host, where Mie resonances are excited in each individual inclusion. At optical frequencies, the variety of high-index materials is poor compared to microwave frequencies. We find water of particular interest because it holds the potential to be the fundamental element in cheap and bio-friendly microwave MS wave transformers (such as transmitarrays and reflectarrays), MS absorbers, and dielectric resonator antennas, to mention a few. Several water-based devices have already been demonstrated; see, e.g., [2–8]. The dynamic properties of water’s permittivity—along with its liquid state—offer multiple tuning parameters. However, the absorption in water constitutes a major obstacle toward its application for nonabsorber devices, and this is particularly the case for high frequencies. Thus, water inclusions belong in general to lossy high-permittivity particles in MSs. Nevertheless, losses are to some extent moderate up to about 2 GHz at 20°C, which is the frequency range of our interest.

The purpose of this work is to study the scattering and absorption efficiencies of a subwavelength resonant

water inclusion. Scattering and absorption of microwaves and light in rain (i.e., a collection of small water droplets) were studied many years ago [9, 10]. We render variations of both temperature and size to provide a more elaborate analysis and deeper insight compared to our previous efforts [11, 12]. Here we focus on the spherical shape because it resembles many of the water inclusions found in previously reported MSs. In addition, the canonical problem can be treated analytically using spherical vector wave formulation, eliminating the need for heavy numerical simulations, and thus enabling more extensive studies. Both electric and magnetic dipoles can be excited in the sphere, but we pay most of our attention to the latter because it is the dominant mode. MSs with dielectric inclusions satisfying the first Kerker condition are currently of great interest [7, 13–15]. We demonstrate that this condition can also be satisfied in a water sphere, and we investigate how it is affected by the water losses.

This letter is organized as follows: section II presents the configuration and quantities as well as the obtained results; a summary and conclusions are given in section III. Throughout the work, the time factor  $\exp(j\omega t)$ , with the angular frequency  $\omega$  and the time  $t$ , is assumed and suppressed.

## 2. Configuration and Results

We consider the canonical configuration sketched in Figure 1a: a linearly polarized plane wave incident on a sphere of distilled water with radius  $r_w$ , relative permittivity  $\epsilon_{r,w} = \epsilon'_{r,w} - j\epsilon''_{r,w}$ , relative permeability  $\mu_{r,w} = 1$ , and temperature  $T_w$ . The sphere is enclosed by free space with the permittivity and permeability  $\epsilon_0$  and  $\mu_0$ , respectively. A rectangular  $(x, y, z)$  coordinate system is introduced with the associated spherical  $(r, \theta, \phi)$  coordinate system. The incident electric field is  $x$ -polarized and given by  $\mathbf{E}^i = \hat{\mathbf{x}}E_0 \exp(-jk_0 z)$  with  $E_0 = 1$  V/m. The model of the relative water permittivity is taken from [16] and is shown in Figure 1b. The response of the sphere is described by the absorption, scattering, and extinction efficiencies, related by  $Q_{\text{abs}} = Q_{\text{ext}} - Q_{\text{sca}}$ , where [10, chap. 4]

$$Q_{\text{sca}} = \frac{2}{(k_0 r_w)^2} \sum_{n=1}^{\infty} (2n+1) (|a_n|^2 + |b_n|^2) \quad (1)$$

$$Q_{\text{ext}} = \frac{2}{(k_0 r_w)^2} \sum_{n=1}^{\infty} (2n+1) \text{Re}\{a_n + b_n\} \quad (2)$$

where  $k_0 = 2\pi/\lambda_0$  is the free-space wavenumber and  $\lambda_0$  the free-space wavelength. The solutions to the

Manuscript received 23 December 2019.

R. E. Jacobsen and A. V. Lavrinenko are with the Department of Photonics Engineering, Technical University of Denmark, Ørstedts Plads 345A, 2800 Kongens Lyngby, Denmark; e-mail: rajac@fotonik.dtu.dk and alav@fotonik.dtu.dk.

S. Arslanagić is with the Department of Electrical Engineering, Technical University of Denmark, Ørstedts Plads 348, 2800 Kongens Lyngby, Denmark; e-mail: sar@elektro.dtu.dk.

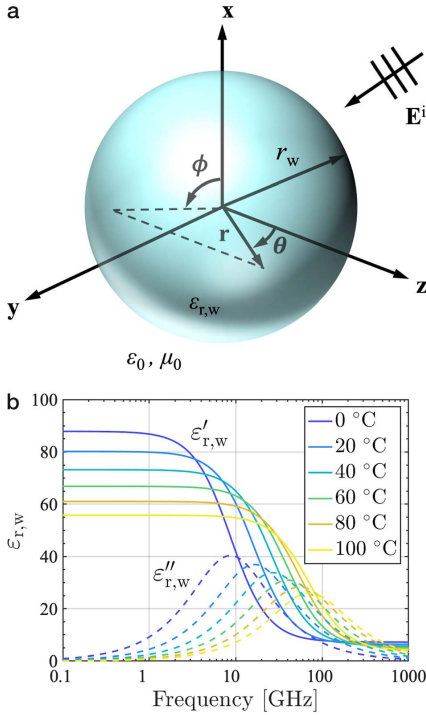


Figure 1. (a) Sketch of the water sphere illuminated by a plane wave and (b) the complex relative permittivity of water ( $\epsilon_{r,w} = \epsilon'_{r,w} - j\epsilon''_{r,w}$ ) as a function of frequency and temperature [13].

expansion coefficients of the TE' and TM' scattered field components,  $a_n$  and  $b_n$ , respectively, can be found in [10, 11]. Each  $n$  corresponds to a different mode excited in the sphere, with  $n = 1$  being the lowest-order dipole mode.

Both magnetic ( $a_1$ ) and electric ( $b_1$ ) dipoles, as well as quadrupoles ( $n = 2$ ), can be excited in the water sphere. However, the largest interaction with the field of the incident plane wave comes with the magnetic dipole as the round shape of the sphere stimulates circulating polarization currents [2, 11]. At resonance, the magnetic dipole gives rise to a peak in both scattering and absorption. The losses in water reduce the overall efficiency, especially at frequencies above 1 GHz, but this also depends on the temperature of water; cf. Figure 1b. The total magnetic and electric fields in the  $xz$ -plane of a sphere with  $r_w = 50$  mm at its magnetic dipole resonance frequency (331 MHz) is shown in Figure 2. The electric field is maximal near the periphery inside the water sphere, around which it circulates. This results

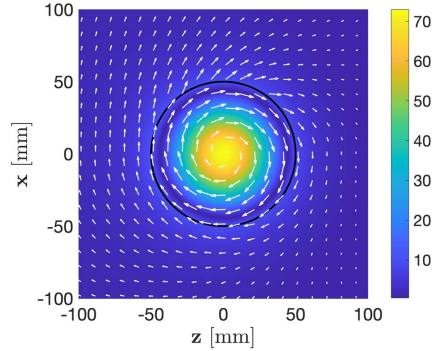


Figure 2. Total magnetic and electric fields in the  $xz$ -plane for a sphere with  $r_w = 50$  mm and  $T_w = 20$  C. The frequency is 331 MHz. Colors show the total magnetic field magnitude normalized with the incident magnetic field magnitude. The arrows display the magnitude and direction of the total electric field (linear scale).

in an enhanced magnetic field at the center of the sphere.

As the efficiency of a system composed of resonant water spheres—or any other resonant water structures—depends on both frequency and water temperature, we investigate the performance for single resonant spheres of various sizes and resonance frequencies. We use the single-scattering albedo  $Q_{\text{scat}}/Q_{\text{ext}}$  to show the amount of the extinct power that is scattered. The magnetic dipole resonance frequency  $f_r$  and the single-scattering albedo (as a percentile) as functions of the sphere radius and water temperature are shown in Figure 3. The calculation is performed for radii (temperatures) between 20 mm (0°C) and 200 mm (100°C). The resonance frequency increases with a decreasing radius and/or temperature due to the change in the water's permittivity. As a consequence of the higher frequency and/or lower temperature, the efficiency decreases. The 50% albedo level is shown by the red line in the figures, and we observe that the increase in the resonance frequency dramatically reduces the range of spheres with an albedo level above 50%. At room temperature (20°C), the spheres with resonance frequencies higher than 144 MHz exhibit albedo levels lower than 50%, and at 1 GHz, the albedo level is reduced to only 13%. The calculated albedo levels are comparable to the albedo levels for systems composed of resonant spherical water elements as well as other types of resonant electrically small water elements [2, 8].

Having considered fundamental properties of dipole resonances in water spheres, we next explore their possibility of providing enhanced scattering in the forward directions because transmitting MSs rely on such elements. This can be achieved with elements satisfying Kerker's first condition, which exhibit

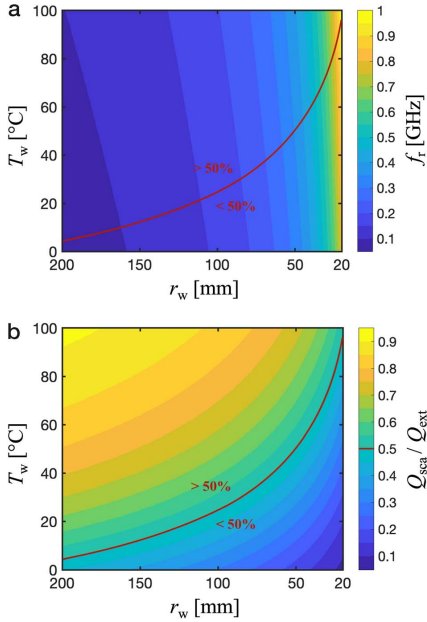


Figure 3. Colors show (a) the magnetic dipole resonance frequency ( $f_r$ ) and (b) the single-scattering albedo ( $Q_{\text{sca}}/Q_{\text{ext}}$ ) as functions of the sphere radius ( $r_w$ ) and water temperature ( $T_w$ ). The red lines display the 50% efficiency boundary.

suppressed (enhanced) backward (forward) scattering [15]. For a sphere this occurs when  $a_1 \approx b_1$  corresponding to  $m = \nu p$ , with  $m$  ( $p$ ) being the induced magnetic (electric) dipole moment and  $\nu$  the speed of the electromagnetic wave in the host medium. This assumes that the dipole modes are the dominant modes in the sphere, and at low frequencies they are dominant. We analyze this condition by evaluating the front-to-back ratio (FBR):

$$\text{FBR} = \frac{\sigma'_s(0, 0)}{\sigma'_s(\pi, 0)} = \frac{\left| \sum_{n=1}^{\infty} (2n+1)(a_n + b_n) \right|^2}{\left| \sum_{n=1}^{\infty} (2n+1)(-1)^n (a_n - b_n) \right|^2} \quad (3)$$

where  $\sigma'_s(\theta, \phi)$  is the differential scattering cross section [10, chap. 4]. From the denominator in Eq. (3), it is obvious that for  $a_1 = b_1$  FBR will increase dramatically if we assume that the other modes are weakly contributing to scattering. The maximized FBR, where Kerker's first condition is satisfied, was computed for various sphere sizes at 20°C. The result is shown in Figure 4 with the frequency included. As the radius increases, the FBR increases significantly because of the

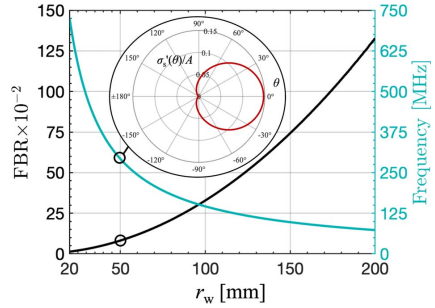


Figure 4. FBR and frequency as functions of the sphere radius ( $r_w$ ) at 20°C water temperature. The inset shows the normalized differential scattering cross section  $\sigma'_s(\theta)/A$  (with  $A = \pi r_w^2$ ) in the  $xz$ -plane for a sphere with  $r_w = 50$  mm.

decrease in frequency and, hence, the decrease of losses in water. This shows that the Kerker condition is highly affected by losses. The normalized differential scattering cross section  $\sigma'_s(\theta, 0)/A$ , with  $A = \pi r_w^2$  being the cross-sectional area of the sphere, is shown as an inset in Figure 4 for a sphere with  $r_w = 50$  mm. The scattering pattern resembles the characteristic cardioid that two balanced magnetic and electric dipoles exhibit. It should be noted that the total scattering is very low because the dipoles are weakly excited. To maximize the scattering, the dipole resonance frequencies must overlap, but the fulfillment of the condition  $a_1 = b_1$  remains. Other larger element shapes satisfying Kerker's first condition exhibit greater scattering, but their sizes are also significantly larger [7, 13–15]. Using elements composed of both metal and water, it can be shown that the FBR can be enhanced as well as the total scattering efficiency. These results will be reported elsewhere.

As a final remark we note that related cylindrical structures were also investigated [12]. Both TE and TM polarizations were studied, with the latter having a dominating monopole mode. The TE polarization response resembles that of the sphere, and, only for this polarization, Kerker's conditions can be satisfied. We calculated the dipole moments and found that the electric dipole moment is highly polarization sensitive, whereas the magnetic dipole moment is identical for both polarizations. The cylindrical structures may prove useful for, e.g., anisotropic MSs.

#### 4. Summary and Conclusions

Scattering of plane waves by resonant water spheres of various sizes and temperatures was investigated. The scattering and extinction efficiencies were calculated and compared, and we showed that water spheres at room temperature (20°C) and with resonance frequencies above 144 MHz have single-scattering albedo levels lower than 50%. The efficiencies of the

single spheres are similar to those for the systems of spheres reported previously. In addition, the differential scattering cross section was analyzed with a focus on maximizing (minimizing) the forward (backward) scattering, where the water losses also had a negative impact. Finally, we discussed the main difference between water spheres and cylinders. The results can be applied directly or as guidelines for designing metamaterial-based elements of circuitry as well as for constructing water-based dielectric resonator antennas.

### 5. References

1. S. Jahani and Z. Jacob, "All-Dielectric Metamaterials," *Nature Nanotechnology*, **11**, 1, January 2016, pp. 23–36.
2. A. Andryieuski, S. M. Kuznetsova, S. V. Zhukovsky, Y. S. Kivshar, and A. V. Lavrinenko, "Water: Promising Opportunities for Tunable All-Dielectric Electromagnetic Metamaterials," *Scientific Reports*, **5**, August 2015, p. 13535.
3. X. Cai, S. Zhao, M. Hu, J. Xiao, N. Zhang, et al., "Water-Based Fluidic Radio Frequency Metamaterials," *Journal of Applied Physics*, **122**, 18, November 2017, p. 184101.
4. R. E. Jacobsen, A. V. Lavrinenko, and S. Arslanagić, "Water-Based Metasurfaces for Effective Switching of Microwaves," *IEEE Antennas and Wireless Propagation Letters*, **17**, 4, February 2018, pp. 571–574.
5. X. Yang, D. Zhang, S. Wu, Y. Yin, L. Li, et al., "Reconfigurable All-Dielectric Metasurface Based on Tunable Chemical Systems in Aqueous Solution," *Scientific Reports*, **7**, June 2017, p. 3190.
6. Y. J. Yoo, S. Ju, S. Y. Park, Y. J. Kim, J. Bong, et al., "Metamaterial Absorber for Electromagnetic Waves in Periodic Water Droplets," *Scientific Reports*, **5**, September 2015, p. 14018.
7. P. J. Bradley, M. O. M. Torrico, C. Brennan, and Y. Hao, "Printable All-Dielectric Water-Based Absorber," *Scientific Reports*, **8**, September 2018, p. 14490.
8. R. E. Jacobsen, A. V. Lavrinenko, and S. Arslanagić, "Electrically Small Water-Based Hemispherical Dielectric Resonator Antenna," *Applied Sciences*, **9**, 22, November 2019, p. 4848.
9. A. L. Aden, "Microwave Reflection From Water Spheres," *American Journal of Physics*, **19**, 163, 1951, pp. 163–167.
10. C. F. Bohren and D. R. Huffman, *Absorption and Scattering of Light by Small Particles*, Weinheim, Germany, Wiley-VCH, 1983.
11. R. E. Jacobsen, S. Arslanagić, and A. V. Lavrinenko, "Fundamental Properties of Mie Resonances in Water Spheres," Presented at URSI EM Theory Symposium, EMTS 2019, San Diego, CA, May 27–31, 2019, pp. 1–4.
12. R. E. Jacobsen, S. Arslanagić, and A. V. Lavrinenko, "Fundamental Properties of Mie Resonances in Water Cylinders—TM and TE Case Studies," Presented at URSI EM Theory Symposium, EMTS 2019, San Diego, CA, May 27–31, 2019, pp. 1–4.
13. I. Staude, A. E. Miroshnichenko, M. Decker, N. T. Fofang, S. Liu, et al., "Tailoring Directional Scattering Through Magnetic and Electric Resonances in Subwavelength Silicon Nanodisks," *Optical Letters*, **7**, 9, August 2013, pp. 7824–7832.
14. M. Odit, P. Kapitanova, P. Belov, R. Alaei, C. Rockstuhl, et al., "Experimental Realisation of All-Dielectric Biotropic Metasurfaces," *Applied Physics Letters*, **108**, 22, May 2016, p. 221903.
15. D. Tzarouchis and A. Sihvola, "Light Scattering by a Dielectric Sphere: Perspectives on the Mie Resonances," *Applied Sciences*, **8**, 2, January 2018, p. 184.
16. W. Ellison, "Permittivity of Pure Water, at Standard Atmospheric Pressure, Over the Frequency Range 0–25 THz and the Temperature Range 0–100 °C," *Journal of Physics Chemistry Reference Data*, **36**, 1, March 2007, pp. 1–18.





## APPENDIX C

# Paper 3: “Tunable water-based metasurface for anomalous wave reflection”

---

A water-based metasurface MS reflectarray with reconfigurable reflection angle is demonstrated. The manuscript is published.




The citations in the manuscript refer to reference list included at the end of the manuscript.

Work contributions by the present author: Part of the numerical calculations and manuscript drafting.

Reference information:

**R. E. Jacobsen**, J. Ø. Nielsen, A. V. Lavrinenko and S. Arslanagić, “Tunable water-based metasurface for anomalous wave reflection,” *Journal of Physics D: Applied Physics*, vol. 53, pp. 505104, Oct. 2020. doi:10.1088/1361-6463/abb2bb

# Tunable water-based metasurface for anomalous wave reflection

Rasmus E Jacobsen<sup>1</sup> , Jonas Ø Nielsen<sup>2</sup>, Andrei V Lavrinenko<sup>1</sup>   
and Samei Arslanagic<sup>2</sup> 

<sup>1</sup> Department of Photonics Engineering, Technical University of Denmark, Kgs. Lyngby 2800, Denmark

<sup>2</sup> Department of Electrical Engineering, Technical University of Denmark, Kgs. Lyngby 2800 Denmark

E-mail: [rajac@fotonik.dtu.dk](mailto:rajac@fotonik.dtu.dk)

Received 1 July 2020, revised 14 August 2020

Accepted for publication 26 August 2020

Published 1 October 2020



CrossMark

## Abstract

Metasurfaces (MSs) are artificial structures which enable the full control of electromagnetic waves and they continue to be of great scientific importance. In particular, they can tailor their reflection and transmission properties by using electrically small metallic/dielectric scatterers with imprinted spatial phase variation. In the present work, we design and characterize a water-based MS with a tunable reflection at 1 GHz. The MS comprises a collection of water cylinders and we demonstrate its ability to reflect a normally incident wave at an angle of 51.3° and with a total reflection efficiency of 33%. A prototype was fabricated and is shown to exhibit an excellent agreement with the simulation results. The proposed water-based MS may serve as a cheap and bio-friendly tunable alternative for a variety of microwave communication systems.

Keywords: water, liquid, metasurface, reflectarray, bio-friendly, reconfigurable

(Some figures may appear in color only in the online journal)

## 1. Introduction

Various devices have been demonstrated since the introduction of metasurfaces (MSs) [1–3]. Especially all-dielectric versions of the latter have paved the way for efficient wave tailoring of visible and infrared light. However, a limiting factor at such high frequencies is the availability of high-permittivity materials required to realize these structures. This is not a problem at radio and microwave frequencies, where many high-permittivity ceramics are commercially available [4]. Recently, another high-permittivity candidate was proposed, namely water, as an abundant, cheap and environmentally friendly alternative for microwave metamaterials and MSs as well as dielectric resonator antennas (DRAs), absorbers and heating systems, to mention a few [5–16]. With its frequency- and temperature-dependent high permittivity as well as its liquid form, water introduces numerous tuning parameters enabling easy tuning of the devices. The losses in water can, however, be an issue at some frequencies consequently reducing its potential in a variety of potential applications. Yet in a time with increasing demand for environmentally

friendly products, water holds the potential to be a fundamental element in ecological compatible microwave MSs and even bulk metamaterials.

Two special types of wave transformers used in antenna applications are the reflectarray and transmitarray, which are non-uniform surface structures enabling the control of the reflected and transmitted waves, respectively. Their working principle relies on discrete spatial phase jumps across their surfaces effectively altering the angle of the reflected/transmitted wave. Many designs, both metallic and dielectric, have been demonstrated recently [1, 2, 17–20], even though the first devices are dated long before [21, 22], and have their historical roots in the antenna theory.

In this work, we design and characterize a MS reflectarray with subwavelength displaced array elements composed of simple cylindrical cavities filled with distilled water. Through proper disposition of the water content in each cavity, the reflected wave direction can be tailored. Presently, a MS with a period (termed a supercell) of eight unit cells (each consisting of a water cavity in a low-permittivity host) is investigated for the possibility of reflecting a normally incident wave

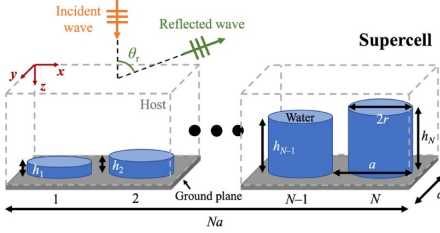


Figure 1. Sketch of one supercell of the MS.

away from the normal and in a direction governed by the generalized Snell's law of reflection. The required phase shift across the MS is obtained as a result of a horizontal magnetic dipole resonance induced in the water cylinders. The operating frequency is 1 GHz, and the unit-cell size and the thickness are, respectively, 6 and 20 times smaller than the free-space wavelength. The MS was characterized numerically in COMSOL Multiphysics, and a prototype was built for experimental demonstration. The plane wave spectrum of the MS is calculated to evaluate the efficiency, bandwidth and polarization sensitivity. The proposed MS may serve as a simple and versatile as well as extremely cheap and environmentally friendly component (e.g. a reflectarray) for microwave communication systems.

The paper is organized as follows. Section II presents the configuration of the proposed MS. It also includes a discussion on its design as well as on the obtained numerical and experimental results. Section III includes a summary and conclusions of this work. Throughout the work, the time-factor  $\exp(j\omega t)$ , where  $\omega$  is the angular frequency, and  $t$  is the time, is assumed and suppressed.

## 2. Configuration and results

One period of the MS is sketched in figure 1. It consists of  $N$  cylindrical distilled water elements in a rectangular cuboid Rohacell 51 RF host medium with a conducting ground plane on the backside to cancel the transmission. A rectangular coordinate system  $(x, y, z)$  is introduced as shown in figure 1. The water cylinders have equal radii ( $r = 20$  mm) and different heights ( $h_n$  with  $n = 1, 2, \dots, N$ ), and are spaced by a distance  $a$  along the  $x$ -axis. The supercell is periodic in the  $xy$ -plane with the lattice constants  $Na$  and  $a$ . The MS is designed to reflect a linearly  $x$ -polarized plane wave at normal incidence. The angle of the reflected plane wave is denoted  $\theta_r$ . All results are for 20 °C water temperature.

The simulations were performed in COMSOL Multiphysics [23] with a simple model consisting of a rectangular periodic one-port system with the supercell incorporated; the ground plane was emulated as a perfect electric conductor (PEC) effectively cancelling the transmission. A perfect

matched layers is inserted on the backside of the port and the incident electric field magnitude is set to  $E_0 = 1 \text{ V m}^{-1}$ . We used a model for the permittivity of water [24], and at 1 GHz the relative permittivity is  $79.9 - j4.5$ . For the Rohacell 51 HF material, we used the relative permittivity of 1.075 as reported in our previous work [10].

### 2.1. The metasurface design

The generalized Snell's law of reflection states that

$$\sin \theta_r - \sin \theta_i = \Delta\phi/k_0 a, \quad (1)$$

where  $\theta_i$  and  $\theta_r$  are the angles of the incident and reflected waves, respectively,  $\Delta\phi = 360^\circ/N$  is the phase jump between the cylinders in the supercell,  $k_0 = 2\pi/\lambda_0$  is the free-space wavenumber and  $\lambda_0$  is the free-space wavelength. The law shows that by introducing a phase shift of  $360^\circ$  across the supercell, the angle of reflection can be tailored at will. As a consequence of the periodicity of the supercell, several orders of diffractions/reflections can exist as long as their reflection angles  $\theta_{r,m} < 90^\circ$  with integer  $m$  being the order. This is the same principle behind diffraction gratings [25]. Presently, we focus on the first order reflection ( $m = 1$ ). We introduce discrete phase jumps by varying the height of the water cylinders across the supercell. First, the cylinders providing the required phase shift to the reflected wave were determined by considering the unit cell of a square lattice ( $N = 1$ ) of identical cylinders with lattice constant  $a = 48 \text{ mm}$  ( $\approx \lambda_0/6$ ). A plane wave at normal incidence is investigated, and due to the symmetry and periodicity of the MS, only normally reflected plane waves are generated. The height of the cylinders was then swept, and the resulting squared magnitude and phase of the reflection coefficient ( $S_{11}$ ) are shown in figure 2(a) for heights ranging from 6 to 20 mm. Approximately  $330^\circ$  phase shift is achieved albeit with a reduced reflection magnitude. This is coming from a magnetic dipole induced in the water cylinders, which is on resonance for  $h = 10.7 \text{ mm}$ , where the minimum in the reflection coefficient, i.e. maximum absorption, is. The total magnetic field magnitude (colors) and the normalized electric field (arrows) in the  $xz$ -plane of a resonant water cylinder with  $h = 10.7 \text{ mm}$  are shown in figure 2(b) exhibiting the characteristics of a magnetic dipole resonance: the electric field is mirrored by the PEC ground plane and circulates near the periphery inside the water cylinder generating an enhanced magnetic field.

We also studied variation of the radius (result is not included), and the result is similar to that in figure 2(a). However, we found the MS with cylinders of varying heights and fixed radius to be much easier to fabricate.

With the frequency and  $a$  being fixed, the supercell is constrained to  $N > 6$  cylinders for  $\theta_r < 90^\circ$ . Presently, a MS with a super cell of  $N = 8$  cylinders is investigated, which has the expected first order reflection angle of  $\theta_r = 51.3^\circ$ . Higher order reflections do not exist as their reflection angles would be larger than  $90^\circ$ . Cylinders with phase jumps of  $\Delta\phi = 45^\circ$  were selected for the MS and the height for each cylinder is listed in table 1.

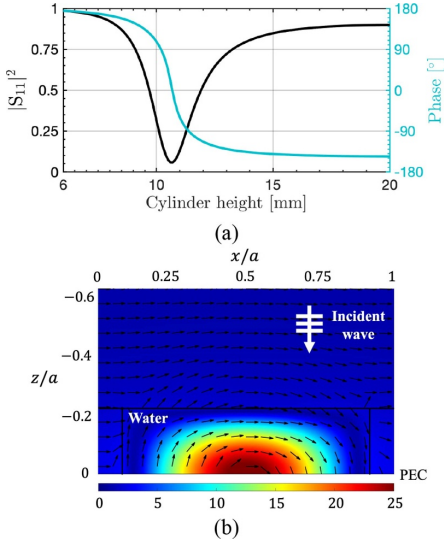


**Figure 2.** Numerical investigation of the square lattice of identical cylinders ( $N = 1$ ). (a) The squared magnitude and relative phase of the reflection coefficient ( $S_{11}$ ) as functions of the cylinder height. (b) The total magnetic field magnitude (colors) in the  $xz$ -plane of the resonant cylinder with  $r = 20$  mm and  $h = 10.7$  mm. The arrows in (c) show the direction of the electric field.

**Table 1.** Heights of the water cylinders for the MS.

Cylinder no.	1	2	3	4	5	6	7	8
Height [mm]	6.0	9.6	10.2	10.5	10.7	10.9	11.5	14.7

## 2.2. Performance of metasurface

The performance of the infinite MS is evaluated by its plane wave spectrum. A simple numerical procedure was developed for the purpose of computing the discrete Fourier transform of the complex reflected field,  $\mathbf{E}^r(x)$ , along a line parallel to the  $x$ -axis. The line was truncated at  $100Na$  to obtain a sufficient resolution. The transformed field represents the  $k_x$ -component of each plane wave travelling in different directions  $k_x = k_0 \sin \theta_r$ . Due to the infinite extent of the MS in the  $(x, y)$ -direction, the reflected power flowing away from the array must be  $-z$ -directed, i.e. only the  $z$ -component of the reflected time-average power flow density,  $S_z^r(\theta) = S_R^r(\theta_r) \cos \theta_r$ , contributes to the far-field [17]. The reflection efficiency is then calculated as

$$\eta_{\text{eff}} = S_z^r(\theta_r) / S_0, \quad (2)$$

where  $S_0 = |E_0|^2 / 2\eta_0$  is the time-average power flow density of the incident wave with  $\eta_0$  being the intrinsic impedance of

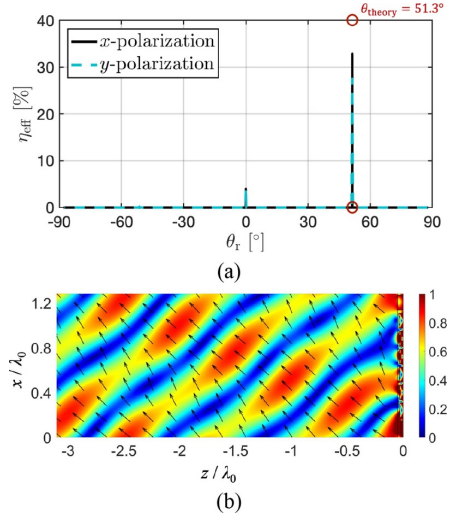


**Figure 3.** Results for the MS at 1 GHz. (a) Reflection efficiency as a function of the reflection angle for  $x$ - and  $y$ -polarized plane wave incidences. The red circles show the theoretical reflection angle  $\theta_{\text{theory}} = 51.3^\circ$ . (b) Magnitude of the instantaneous reflected field (colors) in the  $xz$ -plane of one supercell. The arrows show the direction of the normalized time-average reflected Poynting vector.

free space. Similarly, the reflected time-average power flow density is calculated as  $S_R^r(\theta_r) = |\mathbf{E}^r(\theta_r)|^2 / 2\eta_0$  with  $\mathbf{E}^r(\theta_r)$  being the Fourier transform of  $\mathbf{E}^r(x)$ .

The  $\eta_{\text{eff}}$  efficiency as a function of  $\theta_r$  is shown in figure 3(a) for both  $x$ - and  $y$ -polarized plane wave incidences. The theoretical  $\theta_r = 51.3^\circ$  is shown by the red circles and the MS has a dominating reflection of  $\eta_{\text{eff}} = 33\%$  ( $\eta_{\text{eff}} = 27.5\%$ ) at that exact angle for the  $x$ -polarized ( $y$ -polarized) incidence. All other reflections are much smaller; there is a reflection at  $\theta_r = 0^\circ$  ( $\theta_r = -51.3^\circ$ ) with  $\eta_{\text{eff}} = 4\%$  ( $\eta_{\text{eff}} = 0.1\%$ ) for the  $x$ -polarized incidence. Summing all reflected plane waves gives the total reflected power of 37%. The remaining power must be absorbed by water, and this is confirmed by integrating the power loss density over the volume of the supercell, where the absorption is found to be 63%. Another performance metric used for reflective surfaces is the relative reflection efficiency, which is the reflected power in the desired direction divided with the total reflected power. For the present MS, this is 89% for the  $x$ -polarized incidence.

Although the MS is anisotropic, there is only small difference between the  $x$ - and  $y$ -polarized incidences. This is due to the isotropic water elements, which makes the MS only slightly polarization sensitive. The cross-polarization of the MS was also investigated and was near non-existing due to

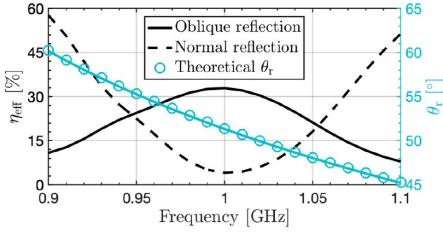


**Figure 4.** Reflection efficiency and angle as functions of frequency. The solid line shows the results for the oblique reflection peak, whereas the dashed line shows the result for the normal reflection ( $\theta_r = 0^\circ$ ). The circles show the theoretical  $\theta_r$ , calculated with equation (1).

the structure symmetry and the subwavelength spacing of the cylinders.

The instantaneous reflected electric field in the  $(x, z)$ -plane is shown in figure 3(b), with the arrows showing the direction of the normalized time-average reflected Poynting vector, plainly displaying a pronounced reflected plane wave travelling at an oblique angle away from the MS. The reflected wave is not uniform, which indicates that some cylinders absorb more power than others as was the case with the squared array in figure 2(a).

The bandwidth of the oblique reflection peak ( $\theta_r > 0^\circ$ ) is investigated in figure 4 with  $\eta_{\text{eff}}$  and  $\theta_r$  as functions of frequency. The theoretical  $\theta_r$ , calculated with equation (1), as well as  $\eta_{\text{eff}}$  for the normal reflection ( $\theta_r = 0^\circ$ ), is also included in the figure. From equation (1), it is obvious that  $\theta_r$  will change with frequency as can be seen in figure 4, and the simulated  $\theta_r$  exhibits excellent agreement with the theory. For frequencies away from 1 GHz, the normal reflection increases dramatically, and the oblique reflection is reduced. The half-power bandwidth of the MS is 14% (140 MHz) with a  $7^\circ$  variation of  $\theta_r$ .

A prototype of the MS was fabricated at the local workshop. The prototype consisted of four supercells each with eight cylinders milled in blocks of Rohacell 51 HF that were put together. An aluminum tape was attached on the backside of the blocks to realize the ground plane as well as for sealing of the water inside the cylinders. For each cylinder height listed in table 1, we calculated the volume ( $V_i = \pi r^2 h_i$ ) and then distributed distilled water by using a syringe. A photograph of the fabricated MS is shown in figure 5(a), and a sketch of the measurement setup established at the measurement facility is shown in figure 5(b). The setup consisted of two ETS-Lindgren 3164-03 horn antennas mounted on a metal beam hoisted 2.64 meter above the floor with two tripods. The antennas constituted a two-port system with one antenna ( $P_1$ ) pointing directly at the ground whereas the position and angle of the other antenna ( $P_2$ ) were adjusted for various angular receptions. The MS was put on the ground below  $P_1$ , and the measured  $S_{11}$  and  $S_{21}$  as functions of the angle is shown in figure 5(c). The power measured with the MS was normalized

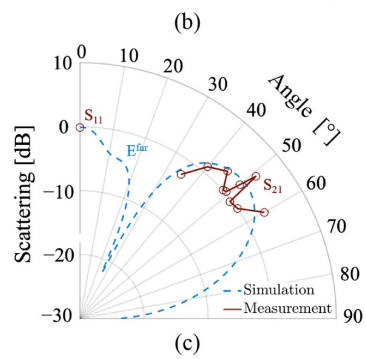
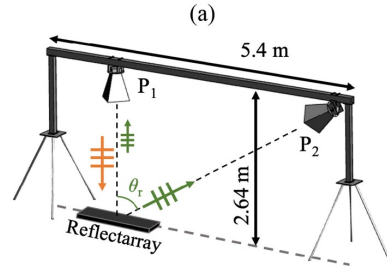
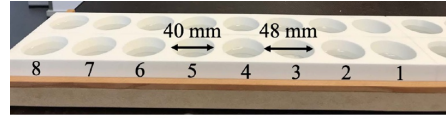


**Figure 5.** (a) Photograph of the fabricated MS, (b) sketch of the experimental setup and (c) measured normalized scattering shown in the logarithmic scale together with the normalized far-field simulation of the truncated MS.

with the power measured without it, and for comparison the normalized electric far-field result from the simulation of the truncated MS is included in figure 5(c). It should be noted that in the simulation model, the size of the ground plane is much smaller than in the experimental setup. Furthermore, the experiment was not conducted in radio anechoic conditions. Still we observe fine agreement between the measurement and simulation. At an angle of  $52^\circ$ , an approximately 6 dB enhancement was measured in the experiment confirming the numerical results. Due to the small size of the MS, there is only a small reduction in the measured normal reflection of  $-0.13$  dB.

The MS can easily be reconfigured for other  $\theta_r$  with just a simple re-distribution of water in the cylindrical cavities. Altering the size of the supercell to  $N = 7$ , while maintaining the  $360^\circ$  phase distribution across the supercell, predicts a  $\theta_r = 63^\circ$ . Similarly,  $N = 9$  and  $N = 10$  predict the first

(second) order  $\theta_r = 44^\circ$  ( $88^\circ$ ) and  $\theta_r = 39^\circ$  ( $78^\circ$ ), respectively. As  $N$  increases, the  $\theta_r$  approaches  $0^\circ$ . Similarly, completely removing the water from the cavities will cancel the oblique reflection leaving only the normal reflection. In addition, the MS should potentially be reconfigurable for other types of wave transformations such as focusing [1–3], however this is not investigated in this work. We envision a piston system by which the height of the water cylinders can be controlled. Such a MS could be used as a tunable component in a base station or cheap amateur communication system for wave front control as well as higher directivity.

The present MS is designed for a  $20^\circ\text{C}$  water temperature, however, it will still function at 1 GHz for temperatures few degrees below and above without the need for changing the water content in the cavities. As the temperature increases, the permittivity of water decreases consequently changing the response of the MS. With temperature changes, the operating frequency and reflection angle will change, e.g. for higher temperatures, the operating frequency is blue-shifted and the reflection angle is reduced. Alternatively, adding more water causes a red-shift, and in this way, the MS can be easily tuned for different water temperatures and/or frequencies. Additionally,  $\eta_{\text{eff}}$  changes as well, due to the lower (higher) losses in water for higher (lower) temperatures. This was studied numerically: by increasing the water temperature in the MS to  $50^\circ\text{C}$ , while adjusting the water content to maintain the phase distribution as well as the operating frequency at 1 GHz; it resulted in a considerable increase in  $\eta_{\text{eff}}$  to 61%. Similar observations were made for a water-based DRA [14].

### 3. Summary and conclusions

A MS consisting of simple cylindrical water-filled cavities in a Rohacell 51 HF host was designed for 1 GHz operation. Inside the water cylinders, magnetic dipoles are induced by the incident wave, bringing a complete change to the reflection. The MS converts 33% of the power of a normally incident plane wave into a reflected plane wave in the desired direction with  $51.3^\circ$ . This is achieved by distributing water across rows of cylinders such that a linear  $360^\circ$  phase evolution is introduced to the reflected wave for each set of eight cylinders. The normally reflected power is minimized to 4%, and 89% of reflected power is channeled into the desired direction. The polarization sensitivity of the MS is very low with only 5.5% difference in the reflected power between the  $x$ - and  $y$ -polarizations. The half-power bandwidth is estimated to be 14% (140 MHz) with a  $7^\circ$  variation of the reflection angle. A prototype of the MS was fabricated and characterized experimentally demonstrating the enhanced reflection in the desired direction.

The reduced efficiency of the MS is due to the strong resonance and losses in water. A simple way to improve the efficiency is to go to lower frequencies where the losses in water are significantly reduced. Similarly, increasing the water temperature will also reduce the losses in water, however, this would require the addition of a heating system. Alternatively, some of the water can be substituted with a different material like e.g. metal or low-loss dielectric.

The proposed MS cannot compete with existing microwave technology in terms of efficiency. Yet it is simple and versatile as well as extremely cheap and bio-friendly and may therefore serve as an alternative component for microwave communication systems. In addition, the Rohacell material used for the prototype is not essential for the functionality and can be replaced with a cheaper and more bio-friendly alternative. This mindset can be expanded to the complete design, such that all materials are ecological compatible that can be recycled or directly decomposed in nature.

By this work, we bring to public an extremely simple realization of water-based MSs, which can provide the same nomenclature of properties as ‘solid’ MSs. Meanwhile, tunable properties are simply granted in our approach by easy reshaping, changing the volume or heating/cooling of water. Real-time tuning (modulation) can be done by applying ultrasound or acoustic waves with specific water containers. This subject is not so trivial for speculations, so extensive analysis is needed to prepare more or less sounding conclusion on possibilities of real-time tuning at the level sufficient for microwave applications. It will be the topic of following studies.

### Acknowledgments

The authors would like to thank the workshop at the Electromagnetic Systems group of the Technical University of Denmark for fabrication of the MS.

### ORCID iDs

Rasmus E Jacobsen  <https://orcid.org/0000-0001-6804-5393>

Andrei V Lavrinenko  <https://orcid.org/0000-0001-8853-2033>

Samel Arslanagic  <https://orcid.org/0000-0001-8150-7732>

### References

- [1] Yu N and Capasso F 2014 Flat optics with designer metasurfaces *Nat. Mat.* **13** 139–50
- [2] Jahani S and Jacob Z 2016 All-dielectric metamaterials *Nat. Nanotechnol.* **11** 23–36
- [3] Chen H T, Taylor A J and Yu N 2016 A review of metasurfaces: physics and applications *Rep. Prog. Phys.* **79** 076401
- [4] MARUWA, 2019 *Ceramics Products*. Accessed on: December 6 2019 (Available: [www.maruwa-g.com/e/products/ceramic/](http://www.maruwa-g.com/e/products/ceramic/))
- [5] Gorlach M A, Song M, Slobozhanyuk A P, Bogdanov A A and Belov P 2016 Topological transition in coated wire medium *Phys. Status Solidi RRL* **10** 900–4
- [6] Andryieuski A, Kuznetsova S M, Zhukovsky S V, Kivshar Y S and Lavrinenko A V 2015 Water: promising opportunities for tunable all-dielectric electromagnetic metamaterials *Sci. Rep.* **5** 13535
- [7] Odit M, Kapitanova P, Andryieuski A, Belov P and Lavrinenko A V 2016 Experimental demonstration of water based tunable metasurface *Appl. Phys. Lett.* **109** 011901

- [8] Cai X, Zhao S, Hu M, Xiao J, Zhang N and Yang J 2017 Water based fluidic radio frequency metamaterials *J. Appl. Phys.* **122** 184101
- [9] Yang X, Zhang D, Wu S, Yin Y, Li L, Cao K and Huang K 2017 Reconfigurable all-dielectric metasurface based on tunable chemical systems in aqueous solution *Sci. Rep.* **7** 3190
- [10] Jacobsen R E, Lavrinenko A V and Arslanagic S 2018 Water-based metasurfaces for effective switching of microwaves *IEEE Antennas Wirel. Propag. Lett.* **17** 571–4
- [11] Yoo Y J, Ju S, Park S Y, Ju Kim Y, Bong J, Lim T, Kim K W, Rhee J Y and Lee Y 2015 Metamaterial absorber for electromagnetic waves in periodic water droplets *Sci. Rep.* **5** 14018
- [12] Pang Y, Wang J, Cheng Q, Xia S, Zhou X Y, Xu Z, Cui T J and Qu S 2017 Thermally tunable water-substrate broadband metamaterial absorbers *Appl. Phys. Lett.* **110** 104103
- [13] Pang Y, Shen Y, Li Y, Wang J, Xu Z and Qu S 2018 Water-based metamaterial absorbers for optical transparency and broadband microwave absorption *J. Appl. Phys.* **123** 155106
- [14] Jacobsen R E, Lavrinenko A V and Arslanagic S 2019 Electrically small water-based hemispherical dielectric resonator antenna *Appl. Sci.* **9** 4848
- [15] Motovilova E and Huang S Y 2020 A review on reconfigurable liquid dielectric antennas *Materials* **13** 1863
- [16] Jacobsen R E, Arslanagic S and Lavrinenko A V 2019 Continuous heating microwave system based on Mie resonances *AMPERE 2019 Book of Abstracts*, 160
- [17] Asadchy V S, Albooyeh M, Tsvetkova S N, Díaz-Rubio A, Ra'di Y and Tretyakov S A 2016 Perfect control of reflection and refraction using spatially dispersive metasurfaces *Phys. Rev. B* **94** 075142
- [18] Díaz-Rubio A, Asadchy V S, Elsakka A and Tretyakov S A 2017 From the generalized reflection law to the realization of perfect anomalous reflectors *Sci. Adv.* **3** e1602714
- [19] Mao R, Wang G, Cai T, Hou H, Wang D, Wu B, Zhang W and Zhang Q 2020 Tunable metasurface with controllable polarizations and reflection/transmission properties *J. Phys. D: Appl. Phys.* **53** 155102
- [20] Zhang L et al 2018 Transmission-reflection-integrated multifunctional coding metasurface for full-space controls of electromagnetic waves *Adv. Funct. Mater.* **28** 1802205
- [21] Berry D G, Malech R G and Kennedy W A 1963 The reflectarray antenna *IEEE Trans. Antennas Propag.* **11** 645–51
- [22] Pozar D M, Targonski S D and Syrigos H D 1997 Design of millimeter wave microstrip reflectarray *IEEE Trans. Antennas Propag.* **45** 287–96
- [23] COMSOL 2017 COMSOL MULTIPHYSICS COMSOL ([www.comsol.com](http://www.comsol.com))
- [24] Ellison W 2007 Permittivity of pure water, at standard atmospheric pressure, over the frequency range 0–25 thz and the temperature range 0–100 c. *J. Phys. Chem. Ref. Data* **36** 1–18
- [25] Larouche S and Smith D R 2012 Reconciliation of generalized refraction with diffraction theory *Opt. Lett.* **37** 2391–3





## APPENDIX D

# Paper 4: “Electrically small water-based hemispherical dielectric resonator antenna”

---

The smallest water-based antenna to date was demonstrated. The manuscript is published.

The citations in the manuscript refer to reference list included at the end of the manuscript.



Work contributions by the present author: Numerical calculations, experiments and manuscript drafting.

Reference information:

**R. E. Jacobsen**, A. V. Lavrinenko and S. Arslanagić, “Electrically small water-based hemispherical dielectric resonator antenna,” *Applied Sciences*, vol. 9, 4848, Nov. 2019. doi:10.3390/app9224848

Article

# Electrically Small Water-Based Hemispherical Dielectric Resonator Antenna

Rasmus E. Jacobsen <sup>1,\*</sup>, Andrei V. Lavrinenko <sup>1</sup> and Samel Arslanagić <sup>2</sup>

<sup>1</sup> Department of Photonics Engineering, Technical University of Denmark, 2800 Kgs. Lyngby, Denmark; alav@fotonik.dtu.dk

<sup>2</sup> Department of Electrical Engineering, Technical University of Denmark, 2800 Kgs. Lyngby, Denmark; sar@elektro.dtu.dk

\* Correspondence: rajac@fotonik.dtu.dk

Received: 10 October 2019; Accepted: 5 November 2019; Published: 13 November 2019



**Abstract:** Recently, water has been proposed as an interesting candidate for use in applications such as tunable microwave metamaterials and dielectric resonator antennas due to its high and temperature-dependent permittivity. In the present work, we considered an electrically small water-based dielectric resonator antenna made of a short monopole encapsulated by a hemispherical water cavity. The fundamental dipole resonances supported by the water cavity were used to match the short monopole to its feed line as well as the surrounding free space. Specifically, a magnetic (electric) dipole resonance was exploited for antenna designs with a total efficiency of 29.5% (15.6%) and a reflection coefficient of  $-24.1$  dB ( $-10.9$  dB) at 300 MHz. The dipole resonances were effectively excited with different monopole lengths and positions as well as different cavity sizes or different frequencies in the same cavity. The overall size of the optimum design was 18 times smaller than the free-space wavelength, representing the smallest water-based antenna to date. A prototype antenna was characterized, with an excellent agreement achieved between the numerical and experimental results. The proposed water-based antennas may serve as cheap and easy-to-fabricate tunable alternatives for use in very high frequency (VHF) and the low end of ultrahigh frequency (UHF) bands for a great variety of applications.

**Keywords:** dielectric resonator antenna; electrically small antenna; Mie resonances; tunable antennas; water-based

## 1. Introduction

Modern technology calls for increasingly smaller designs, which in turn ultimately requires increasingly smaller antennas. Even though electrically small antennas have been studied for decades [1–9], their inherently poor matching, low radiation efficiency, and narrow bandwidth pose a serious design obstacle. The matching issue is traditionally tackled with appropriate matching networks; however, such solutions suffer from narrow bandwidths, high tolerance requirements, and modest efficiencies [2]. While some recent approaches toward efficient small antennas have involved either specific shaping of the radiator or addition of conductors around it [3–6], as well as exploiting artificial metamaterials (MMs) and MM-inspired structures [7–9], a more traditional approach to reduce the antenna size has been to load it with a high-permittivity material. Such antennas, known as dielectric resonator antennas (DRAs), rely on resonances supported in high-permittivity structures. A great variety of DRAs has been proposed and demonstrated [10], and, very often, expensive high-permittivity ceramics are used as the dielectric material. To this end, it is interesting to pay attention to water as an alternative material [11]. With its relatively high frequency and temperature-dependent permittivity in the microwave frequency range [12], water holds a great potential as an inexpensive, abundant, and

biofriendly material for not only tunable antennas [11,13–22] but also more broadly as inclusions in MMs and metasurfaces (MSs) [22–27] with tunable dynamic properties. These tunable properties can potentially be used for sensing as well.

Indeed, several water-based DRAs have already been demonstrated [11,13–18], with effective excitation of resonances in water cavities. Cylindrical [13], rectangular [14], and bottle-shaped [18] cavities have been investigated. These antennas mainly operate in the very high frequency (VHF) and the low end of ultrahigh frequency (UHF) bands due to water losses at higher frequencies. Another type of water-based antenna that exploits conductive liquids (e.g., salt water) [19–22] has also been reported. The operational frequency of these antennas can be tuned through a simple change of the conductive liquid volume. The electrical size of an antenna is defined as  $k_0 a$ , with  $a$  being the radius of the so-called Wheeler's radian sphere (the smallest possible sphere enclosing the antenna),  $k_0 = 2\pi/\lambda_0$  being the free-space wavenumber, and  $\lambda_0$  being the free-space wavelength. In the presence of a ground plane,  $k_0 a \leq 0.5$  in order for the antenna to be qualified as electrically small [5]. Following this definition, we find that most of the water-based antennas demonstrated thus far are not electrically small.

The purpose of the present work was to investigate an electrically small water-based DRA consisting of a short monopole antenna encapsulated by a hemispherical water cavity and fed against a large ground conducting plane. The working principle of the proposed DRA relies on the fundamental electric and magnetic dipole resonances (equivalent to the transverse magnetic (TM) and transverse electric (TE) modes, respectively), which can be excited in the high-permittivity water cavity. The spherical shape of the cavity maximizes the antenna volume, making it possible to obtain much smaller water-based antennas compared to any of those reported thus far. Specifically, the size of the smallest antenna proposed presently is  $\lambda_0/18$ , representing the smallest water-based antenna to date. On the other hand, the dipole resonances in the water cavity are used to effectively match an otherwise inefficient short monopole antenna to its feed line as well as the surrounding free space. The length and the position (with respect to the water cavity) of the short monopole were determined for the optimal performance of the DRAs. A prototype antenna operating at 300 MHz was characterized, and measurements exhibited an excellent agreement with the numerical predictions.

The rest of the paper is organized as follows. Section 2 introduces the configuration of the water-based DRA as well as the numerical model. Section 3 presents the numerical and experimental results. Section 4 includes a summary and the conclusions of this work. Appendices A and B contain the antenna parameter definitions and additional results, respectively. Throughout the work, the time factor  $\exp(j\omega t)$ , where  $\omega$  is the angular frequency and  $t$  is the time, was assumed and suppressed.

## 2. Configuration

The water-based DRA is shown in Figure 1. The hemispherical cavity has radius  $r_w$ , and the feed line is a coaxial transmission line with an inner and outer radii of  $r_i = 0.92$  mm and  $r_o = 2.99$  mm, respectively, and a dielectric material with the relative permittivity of  $\epsilon_c \approx 2.1$ . The characteristic impedance of the feed line is  $48.75 \Omega$ , and its length was set to  $l_c = 10$  mm in the numerical model. The monopole of length  $l_m$  is displaced from the center by distance  $x_m$ . A Cartesian coordinate system was introduced, as shown in Figure 1. The permittivity of water was described by the Debye model [12]. A model of the water-based DRA was built in COMSOL Multiphysics 5.3 [28], which was used in all numerical calculations. The model consisted of the DRA enclosed by a hemisphere of free space and with a perfect electric conductor (PEC) plane as the ground. An outer perfectly matched layer (PML) terminated the free-space hemisphere. A matched port was placed on the bottom of the transmission line, as shown in Figure 1. The input power was set to 1 W.

See Appendix A for definitions and more details of the antenna parameters used in this work.

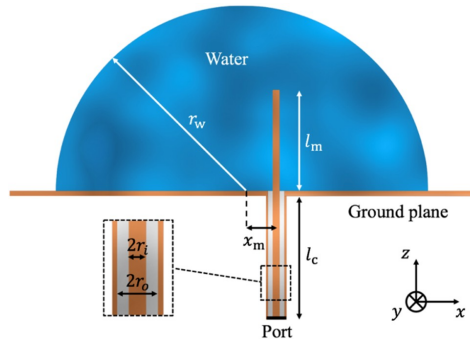


Figure 1. A sketch of the water-based dielectric resonator antenna (DRA).

### 3. Results and Discussion

We designed the antenna to operate at 300 MHz and 20 °C, where the relative permittivity of water was  $80.2 - j1.34$ . However, to study the influence of the dispersion of water, we compared it with an antenna designed for 1000 MHz, where the relative permittivity of water was  $79.9 - j4.46$ , clearly showing higher losses. We used two designs exciting different resonances in the hemisphere. With the PEC plane imaging the induced volume currents inside the hemisphere, the resonances will effectively be similar to the ones in the full sphere (the resonant properties of spherical configurations are known [29] also when water is used as the dielectric [30] and were utilized presently for the design of water-based DRAs. See also Appendix B.1 for more details). After a systematic parametric study of the two parameters  $l_m$  and  $x_m$ , the most efficient designs were found, and the final results are summarized in Table 1 for both frequencies. The total efficiency ( $\eta_{\text{eff}}$ ) is shown as a function of frequency in Figure 2a for both designs. At 300 MHz, a magnetic (electric) dipole resonance could be excited in a sphere with the radius 55.18 mm (78.53 mm) equal to  $\lambda_0/18$  ( $\lambda_0/14$ ). The maximum total efficiency for the magnetic (electric) dipole antenna was 29.5% (15.6%). For comparison, the total efficiency without water was only 0.037% (0.0013%), with almost total reflection of the input power. Thus, introducing water not only matched the antenna to the transmission line but also to the ambient free space, as also confirmed by the reflection coefficient ( $S_{11}$ ) and radiation efficiency ( $\eta_{\text{rad}}$ ) in Figure 2b. The magnetic dipole resonance in a water sphere is the most pronounced [30]. This was also the case here, as illustrated in Figure 2. However, due to the losses in water, both antennas absorbed (i.e., dissipated) more power than they radiated: the magnetic (electric) dipole antenna absorbed 70.1% (76.3%). Compared to the antennas at 1000 MHz, where the losses of water were even greater, we found that the total efficiency dropped by approximately a factor of 3 (see Table 1).

As both resonances could be excited in a single hemisphere but at different frequencies, we fabricated one antenna, where the position and the length of the monopole could be adjusted for each resonance type. The antenna was fabricated by hollowing out a hemisphere with the radius 55.18 mm in a Rohacell 51 HF block. The permittivity of Rohacell 51 HF was measured to be 1.075 [26]. The Rohacell block was then glued to an aluminum plate in which holes were drilled for insertion of the monopole antennas and water. Photographs of the antenna are shown in Figure 3a. Two holes ( $x_m = 7$  mm and  $x_m = 0$  mm) and two monopole antennas ( $l_m = 43.6$  mm and  $l_m = 15.3$  mm) were made so that both dipole DRA resonances could be excited. The ground plane was realized by attaching a circular aluminum plate with a diameter of 1 m to the antenna. The antenna was mounted on a tripod with a rotating joint, and the reflection coefficient was measured with an Anritsu MS2024B vector network analyzer calibrated for 50 Ohm matching.

**Table 1.** Geometrical and important antenna parameters for magnetic and electric dipole antennas designed for 300 and 1000 MHz.

Parameter	300 MHz		1000 MHz	
	Magnetic Dipole	Electric Dipole	Magnetic Dipole	Electric Dipole
$r_w$ (mm)	55.18	78.53	16.56	22.5
$l_m$ (mm)	43.6	16	15.4	7.9
$x_m$ (mm)	7	0	2.4	0
$f$ (MHz)	300	298	1000	1010
$G_{\text{real}}$ (dBi)	0.16	-3.1	-4.3	-8.2
$\eta_{\text{eff}}$	29.5%	15.6%	9.1%	4.8%
$\eta_{\text{rad}}$	29.6%	17%	9.5%	4.8%
$ S_{11} $ (dB)	-24.1	-10.9	-13.7	-19.1
$Z_A$ ( $\Omega$ )	$43 - j0.7$	$28 - j6.7$	$32.1 - j0.9$	$40 + j3.5$
$k_0 a$ (rad)	0.35	0.46	0.35	0.48
FBW <sub>3dB</sub>	7.81%	2.85%	24%	11.4%
$Q_{\text{ratio}}$	1.06	22.4	1.10	21.5

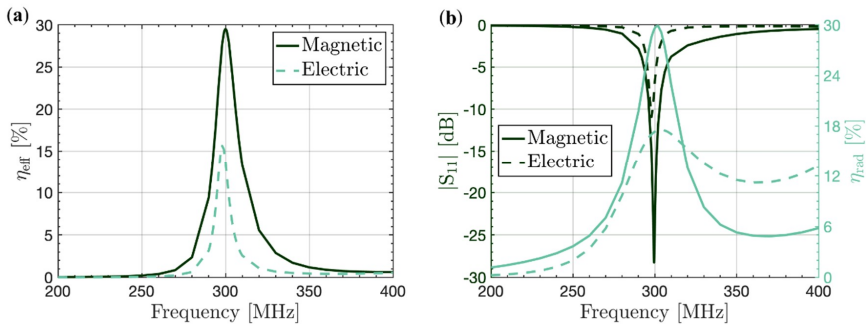


**Figure 2.** The numerical results for (a) total efficiency and (b) reflection coefficient and radiation efficiency as functions of frequency. Water temperature was 20 °C.

The water inlet made it easy to insert and extract water from the antenna. With no water, we measured a reflection coefficient of 0 dB with both monopole antennas. The measured reflection coefficients for the antenna filled with water are shown in Figure 3b. Clearly, the reflected power was reduced at the resonance frequencies for specific combinations of  $x_m$  and  $l_m$ . When the monopole antenna was positioned in the center of the hemisphere, the magnetic dipole resonance was not excited, and thus most of the power was reflected at 300 MHz. The electric dipole was optimally excited around 420 MHz with  $x_m = 0$  and  $l_m = 43.6$  mm. The numerical results are included in Figure 3b, showing full agreement with the measurements. The small mismatch of 0.4 MHz in frequency between experimental and numerical reflection minimum can be explained by a small difference in temperature and/or water filling in the hemisphere.

The water was removed from the hemisphere and then filled in to check the reproducibility of the measurements. This was done five times, and only a slight difference was observed between the measurements, with the values of the mean and maximum deviation being 299.725 MHz and 0.375 MHz, respectively. We found some differences in the magnitude of the reflection coefficient too (between -23 and -35 dB), but because its absolute value was very low, these differences could have come from small changes in the experimental conditions.

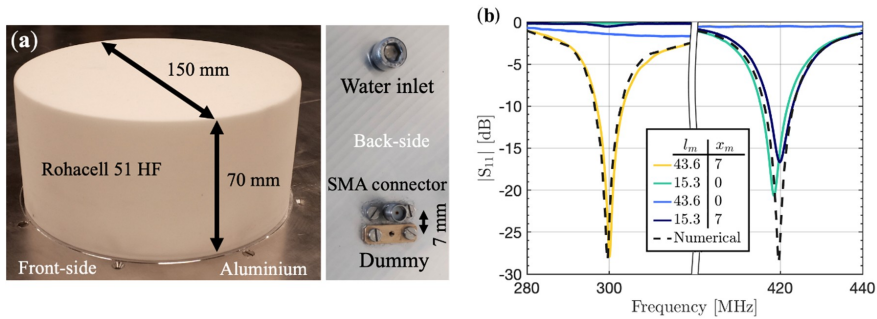


**Figure 3.** (a) Photographs of the front and back of the fabricated antenna and (b) measured reflection coefficient with different displacement positions  $x_m$  and monopole antenna lengths  $l_m$ , both in mm. Water temperature was 19–20 °C. The numerical results are shown with the optimized antenna lengths and positions at 20 °C.

In Figure 4a, the electric field distribution in the  $xz$ -plane of the magnetic dipole antenna is shown at 300 MHz. From the direction of the electric field (shown by the arrows), it is clear why the monopole cannot be positioned in the center of the hemisphere ( $x_m \neq 0$ ) if the magnetic resonance is to be excited. In order to excite a circulating electric displacement current, the monopole has to be displaced from the center of the hemisphere.

The calculated radiation pattern for the magnetic dipole antenna is shown in Figure 4b by the normalized radiation intensity in the  $xz$ - and  $xy$ -planes. It can be seen that there was no radiation in the negative  $z$  direction because of the ground plane. The radiation pattern was similar to that of a half-loop antenna, while the radiation pattern of the electric dipole antenna was similar to that of the monopole antenna (see Appendix B.2). The magnetic (electric) dipole antenna had isotropic radiation in the  $xz$ -plane ( $xy$ -plane) with the maximum realized gain ( $G_{real}$ ) of 0.16 dBi (−3.1 dBi).

The radiation pattern was also measured with a simple dipole antenna designed for 300 MHz. By rotating the antenna under test, the transmission coefficient was measured at different angles in the  $xz$ -plane of the antenna. The normalized transmission coefficient is included in Figure 4b. From 0° to ±90°, the measurements were similar to the numerical results. However, at higher angles, they started to deviate. This was expected because the simulated ground plane was infinite, whereas a ground plane of 1 m diameter was used in the measurements.

The 3 dB fractional bandwidth,  $FBW_{3dB}$ , of the magnetic (electric) dipole antenna was 7.81% (2.85%). This gave a radiation quality factor,  $Q_r$ , of 1.06 (22.4) times the so-called lower bound,  $Q_{lb}$ , (also known as the Chu limit, see Appendix A) with  $k_0a \approx 0.35$  ( $k_0a \approx 0.46$ ) for the magnetic (electric) dipole antenna. As  $k_0a \leq 0.5$  for both antennas, they are electrically small. For a quarter wavelength monopole,  $k_0a = \pi/2$ ; thus, water reduced the size of the antenna by a factor of 4.5 (3.2). Moreover, the magnetic dipole water-based DRA reported herein represents the electrically smallest water-based antenna to date. The cost is a reduction in radiated power (and thus the total efficiency) due to the losses in water as well as the bandwidth. Nevertheless, its fractional bandwidth is higher than many other compact antennas [9,10]. In addition, bearing in mind that the present design does not require any expensive or rare materials, the antenna will be very cheap and easy to produce. Furthermore, water adds flexibility to the design, allowing tuning by temperature and extraction of water, which we have examined both numerically and experimentally. The results are included in Appendix B.3.

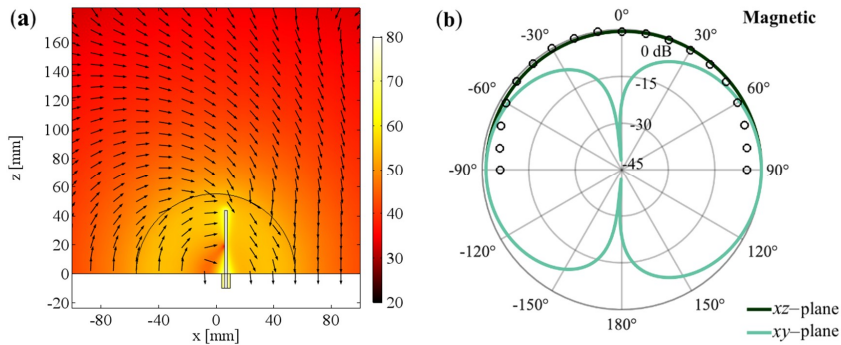


**Figure 4.** (a) The electric field distribution in the  $xz$ -plane for the magnetic dipole antenna. The colors show the intensity of the electric field in logarithmic scale, whereas the arrows show the direction. (b) Radiation pattern shown by the normalized radiation intensity in the  $xz$ - and  $xy$ -planes for the magnetic dipole antenna. The black circles show the measured radiation pattern. See Appendix B.2 for the electric field intensity and radiation pattern for the electric dipole antenna.

#### 4. Conclusions

In summary, simple electrically small water-based DRAs were investigated both numerically and experimentally. The fundamental resonances were excited in a water hemispherical cavity and used to effectively match a short monopole antenna to both its feed line and the surrounding free space. The final antennas were optimized by varying the length and the displacement of the monopole. As a result, compact water-based DRAs were designed. The optimum antenna had an electrical size of  $\lambda_0/18$ , making it the smallest water-based antenna to date, albeit with lowered total efficiency due to water losses. We believe that the proposed electrically small water-based DRAs may serve as cheap and easy-to-fabricate tunable alternatives for VHF and the low end of UHF bands.

**Author Contributions:** Formal analysis, software, investigation, and writing—original draft preparation, R.E.J.; supervision and writing—review and editing, A.V.L. and S.A.

**Funding:** This research received no external funding.

**Acknowledgments:** The authors would like to thank the workshop at the Electromagnetic Systems group of the Technical University of Denmark for fabrication of the antennas.

**Conflicts of Interest:** The authors declare no conflict of interest.

#### Appendix A

This appendix presents the definition of the antenna parameters used in this work. The water-based DRA can be described by the equivalent circuit diagram in Figure A1. We were interested in maximizing the total efficiency given by [2]:

$$\eta_{\text{eff}} = \frac{P_{\text{rad}}}{P_{\text{in}}} = \eta_{\text{rad}}(1 - |S_{11}|^2) \quad (\text{A1})$$

where  $P_{\text{rad}}$  is the total radiated power, and  $P_{\text{in}}$  is the input power to the transmission line.  $\eta_{\text{rad}} = P_{\text{rad}} / (P_{\text{rad}} + P_{\text{d}})$  is the radiation efficiency, with  $P_{\text{d}}$  being the power dissipated in the antenna, and  $|S_{11}|^2 = P_{\text{r}} / P_{\text{in}}$  is the fraction of the power reflected ( $P_{\text{r}}$ ) due to mismatch of the antenna input impedance ( $Z_{\text{A}}$ ) to that of the transmission line ( $Z_0$ ).  $S_{11}$  designates the antenna reflection coefficient.

We characterized the impedance bandwidth of the antenna by the 3 dB fractional voltage standing wave ratio (VSWR) bandwidth  $\text{FBW}_{3\text{dB}} = (f_{-3\text{dB}} - f_{+3\text{dB}}) / f_0$ , with  $f_{\pm 3\text{dB}}$  being the  $\pm 3$  dB frequencies



of  $S_{11}$  and  $f_0$  being the resonance frequency [3]. For electrically small antennas, the quality factor  $Q = 2/\text{FBW}_{3\text{dB}}$ , and presently we applied the following ratio:

$$Q_{\text{ratio}} = \frac{Q}{Q_{\text{lb}}} \tag{A2}$$

with  $Q_{\text{lb}} = b_i \eta_{\text{rad}} Q_{\text{Chu}} = b_i \eta_{\text{rad}} \left( \frac{1}{k_0^2} + \frac{1}{(k_0 a)^3} \right)$  being the lower bound of  $Q$ , where  $b_i$  is a resonance mode factor with  $i = m, e$  denoting the mode, and  $Q_{\text{Chu}}$  is the Chu limit [1–5]. For magnetic (electric) resonant antennas,  $b_m = 3$  ( $b_e = 1.5$ ). We used Equation (A2) to determine how close the  $Q$  of the antenna was to the theoretical minimum.

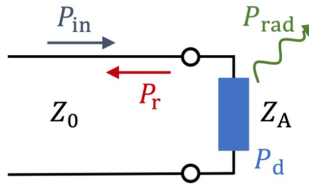


Figure A1. Equivalent circuit diagram of antenna.

The realized antenna gain in a given direction can be calculated as follows [2]:

$$G_{\text{real}}(\theta, \phi) = \eta_{\text{eff}} D(\theta, \phi) \tag{A3}$$

where  $D(\theta, \phi) = 4\pi U(\theta, \phi)/P_{\text{rad}}$  is the directivity, with  $U(\theta, \phi)$  being the radiation intensity and  $(\theta, \phi)$  denoting the direction of radiation.

### Appendix B

This appendix contains the additional results for the scattering analysis of a water sphere and the electric dipole antenna as well as the sensitivity and tunability of the antennas.

#### Appendix B.1 Scattering Analysis of Water Sphere

The solution to a plane wave incidence on a dielectric sphere is well known [29], and it was studied in a previous work [30]. The configuration is shown in Figure A2a. The amplitude coefficients are [29]

$$a_n = \frac{\varepsilon_{r,w} j_n(k_w r_w) j_n'(k_0 r_w) - j_n'(k_w r_w) j_n(k_0 r_w)}{\varepsilon_{r,w} j_n(k_w r_w) h_n^{(2)'}(k_0 r_w) - j_n'(k_w r_w) h_n^{(2)}(k_0 r_w)} \tag{A4}$$

$$b_n = \frac{j_n(k_w r_w) j_n'(k_0 r_w) - j_n'(k_w r_w) j_n(k_0 r_w)}{j_n(k_w r_w) h_n^{(2)'}(k_0 r_w) - j_n'(k_w r_w) h_n^{(2)}(k_0 r_w)} \tag{A5}$$

for the  $\text{TM}'$  and  $\text{TE}'$  scattering field components, respectively.  $\varepsilon_{r,w}$  and  $k_w$  are the relative permittivity and the wavenumber in water, respectively.  $j_n$  and  $h_n^{(2)}$  are the  $n$ th order spherical Bessel function of the first kind and spherical Hankel function of the second kind, respectively. The prime ' denotes the operation  $g_n'(x) = d[xg_n(x)]/dx$ .

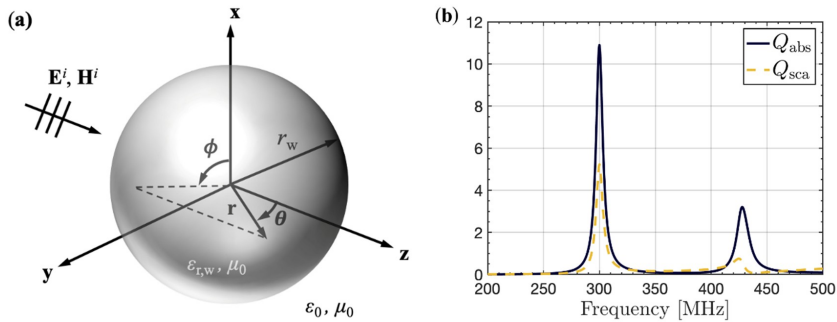


**Figure A2.** (a) Sketch of the water sphere in free space illuminated by a plane wave and (b) the spectrum of the scattering and absorption efficiencies for a sphere with  $r_w = 55.18$  mm and a water temperature of  $20^\circ\text{C}$ .

The absorption, extinction, and scattering efficiencies were used to describe the response of the water sphere, and they are related by  $Q_{\text{abs}} = Q_{\text{ext}} - Q_{\text{sca}}$ , where

$$Q_{\text{sca}} = \frac{2}{(k_0 r_w)^2} \sum_{n=1}^{\infty} (2n + 1) (|a_n|^2 + |b_n|^2) \tag{A6}$$

$$Q_{\text{ext}} = \frac{2}{(k_0 r_w)^2} \sum_{n=1}^{\infty} (2n + 1) \text{Re}\{a_n + b_n\}. \tag{A7}$$

The spectrum of the scattering and absorption efficiencies are shown in Figure A2b for a sphere with  $r_w = 55.18$  mm and a water temperature of  $20^\circ\text{C}$ . Peaks at 300 and 430 MHz can be seen, caused by the magnetic dipole ( $b_1$ ) and electric dipole ( $a_1$ ) resonances, respectively. These were the resonances that we utilized in the antennas. We found that 32% (68%) of the extinct power was scattered (absorbed) at the magnetic dipole resonance frequency, which was very similar to the efficiency found for the magnetic dipole antenna.

#### Appendix B.2 Electric Dipole Antenna for 300 MHz

The electric field distribution in the  $xz$ -plane at 300 MHz is shown in Figure A3a. The calculated radiation pattern is shown in Figure A3b by the normalized radiation intensity in the  $xz$ - and  $xy$ -planes. The field distribution was symmetrical as the monopole was positioned in the center of the hemisphere. Notice that there was no radiation in the negative  $z$  direction because of the ground plane.

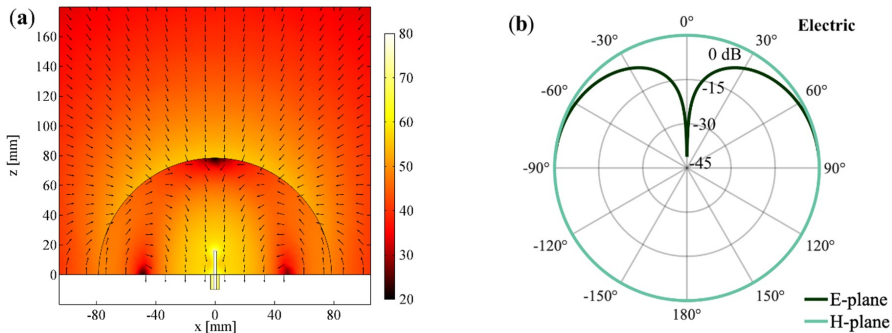


**Figure A3.** (a) The electric field distribution in the  $xz$ -plane as well as (b) the radiation pattern in the  $xz$ - and  $xy$ -plane for electric dipole antenna. The colors in (a) show the intensity of the electric field in logarithmic scale, whereas the arrows show the direction.

### Appendix B.3 Sensitivity and Tunability

Variation in the cable type of same characteristic impedance had a minimum impact on the radiated power. The same was the case for the length of the transmission line below the ground plane ( $l_c$ ). However, variation of the length and position of the monopole ( $\Delta l_m$  and  $\Delta x_m$ ) as well as the hemisphere radius and temperature of water ( $\Delta r_w$  and  $\Delta T_w$ ) affected the radiated power. Analysis of the different parameters showed that changes of  $\Delta l_m \approx 1.7$  mm,  $\Delta x_m \approx 0.7$  mm,  $\Delta V_w \approx 1.4$  mL, and  $\Delta T_w \approx 0.4$  °C resulted in a 1% decrease in radiated power for the magnetic dipole antenna at 300 MHz. This information is important because it shows how sensitive the antenna is to fabrication imperfections. However, this can also be seen as a way to tune the antenna. This is illustrated in Figure A4 by the results of simulated temperature tuning and measurements of water extraction from the hemisphere for the magnetic dipole antenna. In Figure A4a, the total efficiency as a function of frequency and temperature is shown. Clearly, the resonance frequency was shifted by a change in temperature. From 0 to 100 °C, the peak of the efficiency was blue-shifted linearly (as indicated by the black tendency line) from 286 to 358 MHz, corresponding to a shift of 25%. This blue-shift was obviously due to the permittivity of water changing from  $87.8 - j2.8$  to  $55.8 - j0.22$ , effectively bringing a change of 25% to the wavenumber in water. Furthermore, the temperature growth decreased the losses in water, and the total efficiency was above 50% from around 55 °C.

The reflection coefficient was moreover measured for different water fillings extracting 1% ( $\approx 3.5$  mL) volume of water at the time from the completely filled hemisphere. During the measurements, the ground plane was kept in horizontal level. The results are shown in Figure A4b, and it can be seen that there was a linear blue-shift and increment of the minimum in the reflection coefficient as water was extracted, demonstrating yet another means of tunability in the water-based antenna.

The tunability properties of the antenna can, in principle, also be used for sensing. Several antennas designed for sensing temperature changes of up to 1000 °C have already been demonstrated [31–33].

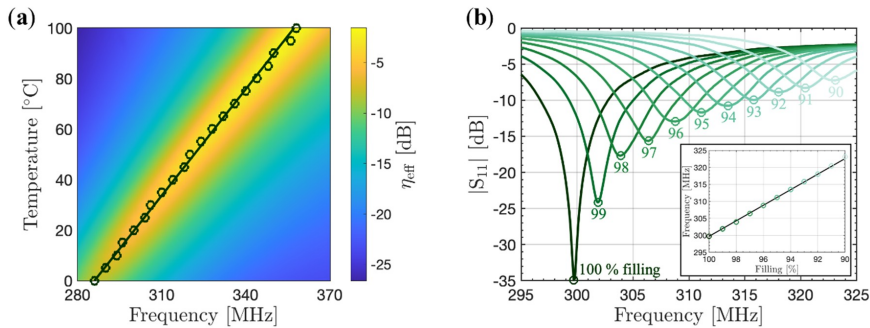


**Figure A4.** (a) Simulated temperature tuning and (b) experimental water fill tuning for the magnetic dipole antenna. The black circles and line in (a) indicate the maximum efficiency at each 5 °C temperature and the tendency, respectively. The inset in (b) shows the frequency of the minimum reflection coefficient for each filling.

## References

1. Chu, L.J. Physical limitations of omnidirectional antennas. *J. Appl. Phys.* **1948**, *19*, 1163–1175. [[CrossRef](#)]
2. Balanis, C.A. *Antenna Theory*, 3rd ed.; Wiley: New York, NY, USA, 2005; Volume 64–69, pp. 637–641.
3. Yaghjian, A.D.; Best, S.R. Impedance, bandwidth, and Q of antennas. *IEEE Trans. Antennas Propag.* **2005**, *53*, 1298–1324. [[CrossRef](#)]
4. Thal, H.L. New radiation Q limits for spherical wire antennas. *IEEE Trans. Antennas Propag.* **2006**, *44*, 2757–2763. [[CrossRef](#)]
5. Best, S.R. The radiation properties of electrically small folded spherical helix antennas. *IEEE Trans. Antennas Propag.* **2004**, *52*, 953–960. [[CrossRef](#)]
6. Best, S.R. Low Q electrically small linear and elliptically polarized spherical dipole antennas. *IEEE Trans. Antennas Propag.* **2005**, *53*, 1047–1053. [[CrossRef](#)]
7. Erentok, A.; Kim, O.S.; Arslanagić, S. Cylindrical metamaterial-based subwavelength antenna. *Microw. Opt. Technol. Lett.* **2009**, *51*, 1496–1500. [[CrossRef](#)]
8. Ziolkowski, R.W.; Erentok, A. Metamaterial-based efficient electrically small antennas. *IEEE Trans. Antennas Propag.* **2006**, *54*, 2113–2130. [[CrossRef](#)]
9. Erentok, A.; Ziolkowski, R.W. Metamaterial-inspired efficient electrically small antennas. *IEEE Trans. Antennas Propag.* **2008**, *56*, 691–707. [[CrossRef](#)]
10. Petosa, A.; Ittipiboon, A. Dielectric Resonator Antennas: A Historical Review and the Current State of the Art. *IEEE Antenn. Propag. Mag.* **2010**, *52*, 91–116. [[CrossRef](#)]
11. Kingsley, S.P.; O’Keefe, S.G. Beam steering and monopulse processing of probe-fed dielectric resonator antennas. *Proc. IEEE Radar Sonar Navig.* **1999**, *146*, 121–125. [[CrossRef](#)]
12. Ellison, W. Permittivity of pure water, at standard atmospheric pressure, over the frequency range 0–25 THz and the temperature range 0–100 °C. *J. Phys. Chem. Ref. Data* **2007**, *36*, 1–18. [[CrossRef](#)]
13. O’Keefe, S.G.; Kingsley, S.P. Tunability of liquid dielectric resonator antennas. *IEEE Antennas Wirel. Propag. Lett.* **2007**, *6*, 533–536. [[CrossRef](#)]
14. Zhou, R.; Zhang, H.; Xin, H. Liquid-based dielectric resonator antenna and its application for measuring liquid real permittivities. *IET Microw. Antennas Propag.* **2014**, *8*, 255–262. [[CrossRef](#)]
15. Mobashsher, A.T.; Abbosh, A. Reconfigurable water-substrate based antennas with temperature control. *Appl. Phys. Lett.* **2017**, *110*, 253503. [[CrossRef](#)]
16. Li, Y.; Luk, K.M. A water dense dielectric patch antenna. *IEEE Access* **2015**, *3*, 274–280. [[CrossRef](#)]
17. Sun, J.; Luk, K.M. A wideband low cost and optically transparent water patch antenna with omnidirectional conical beam radiation patterns. *IEEE Trans. Antennas Propag.* **2017**, *65*, 4478–4485. [[CrossRef](#)]

18. Chen, Y.; Wang, C. Dual-band directional/omni-directional liquid dielectric resonator antenna designs using characteristic modes. In Proceedings of the IEEE Antennas and Propagation Society International Symposium (APSURSI), Memphis, TN, USA, 6–11 July 2014; pp. 848–849.
19. Xing, L.; Huang, Y.; Xu, Q.; Aljaafreh, S. Wideband, hybrid rectangular water antenna for DVB-H applications. *Microw. Opt. Technol. Lett.* **2015**, *59*, 2160–2164. [[CrossRef](#)]
20. Fayad, H.; Record, P. Broadband liquid antenna. *Electron. Lett.* **2006**, *42*, 133–134. [[CrossRef](#)]
21. Xing, L.; Huang, Y.; Shen, Y.; Al Ja'afreh, S.; Xu, Q.; Alrawashdeh, R. Further investigation on water antennas. *IET Microw. Antennas Propag.* **2015**, *9*, 735–741. [[CrossRef](#)]
22. Xing, L.; Meng, X.; Yang, L.; Xu, B.; Pan, Y. A wideband water antenna for WiFi applications. In Proceedings of the International Workshop on Antenna Technology (iWAT), Nanjing, China, 5–7 March 2018; pp. 1–3.
23. Andryieuski, A.; Kuznetsova, S.M.; Zhukovsky, S.V.; Kivshar, Y.S.; Lavrinenko, A.V. Water: Promising opportunities for tunable all—Dielectric electromagnetic metamaterials. *Sci. Rep.* **2015**, *5*, 13535. [[CrossRef](#)]
24. Gorlach, M.A.; Song, M.; Slobozhanyuk, A.P.; Bogdanov, A.A.; Belov, P. Topological transition in coated wire medium. *Phys. Status Solidi RRL* **2016**, *10*, 900–904. [[CrossRef](#)]
25. Yang, X.; Zhang, D.; Wu, S.; Li, L.; Cao, K.; Huang, K. Reconfigurable all-dielectric metasurface based on tunable chemical systems in aqueous solution. *Sci. Rep.* **2017**, *7*, 3190. [[CrossRef](#)]
26. Jacobsen, R.E.; Lavrinenko, A.V.; Arslanagić, S. Water-Based Metasurfaces for Effective Switching of Microwaves. *IEEE Antennas Wirel. Propag. Lett.* **2018**, *17*, 571–574. [[CrossRef](#)]
27. Yoo, Y.J.; Ju, S.; Park, S.Y.; Kim, Y.J.; Bong, J.; Lim, T.; Kim, K.W.; Rhee, J.Y.; Lee, Y.P. Metamaterial absorber for electromagnetic waves in periodic water droplets. *Sci. Rep.* **2015**, *5*, 14018. [[CrossRef](#)]
28. COMSOL Multiphysics 5.3. Available online: <https://www.comsol.com/> (accessed on 4 October 2019).
29. Bohren, C.F.; Huffman, D.R. *Absorption and Scattering of Light by Small Particles*, 1st ed.; Wiley: Weinheim, Germany, 1998; pp. 82–129.
30. Jacobsen, R.E.; Arslanagić, S.; Lavrinenko, A.V. Fundamental properties of Mie resonances in water spheres. In Proceedings of the URSI International Symposium on Electromagnetic Theory (EMTS), San Diego, CA, USA, 27–31 May 2019.
31. Boccard, J.-M.; Aftab, T.; Hoppe, J.; Yousaf, A.; Hütter, R.; Reindl, L.M. High-resolution, far-field, and passive temperature sensing up to 700 °C using an isolated ZST microwave dielectric resonator. *IEEE Sens. J.* **2016**, *16*, 715–722. [[CrossRef](#)]
32. Cheng, H.; Ebadi, S.; Gong, X. A low-profile wireless passive temperature sensor using resonator/antenna integration up to 1000 °C. *IEEE Antennas Wirel. Propag. Lett.* **2012**, *11*, 369–372.
33. Yao, J.; Tchafa, F.M.; Jain, A.; Tjuatja, S.; Huang, H. Far-field interrogation of microstrip patch antenna for temperature sensing without electronics. *IEEE Sens. J.* **2016**, *16*, 7053–7060. [[CrossRef](#)]



## APPENDIX E

# Paper 5: "A water-based Huygens dielectric resonator antenna"

---

A water-based antenna with balanced electric and magnetic dipole modes for enhanced directivity. The manuscript is published.

The citations in the manuscript refer to reference list included at the end of the manuscript.

Work contributions by the present author: Numerical calculations, experiments and manuscript drafting.

Reference information:

**R. E. Jacobsen**, A. V. Lavrinenko and S. Arslanagić, "A water-based Huygens dielectric resonator antenna," *IEEE Open Journal of Antennas and Propagation*, vol. 1, pp. 493-499, Sept. 2020. doi:10.1109/OJAP.2020.3021802

# A Water-Based Huygens Dielectric Resonator Antenna

RASMUS E. JACOBSEN<sup>1</sup> (Graduate Student Member, IEEE), ANDREI V. LAVRINENKO<sup>1</sup>,  
AND SAMEL ARSLANAGIĆ<sup>2</sup> (Senior Member, IEEE)

<sup>1</sup>Department of Photonics Engineering, Technical University of Denmark, 2800 Kongens Lyngby, Denmark

<sup>2</sup>Department of Electrical Engineering, Technical University of Denmark, 2800 Kongens Lyngby, Denmark

CORRESPONDING AUTHOR: R. E. JACOBSEN (e-mail: rajac@fotonik.dtu.dk)

**ABSTRACT** With its high-permittivity in the microwave frequency range, water has the potential as an alternative, inexpensive, bio-friendly and abundant material for many microwave applications such as dielectric resonator antennas and tunable metamaterials. Huygens antennas, composed of single-element structures supporting a special combination of electric and magnetic modes, provide an alternative route for compact and directive antennas. In this work, we investigate a subwavelength water-based Huygens dielectric resonator antenna with strongly excited electric and magnetic dipoles at around 350 MHz. Our antenna leads to the directivity of 6 and a radiation front-to-back ratio of 40.3 dB. Additionally, good matching to the feed-line and the surrounding free space were achieved with a reflection coefficient of  $-38.3$  dB and a total efficiency of 57.8 %. The antenna was fabricated and characterized with excellent agreement between the measurements and the numerical results. Furthermore, several means of tuning the antenna were tested numerically and experimentally. We believe that the proposed water-based Huygens dielectric resonator antenna may serve as an easy-to-fabricate and cheap alternative for the VHF and low end of the UHF bands.

**INDEX TERMS** Dielectric resonator antenna, reconfigurable antennas, water.

## I. INTRODUCTION

OVER several decades, dielectric resonator antennas (DRAs) have been of great interest as compact alternatives to traditional dipole and waveguide antennas [1]. Many designs have been proposed demonstrating different attributes such as low-profile, large bandwidth, frequency-tunability and phase-steering capabilities. Generally, DRAs rely on electric and magnetic modes supported in expensive high-permittivity ceramic structures. Alternatively, water-filled cavities exploiting water's relatively high permittivity in the microwave frequency range can be used instead [2]. Water holds great potential as an abundant, inexpensive and bio-friendly material for tunable antennas [3]–[5], as well as inclusions in metamaterials (MMs) and metasurfaces (MSs) [6]–[11].

Various liquid-based antennas have been demonstrated with some relying on water's high real and low imaginary parts of permittivity, whereas other use conductive

liquids [3]–[5], [12]. In general, many of these antennas operate in the VHF and UHF bands due to the decreasing (increasing) real part of water's permittivity at higher frequencies. The working principle of water-based DRAs relies on resonant electric (TM) and magnetic (TE) modes in water-filled cavities. These modes are the natural eigenmodes belonging to the dielectric cavity, and they can be excited by sources placed outside and inside the cavity. In general, a single cavity has multiple modes spread-out in narrow bands of frequencies across the spectrum. In [5], we demonstrated an electrically small water-based hemispherical DRA with such characteristics. The water provided an excellent way to place an adjustable metallic monopole antenna inside the cavity without the issues of air gaps between the dielectric and the monopole antenna. Furthermore, the water-based DRA could be tuned by changing the water-temperature and/or the water-volume in the cavity.

In antenna configurations, the dipole modes are the most broadly used, which by their nature have low directivity. Higher-order modes can also be exploited for high-directivity antennas, but such higher-order modes require larger dielectric structures, have very small bandwidths and are more sensitive to losses [1]. Another way to increase the directivity in a compact single-element configuration is to combine magnetic and electric modes [13]–[15], and such antennas are often referred to as Huygens antennas. Furthermore, when the fundamental dipole modes are combined in dielectric structures, Kerker's condition may be satisfied [16]–[17], which is also of great interest in MMs and MSs. Additionally, dipoles and higher-order modes can also be combined to increase the directivity even further [17]–[18]. Kerker's condition is satisfied in many types of dielectric structures, including dielectric spheres and cylinders [19]–[20]. However, the dipole modes are often weakly excited resulting in very low scattering. Designing structures exhibiting strongly excited magnetic and electric modes with the right integration of their magnitudes and phases is not a simple task. Combining an electric and magnetic dipole will increase the directivity in one direction to twice of that of a single dipole, while in the opposite direction, the directivity is greatly minimized. Several Huygens antenna designs have already been demonstrated [13]–[14], [18], but thus far no water-based Huygens DRAs have been proposed.

The purpose of the present work is to investigate a simple subwavelength water-based Huygens DRA. The antenna consists of a short monopole antenna fed against a large ground conducting plane and encapsulated by a rectangular cuboid-shaped cavity filled with distilled water. The DRA is designed with overlapping fundamental electric and magnetic dipole modes at around 350 MHz. The final design has a directivity of 6 and a front-to-back ratio (FBR) of 40.3 dB. Furthermore, our antenna is well matched to both its feed-line and the surrounding free space with a reflection coefficient of  $-38.3$  dB and a total efficiency of 57.8%. The size of the antenna is  $a \approx 147$  mm  $\approx \lambda_0/6$  (sometimes provided as  $k_0 a \approx 1.08$ ), where  $\lambda_0$  ( $k_0 = 2\pi/\lambda_0$ ) is the free-space wavelength (wave number). A prototype of the antenna is fabricated with excellent agreement between numerical results and measurements. In addition, we demonstrate and discuss several ways of tuning the antenna. We believe that the simple and cheap antenna serve as an easy-to-fabricate and cheap alternative for the VHF and low end of the UHF bands.

Throughout this article, the time-factor  $\exp(j\omega t)$ , with  $\omega$  being the angular frequency and  $t$  being the time, is assumed and suppressed.

## II. ANTENNA CONFIGURATION AND PARAMETERS

A sketch of the water-based Huygens DRA is shown in Fig. 1. It consists of a rectangular cuboid-shaped Rohacell 51 HF cavity attached to a ground conducting plane and filled with distilled water. The Rohacell 51 HF materials has a measured relative permittivity of 1.075 [9]. A Cartesian

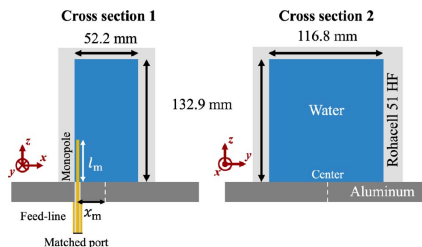


FIGURE 1. A sketch of the water-based Huygens DRA.

coordinate system is introduced as shown in Fig. 1 with the associated spherical angular coordinates  $(\theta, \phi)$ . A short monopole is inserted into the cavity as shown in Fig. 1. The feed line is a coaxial transmission line with the inner and outer diameter of 1.28 mm and 4.1 mm, respectively, and a dielectric material with the relative permittivity of 2.1. The characteristic impedance of the feed line is 48.15  $\Omega$ . The diameter and the length of the monopole is 1.6 mm and  $l_m$ , respectively. The monopole is displaced by  $x = -x_m$  from the center of the Huygens DRA to excite the magnetic mode. The Huygens DRA is designed for 350 MHz operation with a water temperature of 20°C. The final design with the highest total efficiency ( $\eta_{\text{tot}}$ ) and FBR were determined through a parametric study. In a previous work, we investigated a water-based hemispherical DRA, which exhibited both magnetic and electric dipole resonances, however, with the latter being at higher frequencies [5]. A cubic DRA has similar behavior, and to shift the electric resonance to lower frequencies, we simply extend the dielectric along the  $y$ - and  $z$ -axis until we obtain the wanted properties of the antenna. The cavity size and the values of  $x_m$  and  $l_m$  are listed in Table 1 for the final antenna design.

The  $xz$ - and  $xy$ -planes correspond to the E- and H-planes of the antenna, respectively. The Debye model is used to describe the permittivity of distilled water inside the cavity [2], and at 350 MHz and 20°C, the relative permittivity is  $\epsilon_{r,\text{water}}(350 \text{ MHz}, 20^\circ\text{C}) = 80.2 - j1.6$ . A model of the Huygens DRA is built in COMSOL Multiphysics 5.4 used for all numerical calculations [21]. The COMSOL model consists of the Huygens DRA enclosed by a hemisphere of free space and with a Perfect Electric Conductor (PEC) plane as the ground. The Huygens DRA is simulated without the Rohacell 51 HF material as its low permittivity minimally affects the antenna response. An outer layer of PML is attached to the free-space hemisphere and a matched port is placed on the bottom of the feed line. A symmetry plane was employed at  $y = 0$  to half the model size and a convergence test was conducted leading to total of 1,283,616 Number of Degrees of Freedom solved for in the final model.

We use different well-known antenna parameters in this article, such as total efficiency (including the mismatch loss)



TABLE 1. Simulated water-based Huygens antenna parameters.

Parameter	Value
Cavity size [mm <sup>3</sup> ]	116.8×52.2×132.9
$l_m$ [mm]	27.2
$x_m$ [mm]	24
$f$ [MHz]	351.6
$G_{\text{realized,max}}$ [dBi]	5.42
$D_{\text{max}}$	6
$\eta_{\text{tot}}$	57.8 %
$\eta_{\text{rad}}$	57.8 %
$ S_{11} $ [dB]	-38.3
$Z_A$ [ $\Omega$ ]	47.27 + $j$ 0.77
FBW <sub>10dB</sub>	4.0 %
FBR <sub>max</sub> [dB]	40.3
$k_0\alpha$ [rad]	1.08
$\epsilon_{r,\text{water}}$ (350 MHz, 20 °C)	80.2 - $j$ 1.6

$\eta_{\text{tot}}$ , radiation efficiency  $\eta_{\text{rad}}$ , reflection coefficient  $S_{11}$  etc., and we refer to [5] or [22] for more information about these parameters. Throughout the paper we use the front-to-back ratio (FBR) to evaluate how well the radiated power is concentrated in one direction. The FBR is defined as

$$\text{FBR} = D_{+x}/D_{-x}, \quad (1)$$

where  $D_{\pm x}$  is the directivity in the  $\pm x$ -direction (in angular coordinates:  $(\theta, \phi)_{+x} = (90^\circ, 0^\circ)$  and  $(\theta, \phi)_{-x} = (90^\circ, 180^\circ)$ ).

### III. NUMERICAL AND EXPERIMENTAL RESULTS

#### A. ANTENNA CHARACTERIZATION

The final results are summarized in Table 1. We present  $\eta_{\text{tot}}$  and  $\eta_{\text{rad}}$  as functions of frequency in Fig. 2(a). The magnitude of  $S_{11}$  as function of frequency is shown in Fig. 2(b). Around 350 MHz the efficiencies are high, and  $S_{11}$  is low. At 351.6 MHz, where FBR is maximum (see Fig. 4(a)), the  $S_{11}$  drops to -38.3 dB indicating excellent matching of the antenna to the feed-line. The antenna input impedance  $Z_A$  is calculated using  $S_{11}$ , and its real and imaginary parts are shown in Fig. 2(c) as functions of frequency. At 351.6 MHz,  $Z_A = 47.27 + j0.77\Omega$ .  $\eta_{\text{tot}}$  is modest and is 57.8 % as the water absorbs 42.2 % of the input power. The absorbed power was calculated in COMSOL by integrating the power loss density over the volume of water.

The peak in  $\eta_{\text{tot}}$  comes from the modes excited in the water-filled cavity. From Fig. 2, we would conclude that a single resonant mode is excited around 350 MHz. However, inspecting the near fields of the antenna in both the  $xz$ - and  $xy$ -plane, which are shown in Fig. 3, we observe two dipoles being excited. The displacement of the monopole along the  $x$ -axis inside the water cavity renders an asymmetric field distribution, and in the  $xz$ -plane in Fig. 3(a), we see that the electric field (arrows) forms a half-loop

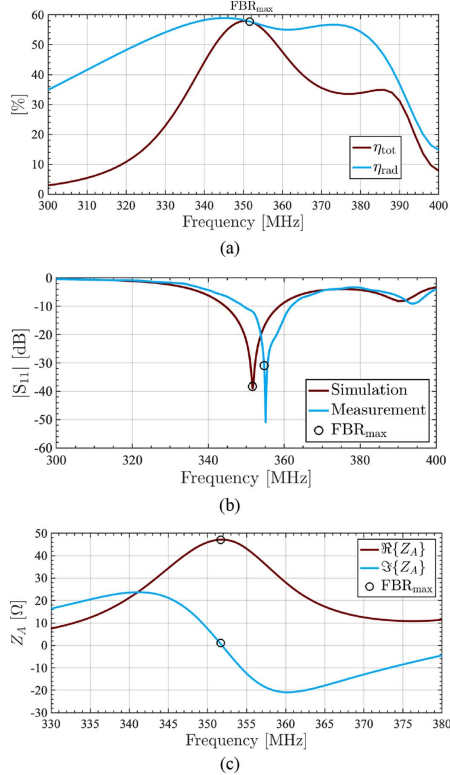
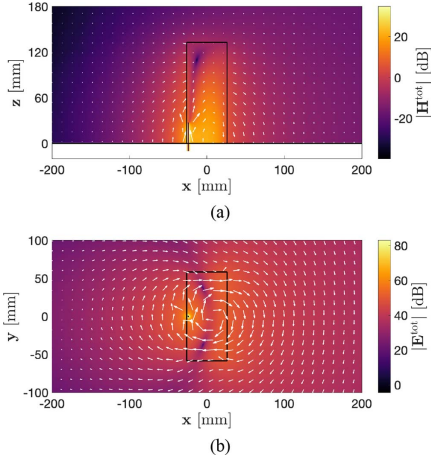


FIGURE 2. The simulated (a) total efficiency ( $\eta_{\text{tot}}$ ) and radiation efficiency ( $\eta_{\text{rad}}$ ) and (b) the reflection coefficient ( $S_{11}$ ) as functions of frequency. The circles indicate the location of maximum FBR. In (b),  $S_{11}$  is given in logarithmic scale, and the measured  $S_{11}$  is included. The antenna input impedance  $Z_A$  is shown as a function of frequency in (c).

with an enhanced magnetic field intensity (colors) near the ground plane inside the water. This is identified as a magnetic dipole mode ( $\text{TE}_{111}$ ). If we turn our attention to the  $xy$ -plane in Fig. 3(b), we find an alternated field distribution: the magnetic field (arrows) forms a loop with an enhanced electric field intensity (colors), i.e., an electric dipole ( $\text{TM}_{011}$ ). In our previous work on water-based antennas, such strong dipole modes were also excited, but at different frequencies [5]. In the present configuration, the dipoles are excited at the same frequency. The outcome of the double dipole excitation can also be observed in the far-field, see Fig. 4(a), where the directivity pattern has the cardioid shape. The directivity in the  $-x$ -direction is greatly



**FIGURE 3.** (a) The total magnetic (electric) field intensity,  $H^{\text{tot}}$  ( $E^{\text{tot}}$ ), shown as colors (arrows) in the  $xz$ -plane. (b)  $E^{\text{tot}}$  ( $H^{\text{tot}}$ ) shown as colors (arrows) in the  $xy$ -plane. Both colors and arrows are in logarithmic scale. Frequency is 351.6 MHz. There is no radiation in the negative  $z$ -direction because of the ground plane.

reduced, whereas the maximum in the  $+x$ -direction is still maintained. Such behavior is highlighted in Fig. 4(b) with the FBR shown as a function of frequency. At 351.6 MHz, the FBR has the remarkable peak value of 40.3 dB. The maximum directivity  $D_{\text{max}} = D_{+x}$  as a function of frequency is included in Fig. 4(b). At 351.6 MHz,  $D_{\text{max}} = 6$ , which is expected for ground-supported Huygens antennas [15]: a single dipole antenna has a directivity of 1.5, and with two dipoles and a ground plane, the directivity is increased by a factor of 4. Furthermore, the maximum realized gain is  $G_{\text{realized,max}} = 5.42$  dBi, which is 0.65 dB higher than that of a matched and lossless monopole antenna.

The antenna was fabricated at the local workshop, and a photograph is shown in Fig. 5(a). The antenna was made by hollowing out the cavity in a Rohacell 51 HF block, which was then glued on to a circular aluminum plate of 1 m in diameter. Holes for insertion of the monopole antenna and distilled water were drilled in the aluminum plate. A sketch of the measurement setup is shown in Fig. 5(b). The antenna was mounted on a tripod with a rotating joint such that the antenna could be rotated  $\theta'$  as shown in Fig. 5(b). In this way, the radiation pattern was recorded using a simple dipole antenna designed for 350 MHz operation and positioned 3.3 m away. Accordingly to the definition of the far-field distance, if we use the ground plane as the largest dimension ( $d = 1$  m is the size of the ground plane), we get  $d_{\text{ff}} > 2d^2/\lambda_0 \approx 2.3$  m and thus fulfill the far-field condition. For measurement angles  $\theta' = [90^\circ, 0^\circ]$ , the antenna was rotated  $180^\circ$  in the  $xy$ -plane. The reflection

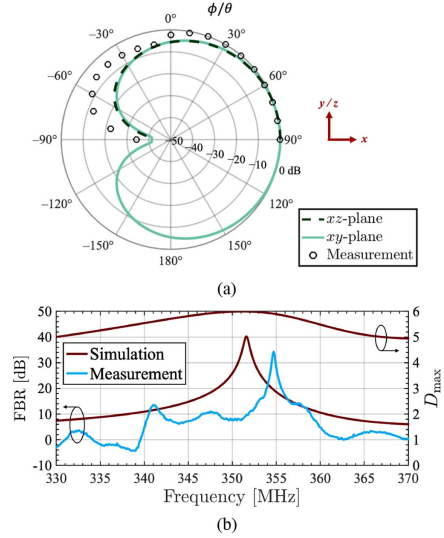


**FIGURE 4.** (a) Simulated radiation pattern shown by the normalized directivity in the  $xz$ - and  $xy$ -planes at the frequency of 351.6 MHz. The black circles show the measured normalized  $|S_{21}|$  in the  $xz$ -plane at the frequency of 354.7 MHz. The simulated directivity and measured  $S_{21}$  are normalized with their maximum values and given in logarithmic scale for easier comparison. (b) Simulated and measured front-to-back ratio (FBR) in logarithmic scale, as well as the maximum directivity ( $D_{\text{max}}$ ), as functions of frequency.

( $S_{11}$ ) and transmission coefficients ( $S_{21}(\theta')$ ) were measured with an Anritsu MS2024B vector network analyzer calibrated for 50 Ohm matching. The measured  $S_{11}$  is shown in Fig. 2(b) and the measured FBR is included in Fig. 4(b), which is calculated as  $S_{21}(\theta' = 90^\circ)/S_{21}(\theta' = -90^\circ)$ . The measured FBR is maximal at 354.7 MHz with a measured  $S_{11}$  of  $-30.9$  dB showing nice agreement with the numerical predictions. The small mismatch of 3.1 MHz in frequency between experimental and numerical results can be explained by a small difference in temperature and/or water filling in the cavity. The normalized measured  $S_{21}(\theta')$  in the  $xz$ -plane is included in Fig. 4(a), and is in good agreement with the numerical results.

By default, the antenna bandwidth is characterized by its 3-dB fractional matched voltage standing wave ratio bandwidth  $\text{FBW}_{3\text{dB}}$  [22]. However, due to the second resonance around 390 MHz, this is quite large (19.7 %). Therefore, it is more convenient in this case to use the 10-dB fractional matched voltage standing wave ratio bandwidth  $\text{FBW}_{10\text{dB}}$ , which is 4.0 %. According to [23], the quality factor  $Q$  is given by  $Q = 2/3\text{FBW}_{10\text{dB}}$ , which in the case of our Huygens DRA gives around 17. In the absence of water, one is left with the monopole antenna alone, which resonates

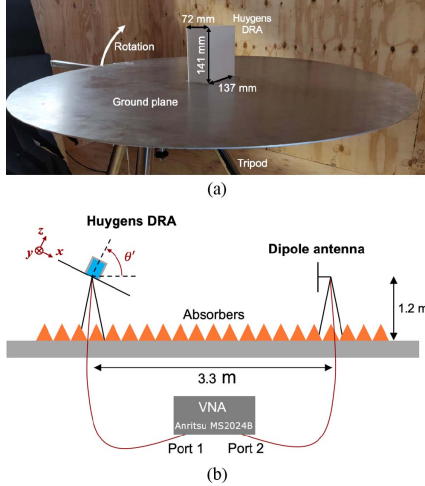


FIGURE 5. (a) Photograph of the fabricated antenna mounted the tripod with the rotatable joint and (b) sketch of the measurement setup.

at a higher frequency (around 2.8 GHz) with an associated quality factor of around 7 [22]. From Fig. 4(b), we see that the high FBR is narrow-banded. Obviously, this is coming from the tight overlap of the resonant dipole modes. The  $FBR_{10dB}$  bandwidth is 6.5 %.

### B. TUNABILITIES AND SENSITIVITIES

Water-based antennas have multiple tuning parameters, and in this work, we have tested variations of the position of the monopole, water content in the cavity and temperature of water.

In total three holes were drilled for the insertion of the monopole, and the measured  $S_{11}$  for each of them is shown in Fig. 6(a). For the alternative monopole positions,  $x_m = 0$  and  $x_m = 12$  mm, we find several minima spread out over their spectra, each representing different mode excitations. None of these modes produce reflection coefficients below  $-20$  dB, and their radiation patterns are different from that shown in Fig. 4(a). In Fig. 7(a), we have included the simulated realized gain  $G_{realized}$  as a function of  $\theta$  in the  $xz$ -plane as the monopole antenna position is shifted along the  $x$ -axis. The inset shows the angle of each minima (null) in  $G_{realized}$ ,  $\theta_{min}$ , as a function of  $x_m$ . At  $x_m = 0$ , the radiation pattern is symmetric with the null being at  $0^\circ$ . As  $x_m$  increases, the null shifts towards the negative angles, and at  $x_m = 24$  mm, the null reaches  $-90^\circ$ . These results demonstrate the beam-steering capabilities of the antenna with a simple re-positioning of the monopole antenna. Similar study was

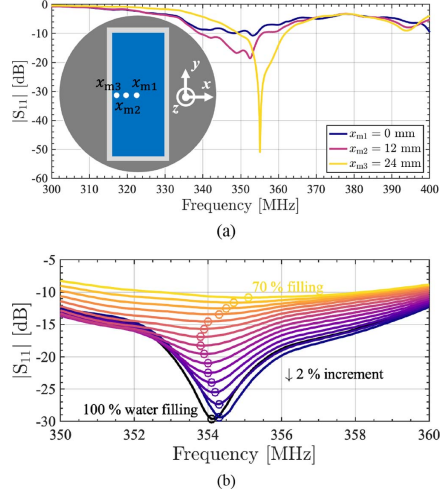
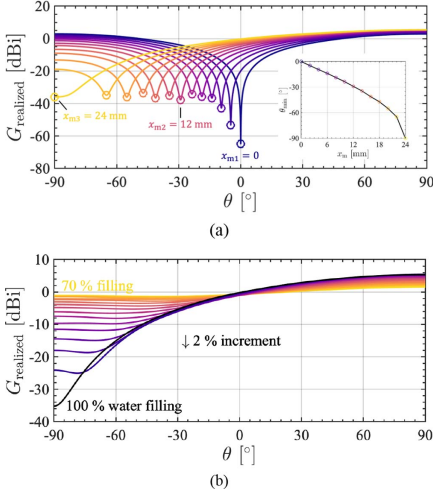


FIGURE 6. Measured  $S_{11}$  in logarithmic scale as a function of frequency for different positions of the monopole antenna ( $x = -x_m$ ) in (a) and for variation of the water content in (b). A sketch of the antenna cross section with the monopole antenna positions is included as an inset in (a). The circles in (b) show the minimum of each graph.

conducted in [3] showing same tendency. Additionally, further beam-steering should be possible by also displacing the monopole antenna in the  $y$ -direction.

Another way to tune the water-based antennas is to simply remove/add water (see, e.g., [4]–[5]). Presently, we stepwise remove 2 % of the water from the cavity, until 70 % water is left, measuring  $S_{11}$  after each water extraction. The result is shown in Fig. 6(b) and an aggravation of  $S_{11}$  is observed as the water content in the cavity is reduced (please note that the measurements in Fig. 6(a) and Fig. 6(b) were carried out at days with different temperatures causing the minor differences in the measured  $S_{11}$ ). A similar study has previously been conducted for another water-based DRA, where a linear blue-shift was observed [5]. However, we do not observe similar tendency for the present design. As the water content is reduced, the radiation in the  $xz$ -plane becomes less directive and more omnidirectional as shown in Fig. 7(b) by  $G_{realized}$  as a function of  $\theta$  in the  $xz$ -plane. The antenna has the response shown in Fig. 6(b) and Fig. 7(b) as long as it is kept in level. If any deviations in angle theta in positioning of the AUT happens, then water no more can be accurately described as a cuboid dielectric. This is quite complicated behavior as the resonance frequency and radiation pattern will change for different theta angles. This can be a subject of further analysis. Seen from another perspective, this presents a great way to, e.g., completely level the antenna or to check if the cavity is 100 % filled. In addition,



**FIGURE 7.** Simulated realized gain ( $G_{\text{realized}}$ ) as a function of  $\theta$  in the  $xz$ -plane for (a) different positions of the monopole antenna ( $x_m$ ) and (b) for variation of the water content. Frequency is 351.6 MHz and  $G_{\text{realized}}$  is shown in logarithmic scale. The circles in (a) show the minima (null) of each graph and their angles,  $\theta_{\text{min}}$ , are plotted as a function of  $x_m$  in the inset.

the antenna should be sensitive to vibrations. We have not made such comprehensive studies this work.

Water’s complex permittivity is temperature-dependent, and it decreases with increasing temperature. This property can also be exploited to tune the response of water-based antennas as well as other types of water-based devices [4]. Presently, we simulate minor variations of water’s temperature, and in Fig. 8,  $S_{11}$ , FBR and  $\eta_{\text{tot}}$  are shown as functions of frequency. As the temperature increases from 10°C to 30°C, the response is blue-shifted by approximately 16 MHz. Furthermore, both  $\eta_{\text{tot}}$  and FBR improve due to the lower losses, whereas the matching, indicated by the minimum of  $S_{11}$ , is optimum around 20 °C. Still, the minimum of  $S_{11}$  stays below  $-20$  dB at all simulated temperatures.

The results in Fig. 6, 7 and 8 demonstrate the antenna’s tunabilities, but it can also be viewed as its sensitivities to fabrication variations and defects as well as changes in the local environment. The antenna has other tunabilities/sensitivities as, e.g., the impurities in the water, which we did not test in this work.

**C. FURTHER DISCUSSIONS**

The antenna’s electrical size is  $k_0a \approx 1.08 (\lambda_0/6)$ , and therefore, not categorized as being electrically small, which requires  $k_0a \leq 0.5$  for ground-supported antennas, see, e.g., [5] and [24]. Still, the antenna is several times smaller than many other DRAs [1], [4], and the modest efficiency

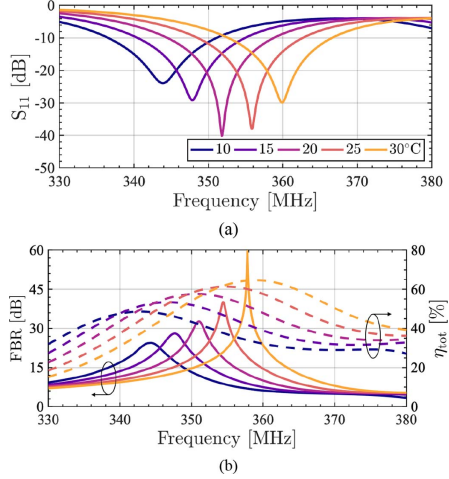


**FIGURE 8.** Simulated temperature variations from 10°C to 30°C. (a)  $S_{11}$  and (b) FBR and  $\eta_{\text{tot}}$  shown as functions of frequency.  $S_{11}$  and FBR are given in logarithmic scale.

is higher than, e.g., a directive subwavelength DRA composed of an expensive low-loss ceramic material [18]. In our case, we have a simple and cheap antenna. Furthermore, the antenna is tunable and self-matched to a 50 Ohm transmission line, and thus, no matching components are needed. The directivity is twice that of traditional single-unit DRAs in which only magnetic or electric modes are excited [1]. Due to the losses in water and the compact design, the efficiency is modest compared to other DRAs.

In Fig. 2, we find a second mode being excited around 385 MHz. The mode is weakly excited, which explains the low efficiency. Inspecting the field distribution and radiation pattern (not shown in the manuscript), we conclude that it is another magnetic mode.

**IV. SUMMARY AND CONCLUSION**

A simple water-based Huygens DRA consisting of a short monopole antenna fed against a large conducting ground plane and encapsulated by a rectangular cuboid-shaped cavity filled with water was investigated. With strongly excited magnetic and electric dipoles, an excellent front-to-back ratio of 40.3 dB was achieved as well as good matching to the feed-line and the surrounding space with a reflection coefficient of  $-38.3$  dB and a total efficiency of 57.8 %. Furthermore, the achieved maximum directivity was 6 in accordance with the expectations. The antenna was fabricated and characterized with the measurements exhibiting

excellent agreement with the numerical results. We demonstrated several ways of tuning the Huygens DRA's response with both numerical and experimental studies.

With its simple and versatile, as well as extremely cheap and bio-friendly design, the Huygens DRA may serve as an alternative antenna for microwave communication systems operating in the VHF and low end of the UHF bands. Additionally, the Rohacell material is not essential for the functionality of the antenna and can therefore be replaced by cheaper and more bio-friendly alternatives to even further minimize the ecological footprint of the device.

#### ACKNOWLEDGMENT

The authors would like to thank the workshop at the Electromagnetic Systems group of the Technical University of Denmark for fabrication of the antennas.

#### REFERENCES

- [1] A. Petosa and A. Ittipiboon, "Dielectric resonator antennas: A historical review and the current state of the art," *IEEE Antenn. Propag. Mag.*, vol. 52, no. 5, pp. 91–116, Oct. 2010.
- [2] W. Ellison, "Permittivity of pure water, at standard atmospheric pressure, over the frequency range 0–25 THz and the temperature range 0–100°C," *J. Phys. Chem. Ref. Data*, vol. 36, pp. 1–18, Feb. 2007.
- [3] S. P. Kingsley and S. G. O'Keefe, "Beam steering and monopulse processing of probe-fed dielectric resonator antennas," *IEE Proc. Radar Sonar Navig.*, vol. 146, no. 3, pp. 121–125, Jun. 1999.
- [4] E. Motovilova and S. Y. Huang, "A review on reconfigurable liquid dielectric antennas," *Materials*, vol. 13, no. 8, p. 1863, Apr. 2020.
- [5] R. E. Jacobsen, A. V. Lavrinenko, and S. Arslanagić, "Electrically small water-based hemispherical dielectric resonator antenna," *Appl. Sci.*, vol. 9, no. 22, pp. 2076–3417, Nov. 2019.
- [6] A. Andryieuski, S. M. Kuznetsova, S. V. Zhukovsky, Y. S. Kivshar, and A. V. Lavrinenko, "Water: Promising opportunities for tunable all-dielectric electromagnetic metamaterials," *Sci. Rep.*, vol. 5, Aug. 2015, Art. No. 13535.
- [7] M. A. Gorlach, M. Song, A. P. Slobozhanyuk, A. A. Bogdanov, and P. Belov, "Topological transition in coated wire medium," *Phys. Status Solidi RRL*, vol. 10, no. 12, pp. 900–904, Oct. 2016.
- [8] X. Yang, D. Zhang, S. Wu, L. Li, K. Cao, and K. Huang, "Reconfigurable all-dielectric metasurface based on tunable chemical systems in aqueous solution," *Sci. Rep.*, vol. 7, p. 3190, Jun. 2017.
- [9] R. E. Jacobsen, A. V. Lavrinenko, and S. Arslanagić, "Water-based metasurfaces for effective switching of microwaves," *IEEE Antennas Wireless Propag. Lett.*, vol. 17, pp. 571–574, 2018.
- [10] Y. J. Yoo *et al.*, "Metamaterial absorber for electromagnetic waves in periodic water droplets," *Sci. Rep.*, vol. 5, Sep. 2015, Art. No. 14018.
- [11] F. Yang *et al.*, "Ultrabroadband metamaterial absorbers based on ionic liquids," *Appl. Phys. A*, vol. 125, no. 2, pp. 1–9, Feb. 2019.
- [12] L. Xing, Y. Huang, Q. Xu, and S. Al Ja'afreh, "Overview of water antenna designs for wireless communications," in *Proc. IEEE 4th Asia-Pac. Conf. Antennas Propag. (APCAP)*, Kuta, Indonesia, 2015, pp. 233–234.
- [13] M. C. Tang, B. Zhou, and R. W. Ziolkowski, "Low-profile, electrically small, Huygens source antenna with pattern-reconfigurability that covers the entire azimuthal plane," *IEEE Trans. Antennas Propag.*, vol. 65, no. 3, pp. 1063–1072, Mar. 2017.
- [14] M. C. Tang, W. Zhentian, T. Shi, and R. W. Ziolkowski, "Dual-band, linearly polarized, electrically small Huygens dipole antennas," *IEEE Trans. Antennas Propag.*, vol. 67, no. 1, pp. 37–47, Jan. 2019.
- [15] R. W. Ziolkowski, "Using Huygens multipole arrays to realize unidirectional needle-like radiation," *Phys. Rev. X*, vol. 7, no. 3, Jul. 2017, Art. no. 031017.
- [16] M. Kerker, D.-S. Wang, and C. L. Giles, "Electromagnetic scattering by magnetic spheres," *J. Opt. Soc. Amer.*, vol. 73, no. 6, pp. 765–767, 1983.
- [17] R. Alaei, R. Filter, D. Lehr, F. Lederer, and C. Rockstuhl, "A generalized Kerker condition for highly directive nanoantennas," *Opt. Lett.*, vol. 40, no. 11, pp. 2645–2648, 2015.
- [18] A. E. Krasnok, D. S. Filonov, C. R. Simovski, Y. S. Kivshar, and P. A. Belov, "Experimental demonstration of superdirective dielectric antenna," *Appl. Phys. Lett.*, vol. 104, no. 13, Mar. 2014, Art. no. 133502.
- [19] M. Decker *et al.*, "High-efficiency dielectric Huygens' surfaces," *Adv. Opt. Mater.*, vol. 3, no. 6, pp. 813–820, Feb. 2015.
- [20] D. Tsarouchis and A. Sihvola, "Light scattering by a dielectric sphere: Perspectives on the Mie resonances," *Appl. Sci.*, vol. 8, no. 2, p. 184, 2018.
- [21] (2018). *COMSOL Multiphysics 5.4*. [Online]. Available: <https://www.comsol.com/>
- [22] C. A. Balanis, *Antenna Theory*, 4th ed. Hoboken, NJ, USA: Wiley, 2016, pp. 60–63.
- [23] A. D. Yaghjian and S. R. Best, "Impedance, bandwidth, and Q of antennas," *IEEE Trans. Antennas Propag.*, vol. 53, no. 4, pp. 1298–1324, Apr. 2005.
- [24] A. Erentok and R. W. Ziolkowski, "Metamaterial-inspired efficient electrically small antennas," *IEEE Trans. Antennas Propag.*, vol. 56, no. 3, pp. 691–707, Mar. 2008.



**RASMUS E. JACOBSEN** (Graduate Student Member, IEEE) received the M.Sc. degree in electrical engineering from the Technical University of Denmark in 2017, where he is currently pursuing the Doctoral degree with Photonics Engineering and Electrical Engineering Departments.

He was a Visiting Scholar with the Advanced Science Research Center, City University of New York, USA, in the winter of 2020. His current research interests include water-based electromagnetic devices such as metamaterials, antennas, and sensors.



**ANDREI V. LAVRINENKO** received the M.S., Ph.D., and D.Sci. degrees from the Belarusian State University (BSU), Minsk, Belarus, in 1982, 1989, and 2004, respectively.

He was an Assistant Professor and an Associate Professor with the Department of Physics, BSU, from 1990 to 2004. Since 2004, he has been an Associate Professor with the Department of Photonics Engineering, Technical University of Denmark, Kongens Lyngby, Denmark, where he has been leading the Metamaterials Group since

2008. He has authored five textbooks, ten book chapters, and more than 190 journal papers. His research interests include metamaterials, plasmonics, photonic crystals, quasicrystals and photonic circuits, slow light, and numerical methods in electromagnetics and photonics.



**SAMELE ARSLANAGIĆ** (Senior Member, IEEE) was born in Sarajevo, Bosnia and Herzegovina, in 1979. He received the M.Sc. and Ph.D. degrees from the Department of Electrical Engineering, Technical University of Denmark (DTU) in 2004 and 2007, respectively.

He was appointed as an Associate Professor in applied electromagnetics with DTU in 2012. He was a Visiting Scholar with the Electromagnetics Laboratory, University of Arizona, USA, in the fall of 2005 and the summer of 2011. He has authored or coauthored more than 30 journal papers, 66 conference papers, four book chapters and three technical reports. His research interests include, in brief, radiation and scattering of electromagnetic waves from complex material structures from radio to optical frequencies, as well as the broad area of electromagnetic education. He received the DTU Student Union's Teacher of the Year Award in 2018 for his teaching in electromagnetics and wireless communication courses.

## APPENDIX F

# Paper 6: “Boundary-induced embedded eigenstate in a single resonator for advanced sensing”

---

Symmetry-protected BIC structure based on a single resonator with advantageous sensing capabilities. The work was initiated during the external stay of the present author at the Advanced Science Research Center, City University of New York, New York. The manuscript has been submitted.

The citations in the manuscript refer to reference list included at the end of the manuscript.

Work contributions by the present author: Numerical calculations, experiments and manuscript drafting.

Reference information:

**R. E. Jacobsen**, A. Krasnok, S. Arslanagić, A. V. Lavrinenko and A. Alú, “Boundary-induced embedded eigenstate in a single resonator for advanced sensing,” *submitted*, Dec. 2020. <https://arxiv.org/abs/2103.03685>

# Boundary-Induced Embedded Eigenstate in a Single Resonator for Advanced Sensing

**AUTHORS:** Rasmus E. Jacobsen<sup>1</sup>, Alex Krasnok<sup>2</sup>, Samel Arslanagić<sup>3</sup>, Andrei V. Lavrinenko<sup>1\*</sup>, and Andrea Alú<sup>2,4\*</sup>

## AFFILIATIONS:

<sup>1</sup>Department of Photonics Engineering, Technical University of Denmark, Bld. 345A, Ørsteds Plads, 2800 Kgs. Lyngby, Denmark (e-mail: [rajac@fotonik.dtu.dk](mailto:rajac@fotonik.dtu.dk), [alav@fotonik.dtu.dk](mailto:alav@fotonik.dtu.dk))

<sup>2</sup>Photonics Initiative, Advanced Science Research Center, City University of New York, New York, NY 10031, USA ([akrasnok@gc.cuny.edu](mailto:akrasnok@gc.cuny.edu), [aalu@gc.cuny.edu](mailto:aalu@gc.cuny.edu))

<sup>3</sup>Department of Electrical Engineering, Technical University of Denmark, Bld. 348, Ørsteds Plads, 2800 Kgs. Lyngby, Denmark (e-mail: [sar@elektro.dtu.dk](mailto:sar@elektro.dtu.dk))

<sup>4</sup>Physics Program, Graduate Center, City University of New York, New York, NY 10016, USA

\*Corresponding author: e-mail: [alav@fotonik.dtu.dk](mailto:alav@fotonik.dtu.dk), [aalu@gc.cuny.edu](mailto:aalu@gc.cuny.edu)

## ABSTRACT

Electromagnetic embedded eigenstates, also known as bound states in the continuum (BICs), hold a great potential for applications in sensing, lasing, enhanced nonlinearities and energy harvesting. However, their demonstrations so far have been limited to large-area periodic arrays of suitably tailored elements, with fundamental restrictions on the overall footprint and performance in presence of inevitable disorder. In this work, we demonstrate a BIC localized in a single subwavelength resonator obtained by suitably tailoring the boundaries around it, enabling a new degree of control for on-demand symmetry breaking. We experimentally demonstrate how boundary-induced BICs open exciting opportunities for sensing by tracing the dissolution of NaCl in water, determining evaporation rates of distilled and saltwater with a resolution of less than 1  $\mu\text{L}$  using a tabletop experimental setup.

## ONE SENTENCE SUMMARY

We realized a localized embedded eigenstate in a single resonator by suitably controlling the boundaries around it, and explored its operation for advanced sensing and tracing of chemical reactions.

## MAIN TEXT

Embedded eigenstates, also known as bound states in the continuum (BICs), have recently become an area of great interest in wave physics. They were predicted in the seminal work by von Neumann and Wigner as a curious eigen-solution of single-particle Schrödinger equation that can reside within the continuum despite being compatible with decay in terms of

momentum (1). Given the mathematical analogies with the wave equation in electrodynamics, optics and linearized acoustics, this phenomenon has been experimentally observed in several wave settings (2). Theoretically speaking, a BIC is a resonant state of an open system that supports an infinite quality factor (Q-factor), despite supporting a momentum compatible with radiation (3). Due to this fascinating property, BICs offer exciting prospectives for various applications, including sensing (4), lasing (5–7), nonreciprocity (8), enhanced thermal emission (9, 10) and energy harvesting (11).

BICs can be classified according to the number of eigenmodes involved in the scattering process (single or multiple) and to the nature of the underlying interference mechanisms (symmetry-enabled or accidental). The simplest example of nonradiative, symmetry-enabled, single-mode BIC in an open system is a hedgehog-like collection of dipoles longitudinally arranged over a sphere or a charged pulsating spherical shell, for which radiation is forbidden due to symmetry (12). This non-radiating current distribution was employed as a first attempt to explain the stability of atoms (13–16). While this idealized model is practically challenging to implement, BICs have been demonstrated in periodic 2D arrays of dipoles that do not radiate due to mutual destructive interference. Accidental single-mode BICs can also be supported by multilayers involving epsilon-near-zero (ENZ) or other extreme material parameters (10, 17–19). Friedrich and Wintgen predicted BICs in systems involving multiple, not orthogonal coupled modes (20). These BICs leverage destructive interference of at least two resonant modes coupled to the same radiation channel, and they can exist in both symmetry-protected and accidental form. This approach has been of great interest in the recent literature, as it enables nonradiative states tailored by variations of the system parameters, e.g., angle of incidence or refractive index, becoming particularly attractive in various photonic crystal setups (2, 21–27).

In this context, the formation of a symmetry-protected BIC at the  $\Gamma$ -point of a periodic array is schematically illustrated in Fig. 1. We first consider an individual resonator, in the form of a metallic cylindrical disk placed over on a conducting ground plane, which resonantly scatters light as a vertical electric dipole (28) around the frequency of interest, Fig 1A. When illuminated by an incident wave, the scattering pattern has a null along the dipole, and the resonant spectrum is characterized by a Q-factor controlled by the power scattered towards all other directions into the radiation continuum. Next, we consider a periodic array of such resonators: choosing a subwavelength periodicity, the scattered power is directed towards the zeroth diffraction order (except at the ends of the array), i.e., a single direction, due to destructive interference among the array elements for all other angles. By aligning this outgoing diffraction channel with the null in the scattering pattern of each resonator, a symmetry-protected BIC emerges at the  $\Gamma$ -point of the first Brillouin zone, i.e., in the direction normal to the array (2, 3, 5, 29). In this scenario, the resonant mode sustains vertical dipoles all with the same amplitude and phase, as sketched in Fig. 1B, which cannot radiate towards the normal. Because of reciprocity, the periodic array cannot be excited by a plane wave at normal incidence, hence forming a nonradiating mode unobservable in the scattering spectra. Coupling to outgoing radiation can be triggered by small broken symmetries along the array, resulting in a sharp Fano line-shape in the radiation spectrum often referred to as a quasi-BIC (27, 30, 31). These phenomena can be observed in large-area arrays, implying large footprints and challenges in ensuring these precise symmetries across large areas. More importantly, these



features are not well suited for sensing: the BIC mode is extended in space, and therefore the asymmetries controlling the coupling to radiation need to be equally extended. For similar reasons, despite the very large Q factors, these BICs do not support large local density of states (LDOS) (17).

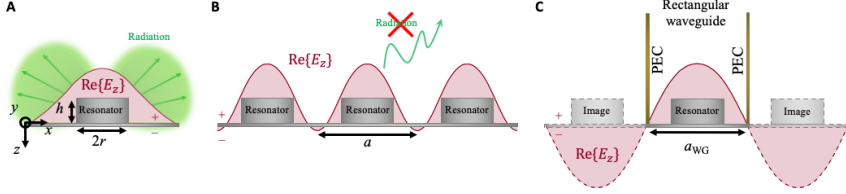


**Fig. 1. Concept of an extended BIC in a periodic array and a boundary-induced localized BIC in a single resonator.** (A) Sketch of a single metallic resonant disk over a ground plane, along with the  $z$ -component of the E-field distribution of its vertical dipole mode. The parameters are  $h = 25$  mm,  $r = 30$  mm,  $f_r \approx 1,940$  MHz. The corresponding Q-factor of the eigenmode is  $\sim 2$ . (B) Periodic array of metallic resonators. An infinite array supports an extended  $\Gamma$ -point BIC when all vertical dipole moments are excited with the same amplitude and phase. This  $\Gamma$ -point BIC turns into a quasi-BIC in the case of a finite structure and/or the presence of asymmetries or material loss. The corresponding near-field distribution is shown in red, and the calculated Q-factor of the eigenmode is  $\sim 21,000$ . The parameters are  $h = 25$  mm,  $r = 30$  mm,  $a = 110$  mm,  $f_r \approx 2,470$  MHz. (C) Single metallic resonator in a rectangular waveguide: even though we use a single resonant element, the structure can support a localized BIC. If the waveguide walls and the metallic resonator are not perfectly conductive, the BIC turns into a quasi-BIC. In our case, the calculated Q-factor of the eigenmode is  $\sim 8,000$ , which can be increased using lower loss materials. The parameters are  $h = 27$  mm,  $r = 18$  mm,  $a_{\text{WG}} = b_{\text{WG}}/2 = 54.61$  mm,  $f_r \approx 1,890$  MHz. All  $E_z(x)$  are taken at 20 mm above the disks' top base. The lines above/below the ground plane correspond to positive/negative real values of  $E_z(x)$ .

The BICs demonstrated to date have been based on these principles, hence they emerge in spatially extended and bulky periodic structures, hindering their implementation and effective use as sensors or other forms of enhanced light-matter interactions. In contrast to these structures, localized BICs in single resonators have been predicted to offer extremely large LDOS, ideal for sensing applications (32, 33). However, to date localized BICs have been leveraging the use of extreme material parameters, making them prone to losses and challenging in their practical implementation. Friedrich-Wintgen supercavity modes in high-index dielectric nanoparticles are intrinsically open to radiation, and therefore they cannot support true BICs even in theory (34).

In this work, we explore a different approach to enable localized BICs. We suitably modify the boundary conditions around a single resonator in order to control the destructive interference between the resonator and its images induced by the tailored boundaries, thus inducing nonradiating resonant modes. In particular, we can place the individual resonant disk at a suitable location within two lateral metallic walls, Fig. 1C. The resonator, excited by the fundamental  $\text{TE}_{10}$  mode of the resulting waveguide, interacts with its images created by the lateral walls, assuming that they are good conductors. The result is an effectively 2D periodic

array with alternating field signs, as sketched in Fig. 1C and further analyzed in Fig. S1-S3. This opens the opportunity to induce a localized BIC, controlled by the resonator geometry and the distance between the lateral walls, confining the extended BIC in the periodic array of Fig. 1B into a single resonant element. A tailored asymmetry introduced in our resonator is automatically extended to the image array, offering a powerful tool to tailor the Q-factor at will, as envisioned in (27), but without having to control an extended broken symmetry across the entire array.

We control the asymmetry in our structure by introducing a tiny water droplet placed atop the metallic resonator, leveraging the high permittivity of water at microwaves to trigger non-negligible perturbations in the local fields (36–38). Different from the case of extended BICs, here the LDOS in the resonator is largely enhanced at the BIC condition, with a controllable Q-factor that enables sensing of deeply subwavelength variations to the water volume, as well as small changes in its refractive index. Remarkably, as we show in the following, we can use this platform to trace in real time the occurrence of chemical reactions, e.g., the dissolution of NaCl in water. Similarly, we can determine the evaporation rates of distilled and salt water with a resolution of less than 1  $\mu\text{L}$ .

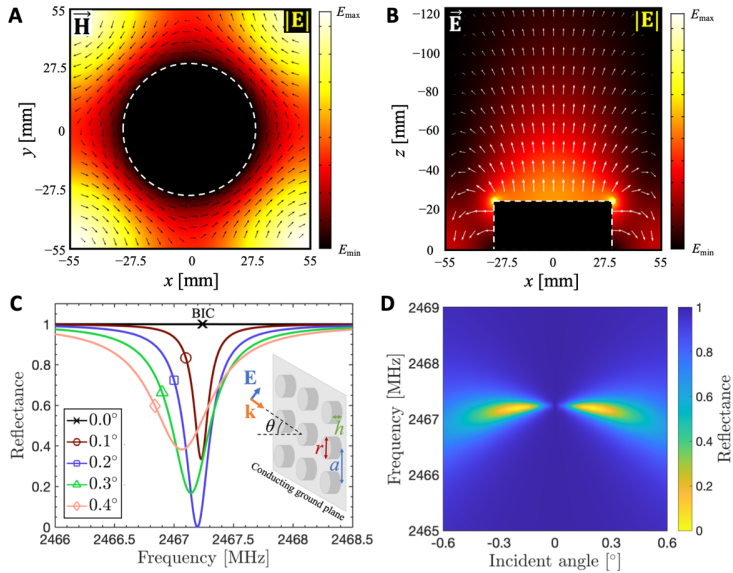


**Fig. 2. Symmetry-protected extended BIC in a periodic array.** (A) and (B) Magnitude of the total E-field [V/m] (colorbars) of the eigenmode in the  $xy$ - and  $yz$ -plane. (C) and (D) Numerically calculated reflectance spectra for different incident angles. The black and white arrows show the instantaneous magnetic and electric fields, respectively, both in a logarithmic scale. The geometric parameters are  $r = 30$  mm,  $h = 25$  mm and  $a = 110$  mm, and the intrinsic metal conductivity is  $\sigma = 5.8 \times 10^7$  S/m corresponding to that of copper. The calculated real eigenfrequency is 2,467 MHz, and the Q-factor using realistic metal loss is 21,000.

### Symmetry-protected extended BIC

In order to outline the physical mechanisms supporting our boundary-induced localized BIC, in Fig. 2 we first numerically analyze the conventional extended BIC supported by a periodic array of resonant metallic disks backed by a conducting ground plane, as in Fig. 1B (for details of our analysis, see *Supplementary Materials*). For the chosen geometrical parameters, an eigenmode analysis of the array predicts an extended BIC arising at the frequency of 2,467 MHz, with an unbounded Q-factor in the ideal scenario of perfect electric conductors (PEC). Considering a realistic metal conductivity, the calculated resonance Q-factor is 21,000. Figs. 2 A and B show the magnitude of the E-field distribution of the corresponding eigenmode in the cross-sections of one of the resonators. The disk supports a high-intensity electric field on its top side, decaying away from the disk. The circulating magnetic field and vertical electric field distributions, plotted as white and black arrows in Fig. 2, A and B, respectively, confirm that the resonance is dominated by a vertical electric dipole component. Standing wave patterns arise in the  $xy$ -plane due to the coupling with neighboring resonators.

By illuminating the array with a  $p$ -polarized (i.e., parallel to the plane of incidence) plane wave at different incident angles  $\theta$ , the reflection spectra (Fig. 2, C and D) showcase the emergence of a BIC. At any incident angle other than  $0^\circ$ , the incident wave strongly couples to the array resonance, inducing an absorption dip. For normal incidence, the wave is fully reflected and cannot couple to the resonant dip. With the considered level of metal loss, critical coupling and full absorption is achieved at  $0.2^\circ$ , for which the radiated power from the dipoles equals the absorbed power in the metal. At larger (smaller) incident angles, the array is over (under) coupled. Approaching normal incidence, the resonant linewidth gets narrower and narrower, until it vanishes because of symmetry at  $0^\circ$ , when the resonant mode becomes a BIC and cannot be excited by the incoming wave.

### Symmetry breaking

By adding a tailored asymmetry in the array, we can control the coupling of this nonradiating mode to normally incident waves. We achieve symmetry breaking by adding a drop of distilled water [permittivity model taken from (39)] on the top side of each metallic resonator. The drops are modeled as hemi-spherical particles with radius  $r_w$ , and their center is displaced from the disk center by  $(x, y) = (d_w, 0)$ . By varying the drop size and position in each array element, we can control the coupling to a normally incident  $x$ -polarized plane wave, as shown in Fig. 3. In Fig. 3A, we fix the drop position, so that there is a gap of 1 mm between the drop and the resonator boundaries ( $d_w = r - r_w - 1$  mm). We observe no change in reflection for  $r_w = 2$  mm, due to the finite spectral resolution of our simulations. As more water is added, a narrow reduction in reflection can be observed, and critical coupling is reached with  $r_w = 4.8$  mm (96.5  $\mu$ L). A further increase in drop size results in a significant broadening of the reflection spectrum due to over-coupling. In the under-coupled regime, the resonance frequency is red-shifted as more water is added. Furthermore, the losses in water reduce the Q-factor from 21,000 (no water) to 4,300 for a drop size  $r_w = 4.8$  mm.

In Fig. 3B we study variations in the drop position, where the drop size is fixed at  $r_w = 4.8$  mm. When  $d_w = 0$ , the configuration is symmetric, and therefore the BIC is preserved. As the drop moves away from the center of the metallic disk, the incident wave couples to the array, and at  $d_w = 24.2$  mm, the coupling is critical. As the drop approaches the edge of the resonator,

the proximity effects cause the resonance frequency to change from blue-shifted to red-shifted. In Fig. 3C and D, the magnitude of the total E-field in the  $xy$ - and  $xz$ -planes are shown for a drop with  $r_w = 4.8$  mm and  $d_w = 24.2$  mm. The similarities between the field distributions in Fig. 2 and Fig. 3 confirm that the BIC mode is only slightly perturbed by adding water, and it can be excited despite the excitation at normal incidence due to the broken symmetry.

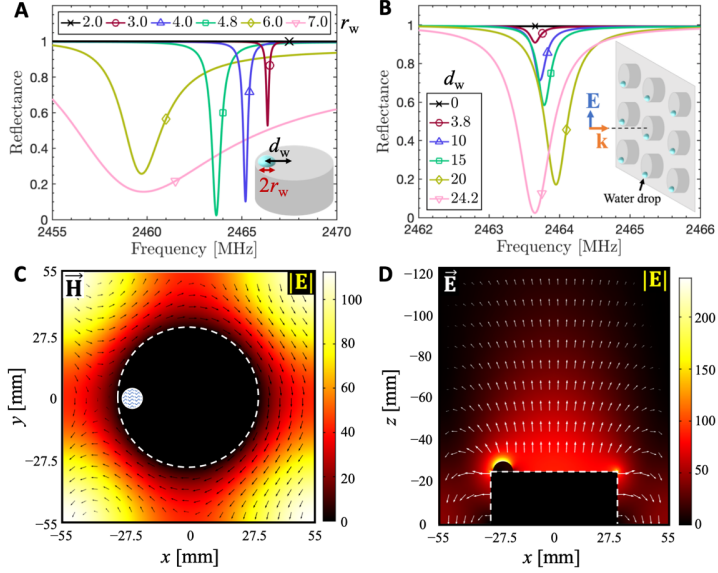


**Fig. 3. Symmetry breaking in an extended BIC.** (A) Numerically calculated reflectance spectra for different water drop sizes with  $d_w = r - r_w - 1$  mm (legend shows the hemisphere radius in mm). (B) Reflectance spectrum for different water drop positions. The drop radius is  $r_w = 4.8$  mm (legend shows the displacement  $d_w$  in mm). (C) and (D) Magnitude of the total E-field [V/m] (colorbars) in the  $xy$ - and  $xz$ -plane for a plane wave at normal incidence with  $r_w = 4.8$  mm and  $d_w = 24.2$  mm. Black and white arrows show the instantaneous magnetic and electric fields, respectively, both in logarithmic scale. The Q-factor is 4,300 for water drops with  $r_w = 4.8$  mm and  $d_w = 24.2$  mm. The water temperature is 20 °C in all simulations.

### Boundary-induced localized BIC

The results in Fig. 3 show how it is possible to couple an extended BIC mode to a normally incident plane wave by introducing an array of symmetry-breaking defects in each element. Arguably this is practically challenging, and not amenable to a sensing platform, in which the sensor is typically localized. We overcome this challenge by considering a boundary-induced localized BIC, as introduced in Fig. 1C, confined into a single resonator placed in a rectangular metallic WR-430 waveguide. Our design dimensions are adapted to the WR-430 waveguide, with  $r = 18$  mm and  $h = 27$  mm, corresponding to a BIC eigenfrequency around 1,880 MHz according to a numerical eigenmode analysis (Fig. S4). A photograph of the resonator inserted

in the waveguide section is shown in Fig. 4A. Both the resonator and ground plane are made of aluminum, and a small water container consisting of a cylindrical shell of Rohacell 51 HF is glued on the resonator. The low permittivity of Rohacell, measured in-house to be 1.075 (36), has a negligible effect on the response. Fig. 4B shows photographs of the resonator with different water amounts. The reflection coefficient is measured with a vector network analyzer (VNA), and the full experimental setup is sketched in Fig. 4C.

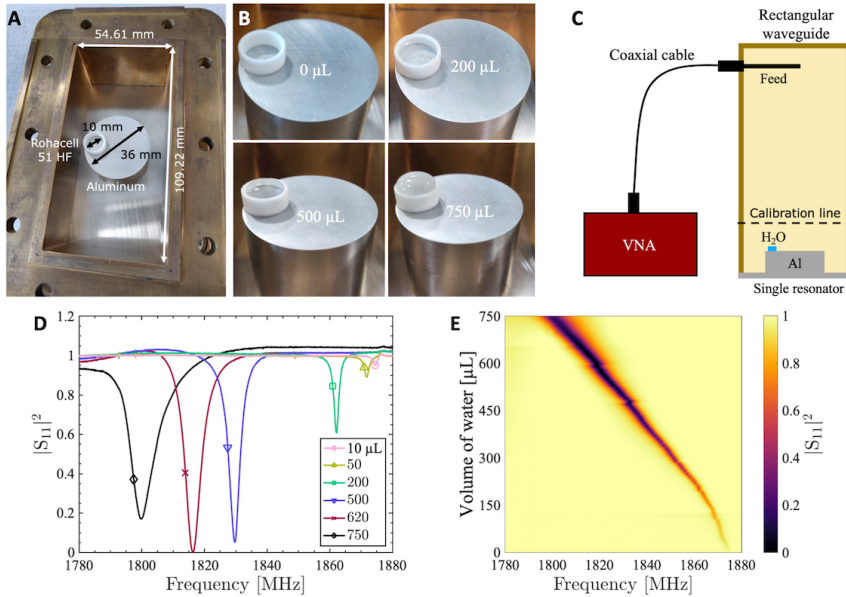


**Fig. 4. Localized BIC in a metallic waveguide.** (A) Photograph of a single disk resonator inserted in a WR-430 waveguide section. (B) Photographs of the resonator with different water fillings. (C) Sketch of the experimental setup. (D) Normalized reflection coefficient as a function of frequency and water volume. The water temperature is 24 °C. (E) Evolution of the quasi-BIC resonance evolving towards the BIC at ~1,880 MHz as water evaporates from the system (see Fig. S5C for the reflection phase).

The addition of a single water droplet in our localized boundary-induced BIC enables controlled symmetry breaking, hence leading to an efficient way to control the coupling of the BIC mode to the continuum of propagating modes in the waveguide. The results summarized in Fig. 4D show the frequency dependence of the measured reflection coefficient for different water volumes. The results have been normalized to the spectra of the resonator without water (for details, see *Supplementary Materials*, Fig. S5A). No resonance is excited with 0  $\mu\text{L}$  water, since the system supports a nonradiating localized BIC, whereas with 10  $\mu\text{L}$  the mode evolves to a quasi-BIC arising in the measured spectrum around 1,875 MHz. Adding more water increases the intensity of the resonance and shifts it towards lower frequencies. From 10 to 610  $\mu\text{L}$ , we are in the under-coupled regime, and at 620  $\mu\text{L}$  we hit critical coupling, for which the

reflection coefficient is reduced to near-zero. Above 620  $\mu\text{L}$ , the resonator is over-coupled and we observe an increase in reflection and resonance broadening. The frequency shift is directly proportional to the water volume from around 200  $\mu\text{L}$ . Below 200  $\mu\text{L}$ , the water is not evenly distributed in the Rohacell container due to surface tension, and therefore its volume shape changes as more water is added.

The system is ideally suited to observe in real time water evaporation from the system: Fig. 4E demonstrates how the quasi-BIC evolves towards the localized BIC as water is removed. The Q-factor as a function of water volume (see Fig. S5E) displays a steady growth as the water volume is reduced, due to the system approaching the BIC and the reduced water losses. At 10  $\mu\text{L}$ , the Q-factor is  $\sim 1,500$ , but at the critical coupling regime (620  $\mu\text{L}$ ), the Q-factor decreases to 250.

### Sensing chemical reactions with a localized BIC

Our results reveal that the resonance frequency linearly decreases with the water volume as  $\sim 0.1124$  MHz/ $\mu\text{L}$  starting from 200  $\mu\text{L}$ , Fig. 4E (see also Fig. S5B – D), allowing a precise determination of volume changes as low as 1  $\mu\text{L}$ . We can use this tool to estimate the evaporation rates of distilled water and a NaCl solution, as shown in Fig. 5. Since the Rohacell container is open, water evaporates over time, causing a shift in resonance frequency ( $\Delta f_{\min}$ ) and of the reflection minimum,  $(|S_{11}|^2)_{\min}$ . Figs. 5, A and B, demonstrate the dependence of  $|S_{11}|^2_{\min}$  and  $\Delta f_{\min}$  in function of time. From the curve slopes, we can carefully estimate the evaporation rate, and the estimated evaporated water volume as a function of time, shown in Fig. 5C.

We can also exploit the localized BIC to monitor in real time the effect of salination in water. The addition of a salt crystal triggers a rapid change in the response (see Fig. 5, A and B, period I). The NaCl density is lower when dissolved in water, thus the volume expands and we observe a red-shift in the resonance frequency. Hereafter (period II), the resonance frequency is blue-shifted as  $\text{Na}^+$  and  $\text{Cl}^-$  ions are dispersed in water (hydration), effectively increasing the solution density. Furthermore, the conductivity increases, thus increasing the reflection. After 20 minutes, the NaCl is fully dissolved (period III), and the slope is stabilized, such that we can estimate the evaporation rate.

The estimated evaporation rate is 213 nL/min for distilled water, whereas, for a 7.1 ppt NaCl solution, it is 201 nL/min, Fig. 5C, confirming that salt water evaporates more slowly than distilled water, since water molecules are attracted to the dissolved salt ions, and more energy is thus required to break them apart. We experimented with different sizes of NaCl crystals, Fig. 5D (see Fig. S6 for the frequency shift). Larger NaCl crystals change the response faster due to their size, but it also takes longer time to dissolve them, as seen by the slope changes. Even a small NaCl crystal of 0.3 mg ( $\approx 0.6$  ppt in 500  $\mu\text{L}$  water) can be clearly measured. Such a small change in salinity corresponds to an increase in the loss tangent of approximately 0.0066 [7.7 %, (40)].

There are several processes during the reaction that cause changes in volume and permittivity. A temperature shift changes both, as studied in Fig. S7 by simply heating the water before insertion. A temperature increase causes a decrease in density (i.e., larger volume) and permittivity, and therefore a red-shift and a blue-shift in frequency, respectively. In

experiments, the frequency is blue-shifted, revealing that the volume change is the governing factor. This is interesting to observe, since only permittivity changes are typically considered in water-based structures (37),(41). In Fig. 5, E and F, we have isolated the permittivity change due to a variation in salinity by measuring NaCl solutions of equal volume of 500  $\mu\text{L}$ . The reflectance (resonance frequency) increases (decreases) with increasing salinity due to the higher conductivity in the solution. The higher conductivity reduces the field penetration in the solution, and thus less power is absorbed. We measure changes with concentrations as low as 0.2 ppt ( $\approx 0.1$  mg in 500  $\mu\text{L}$  water), and from 0 to 5 ppt the change in response is linear with good approximation.

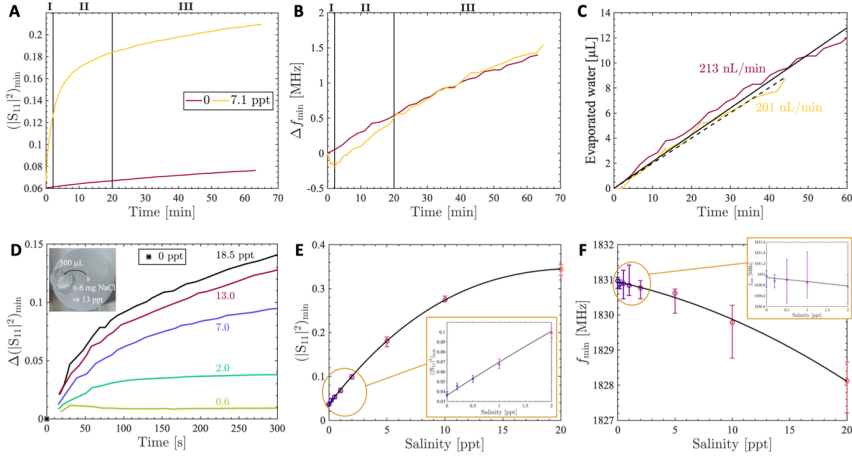


**Figure 5. Sensing and chemical reaction tracing with localized BIC.** (A), (B) and (C)  $|S_{11}|^2_{\min}$ ,  $\Delta f_{\min}$ , and estimated evaporated water volume, respectively, as a function of time. Time 0 designates the point of the first measurement in (A) and (B), whereas it designates the point of full dissolution of NaCl in water in (C). The black solid and dashed lines in (C) are the tendency lines of 0 ppt and 7.1 ppt solutions, respectively. (D) Chemical reaction of single NaCl crystals added to 500  $\mu\text{L}$  of water. (E) and (F) show the response of 500  $\mu\text{L}$  NaCl solutions with different salinities. (D) Change in the reflectance minimum  $\Delta(|S_{11}|^2)_{\min}$  as a function of time since NaCl was added. The concentration values specify the NaCl solution after full dissolution. (E) Reflectance  $(|S_{11}|^2)_{\min}$  and (F) frequency as a function of salinity for 500  $\mu\text{L}$  NaCl solutions. The solid black lines show the fitting. The insets show the magnified plot in the range from 0 to 2 ppt.

## Discussion

In this work, we have shown how the possibility of inducing a highly controllable localized BIC in a compact resonant structure by suitably tailoring the boundary conditions around it. Based on this concept, we have realized controllable on-demand symmetry breaking for advanced sensing. Specifically, we have exploited the natural attributes of rectangular waveguides to generate a single-resonator BIC whose coupling to the continuum of propagating modes in the waveguide can be controlled by a tiny drop of water. This approach

overcomes the need for extreme materials or large-area geometries to induce BIC phenomena. Based on this platform, we have demonstrated the feasibility of the proposed system for sensing and to trace chemical reactions in real time by monitoring dissolution of NaCl in water and determining evaporation rates of distilled and salt water with a resolution of less than 1  $\mu\text{L}$ . Although in our prototype design water was manually inserted with a pipette, the system can easily be extended to introduce a control system to manage the water insertion. Similar principles can be applied to more advanced microfluidic sensing platforms. In our design, the Q-factor of our BIC is limited by material losses, which can be reduced in different ways, including the use of better conducting materials and/or lower temperatures, further enhancing the overall sensitivity. Besides sensing, boundary-induced localized BICs can find applications in classical and quantum nanophotonic settings. For instance, the demonstrated enhanced sensitivity can be directly translated into enhanced light-matter interactions, offering a unique platform for drastically enhanced nonlinearities. In the context of qubits, these localized resonances may enable much enhanced quantum coherence times (42, 43).

## REFERENCES AND NOTES

1. J. von Neumann, E. P. Wigner, in *The Collected Works of Eugene Paul Wigner* (Springer Berlin Heidelberg, Berlin, Heidelberg, Heidelberg, 1993), pp. 291–293.
2. C. W. Hsu, B. Zhen, A. D. Stone, J. D. Joannopoulos, M. Soljacic, Bound states in the continuum. *Nat. Rev. Mater.* **1**, 16048 (2016).
3. A. Krasnok, D. Baranov, H. Li, M.-A. Miri, F. Monticone, A. Alú, Anomalies in light scattering. *Adv. Opt. Photonics.* **11**, 892 (2019).
4. F. Yesilkoy, E. R. Arvelo, Y. Jahani, M. Liu, A. Tittl, V. Cevher, Y. Kivshar, H. Altug, Ultrasensitive hyperspectral imaging and biodetection enabled by dielectric metasurfaces. *Nat. Photonics.* **13**, 390–396 (2019).
5. A. Kodigala, T. Lepetit, Q. Gu, B. Bahari, Y. Fainman, B. Kanté, Lasing action from photonic bound states in continuum. *Nature.* **541**, 196–199 (2017).
6. C. Huang, C. Zhang, S. Xiao, Y. Wang, Y. Fan, Y. Liu, N. Zhang, G. Qu, H. Ji, J. Han, L. Ge, Y. Kivshar, Q. Song, Ultrafast control of vortex microlasers. **1021**, 1018–1021 (2020).
7. S. T. Ha, Y. H. Fu, N. K. Emani, Z. Pan, R. M. Bakker, R. Paniagua-Domínguez, A. I. Kuznetsov, Directional lasing in resonant semiconductor nanoantenna arrays. *Nat. Nanotechnol.* **13**, 1042–1047 (2018).
8. M. Cotrufo, A. Alù, Excitation of single-photon embedded eigenstates in coupled cavity–atom systems. *Optica.* **6**, 799 (2019).
9. R. Duggan, Y. Ra’di, A. Alù, Temporally and Spatially Coherent Emission from Thermal Embedded Eigenstates. *ACS Photonics.* **6**, 2949–2956 (2019).
10. Z. Sakotic, A. Krasnok, N. Cselyuszka, N. Jankovic, A. Alú, Berreman Embedded Eigenstates for Narrow-Band Absorption and Thermal Emission. *Phys. Rev. Appl.* **13**, 064073 (2020).
11. Y. Ra’di, A. Krasnok, A. Alù, Virtual Critical Coupling. *ACS Photonics.* **7**, 1468–1475 (2020).
12. G. Gbur, Nonradiating sources and other invisible objects. *Prog. Opt.* **45**, 273 (2003).
13. A. Sommerfeld, Zur Elektronentheorie. I. Allgemeine Untersuchung des Feldes eines beliebig bewegten Elektrons. *Nachr. Akad. Wiss. Göttingen, Math.-Phys. Klasse*, 99–130 (1904).
14. A. Sommerfeld, Zur Elektronentheorie. II. Grundlagen für eine allgemeine Dynamik des Elektrons. *Nachr. Akad. Wiss. Göttingen, Math.-Phys. Klasse*, 363–439 (1904).



15. P. Ehrenfest, Ungleichförmige Elektrizitätsbewegungen ohne Magnet- und Strahlungsfeld. *Phys. Zeitschrift*. **11**, 708–709 (1910).
16. G. A. Schott, The electromagnetic field of a moving uniformly and rigidly electrified sphere and its radiationless orbits. *London, Edinburgh, Dublin Philos. Mag. J. Sci.* **15**, 752–761 (1933).
17. F. Monticone, H. M. Doleman, W. Den Hollander, A. F. Koenderink, A. Al, W. Den Hollander, A. F. Koenderink, A. Alù, Trapping Light in Plain Sight: Embedded Photonic Eigenstates in Zero-Index Metamaterials. *Laser Photon. Rev.* **12**, 1700220 (2018).
18. A. Krasnok, A. Alù, Embedded scattering eigenstates using resonant metasurfaces. *J. Opt.* **20**, 064002 (2018).
19. L. Vertchenko, R. Malureanu, C. DeVault, E. Mazur, A. V. Lavrinenko, in *Conference on Lasers and Electro-Optics* (OSA, Washington, D.C., 2020; [https://www.osapublishing.org/abstract.cfm?URI=CLEO\\_SI-2020-SM1J.2](https://www.osapublishing.org/abstract.cfm?URI=CLEO_SI-2020-SM1J.2)), p. SM1J.2.
20. H. Friedrich, D. Wintgen, Physical realization of bound states in the continuum. *Phys. Rev. A*. **31**, 3964–3966 (1985).
21. C. W. Hsu, B. Zhen, J. Lee, S.-L. Chua, S. G. Johnson, J. D. Joannopoulos, M. Soljačić, Observation of trapped light within the radiation continuum. *Nature*. **499**, 188–191 (2013).
22. B. Zhen, C. W. Hsu, L. Lu, A. D. Stone, M. Soljačić, Topological Nature of Optical Bound States in the Continuum. *Phys. Rev. Lett.* **113**, 257401 (2014).
23. S. I. Azzam, V. M. Shalaev, A. Boltasseva, A. V. Kildishev, Formation of Bound States in the Continuum in Hybrid Plasmonic-Photonic Systems. *Phys. Rev. Lett.* **121**, 1–5 (2018).
24. J. Lee, B. Zhen, S. L. Chua, W. Qiu, J. D. Joannopoulos, M. Soljačić, O. Shapira, Observation and differentiation of unique high-Q optical resonances near zero wave vector in macroscopic photonic crystal slabs. *Phys. Rev. Lett.* **109**, 067401 (2012).
25. H. M. Doleman, F. Monticone, W. Den Hollander, A. Alù, A. F. Koenderink, Experimental observation of a polarization vortex at an optical bound state in the continuum. *Nat. Photonics*. **12**, 397–401 (2018).
26. A. I. Ovcharenko, C. Blanchard, J.-P. Hugonin, C. Sauvan, Bound states in the continuum in symmetric and asymmetric photonic crystal slabs. *Phys. Rev. B*. **101**, 155303 (2020).
27. K. Koshelev, S. Lepeshov, M. Liu, A. Bogdanov, Y. Kivshar, Asymmetric Metasurfaces with High-Q Resonances Governed by Bound States in the Continuum. *Phys. Rev. Lett.* **121**, 193903 (2018).
28. C. A. Balanis, *Antenna theory: analysis and design* (New York ; Brisbane : J. Wiley, 1997).
29. S. Murai, D. R. Abujetas, G. W. Castellanos, J. A. Sánchez-Gil, F. Zhang, J. G. Rivas, Bound States in the Continuum in the Visible Emerging from out-of-Plane Magnetic Dipoles. *ACS Photonics* (2020), doi:10.1021/acsp Photonics.0c00723.
30. E. N. Bulgakov, A. F. Sadreev, Bound states in the continuum in photonic waveguides inspired by defects. *Phys. Rev. B*. **78**, 075105 (2008).
31. Z. Liu, Y. Xu, Y. Lin, J. Xiang, T. Feng, Q. Cao, J. Li, S. Lan, J. Liu, High-Q Quasibound States in the Continuum for Nonlinear Metasurfaces. *Phys. Rev. Lett.* **123**, 253901 (2019).
32. F. Monticone, A. Alù, Embedded Photonic Eigenvalues in 3D Nanostructures. *Phys. Rev. Lett.* **112**, 213903 (2014).
33. S. Lannebère, M. G. Silveirinha, Optical meta-atom for localization of light with

- quantized energy. *Nat. Commun.* **6**, 8766 (2015).
34. M. V. Rybin, K. L. Koshelev, Z. F. Sadrieva, K. B. Samusev, A. A. Bogdanov, M. F. Limonov, Y. S. Kivshar, High-Q Supercavity Modes in Subwavelength Dielectric Resonators. *Phys. Rev. Lett.* **119**, 243901 (2017).
  35. A. M. Nicolson, G. F. Ross, Measurement of the Intrinsic Properties Of Materials by Time-Domain Techniques. *IEEE Trans. Instrum. Meas.* **19**, 377–382 (1970).
  36. R. E. Jacobsen, A. V Lavrinenko, S. Arslanagic, Water-Based Metasurfaces for Effective Switching of Microwaves. *IEEE Antennas Wirel. Propag. Lett.* **17**, 571–574 (2018).
  37. A. Andryieuski, S. M. Kuznetsova, S. V Zhukovsky, Y. S. Kivshar, A. V Lavrinenko, *Sci. Rep.*, in press, doi:10.1038/srep13535.
  38. M. V Rybin, D. S. Filonov, K. B. Samusev, P. A. Belov, Y. S. Kivshar, M. F. Limonov, Phase diagram for the transition from photonic crystals to dielectric metamaterials. *Nat. Commun.* **6**, 10102 (2015).
  39. W. J. Ellison, Permittivity of Pure Water, at Standard Atmospheric Pressure, over the Frequency Range 0–25THz and the Temperature Range 0–100°C. *J. Phys. Chem. Ref. Data.* **36**, 1–18 (2007).
  40. A. Stogryn, Equations for Calculating the Dielectric Constant of Saline Water (Correspondence). *IEEE Trans. Microw. Theory Tech.* **19**, 733–736 (1971).
  41. R. E. Jacobsen, A. V Lavrinenko, S. Arslanagic, A Water-Based Huygens Dielectric Resonator Antenna. *IEEE Open J. Antennas Propag.* **1**, 493–499 (2020).
  42. M. Reagor, W. Pfaff, C. Axline, R. W. Heeres, N. Ofek, K. Sliwa, E. Holland, C. Wang, J. Blumoff, K. Chou, M. J. Hatridge, L. Frunzio, M. H. Devoret, L. Jiang, R. J. Schoelkopf, Quantum memory with millisecond coherence in circuit QED. *Phys. Rev. B.* **94**, 014506 (2016).
  43. A. Blais, S. M. Girvin, W. D. Oliver, Quantum information processing and quantum optics with circuit quantum electrodynamics. *Nat. Phys.* **16**, 247–256 (2020).

## ACKNOWLEDGEMENTS

The authors would like to thank the workshop at the Electromagnetic Systems group of the Technical University of Denmark for the fabrication of water-metal resonator elements for the experimental characterization.

**Funding:** This work was supported in part by the Simons Foundation and the Department of Defense.

**Authors contributions:** REJ, AK, AA conceived the idea. REJ designed the structure and carried out numerical and experimental work. REJ, AK, AA wrote the draft of the manuscript, which after several iterations, inputs and discussions of results with all authors, resulted in its final version.

**Competing interests:** The authors declare no competing interests.

**Data and materials availability:** All data are reported in the main paper and supplementary materials. Codes for the processing of data are given upon request.

## LIST OF SUPPLEMENTARY MATERIALS

Materials and Methods

Fig. S1–S10

# Supplementary Materials to “Boundary-Induced Embedded Eigenstate in a Single Resonator for Advanced Sensing”

**AUTHORS:** Rasmus E. Jacobsen<sup>1</sup>, Alex Krasnok<sup>2</sup>, Samel Arslanagić<sup>3</sup>, Andrei V. Lavrinenko<sup>1\*</sup>,  
and Andrea Alú<sup>2,4\*</sup>

## **AFFILIATIONS:**

<sup>1</sup>Department of Photonics Engineering, Technical University of Denmark, Bld. 345A, Ørstedes Plads, 2800 Kgs. Lyngby, Denmark (e-mail: [rajac@fotonik.dtu.dk](mailto:rajac@fotonik.dtu.dk), [alav@fotonik.dtu.dk](mailto:alav@fotonik.dtu.dk))

<sup>2</sup>Photonics Initiative, Advanced Science Research Center, City University of New York, New York, NY 10031, USA ([akrasnok@gc.cuny.edu](mailto:akrasnok@gc.cuny.edu), [aalu@gc.cuny.edu](mailto:aalu@gc.cuny.edu))

<sup>3</sup>Department of Electrical Engineering, Technical University of Denmark, Bld. 348, Ørstedes Plads, 2800 Kgs. Lyngby, Denmark (e-mail: [sar@elektro.dtu.dk](mailto:sar@elektro.dtu.dk))

<sup>4</sup>Physics Program, Graduate Center, City University of New York, New York, NY 10016, USA

\*Corresponding author: e-mail: [alav@fotonik.dtu.dk](mailto:alav@fotonik.dtu.dk), [aalu@gc.cuny.edu](mailto:aalu@gc.cuny.edu)

## **This PDF file includes:**

Materials and Methods  
Supplementary Text  
Figs. S1 to S10

## **Materials and Methods**

### Simulations

COMSOL Multiphysics 5.5 was used for all numerical simulations. The Electromagnetic Waves, Frequency Domain physics, was used with the Frequency Domain and Eigenfrequency studies. The permittivity model for water was implemented (see equations in the next section). Impedance boundary conditions with finite intrinsic conductivity were applied on the metallic surfaces. The magnitude of the incidence wave is 1 V/m in all simulations. Two models were used (sketches are shown in Fig. S10):

1. **2-D array:** Periodic boundary conditions were applied to emulate the infinite extent of the array. A periodic port backed with PML and plane wave excitation was used to retrieve the  $S_{11}$  scattering parameter. Intrinsic conductivity of  $5.8 \times 10^7$  S/m (corresponding to copper) were applied on the metallic surfaces.
2. **Single resonator in WR-430 rectangular waveguide:** Perfect electric conductors (PECs) were applied on the metallic walls of the waveguide. A rectangular port backed with Perfect Matched Layers (PML) and  $TE_{10}$  excitation was used to retrieve the  $S_{11}$  scattering parameter. Intrinsic

conductivity of  $3.8 \times 10^7$  S/m (corresponding to aluminum) were applied on the metallic surfaces of the resonator and conducting ground plane. Permittivity of 1.075 is applied for the Rohacell 51 HF material.

#### Permittivity model for water

The permittivity for distilled water was calculated using the following equations. The relative permittivity as a function of temperature  $T_w$  [°C] and angular frequency  $\omega$  [rad/s] is (39)

$$\varepsilon_{r,w}(\omega, T_w) = \varepsilon'_{r,w} - j\varepsilon''_{r,w} = \varepsilon_{\infty}(T_w) + \frac{\varepsilon_s(T) - \varepsilon_{\infty}(T_w)}{1 - j\omega\tau(T_w)} \quad (1)$$

with  $\varepsilon_s(T_w) = a_1 - b_1 T_w + c_1 T_w^2 - d_1 T_w^3$  and  $\varepsilon_{\infty}(T_w) = \varepsilon_s(T_w) - a_2 \exp(-b_2 T_w)$  being the optical and static permittivities, respectively.  $\tau(T_w) = \tau_0 \exp[T_1/(T_w - T_0)]$  is the rotational relaxation time. The values for the constants are  $a_1 = 87.9$ ,  $b_1 = 0.404 \text{ K}^{-1}$ ,  $c_1 = 9.59 \times 10^{-4} \text{ K}^{-2}$ ,  $d_1 = 1.33 \times 10^{-6} \text{ K}^{-3}$ ,  $a_2 = 80.7$ ,  $b_2 = 4.42 \times 10^{-3} \text{ K}^{-1}$ ,  $\tau_0 = 0.137 \text{ ps}$ ,  $T_1 = 651 \text{ °C}$  and  $T_0 = 133 \text{ °C}$ .

#### Experiment with a single resonator in the rectangular waveguide

The resonator was fabricated at the local workshop and is made of an aluminum cylinder mounted on an aluminum plate with screws on the back. Holes were drilled on the aluminum plate for the attachment to the rectangular waveguide. The water container was made by drilling a hole in a small cylindrical Rohacell 51 HF block, which was then glued on the aluminum cylinder with glue.

The standard WR-430 rectangular waveguide is made of brass and has a cross-section of  $109.22 \times 54.61 \text{ mm}^2$ . A WR-430 flange waveguide to coax adapter was attached to it, which was connected to Anritsu MS2024B Vector Network Analyzer (VNA) with a 1 m RG58 50 Ohm coaxial cable. The VNA was calibrated for  $S_{11,\text{VNA}}$  magnitude response using a short (brass plate). To retrieve the phase change as well as to remove the oscillations caused by the Fabry–Pérot interferometer effects, we defined the scattering parameter as  $S_{11} = S_{11,\text{VNA}}(V_{\text{water}}) / S_{11,\text{VNA}}(0 \text{ }\mu\text{L})$ , where  $V_{\text{water}}$  is the volume of water. See Fig. 4C for sketch of the experimental setup.

Local distilled water was used, and an Eppendorf Research 10–200  $\mu\text{L}$  pipette was used to insert the liquids. The solid NaCl crystals were weighted with a scale at the local laboratory. The NaCl solution was made using a weight scale and by mixing the distilled water with solid NaCl crystals. The water and the NaCl solutions were stored together in closed containers to ensure similar temperatures. For heating of water, we used a simple boiler.

The measurements were done with the following steps

1. Insert liquid.
2. Close waveguide.
3. Wait for the stable response due to mechanical vibrations and record the  $S_{11}$ -response.
4. Prepare for the next measurement by removing the waveguide and dry for liquid.

#### Normalization

The extracted reflection coefficient oscillates around 1, which is unphysical, and must be an artifact coming from the VNA calibration. Such oscillations have been observed previously with other structures inserted in waveguides (36). The waveguide is a closed cavity and inside the waves reflects multiple times, causing interference just like in Fabry–Pérot interferometers. The oscillations in Fig. S5A occur due to a shift in the interfering reflections. Since we are not interested in these oscillations, we suppress them by defining a normalized reflection coefficient as  $S_{11} = S_{11,\text{VNA}}(V_{\text{water}}) / S_{11,\text{VNA}}(0$

$\mu\text{L}$ ). The magnitude and phase of  $S_{11}$  are shown in Fig. S5, B and C, respectively, as functions of frequency for different volumes of water.

#### Quality factor

The quality factor has been calculated using  $Q = f_r/\Delta f$ , where  $f_r$  is the resonance frequency and  $\Delta f$  is the bandwidth at half maximum. The quality factor as a function of the volume of water is shown in Fig. S5E. We observe a decreasing linear proportionality of the quality factor with an increasing volume of water. This is expected since water is lossy. At critical coupling, the quality factor is around 250.

#### Reproducibility of the experiment

We tested the reproducibility of the experiment, see Fig. S5F, and we measured a variation in the resonance frequency (the frequency of the minimum of the reflection coefficient) of approximately  $\pm 0.008\%$  ( $\pm 0.15$  MHz), whereas the reflection magnitude had a variation around  $\pm 4\%$ . These deviations come from small variations in water (shape and volume) and are due to the manual insertion of the water.

It should be noted that the resolution is profoundly dependent on the accuracy and precision of the water insertion. Although in our prototype, the water was manually inserted with a pipette, it can be improved with a control system to manage the water insertion.

#### Water outside of the Rohacell container

We also studied placing the water outside the Rohacell container, and we observe similar behavior for the volume change. These results are shown in Fig. S8 and S9. As the water can move freely on the metallic cylinder, we get far more variations in the measurements, and therefore the measurements are more difficult to replicate, but at the same time, makes our device far more sensitive to movements. The position of water is very important, and only displacement parallel to the incident electric field will excite the resonance.

#### Supplementary figures

See next pages.

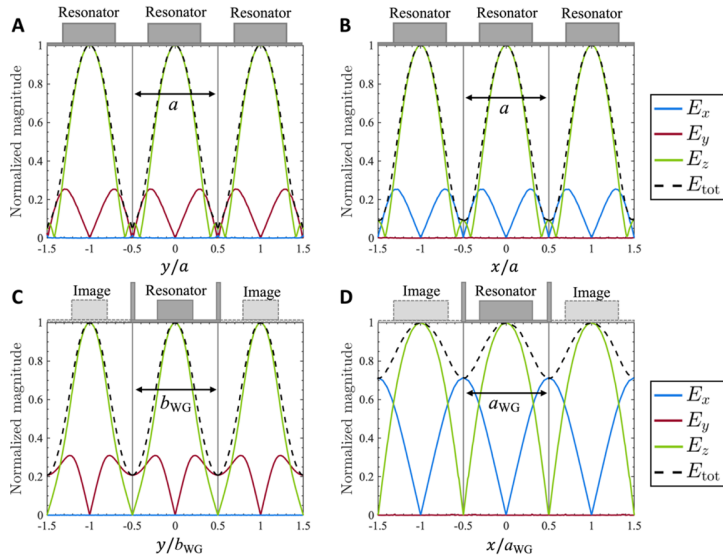


**Figure S1. Difference between the rectangular waveguide with perfect electric conductor (PEC) walls and the periodic array ( $TE_{10}$  mode off).** Magnitude of the local E-field components normalized with the total E-field ( $E_{tot}$ ) at  $z = h_{cyl} - 20$  mm for the eigenmode analyses. (A) and (B) Periodic array:  $f_i \approx 2470$  MHz,  $r = 30$  mm,  $h = 25$  mm and  $a = 110$  mm. (C) and (D) Rectangular waveguide with PEC walls:  $f_i \approx 1890$  MHz,  $r = 18$  mm,  $h = 27$  mm and  $a_{WG} = b_{WG}/2 = 54.61$  mm. In (A) and (C),  $x = 0$ , whereas  $y = 0$  in (B) and (D). The  $z$ -component of the E-field is the most pronounced in both configurations. The  $z$ -component of the images in (B) and (D) lags  $180^\circ$  due to the PEC walls of the waveguide, see e.g. Fig. S3.

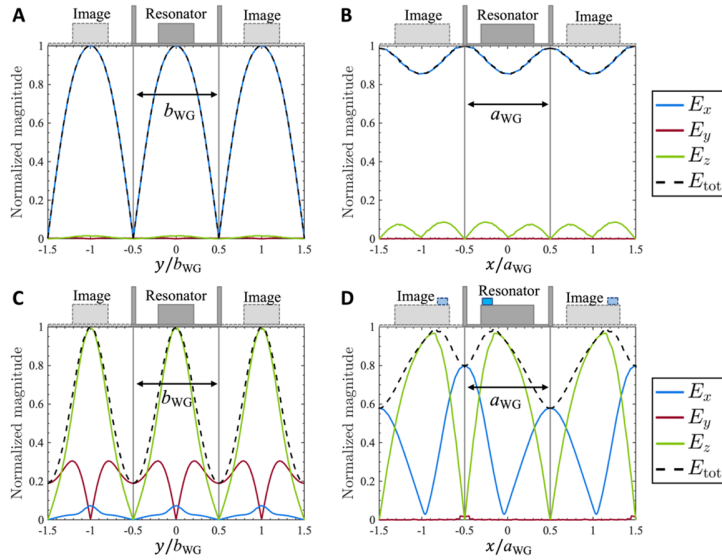


**Figure S2. Rectangular waveguide of perfect electric conductor (PEC) walls with and without water ( $TE_{10}$  mode on).** Magnitude of the local E-field components normalized with the total E-field ( $E_{\text{tot}}$ ) at  $z = h_{\text{cyl}} - 20$  mm for the  $TE_{10}$  mode excitation at resonance frequency. The geometrical parameters are  $r = 18$  mm,  $h = 27$  mm and  $a_{\text{WG}} = b_{\text{WG}}/2 = 54.61$  mm. (A) and (B) Without water at  $f_r \approx 1890$  MHz. (C) and (D) With 500  $\mu\text{L}$  water at  $f_r \approx 1830$  MHz. In (A) and (C),  $x = 0$ , whereas  $y = 0$  in (B) and (D). The  $z$ -component of the E-field is nearly absent without water as we do not excite the resonance. With water, there is a large  $z$ -component since the resonance is now excited. The  $z$ -component of the images in (B) and (D) lags  $180^\circ$  due to the PEC walls of the waveguide, see Fig. S3.

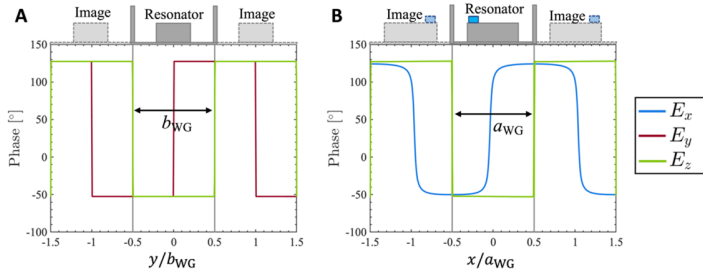


**Figure S3. Same configuration as in Fig. S2C and D, but showing phase instead.** Phase of the local electric field components at  $z = h_{\text{cyl}} - 20$  mm. In (A)  $x = 0$ , whereas  $y = 0$  in (B). The  $z$ -component of the images lags  $180^\circ$  due to the PEC walls of the waveguide.

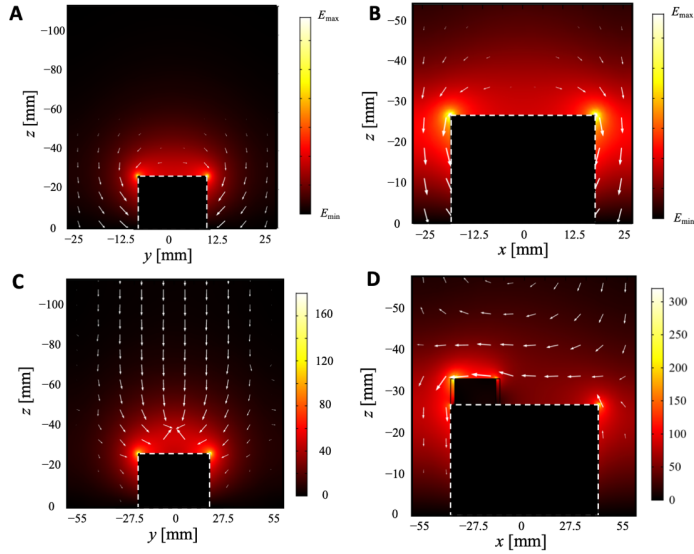


**Figure S4. Total E-field magnitude in the rectangular waveguide with the metallic resonator.** (A) and (B) Eigenmode analysis of the resonator in the waveguide. The real eigenfrequency is 1878.9 MHz and Q-factor is 8,300. (C) and (D) TE<sub>10</sub> mode wave excitation with 500  $\mu\text{L}$  of distilled water in a cylindrical Rohacell 51 HF container of height 6.4 mm as well as inner and outer radii of 5 mm and 6 mm, respectively, atop of the resonator. The edge of Rohacell 51 HF container coincides with the edge of the resonator. The frequency is 1829.1 MHz, the Q-factor is 600 and the reflectance is 0.06. (A)-(D) Colorbar shows the total E-field magnitude in V/m. Arrows show the power flow density in logarithmic scale. The radius and height of the metallic resonator are  $r = 18$  mm and  $h = 27$  mm, respectively. The material of the metallic resonator and conducting ground plane is aluminum with intrinsic conductivity  $\sigma = 3.8 \times 10^7$  S/m. The walls of the waveguide are PEC. The temperature of water is 20  $^{\circ}\text{C}$  in all simulations.



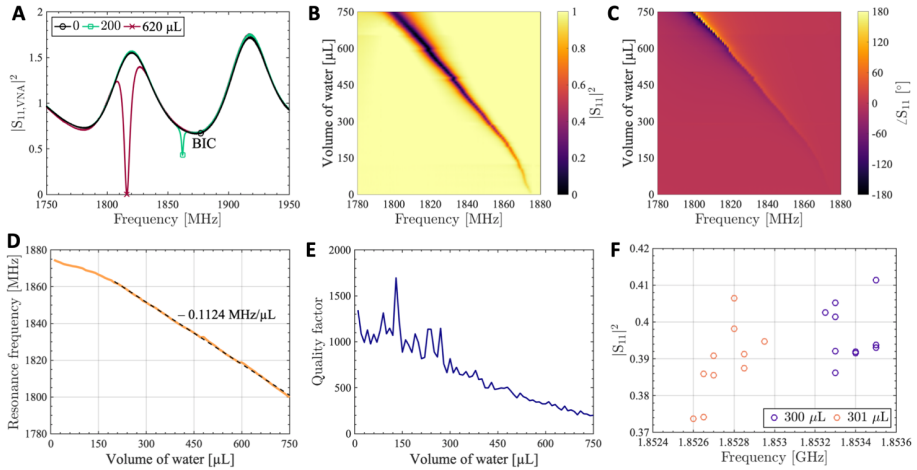


**Figure S5. Supplementary figures to Fig. 4.** (A) Measured reflection coefficient  $S_{11,VNA}$  as a function of frequency for different volumes of water inserted in the Rohacell container. (B) and (C) Magnitude and phase, respectively, of the normalized reflection coefficient  $S_{11}$  as a function of frequency and volume of water. (D) Resonance frequency as a function of the volume of water. The dashed line shows the tendency from 200  $\mu\text{L}$ . (E) Calculated quality factor as a function of the volume of water. (F) Repeatability of measurements. Reflectance  $|S_{11}|^2$  as a function of frequency for 300  $\mu\text{L}$  and 301  $\mu\text{L}$  of water. The measurements are repeated 10 times for both volumes

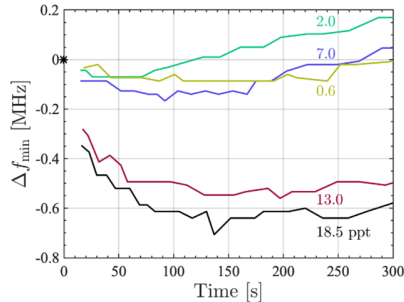


**Figure S6. Supplementary figure to Fig. 5.** Frequency change ( $\Delta f_{\min}$ ) in the reflectance minimum  $(|S_{11}|^2)_{\min}$  as a function of time since NaCl was added. The asterisk symbol shows the frequency of a distilled water (0 ppt).

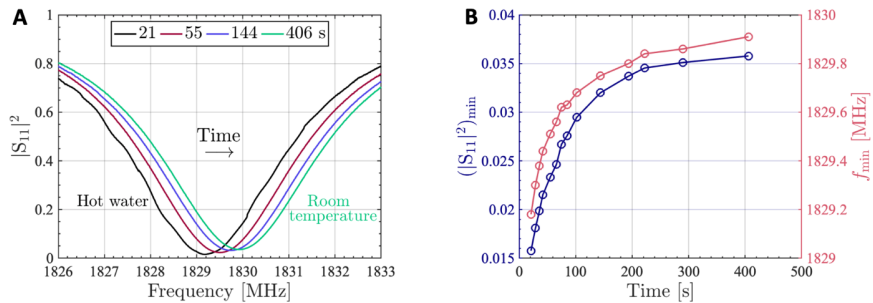


**Figure S7. Change in water temperature.** Initial volume of water is 500  $\mu\text{L}$  for all experiments. **(A)** reflectance as a function of frequency for different time points after adding the heated water. **(B)** The minimum of the reflectance  $(|S_{11}|^2)_{\min}$  and the frequency  $f_{\min}$  as functions of the time after adding the heated water.

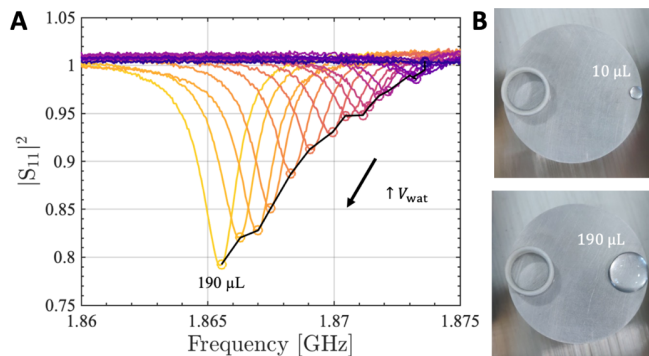


**Figure S8. Water drop outside of the Rohacell container.** **(A)** Reflectance  $|S_{11}|^2$  as a function of frequency for different volumes of water. **(B)** Photographs showing 10  $\mu\text{L}$  and 190  $\mu\text{L}$  of water placed on the resonator.

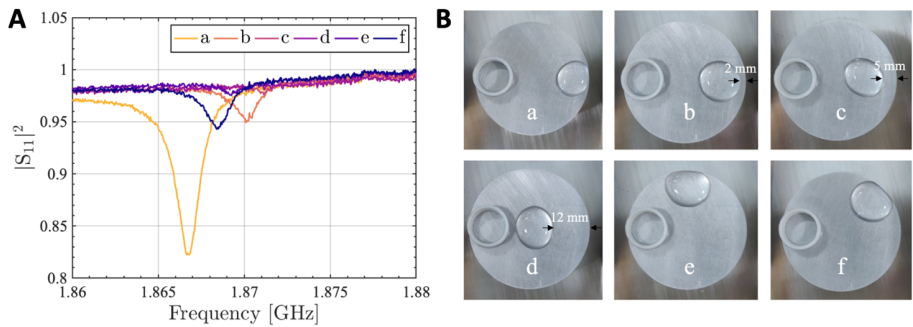


**Figure S9. Water drop of 200  $\mu\text{L}$  outside of the Rohacell container placed at different positions on the the resonator. (A) Reflectance  $|S_{11}|^2$  as a function of frequency for different water drop positions. (B) Photographs showing the positions of the drop on the resonator.**

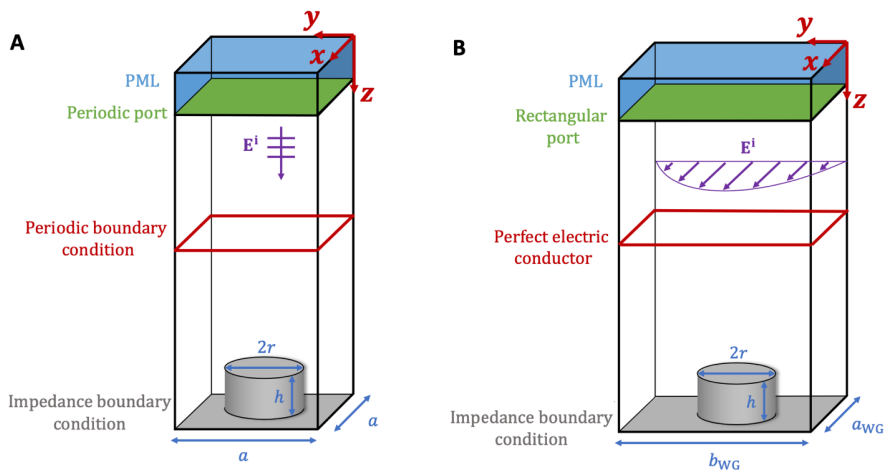


**Figure S10. Sketches of the COMSOL Multiphysics simulation models. (A) Model of the BIC structure with infinite elements. (B) Model of the rectangular waveguide used for the experiments.**

## Equations and values for the extended water permittivity model

---

This appendix includes the full permittivity model for water taken from [16]. The model contains three Debye relaxations (first sum) and two molecular resonance terms (second sum), and takes the form

$$\varepsilon_{r,w}(\omega, T_w) = \varepsilon_s(T_w) - j\omega \sum_{n=1}^3 \frac{\varepsilon_{\infty,n}(T_w)\tau_n(T_w)}{1 + j\omega\tau_n(T_w)} - j\frac{\omega}{2} \sum_{n=4}^5 \left[ \frac{\varepsilon_{\infty,n}(T_w)\tau_n(T_w)}{1 + j\tau_n(T_w)(\omega + \omega_n)} + \frac{\varepsilon_{\infty,n}(T_w)\tau_n(T_w)}{1 + j\tau_n(T_w)(\omega - \omega_n)} \right], \quad (\text{G.1a})$$

where the static and optical relative permittivities and relaxation times are

$$\varepsilon_s(T_w) \approx 87.9 - 0.404T_w + 9.59\text{E-}4T_w^2 - 1.33\text{E-}6T_w^2, \quad (\text{G.1b})$$

$$\varepsilon_{\infty,n}(T_w) = a_n \exp(-b_n T_w), \quad (\text{G.1c})$$

and

$$\tau_n(T_w) = c_n \exp\left(\frac{-d_n}{T_w + T_0}\right) [\text{s}], \quad (\text{G.1d})$$

respectively, for  $n = 1, 2, 3$ . For  $n = 4, 5$ , we have

$$\varepsilon_{\infty,4}(T_w) = 0.838 - 6.12\text{E-}3 T_w - 1.29\text{E-}5 T_w^2, \quad (\text{G.1e})$$

$$\tau_4(T_w) = 9.62\text{E-}14 + 1.80\text{E-}16 T_w - 9.31\text{E-}18 T_w^2 + 1.66\text{E-}19 T_w^3, \quad (\text{G.1f})$$

$$\omega_4(T_w) = 2\pi (4.24\text{E}12 - 1.43\text{E}10 T_w + 2.74\text{E}8 T_w^2 - 1.25\text{E}6 T_w^3), \quad (\text{G.1g})$$

$$\varepsilon_{\infty,5}(T_w) = 0.617 + 7.24\text{E-}3 T_w - 9.52\text{E-}5 T_w^2, \quad (\text{G.1h})$$

$$\tau_5(T_w) = 2.88\text{E-}14 - 3.14\text{E-}16 T_w + 3.53\text{E-}18 T_w^2, \quad (\text{G.1i})$$

$$\omega_5(T_w) = 2\pi (1.60\text{E}13 - 7.44\text{E}10 T_w + 4.97\text{E}8 T_w^2), \quad (\text{G.1j})$$

where  $\omega_n$  [rad/s] are the angular resonance frequencies.  $T_w$  [°C] is the temperature of water and  $T_0 = 133$  °C is the critical temperature. The values for the rest of the parameters in Eq. (G.1) are listed in Table G.1.

**Table G.1:** Parameter values for the Debye relaxations of the permittivity model of water in Eq. (G.1).

$n$	$a_n$	$b_n \times 10^{-3} [^{\circ}\text{C}^{-1}]$	$c_n$ [fs]	$d_n [^{\circ}\text{C}]$
1	79.2	4.30	138	653
2	3.82	11.2	0.351	1250
3	1.63	6.84	6.30	406

**Table G.2:** Size of the permittivity model needed for different frequency bands.

Maximum frequency	Debye relaxations	Molecular resonances	Maximum $n$
$\sim 0$ Hz (static)	Zero	Zero	-
50 GHz	One	Zero	1
500 GHz	Two	Zero	2
3 THz	Three	Zero	3
25 THz	Three	Two	5

# References

---

- [1] M. Sargen, “Biological Roles of Water: Why is water necessary for life?,” sep 2019.
- [2] Howard Perlman, “Water, the Universal Solvent,” 2016.
- [3] P. Ball, *Life’s Matrix: A Biography of Water*. New York: Farrar, Straus & Giroux, 1 ed., 1999.
- [4] UN Water, “World Water Day,” 2021.
- [5] J. D. Smith, C. D. Cappa, K. R. Wilson, B. M. Messer, R. C. Cohen, and R. J. Saykally, “Energetics of hydrogen bond network rearrangements in liquid water,” *Science*, vol. 306, pp. 851–853, oct 2004.
- [6] F. Franks, *Water: A Comprehensive Treatise, vol. 1-5*. New York: Plenum Press, 1 ed., 1975.
- [7] M. Sharma, R. Resta, and R. Car, “Dipolar correlations and the dielectric permittivity of water,” *Physical Review Letters*, vol. 98, no. 24, p. 247401, 2007.
- [8] W. J. Ellison, “Permittivity of pure water, at standard atmospheric pressure, over the frequency range 0-25 THz and the temperature range 0-100 oC,” *Journal of Physical and Chemical Reference Data*, vol. 36, no. 1, pp. 1–18, 2007.
- [9] R. L. Fulton, “The nonlinear dielectric behavior of water: Comparisons of various approaches to the nonlinear dielectric increment,” *Journal of Chemical Physics*, vol. 130, no. 20, p. 204503, 2009.
- [10] H. J. Bakker and J. L. Skinner, “Vibrational spectroscopy as a probe of structure and dynamics in liquid water,” *Chemical Reviews*, vol. 110, pp. 1498–1517, mar 2010.
- [11] N. C. Burch, H. Jasuja, and K. S. Walton, “Water stability and adsorption in metal-organic frameworks,” *Chemical Reviews*, vol. 114, pp. 10575–10612, oct 2014.

- 
- [12] J. O. Richardson, C. Pérez, S. Lobsiger, A. A. Reid, B. Temelso, G. C. Shields, Z. Kisiel, D. J. Wales, B. H. Pate, and S. C. Althorpe, “Concerted hydrogen-bond breaking by quantum tunneling in the water hexamer prism,” *Science*, vol. 351, pp. 1310–1313, mar 2016.
- [13] D. Laage and J. T. Hynes, “A molecular jump mechanism of water reorientation,” *Science*, vol. 311, pp. 832–835, feb 2006.
- [14] I. Popov, P. B. Ishai, A. Khamzin, and Y. Feldman, “The mechanism of the dielectric relaxation in water,” *Physical Chemistry Chemical Physics*, vol. 18, pp. 13941–13953, may 2016.
- [15] D. C. Elton and M. Fernandez-Serra, “The hydrogen-bond network of water supports propagating optical phonon-like modes,” *Nature Communications*, vol. 7, no. 1, p. 10193, 2016.
- [16] D. C. Elton, “The origin of the Debye relaxation in liquid water and fitting the high frequency excess response,” *Physical Chemistry Chemical Physics*, vol. 19, no. 28, pp. 18739–18749, 2017.
- [17] P. Ball, “Water: Water - an enduring mystery,” *Nature*, vol. 452, no. 7185, pp. 291–292, 2008.
- [18] M. Wang and Q. X. Chu, “High-efficiency and wideband coaxial dual-tube hybrid monopole water antenna,” *IEEE Antennas and Wireless Propagation Letters*, vol. 17, pp. 799–802, may 2018.
- [19] H. Fayad and P. Record, “Broadband liquid antenna,” *Electronics Letters*, vol. 42, no. 3, pp. 133–134, 2006.
- [20] John Pavlus, “Navy Antenna Using Seawater instead of Metal,” nov 2010.
- [21] D. W. S. Tam, “Patent: Electrolytic Fluid Antenna with Signal Enhancer,” 2013.
- [22] R.-G. Fan, Y.-H. Qian, and Q.-X. Chu, “Frequency and pattern reconfigurable saline-water antenna array,” *Microwave and Optical Technology Letters*, vol. 59, pp. 2284–2289, sep 2017.
- [23] C. Borda-Fortuny, L. Cai, K. F. Tong, and K. K. Wong, “Low-Cost 3D-Printed Coupling-Fed Frequency Agile Fluidic Monopole Antenna System,” *IEEE Access*, vol. 7, pp. 95058–95064, 2019.

- 
- [24] C. Hua, Z. Shen, and J. Lu, "High-efficiency sea-water monopole antenna for maritime wireless communications," *IEEE Transactions on Antennas and Propagation*, vol. 62, pp. 5968–5973, dec 2014.
- [25] C. Hua and Z. Shen, "Shunt-Excited Sea-Water Monopole Antenna of High Efficiency," *IEEE Transactions on Antennas and Propagation*, vol. 63, pp. 5185–5190, nov 2015.
- [26] L. Xing, Y. Huang, Y. Shen, S. Al Ja'afreh, Q. Xu, and R. Alrawashdeh, "Further investigation on water antennas," *IET Microwave, Antennas and Propagation*, vol. 9, no. 8, pp. 735–741, 2015.
- [27] L. Xing, X. Meng, L. Yang, B. Xu, and Y. Pan, "A wideband water antenna for WiFi applications," *2018 IEEE International Workshop on Antenna Technology, IWAT2018 - Proceedings*, pp. 1–3, 2018.
- [28] Y.-H. Qian and Q.-X. Chu, "A Broadband Hybrid Monopole-Dielectric Resonator Water Antenna," *IEEE Antennas and Wireless Propagation Letters*, vol. 16, pp. 1360–1363, 2017.
- [29] C. Song, E. L. Bennett, J. Xiao, Q. Hua, L. Xing, and Y. Huang, "Compact Ultra-Wideband Monopole Antennas Using Novel Liquid Loading Materials," *IEEE Access*, vol. 7, pp. 49039–49047, 2019.
- [30] L. Xing, J. Zhu, Q. Xu, D. Yan, and Y. Zhao, "A circular beam-steering antenna with parasitic water reflectors," *IEEE Antennas and Wireless Propagation Letters*, vol. 18, pp. 2140–2144, oct 2019.
- [31] A. Singh, I. Goode, and C. E. Saavedra, "A Multistate Frequency Reconfigurable Monopole Antenna Using Fluidic Channels," *IEEE Antennas and Wireless Propagation Letters*, vol. 18, pp. 856–860, may 2019.
- [32] J. J. Liang, G. L. Huang, K. W. Qian, S. L. Zhang, and T. Yuan, "An azimuth-pattern reconfigurable antenna based on water grating reflector," *IEEE Access*, vol. 6, pp. 34804–34811, jun 2018.
- [33] E. Motovilova and S. Y. Huang, "A review on reconfigurable liquid dielectric antennas," *Materials*, vol. 13, no. 8, p. 1863, 2020.



- 
- [34] M. Wang and Q. X. Chu, "A Wideband Polarization-Reconfigurable Water Dielectric Resonator Antenna," *IEEE Antennas and Wireless Propagation Letters*, vol. 18, pp. 402–406, feb 2019.
- [35] C. Song, E. L. Bennett, J. Xiao, A. Alieldin, K. M. Luk, and Y. Huang, "Metasurfaced, broadband, and circularly polarized liquid antennas using a simple structure," *IEEE Transactions on Antennas and Propagation*, vol. 67, pp. 4907–4913, jul 2019.
- [36] L. Xing, Q. Xu, J. Zhu, Y. Zhao, S. Aljaafreh, C. Song, and Y. Huang, "A High-Efficiency Wideband Frequency-Reconfigurable Water Antenna With a Liquid Control System: Usage for VHF and UHF Applications," *IEEE Antennas and Propagation Magazine*, vol. 63, feb 2021.
- [37] Y. Chen and C. F. Wang, "Dual-band directional/omni-directional liquid dielectric resonator antenna designs using characteristic modes," in *IEEE Antennas and Propagation Society, AP-S International Symposium (Digest)*, pp. 848–849, Institute of Electrical and Electronics Engineers Inc., sep 2014.
- [38] R. E. Jacobsen, A. V. Lavrinenko, and S. Arslanagic, "Electrically small water-based hemispherical dielectric resonator antenna," *Applied Sciences*, vol. 9, no. 22, p. 4848, 2019.
- [39] S. P. Kingsley and S. G. O'Keefe, "Beam steering and monopulse processing of probe-fed dielectric resonator antennas," *IEE Proceedings: Radar, Sonar and Navigation*, vol. 146, no. 3, pp. 121–125, 1999.
- [40] R. E. Jacobsen, A. V. Lavrinenko, and S. Arslanagic, "A Water-Based Huygens Dielectric Resonator Antenna," *IEEE Open Journal of Antennas and Propagation*, vol. 1, pp. 493–499, 2020.
- [41] S. G. O'Keefe and S. P. Kingsley, "Tunability of liquid dielectric resonator antennas," *IEEE Antennas and Wireless Propagation Letters*, vol. 6, pp. 533–536, 907916, 2007.
- [42] A. T. Mobashsher and A. Abbosh, "Reconfigurable water-substrate based antennas with temperature control," *Applied Physics Letters*, vol. 110, no. 25, p. 253503, 2017.

- 
- [43] M. Lapierre, Y. M. M. Antar, A. Ittipiboon, and A. Petosa, "Ultra wideband monopole/dielectric resonator antenna," *IEEE Microwave and Wireless Components Letters*, vol. 15, no. 1, pp. 7–9, 2005.
- [44] M. Zou, Z. Shen, and J. Pan, "Frequency-reconfigurable water antenna of circular polarization," *Applied Physics Letters*, vol. 108, no. 1, p. 14102, 2016.
- [45] R. Zhou, H. Zhang, and H. Xin, "Liquid-based dielectric resonator antenna and its application for measuring liquid real permittivities," *IET Microwave, Antennas and Propagation*, vol. 8, no. 4, pp. 255–262, 2014.
- [46] G. H. Huff, D. L. Rolando, P. Walters, and J. McDonald, "A frequency reconfigurable dielectric resonator antenna using colloidal dispersions," *IEEE Antennas and Wireless Propagation Letters*, vol. 9, pp. 288–290, 2010.
- [47] Z. Gong, C. Bartone, F. Yang, and J. Yao, "High-efficiency water-loaded microwave antenna in ultra-high-frequency band," *Applied Physics Letters*, vol. 112, mar 2018.
- [48] S. B. Liu, F. S. Zhang, and Y. X. Zhang, "Dual-band circular-polarization reconfigurable liquid dielectric resonator antenna," *International Journal of RF and Microwave Computer-Aided Engineering*, vol. 29, mar 2019.
- [49] Z. Chen and H. Wong, "Liquid Dielectric Resonator Antenna with Circular Polarization Reconfigurability," *IEEE Transactions on Antennas and Propagation*, vol. 66, pp. 444–449, jan 2018.
- [50] L. Xing, Y. Huang, Q. Xu, and S. Alja'afreh, "Wideband, hybrid rectangular water antenna for DVB-H applications," *Microwave and Optical Technology Letters*, vol. 57, no. 9, pp. 2160–2164, 2015.
- [51] R. E. Jacobsen, M. H. Vandborg, A. V. Lavrinenko, and S. Arslanagic, "Water-Based Microwave Antennas," in *14th European Conference on Antennas and Propagation (EuCAP)*, (Copenhagen, Denmark), 2020.
- [52] Z. Ren, S. S. Qi, Z. Hu, Z. Shen, and W. Wu, "Wideband Water Helical Antenna of Circular Polarization," *IEEE Transactions on Antennas and Propagation*, vol. 67, pp. 6770–6777, nov 2019.

- 
- [53] G. Li, Y. Huang, G. Gao, C. Yang, Z. Lu, and W. Liu, "A broadband helical saline water liquid antenna for wearable systems," *International Journal of Electronics*, vol. 105, pp. 645–658, apr 2018.
- [54] J. Sun and K. M. Luk, "A Wideband Low Cost and Optically Transparent Water Patch Antenna with Omnidirectional Conical Beam Radiation Patterns," *IEEE Transactions on Antennas and Propagation*, vol. 65, no. 9, pp. 4478–4485,7987716, 2017.
- [55] J. Sun and K. M. Luk, "A compact-size wideband optically-transparent water patch antenna incorporating an annular water ring," *IEEE Access*, vol. 7, pp. 122964–122971, 2019.
- [56] Y. Li and K. M. Luk, "A Water Dense Dielectric Patch Antenna," *IEEE Access*, vol. 3, pp. 274–280,7080869, 2015.
- [57] Z. Chen and H. Wong, "Wideband Glass and Liquid Cylindrical Dielectric Resonator Antenna for Pattern Reconfigurable Design," *IEEE Transactions on Antennas and Propagation*, vol. 65, pp. 2157–2164, may 2017.
- [58] M. Konca and P. A. Warr, "A Frequency-Reconfigurable Antenna Architecture Using Dielectric Fluids," *IEEE Transactions on Antennas and Propagation*, vol. 63, pp. 5280–5286, dec 2015.
- [59] J. D. Barrera and G. H. Huff, "A fluidic loading mechanism in a polarization reconfigurable antenna with a comparison to solid state approaches," *IEEE Transactions on Antennas and Propagation*, vol. 62, no. 8, pp. 4008–4014, 2014.
- [60] C. Murray and R. R. Franklin, "Independently Tunable Annular Slot Antenna Resonant Frequencies Using Fluids," *IEEE Antennas and Wireless Propagation Letters*, vol. 13, pp. 1449–1452, 2014.
- [61] Y. H. Qian and Q. X. Chu, "A polarization-reconfigurable water-loaded microstrip antenna," *IEEE Antennas and Wireless Propagation Letters*, vol. 16, pp. 2179–2182, 2017.
- [62] H. Tang and J. X. Chen, "Microfluidically Frequency-Reconfigurable Microstrip Patch Antenna and Array," *IEEE Access*, vol. 5, pp. 20470–20476, sep 2017.
- [63] S. K. Patel and Y. Kosta, "Liquid metamaterial based microstrip antenna," *Microwave and Optical Technology Letters*, vol. 60, no. 2, pp. 318–322, 2018.

- [64] L. Xing, Y. Huang, Q. Xu, S. Alja'afreh, and T. Liu, "A Broadband Hybrid Water Antenna for Hand-Portable Applications," *IEEE Antennas and Wireless Propagation Letters*, vol. 15, pp. 174–177, 2016.
- [65] A. H. Naqvi and S. Lim, "A Beam-Steering Antenna with a Fluidically Programmable Metasurface," *IEEE Transactions on Antennas and Propagation*, vol. 67, no. 6, pp. 3704–3711, 2019.
- [66] Y.-H. Qian and Q.-X. Chu, "A pattern-reconfigurable water-loaded MIMO antenna," *Microwave and Optical Technology Letters*, vol. 59, pp. 1608–1613, jul 2017.
- [67] L. Liu, A. R. Katko, D. Li, and S. A. Cummer, "Broadband electromagnetic metamaterials with reconfigurable fluid channels," *Physical Review B*, vol. 89, no. 24, p. 245132, 2014.
- [68] Z. Shen, H. Yang, X. Huang, and Z. Yu, "Design of negative refractive index metamaterial with water droplets using 3D-printing," *Journal of Optics*, vol. 19, no. 11, p. 115101, 2017.
- [69] M. A. Gorlach, M. Song, A. P. Slobozhanyuk, A. A. Bogdanov, and P. A. Belov, "Topological transition in coated wire medium," *Physica Status Solidi - Rapid Resonances Letters*, vol. 10, no. 12, pp. 900–904, 2016.
- [70] M. V. Rybin, D. S. Filonov, P. A. Belov, Y. S. Kivshar, and M. F. Limonov, "Switching from visibility to invisibility via fano resonances: Theory and experiment," *Scientific Reports*, vol. 5, no. 1, p. 8774, 2015.
- [71] M. V. Rybin, D. S. Filonov, K. B. Samusev, P. A. Belov, Y. S. Kivshar, and M. F. Limonov, "Phase diagram for the transition from photonic crystals to dielectric metamaterials," *Nature Communications*, vol. 6, no. 1, p. 10102, 2015.
- [72] Q. Wang, K. Bi, and S. Lim, "All-Dielectric Transparent Metamaterial Absorber With Encapsulated Water," *IEEE Access*, vol. 8, pp. 175998–176004, sep 2020.
- [73] E. Yang, F. Yang, J. Pei, X. Zhang, S. Liu, and Y. Deng, "All-dielectric ultra-broadband metamaterial absorber based on imidazole ionic liquids," *Journal of Physics D: Applied Physics*, vol. 52, no. 39, p. 395501, 2019.

- [74] D. J. Gogoi and N. S. Bhattacharyya, “Metasurface absorber based on water meta molecule for X-band microwave absorption,” *Journal of Applied Physics*, vol. 124, no. 7, p. 75106, 2018.
- [75] X. Zhang, F. Yan, X. Du, W. Wang, and M. Zhang, “Broadband water-based metamaterial absorber with wide angle and thermal stability,” *AIP Advances*, vol. 10, no. 5, p. 55211, 2020.
- [76] X. Huang, H. Yang, Z. Shen, J. Chen, H. Lin, and Z. Yu, “Water-injected all-dielectric ultra-wideband and prominent oblique incidence metamaterial absorber in microwave regime,” *Journal of Physics D: Applied Physics*, vol. 50, no. 38, p. 385304, 2017.
- [77] B. X. Khuyen, V. T. H. Hanh, B. S. Tung, V. D. Lam, Y. J. Kim, Y. Lee, H. T. Tu, and L. Y. Chen, “Narrow/broad-band absorption based on water-hybrid metamaterial,” *Crystals*, vol. 10, no. 5, p. 415, 2020.
- [78] H. F. Zhang, X. L. Tian, G. B. Liu, and X. R. Kong, “A Gravity Tailored Broadband Metamaterial Absorber Containing Liquid Dielectrics,” *IEEE Access*, vol. 7, pp. 25827–25832,8643996, 2019.
- [79] Y. Pang, J. Wang, Q. Cheng, S. Xia, X. Y. Zhou, Z. Xu, T. J. Cui, and S. Qu, “Thermally tunable water-substrate broadband metamaterial absorbers,” *Applied Physics Letters*, vol. 110, no. 10, p. 104103, 2017.
- [80] J. Ren and J. Y. Yin, “Cylindrical-water-resonator-based ultrabroadband microwave absorber,” *Optical Materials Express*, vol. 8, no. 8, pp. 2060–2071, 2018.
- [81] Y. Shen, J. Zhang, Y. Pang, L. Zheng, J. Wang, H. Ma, and S. Qu, “Thermally Tunable Ultra-wideband Metamaterial Absorbers based on Three-dimensional Water-substrate construction,” *Scientific Reports*, vol. 8, no. 1, p. 4423, 2018.
- [82] Y. J. Yoo, S. Ju, S. Y. Park, Y. Ju Kim, J. Bong, T. Lim, K. W. Kim, J. Y. Rhee, and Y. Lee, “Metamaterial Absorber for Electromagnetic Waves in Periodic Water Droplets,” *Scientific Reports*, vol. 5, p. 14018, 2015.
- [83] Q. Song, W. Zhang, P. C. Wu, W. Zhu, Z. X. Shen, P. H. J. Chong, Q. X. Liang, Z. C. Yang, Y. L. Hao, H. Cai, H. F. Zhou, Y. Gu, G. Q. Lo, D. P.

- Tsai, T. Bourouina, Y. Leprince-Wang, and A. Q. Liu, "Water-Resonator-Based Metasurface: An Ultrabroadband and Near-Unity Absorption," *Advanced Optical Materials*, vol. 5, no. 8, p. 1601103, 2017.
- [84] H. Xiong and F. Yang, "Ultra-broadband and tunable saline water-based absorber in microwave regime," *Optics Express*, vol. 28, no. 4, pp. 5306–5316, 2020.
- [85] Y. Shen, J. Zhang, Y. Pang, J. Wang, H. Ma, and S. Qu, "Transparent broadband metamaterial absorber enhanced by water-substrate incorporation," *Optics Express*, vol. 26, no. 12, pp. 15665–15674, 2018.
- [86] Y. Pang, Y. Shen, Y. Li, J. Wang, Z. Xu, and S. Qu, "Water-based metamaterial absorbers for optical transparency and broadband microwave absorption," *Journal of Applied Physics*, vol. 123, no. 15, p. 155106, 2018.
- [87] D. J. Gogoi and N. S. Bhattacharyya, "Embedded dielectric water "atom" array for broadband microwave absorber based on Mie resonance," *Journal of Applied Physics*, vol. 122, no. 17, p. 175106, 2017.
- [88] F. Yang, J. Gong, E. Yang, Y. Guan, X. He, S. Liu, X. Zhang, and Y. Deng, "Ultrabroadband metamaterial absorbers based on ionic liquids," *Applied Physics A: Materials Science Processing*, vol. 125, no. 2, p. 149, 2019.
- [89] J. Xie, S. Quader, F. Xiao, C. He, X. Liang, J. Geng, R. Jin, W. Zhu, and I. D. Rukhlenko, "Truly all-dielectric ultrabroadband metamaterial absorber: Water-based and ground-free," *IEEE Antennas and Wireless Propagation Letters*, vol. 18, no. 3, pp. 536–540, 2019.
- [90] S. Wei, J. Zhao, Z. Sun, K. Chen, and Y. Feng, "Water Droplets: Toward Broadband Metamaterial Microwave Absorber," *2016 IEEE International Workshop on Electromagnetics: Applications and Student Innovation Competition (IWEM)*, pp. 1–3, 1–3, 2016.
- [91] J. Xie, W. Zhu, I. D. Rukhlenko, F. Xiao, C. He, J. Geng, X. Liang, R. Jin, and M. Premaratne, "Water metamaterial for ultra-broadband and wide-angle absorption," *Optics Express*, vol. 26, no. 4, pp. 5052–5059, 2018.

- [92] D. J. Gogoi and N. S. Bhattacharyya, "Microwave metamaterial absorber based on aqueous electrolyte solution for X-band application," *Journal of Applied Physics*, vol. 125, no. 12, p. 125107, 2019.
- [93] H. Zhang, F. Ling, H. Wang, Y. Zhang, and B. Zhang, "A water hybrid graphene metamaterial absorber with broadband absorption," *Optical Communications*, vol. 463, p. 125394, 2020.
- [94] S. Wang, B. Hou, and C. T. Chan, "Broadband Microwave Absorption by Logarithmic Spiral Metasurface," *Scientific Reports*, vol. 9, 2019.
- [95] J. Zhao, S. Wei, C. Wang, K. Chen, B. Zhu, T. Jiang, and Y. Feng, "Broadband microwave absorption utilizing water-based metamaterial structures," *Optics Express*, vol. 26, no. 7, pp. 8522–8531, 2018.
- [96] X. Zhang, D. Zhang, Y. Fu, S. Li, Y. Wei, K. Chen, X. Wang, and S. Zhuang, "3-D Printed Swastika-Shaped Ultrabroadband Water-Based Microwave Absorber," *IEEE Antennas and Wireless Propagation Letters*, vol. 19, no. 5, pp. 821–825, 2020.
- [97] Z. Wu, X. Chen, Z. Zhang, L. Heng, S. Wang, and Y. Zou, "Design and optimization of a flexible water-based microwave absorbing metamaterial," *Applied Physics Express*, vol. 12, no. 5, p. 57003, 2019.
- [98] Z. Han, J. Zhao, and Y. Feng, "A tunable water-based metamaterial microwave absorber," *2017 IEEE 6th Asia-Pacific Conference on Antennas and Propagation, Apcap 2017 - Proceeding*, p. 8420663, 2017.
- [99] Z. Shen, X. Huang, H. Yang, T. Xiang, C. Wang, Z. Yu, and J. Wu, "An ultra-wideband, polarization insensitive, and wide incident angle absorber based on an irregular metamaterial structure with layers of water," *Journal of Applied Physics*, vol. 123, no. 22, p. 225106, 2018.
- [100] P. J. Bradley, M. O. Torrico, C. Brennan, and Y. Hao, "Printable all-dielectric water-based absorber," *Scientific Reports*, vol. 8, no. 1, p. 14490, 2018.
- [101] Q. Liang, Z. Yang, J. Guo, Z. Li, T. Chen, and D. Li, "A high-efficient tunable liquid metal-based electromagnetic absorbing metamaterial," *Journal of Materials Science: Materials in Electronics*, pp. 1–6., 2020.

- [102] S. K. Patel, K. H. Shah, and J. S. Sonagara, "Broadband liquid metamaterial radome design," *Waves Random Complex Media*, vol. 30, pp. 328–339, apr 2018.
- [103] W. Zhu, C. He, X. Liang, J. Geng, and R. Jin, "Coherent control of absorption in water based metamaterial," *2017 IEEE Antennas and Propagation Society International Symposium, Proceedings*, vol. 2017-, pp. 1267–1268, 2017.
- [104] W. Zhu, I. D. Rukhlenko, F. Xiao, C. He, J. Geng, X. Liang, M. Premaratne, and R. Jin, "Multiband coherent perfect absorption in a water-based metasurface," *Optics Express*, vol. 25, no. 14, pp. 15737–15745, 2017.
- [105] X. Yan, X. Kong, Q. Wang, L. Xing, F. Xue, Y. Xu, S. Jiang, and X. Liu, "Water-based reconfigurable frequency selective absorber with thermally tunable absorption band," *IEEE Transactions on Antennas and Propagation*, vol. 68, no. 8, pp. 6162–6171, 2020.
- [106] K.-L. Zhang, X.-D. Cheng, Y.-J. Zhang, M. Chen, H. Chen, Y. Yang, W.-L. Song, and D. Fang, "Weather-Manipulated Smart Broadband Electromagnetic Metamaterials," *ACS Applied Materials and Interfaces*, vol. 10, no. 47, pp. 40815–40823, 2018.
- [107] Y. Shen, J. Zhang, S. Sui, Y. Jia, Y. Pang, J. Wang, H. Ma, and S. Qu, "Transparent absorption-diffusion-integrated water-based all-dielectric metasurface for broadband backward scattering reduction," *Journal of Physics D: Applied Physics*, vol. 51, no. 48, p. 485301, 2018.
- [108] A. V. Lavrinenko, R. E. Jacobsen, S. Arslanagic, S. Kuznetsova, A. Andryieuski, M. Odit, and P. Kapitanova, "Tunable microwave metamaterials based on ordinary water," *Proceedings of the 2017 47th European Microwave Conference*, pp. 492–495, 2017.
- [109] A. V. Lavrinenko, R. E. Jacobsen, and S. Arslanagic, "Low-loss Water-based Metasurface in Waveguide Environment," *Proceedings of the 2018 48th European Microwave Conference*, no. 8541501, pp. 819–822, 2018.
- [110] R. E. Jacobsen, J. Ø. Nielsen, A. V. Lavrinenko, and S. Arslanagic, "Tunable water-based metasurface for anomalous wave reflection," *Journal of Physics D: Applied Physics*, vol. 53, no. 50, p. 505104, 2020.



- [111] Y. Pang, M. Mo, Y. Li, B. Qu, S. Xia, S. Qu, and Z. Xu, “Dynamically controlling electromagnetic reflection using reconfigurable water-based metasurfaces,” *Smart Materials and Structures*, vol. 29, no. 11, p. 115018, 2020.
- [112] L. Chen, H. L. Ma, X. J. Song, Y. Ruan, and H. Y. Cui, “Dual-functional tunable coding metasurface based on saline water substrate,” *Scientific Reports*, vol. 8, no. 1, p. 2070, 2018.
- [113] M. Odit, A. Sayanskiy, V. Asadchy, and P. Belov, “Microwave reflecting focusing metasurface based on water,” *2018 IEEE Antennas and Propagation Society International Symposium and USNC/URSI National Radio Science Meeting, Apsursi 2018 - Proceedings*, no. 8609338, pp. 773–774, 2018.
- [114] L. Chen, H. L. Ma, Y. Ruan, and H. Y. Cui, “Dual-manipulation on wave-front based on reconfigurable water-based metasurface integrated with PIN diodes,” *Journal of Applied Physics*, vol. 125, no. 2, p. 23107, 2019.
- [115] X. Yang, D. Zhang, S. Wu, Y. Yin, L. Li, K. Cao, and K. Huang, “Reconfigurable all-dielectric metasurface based on tunable chemical systems in aqueous solution,” *Scientific Reports*, vol. 7, no. 1, p. 3190, 2017.
- [116] R. E. Jacobsen, A. V. Lavrinenko, and S. Arslanagic, “Water-Based Metasurfaces for Effective Switching of Microwaves,” *IEEE Antennas and Wireless Propagation Letters*, vol. 17, no. 4, pp. 571–574, 2018.
- [117] R. E. Jacobsen, S. Arslanagic, and A. V. Lavrinenko, “Thermal tuning of a microwave water-based metasurface,” in *Swedish Microwave Days*, (Lund), 2018.
- [118] P. Kapitanova, A. Sayanskiy, M. Odit, A. Miroschnichenko, A. Lavrinenko, and P. Belov, “All-dielectric Metasurfaces as an Efficient Tool for Electromagnetic Waves Manipulation,” in *2018 20th Anniversary International Conference on Transparent Optical Networks (ICTON)*, vol. 2018-July, IEEE, sep 2018.
- [119] J. Ø. Nielsen, R. E. Jacobsen, A. . Laurynenka, and S. Arslanagic, “Water-Based Microwave Reflectarrays,” in *14th European Conference on Antennas and Propagation (EuCAP)*, (Copenhagen, Denmark), 2020.
- [120] M. Odit, A. Saynskiy, I. Munina, and P. Belov, “Functional metasurfaces based on water,” *Journal of Physics: Conference Series*, vol. 1092, no. 1, p. 12103, 2018.

- [121] I. V. Stenishchev and A. A. Basharin, "Toroidal response in all-dielectric metamaterials based on water," *Scientific Reports*, vol. 7, no. 1, p. 9468, 2017.
- [122] A. Keshavarz and Z. Vafapour, "Water-Based Terahertz Metamaterial for Skin Cancer Detection Application," *IEEE Sensors Journal*, vol. 19, no. 4, pp. 1519–1524, 2019.
- [123] A. Andryieuski, S. M. Kuznetsova, S. V. Zhukovsky, Y. S. Kivshar, and A. V. Lavrinenko, "Water: Promising Opportunities For Tunable All-dielectric Electromagnetic Metamaterials," *Scientific Reports*, vol. 5, p. 13535, 2015.
- [124] M. Odit, P. Kapitanova, A. Andryieuski, P. Belov, and A. V. Lavrinenko, "Experimental demonstration of water based tunable metasurface," *Applied Physics Letters*, vol. 109, no. 1, p. 11901, 2016.
- [125] R. E. Jacobsen, S. Arslanagic, and A. V. Lavrinenko, "Fundamental Properties of Mie Resonances in Water Spheres," *Proceedings of 2019 International Symposium on Electromagnetic Theory*, 2019.
- [126] P. Kapitanova, V. Ternovski, A. Miroshnichenko, N. Pavlov, P. Belov, Y. Kivshar, and M. Tribelsky, "Giant field enhancement in high-index dielectric subwavelength particles," *Scientific Reports*, vol. 7, no. 1, p. 731, 2017.
- [127] H. K. Khattak, P. Bianucci, and A. D. Slepko, "Linking plasma formation in grapes to microwave resonances of aqueous dimers," *Proceedings of the National Academy of Sciences of the United States of America*, vol. 116, no. 10, pp. 4000–4005, 2019.
- [128] R. E. Jacobsen, S. Arslanagic, and A. V. Lavrinenko, "Fundamental Properties of Mie Resonances in Water Cylinders - TM and TE Case Studies," *Proceedings of 2019 International Symposium on Electromagnetic Theory*, p. 8931486, 2019.
- [129] H. W. Wu, H. J. Chen, H. F. Xu, R. H. Fan, and Y. Li, "Tunable multiband directional electromagnetic scattering from spoof Mie resonant structure," *Scientific Reports*, vol. 8, no. 1, p. 8817, 2018.
- [130] N. Pavlov, I. Stenishchev, A. Ospanova, P. Belov, P. Kapitanova, and A. Basharin, "Toroidal Dipole Mode Observation In Situ," *Physica Status Solidi B Basic Resonances*, vol. 257, no. 3, p. 1900406, 2020.

- [131] R. E. Jacobsen, S. Arslanagic, and A. V. Lavrinenko, “Mie Resonances in Water Spheres for Microwave Metamaterials and Antennas,” *URSI Radio Science Letters*, vol. 1, 2020.
- [132] E. Motovilova, S. Sandeep, M. Hashimoto, and S. Y. Huang, “Water-Tunable Highly Sub-Wavelength Spiral Resonator for Magnetic Field Enhancement of MRI Coils at 1.5 T,” *IEEE Access*, vol. 7, pp. 90304–90315, 8756238, 2019.
- [133] A. G. Webb, “Visualization and characterization of pure and coupled modes in water-based dielectric resonators on a human 7T scanner,” *Journal of Magnetic Resonance*, vol. 216, pp. 107–113, 2012.
- [134] D. Bahloul and A. B. Kouki, “LTCC-Based fluidic tuners for low microwave frequency reconfigurable circuits,” *IEEE Transactions on Microwave Theory and Technology*, vol. 68, no. 8, pp. 3308–3317, 2020.
- [135] C. H. Chen and D. Peroulis, “Liquid RF MEMS wideband reflective and absorptive switches,” *IEEE Transactions on Microwave Theory and Techniques*, vol. 55, pp. 2919–2929, dec 2007.
- [136] W. Withayachumnankul, K. Jaruwongrungee, A. Tuantranont, C. Fumeaux, and D. Abbott, “Metamaterial-based microfluidic sensor for dielectric characterization,” *Sensors and Actuators, A: Physical*, vol. 189, pp. 233–237, jan 2013.
- [137] A. L. ADEN, “Microwave reflection from water spheres,” *American Journal of Physics*, vol. 19, no. 3, pp. 163–167, 1951.
- [138] R. Crane, “Bistatic scatter from rain,” *IEEE Transactions on Antennas and Propagation*, vol. 22, no. 2, pp. 312–320, 1974.
- [139] Biral, “Microwave Rain Radar, MRR-2, FM-CW mode,” 2021.
- [140] R. E. Jacobsen, A. Krasnok, S. Arslanagic, A. V. Lavrinenko, and A. Alú, “Boundary-Induced Embedded Eigenstates in a Single Resonator for Advanced Sensing,” *Submitted*, 2021.
- [141] R. E. Jacobsen, A. Krasnok, S. Arslanagic, A. V. Lavrinenko, and A. Alú, “Embedded eigenstate in a single resonator for sensing,” in *Conference on Lasers and Electro-Optics 2021 (CLEO)*, (San Jose (CA), US), pp. 1–2, 2021.

- [142] Fricke und Mallah, "Microwave technology at the highest level," 2021.
- [143] Industrial Microwave Systems, "Cylindrical Heating System," 2021.
- [144] P. Coronel, J. Simunovic, K. P. Sandeep, G. D. Cartwright, and P. Kumar, "Sterilization solutions for aseptic processing using a continuous flow microwave system," *Journal of Food Engineering*, vol. 85, pp. 528–536, apr 2008.
- [145] G. B. Gentili, M. Linari, I. Longo, and A. S. Ricci, "A coaxial microwave applicator for direct heating of liquids filling chemical reactors," *IEEE Transactions on Microwave Theory and Techniques*, vol. 57, pp. 2268–2275, jan 2009.
- [146] R. E. Jacobsen, S. Arslanagic, and A. V. Lavrinenko, "Mie Resonance-Based Continuous Heating Microwave Systems," *17th International Conference on Microwave and High Frequency Heating AMPERE 2019, Valencia, Spain, September 9-12, 2019*.
- [147] R. E. Jacobsen, S. Arslanagic, and A. V. Lavrinenko, "Continuous Heating Microwave System Based on Mie Resonances," *Journal of Physics: Conference Series (online)*, vol. 1461, no. 1, p. 12035, 2020.
- [148] B. I. Popa and S. A. Cummer, "Water-based metamaterials: Negative refraction of sound," *Nature Materials*, vol. 14, pp. 363–364, mar 2015.
- [149] C. F. Bohren and D. R. Huffman, *Absorption and scattering of light by small particles*. New York: John Wiley & Sons: Hoboken, 1 ed., 1983.
- [150] D. Tzarouchis and A. Sihvola, "Light Scattering by a Dielectric Sphere: Perspectives on the Mie Resonances," *Applied Sciences*, vol. 8, p. 184, jan 2018.
- [151] S. Jahani and Z. Jacob, "All-dielectric metamaterials," *Nature Nanotechnology*, vol. 11, pp. 23–36, jan 2016.
- [152] A. Petosa and A. Ittipiboon, "Dielectric resonator antennas: A historical review and the current state of the art," *IEEE Antennas and Propagation Magazine*, vol. 52, pp. 91–116, oct 2010.
- [153] J. D. Jackson, *Classical Electrodynamics*. New York: John Wiley & Sons, 3rd ed., 1999.

- 
- [154] L. Saiz, E. Guàrdia, and J. À. Padró, “Dielectric properties of liquid ethanol. A computer simulation study,” *Journal of Chemical Physics*, vol. 113, pp. 2814–2822, aug 2000.
- [155] N. Yu and F. Capasso, “Flat optics with designer metasurfaces,” *Nature Materials*, vol. 13, pp. 139–150, jan 2014.
- [156] S. B. Glybovski, S. A. Tretyakov, P. A. Belov, Y. S. Kivshar, and C. R. Simovski, “Metasurfaces: From microwaves to visible,” *Physics Reports*, vol. 634, pp. 1–72, may 2016.
- [157] R. Alaei, R. Filter, D. Lehr, F. Lederer, and C. Rockstuhl, “A generalized Kerker condition for highly directive nanoantennas,” *Optics Letters*, vol. 40, p. 2645, jun 2015.
- [158] J. K. Svaneborg, “Water-based metasurfaces for enhanced transmission of electromagnetic waves,” Master’s thesis, Technical University of Denmark, 2019.
- [159] R. E. Jacobsen, “Numerical and experimental characterization of reconfigurable all-dielectric metasurfaces,” Master’s thesis, Technical University of Denmark, Denmark, 2017.
- [160] TRIAX, “DIGI 14, LTE 700,” 2021.
- [161] TRIAX, “TDS 80A RAL 7016,” 2021.
- [162] C. A. Balanis, *Antenna theory: analysis and design*. New York ; Brisbane : J. Wiley, 1997.
- [163] R. W. Ziolkowski, “Using Huygens multipole arrays to realize unidirectional needle-like radiation,” *Physical Review X*, vol. 7, p. 031017, jul 2017.
- [164] M. C. Tang, Z. Wu, T. Shi, and R. W. Ziolkowski, “Dual-Band, Linearly Polarized, Electrically Small Huygens Dipole Antennas,” *IEEE Transactions on Antennas and Propagation*, vol. 67, pp. 37–47, jan 2019.
- [165] K. Entesari and A. P. Saghati, “Fluidics in microwave components,” *IEEE Microwave Magazine*, vol. 17, pp. 50–75, jun 2016.
- [166] Y. Huang, E. Sutter, L. M. Wu, H. Xu, L. Bao, H. J. Gao, X. J. Zhou, and P. Sutter, “Thick Layered Semiconductor Devices with Water Top-Gates: High

- On-Off Ratio Field-Effect Transistors and Aqueous Sensors,” *ACS Applied Materials and Interfaces*, vol. 10, no. 27, pp. 23198–23207, 2018.
- [167] C. W. Hsu, B. Zhen, J. Lee, S.-L. Chua, S. G. Johnson, J. D. Joannopoulos, and M. Soljačić, “Observation of trapped light within the radiation continuum,” *Nature*, vol. 499, pp. 188–191, jul 2013.
- [168] A. Krasnok, D. Baranov, H. Li, M.-A. Miri, F. Monticone, and A. Alù, “Anomalies in light scattering,” *Advances in Optics and Photonics*, vol. 11, p. 892, dec 2019.
- [169] “ROHACELL HF - High-performance structural foam cores,” 2021.
- [170] F. Monticone, H. M. Doleman, W. D. Hollander, A. F. Koenderink, A. Al, W. Den Hollander, A. F. Koenderink, and A. Alù, “Trapping Light in Plain Sight: Embedded Photonic Eigenstates in Zero-Index Metamaterials,” *Laser & Photonics Reviews*, vol. 12, p. 1700220, may 2018.
- [171] Z. Liu, Y. Xu, Y. Lin, J. Xiang, T. Feng, Q. Cao, J. Li, S. Lan, and J. Liu, “High-Q Quasibound States in the Continuum for Nonlinear Metasurfaces,” *Physical Review Letters*, vol. 123, p. 253901, dec 2019.
- [172] F. Monticone and A. Alù, “Embedded Photonic Eigenvalues in 3D Nanostructures,” *Physical Review Letters*, vol. 112, p. 213903, may 2014.
- [173] A. Stogryn and A. Stogryn, “Equations for calculating the dielectric constant of saline water,” *IEEE Transactions on Microwave Theory and Technology*, vol. 19, pp. 733–736,733–736, aug 1971.
- [174] M. Reagor, W. Pfaff, C. Axline, R. W. Heeres, N. Ofek, K. Sliwa, E. Holland, C. Wang, J. Blumoff, K. Chou, M. J. Hatridge, L. Frunzio, M. H. Devoret, L. Jiang, and R. J. Schoelkopf, “Quantum memory with millisecond coherence in circuit QED,” *Physical Review B*, vol. 94, p. 014506, jul 2016.
- [175] A. Blais, S. M. Girvin, and W. D. Oliver, “Quantum information processing and quantum optics with circuit quantum electrodynamics,” *Nature Physics*, vol. 16, no. 3, pp. 247–256, 2020.

